ISBN 978-82-326-1144-7 (printed version)
ISBN 978-82-326-1145-4 (electronic version)
ISSN 1503-8181

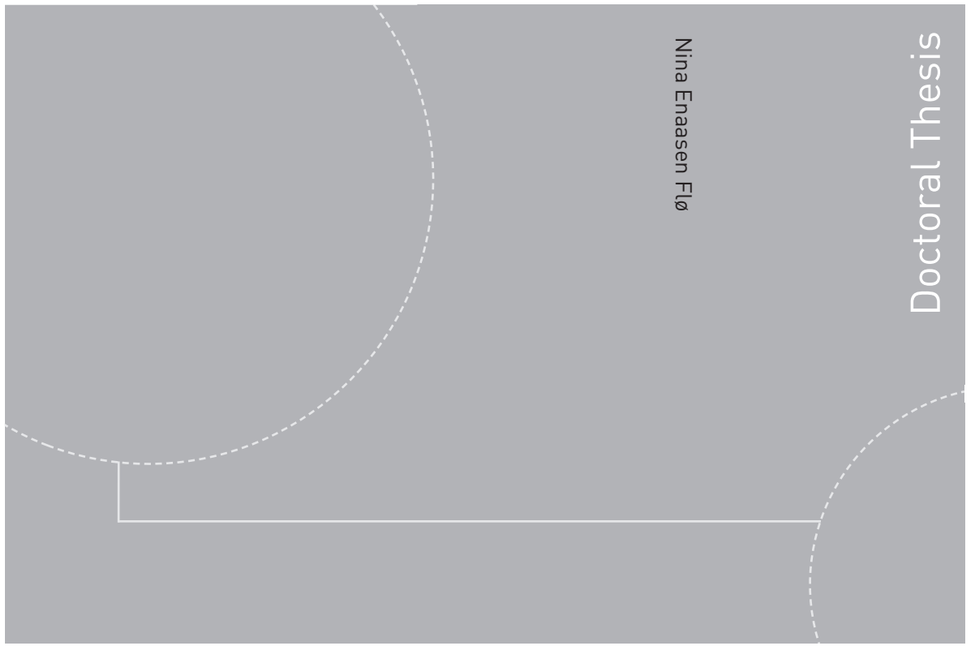

Doctoral theses at NTNU, 2015:244

Nina Enaasen Flø

Post-combustion absorption-based CO2 capture: modeling, validation and analysis of process dynamics

NTNU
Norwegian University of Science and Technology

Doctoral theses at NTNU, 2015:244

NTNU
Norwegian University of Science and Technology
Faculty of Natural Sciences and Technology
Department of Chemical Engineering

NTNU

NTNU
Norwegian University of Science and Technology

Nina Enaasen Flø

Post-combustion absorption-based CO_2 capture: modeling, validation and analysis of process dynamics

Thesis for the degree of Philosophiae Doctor

Trondheim, September 2015

Norwegian University of Science and Technology

NTNU
Norwegian University of
Science and Technology

NTNU
Norwegian University of Science and Technology

Thesis for the degree of Philosophiae Doctor

© Nina Enaasen Flø

ISBN 978-82-326-1144-7 (printed version)
ISBN 978-82-326-1145-4 (electronic version)
ISSN 1503-8181

Doctoral theses at NTNU, 2015:244

Printed by Skipnes Kommunikasjon as

NORWEGIAN UNIVERSITY OF SCIENCE AND TECHNOLOGY

Abstract

Faculty of Natural Sciences and Technology
Department of Chemical Engineering

Doctor of Philosophy

Post-combustion absorption-based CO_2 capture: modeling, validation and analysis of process dynamics

by Nina Enaasen Flø

Meeting the future energy demand while at the same time reducing carbon emissions to a sustainable level is one of the main global challenges in the years to come. Several technologies are suggested to reduce our carbon footprint, however, CCS is the only option where significant reductions can be achieved with the continued use of coal and other fossil fuels. Post-combustion CO_2 capture by chemical absorption is the most mature CCS technology and it has been demonstrated in laboratory and pilot plant scale for many years. Extensive modeling and simulation studies have also been performed in order to optimize the process design, improve the solvent systems and minimize the energy penalty related to solvent regeneration. Most of these studies are performed using steady state models that assume integrated power plants operating at a base load. However, operational issues and the performance of the capture process in a flexible perspective can only be evaluated using dynamic process models.

In the present work, a rigorous dynamic process model of post-combustion amine-based CO_2 absorption is developed in MATLAB®. The process model contains dynamic unit models developed from first principle conservation laws, basic PI-controllers and sub-models for physical, chemical and thermodynamic properties for the H_2O-CO_2-MEA system. A similar process model is also developed in the K-Spice® general simulation tool using the embedded library of process units. Thermodynamic data are generated in Multiflash™ and imported as data tables.

Various approaches for modeling the effects of mass transfer and chemical reaction rates are assessed and it is concluded that the rate-based approach is preferred for accurate steady-state predictions of the absorber temperature and concentration profiles. A simplified equilibrium-stage model gives similar transient results and is considered adequate for prediction of transient responses of the process; however, the absorber profiles are less accurate. Two different correlation sets for mass transfer and column hydraulics are also implemented. The Billet correlations underpredict the effective interface area and must be adjusted by a factor of 2.25 -

2.5 in order to meet the desired absorption rates. The correlations by Rocha give adequate predictions without any adjustments.

The availability of specific dynamic test data in the literature has been scarce, thus proper model validation has remain problematic. A pilot plant campaign with specific focus on process dynamics was therefore planned and executed in the Gløshaugen pilot plant as part of this project. A considerable amount of both steady state and dynamic data sets are obtained, and a very good steady state CO_2 mass balance supports their reliability. CO_2 loading is successfully correlated with online density measurements to provide a detailed time description of the solvent dynamics.

The developed process models are validated against pilot plant data from the Gløshaugen pilot plant and three larger CO_2 capture pilot plants. This gives adequate confidence in the process models, and it is concluded that the simulated transient responses in absorption/desorption rates are in general good agreement with the experimental results. Some stationary deviations are observed, which are believed to be related to inaccuracies in the empirical models used for prediction of mass transfer and effective interface area. However, given the experimental measurement uncertainties, it is concluded that both process models provide satisfactory predictions.

The validated process models are utilized for investigations of process dynamics. The MATLAB model of the Tiller pilot plant is used to investigate time constants at different locations in the process in order to determine the dominant dynamics. It is concluded that considerable stabilization times are required for operational changes that affect the solvent CO_2 loading due to the effect of recirculating the solvent on a closed loop. The overall stabilization time of the process is therefore up to 6 hours, even though the total solvent residence time is only 2 - 3 hours. The transient effects of chemical reaction and heat and mass transfer rates in the absorber column are believed to be very limited.

The K-Spice model of the Brindisi pilot plant is utilized to simulate four different modes of flexible operation based on hypothetical scenarios with varying electricity demand and prices. The CO_2 capture process reacts quickly to power plant load changes, and it is able to stabilize at both part and full load operation. The operating mode of solvent storage gives satisfactory results when it comes to instantaneous and time average capture rate and energy performance in a varying electricity market. However, considerable investments are required for solvent storage tanks and additional operating solvent. The modes of exhaust gas venting and varying solvent regeneration seem to work satisfactory and are easy to conduct without major process modifications. However, these modes rely on the possibility of relaxing the constraint of 90% capture rate for short periods and later increasing it above 90% in order to obtain a 90% time average capture rate.

Acknowledgements

I would like to express my sincere gratitude to all those who made it possible for me to complete this thesis.

First and most of all, I would like to gratefully thank my supervisors, Professor Magne Hillestad and Senior Research Scientist Hanne Kvamsdal, for giving me the opportunity to write my doctoral thesis under their supervision. They have always been supportive, available for discussions and open to share knowledge, and I appreciate their continuous guidance, encouragement and optimism. They are also thanked for giving me the opportunity to contribute to the *Octavius* project. Hanne deserves to be specially thanked for her support and company during the time we stayed abroad together in Austin, Texas. I appreciate the nice outdoor lunches, the everyday discussions and getting to know her also as a friend.

I owe my deepest gratitude to Associate Professor Hanna Knuutila. Her proposal for performing dynamic pilot plant testing has become one of the more important parts of this thesis and certainly a great learning experience for myself. Thanks to Hannas creative mind and her numerous hours working in the pilot plant with me I have gained confidence in the developed process model and proven that it is able to predict realistic results. Her support and encouragement is highly appreciated.

I would also like to thank all my colleagues in the CO_2 technology groups at NTNU, SINTEF and UT at Austin, who all provided amazing work environments. Professor Hallvard Svendsen at NTNU is thanked for his inspiring passion for CO_2 capture. Research Scientist Andrew Tobiesen in SINTEF is thanked for the educational discussions concerning the network solver and for letting me participate in the work making CO2SIM dynamic. Professor Gary Rochelle at UT at Austin is acknowledged for accepting me as a visiting student in his group for 6 months. Professor Rochelle and his group are also thanked for the rewarding discussions and suggestions to my project and for sharing their knowledge, but also for their hospitality and friendships. I would also like to thank Lisbeth Roel at the Department of Chemical Engineering at NTNU and Maeve Cooney at the McKetta Department of Chemical Engineering at UT for all the help managing both small and big administrative problems. Further, I wish to express my special appreciation to my co-workers Diego, Juliana and Solrun Johanne who I also have become close friends with. It's been a pleasure to know them and I hope we still will keep

in touch in the future. The master students who I've been working with during this final stage of the PhD are also thanked, especially Linn for her efforts analyzing the TCM pilot plant data and performing model validation, which is a direct contribution to this thesis. I have really enjoyed getting to know her and working with her has been a pleasure. I wish her all the best for the future.

I appreciate the financial support from the BIGCCS Centre and its partners ConocoPhillips, Gassco, Shell, Statoil, TOTAL, GDF SUEZ and the Research Council of Norway. The European FP7 *Octavius* project is also gratefully acknowledged for the contributions.

Besides all my professional colleagues, I have had strong and continuous support from my dear family and close friends. I'd specially like to thank my parents, Aud and Ole, who have continuously encouraged me through all the years of studies. My parents, my brother and sister and my parents in law are also highly appreciated for their love and support, and for all nice moments we shared. My American roommate, Sara, has earned a big place in my heart and she is gratefully thanked for her hospitality, love and friendship. So are her lovely family, her boyfriend, Todd, and next-door neighbors, Terese, Elaine and Gorman. Lastly, but not least, a very special thanks to my wonderful husband, Øyvind, for his constant love and patience throughout these years. His support has provided me an excellent foundation to focus on my research, and a pleasant and relaxing atmosphere to come home to after work. I would never have accomplish this thesis without him and words can not express how grateful I am for his support.

Contents

List of Figures

List of Tables

Acronyms

2DS	**2**°C **S**cenario
4DS	**4**°C **S**cenario
6DS	**6**°C **S**cenario
AE	**A**lgebraic **E**quation
ARD	**A**verage **R**elative **D**eviation
ASU	**A**ir **S**eparation **U**nit
AVG	**A**verage
CAPEX	**C**aptial **E**xpenditures
CCS	**C**arbon **C**apture and **S**torage
CHP	**C**ombined **H**eat and **P**ower
CV	**C**ontrol **V**ariable
DAE	**D**ifferential and **A**lgebraic **E**quations
EQ	**E**quilibrium-stage
FTIR	**F**ourier **T**ransform **I**nfrared
GC	**G**as **C**hromatography
GDP	**G**ross **D**omestic **P**roduct
GHG	**G**reen **H**ouse **G**as
IEA	**I**nternational **E**energy **A**gency
IGCC	**I**ntegrated **G**asificaton **C**ombined **C**ycle
IPDAE	**I**ntegral, **P**artial **D**ifferential and **A**lgebraic **E**quations
IPPC	**I**ntergovernmental **P**anel on **C**limate **C**hange
IR	**I**nfrared
LC	**L**evel **C**ontroller

MEA	**M**onoethanolamine
MP	**M**edium **P**ressure
MPC	**M**odel **P**redictive **C**ontrol
MV	**M**anipulated **V**ariable
NEQ	**N**on-**E**quilibrium
ODE	**O**rdinary **D**ifferential **E**quation
OPEX	**O**perating **E**xpense
PCC	**P**ost-**C**ombustion **C**apture
PDAE	**P**artial **D**ifferential and **A**lgebraic **E**quations
PDE	**P**artial **D**ifferential **E**quation
PI&D	**P**iping and **I**nstrumentation **D**iagram
PID	**P**roportional-**I**ntegral-**D**erivative
P-F	**P**ressure **F**low
PV	**P**rocess **V**alue
RD	**R**elative **D**eviation
RFCC	**R**esidue **F**luid **C**atalytic **C**racker
SP	**S**et-**P**oint
SRD	**S**pecific **R**eboiler **D**uty
TAME	**T**ert-amyl methyl ether
TCM	**T**echnology **C**entre **M**ongstad
TOC	**T**otal **O**rganic **C**arbon
VLE	**V**apor **L**iquid **E**quilibrium

Symbols

Latin symbols		
a	$[m^2/m^3]$	specific area
A	[-]	matrix of first derivative weights in the collocation method
A	$[m^2]$	area
B	[-]	matrix of second derivative weights in the collocation method
B		base
B_p		packing specific constant
$\bar{C}$	[mol/kg]	molal concentration
C	$[kmol/m^3]$	molar concentration
C_0	[-]	packing specific constant
C_1	[-]	packing specific constant
C_2	[-]	packing specific constant
C_3	[-]	packing specific constant
C_E	[-]	packing specific constant
C_g	[-]	packing specific constant
C_l	[-]	packing specific constant
C_p	$[kJ/(kmol\,K)]$	specific heat capacity at constant pressure
C_v	$[kJ/(kmol\,K)]$	specific heat capacity at constant volume
d_h	[m]	hydraulic diameter
d_p	[m]	particle diameter
D	$[m^2/s]$	diffusivity

$e(t)$		controller error
E	[-]	enhancement factor
F	[kmol/s]	molar flow rate
$\bar{F}$	[kg/h]	mass flow rate
F_{v}		gas load factor
F_{SE}		packing specific factor for surface enhancement
F_{t}		packing specific correction factor
g	$\mathrm{m/s^2}$	gravity constant
G	$[\mathrm{kmol/(m^2\,s)}]$	molar flux
$\bar{G}$	$[\mathrm{kg/(m^2\,s)}]$	mass flux
h	m	height
h	kJ/kmol	molar enthalpy
$\hat{h}$	$[\mathrm{kW/(m^2\,K)}]$	heat transfer coefficient
H	[kJ]	enthalpy
H_l	[m]	level
Ha	[-]	Hatta modulus
He	$[\mathrm{kPa\,m^3/kmol}]$	Henry's law constant
$J_{\mathrm{g/l}}$	$[\mathrm{kmol/(m^2\,s)}]$	Gas-liquid interface mass flux
k	[m/s]	film mass transfer coefficient
k_{rx}	$[\mathrm{m^3/(kmol\,s)}]$	reaction constant
K_2	[-]	packing specific constant
K_{L}	$[\mathrm{kmol/(s\ mbar\sqrt{kPa})}]$	valve constant
K_{Q}	[kW/K]	valve constant
K_{V}	$[\mathrm{kmol/(s\ bar\sqrt{kPa})}]$	valve constant
K_{tot}	$[\mathrm{kmol/(m^2\,s\,kPa)}]$	Overall mass transfer coefficient
$\frac{L}{G}$	[(kg/h)/(kg/h)]	liquid-to-gas ratio
m	[kg/h]	absorption rate
M	[g/mol]	molecular weight
N	[kmol]	molar hold-up
nc	[-]	number of components
P	[kPa]	pressure

$\dot{q}$	[kW/m^2]	heat flux
Q	[kW]	heat
Q	[-]	matrix of quadrature weights in the collocation method
r	[1/s]	reaction rate
R	[J mol/K]	universal gas constant
S	[m]	side dimension of corrugation
t	[s]	time
T	[K]	temperature
$\bar{T}$	[°C]	temperature
u	[m^3/(m^2 s)]	superficial velocity
$u(t)$		control variable
$\bar{u}_\mathrm{l}$	[m/s]	mean effective velocity
H	[kJ]	internal energy
V	[m^3]	volume
V^E	[m^3/mol]	excess molar volume
w	[g/g]	weight fraction
x	[mol/mol]	liquid mole fraction
y	[mol/mol]	gas mole fraction
z	[m]	axial column coordinate

Greek symbols

α	[molCO_2/molMEA]	CO_2 loading
β		ratio of effective to total packing surface area
δ		direction
Δ		difference
$\Delta h^\mathrm{abs}_{CO_2}$	[kJ/kmol]	heat of absorption of CO_2
Δh^vap	[kJ/kmol]	heat of vaporization
η	[Pa s]	viscosity
ε		void fraction or phase hold-up
Φ	[-]	volume expansion

γ	°	contact angle between solid and liquid film
μ	[kg/(m s)]	dynamic viscosity
ν	[-]	stoichiometric coefficient
Ψ_l		resistance coefficient
ρ	[kg/m^3]	density
σ	[kg/s^2]	surface tension

Dimensionless groups

$Fr_l = \frac{u_l^2}{Sg}$	Froude number for liquid
$Re_g = \frac{u_g d_p}{(1-\varepsilon_{void})\mu_g} K$	Reynolds number for gas
$Re_l = \frac{u_l S \rho_l}{\mu_l}$	Reynolds number for liquid
$We_l = \frac{u_l^2 \rho_l S}{\sigma_l}$	Weber number for liquid

Subscripts

∞	infinity
abs	absorber
Am	amine
app	apparent
b	base
b	bulk
c	cold
col	column
cond	condenser
des	desorber
DC	DeCoursey
e	effective
ex	external
fl	flooding point
g	gas
g/l	gas-liquid interface
h	hot

h	horizon
hx	heat exchanger
i, j	indices
if	interface
in	inlet
l	liquid
lean	lean solvent
o	operating
reb	reboiler
rich	rich solvent
obs	observed
out	outlet
s	loading point
sur	surroundings
tot	total

Superscripts

eq*	equilibrium
g	gas
l	liquid
sol	unloaded solution
sp	set-point
T	termolecular

Chapter 1

Introduction

1.1 Background

1.1.1 Economic growth and increasing energy consumption

Global population growth along with an increasing scale of economic activity, which is reflected by growth in gross domestic product (GDP), have resulted in increasing global energy consumption. The world's current energy production is largely based on fossil fuels as indicated by the global electricity generation in Figure 1.1.

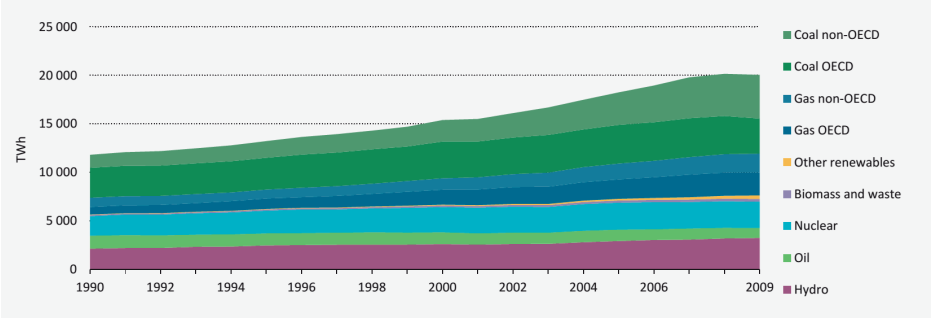

FIGURE 1.1: Global electricity generation by fuel (IEA, 2012).

Fossil-fuel based energy production remains the primary driver for greenhouse gas (GHG) emissions. In fact, 35% of the GHG emissions in 2010 were released by the energy sector, as seen in Figure 1.2, and the total annual anthropogenic GHG emissions has increased by about 10 $GtCO_2$-equivalent between 2000 and 2010

(IPCC, 2014). If current trends persist, the IEA (2012) predicts that both the global energy demand and GHG emissions will double by 2050.

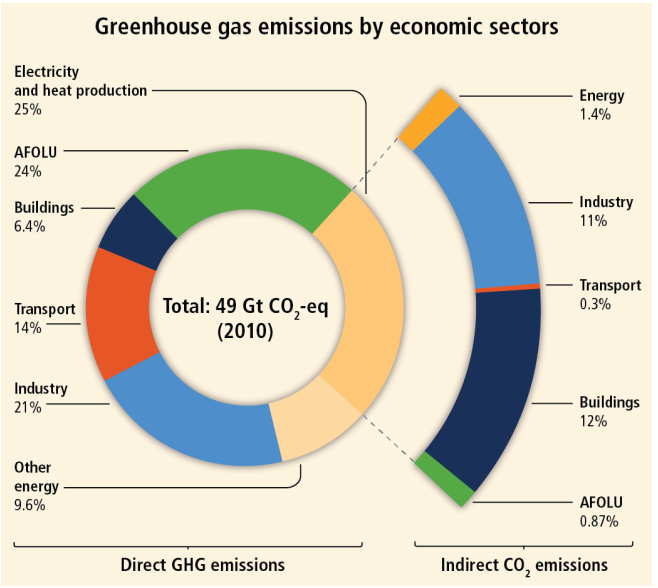

FIGURE 1.2: Total anthropogenic greenhouse gas emissions ($GtCO_2$-equivalent per year) from economic sectors in 2010 (IPCC, 2014).

1.1.2 CCS - an absolute necessity

The most recent report by the Intergovernmental Panel on Climate Change (IPCC) states clearly that human actions are "very likely" (meaning a 90% or greater probability) to be the dominant cause of the observed global warming since 1950 (IPCC, 2014). The report provides clear evidence of globally increasing average temperature, sea level, atmospheric greenhouse gas concentrations and anthropogenic CO_2 emissions, as shown in Figure 1.3. Further, it is highlighted that these developments are occurring faster than anticipated.

We are already seeing the effects of global warming, as some of the changes in extreme weather and climate events observed since 1950 have been linked to human influence. Continued emission of GHGs will cause further warming and changes in the climate system. The more we disrupt our climate, the more we risk severe and irreversible impacts such as food and water shortages, increased displacement of people, increasing poverty and coastal flooding. At the same time IPCC (2014)

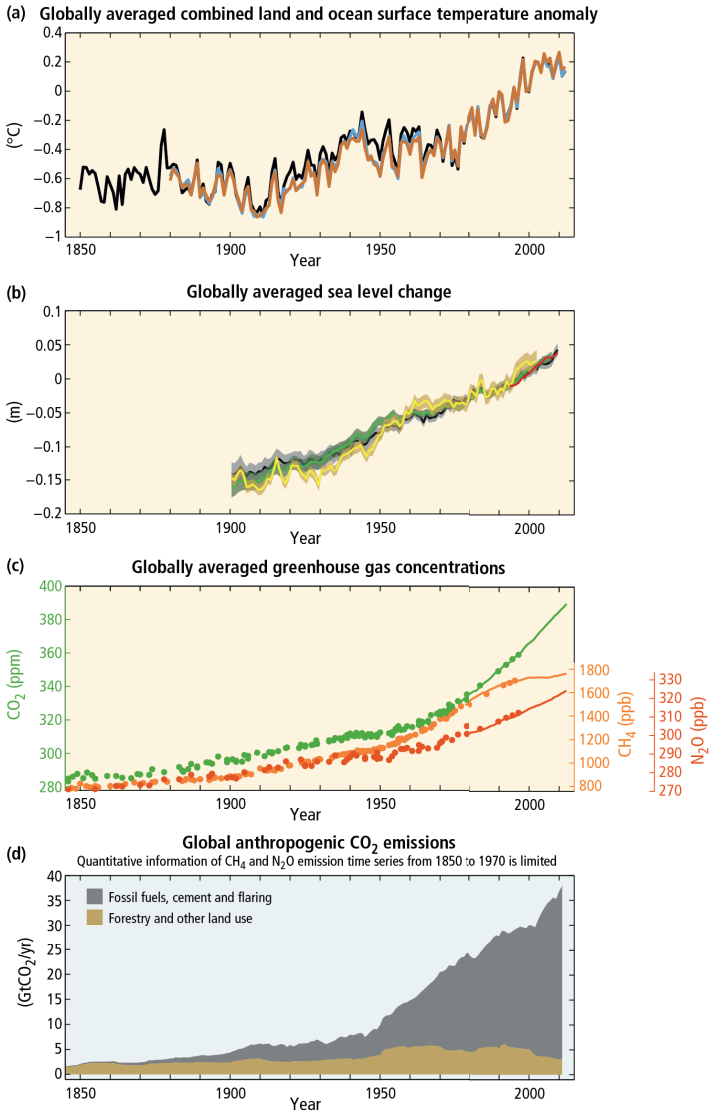

FIGURE 1.3: Observations and other indicators of a changing global climate system (IPCC, 2014). (a) Observed annually and globally averaged combined land and ocean surface temperature anomalies relative to the average over the period 1986 to 2005. (b) Observed annually and globally averaged sea level change relative to the average over the period 1986 to 2005. (c) Observed atmospheric concentrations of the greenhouse gases carbon dioxide (CO_2, green), methane (CH_4, orange) and nitrous oxide (N_2O, red). (d) Global anthropogenic CO_2 emissions.

highlights that we already have the means to limit climate change and build a more prosperous, sustainable future.

The International Energy Agency (IEA) predicts various potential future scenarios reflecting different ambition levels of global GHG emission reductions. What they call the 6°C Scenario (6DS) is largely an extension of current trends. In the absence of efforts to stabilize atmospheric concentrations of GHGs, the average global temperature rise is projected to be at least 6°C in the long term (4°C by 2100) compared to pre-industrial time. The 4°C Scenario (4DS) reflects stated intentions by countries to limit emissions and improve energy efficiency. The projections are 4°C in the long term (3°C by 2100) compared to pre-industrial time. The 2°C Scenario (2DS) describes an energy system consistent with an emission trajectory that recent scientific climate research indicates would give an 80% chance of limiting average global temperature increase to 2°C. It sets the target of cutting energy-related CO_2 emissions by more than half in 2050 compared to 2009, and ensuring that they continue to fall thereafter (IEA, 2012).

Potential sectors and key technologies that can halve CO_2 emissions in order to achieve the 2DS goal are presented in Figure 1.4. The power generation and industry sectors provide the largest contribution with 60% of the total CO_2 emission reduction. Other important sectors are the transport and building sectors. When it comes to technologies, a large increase in the use of renewable energy sources provides almost one third of the total CO_2 emission reduction. Carbon capture and storage (CCS) also contributes a major share with 20% of the total reductions. IEA (2009) has in fact estimated that without CCS, the overall costs to reduce the emissions by 50% over the period to 2050 would increase by 70%.

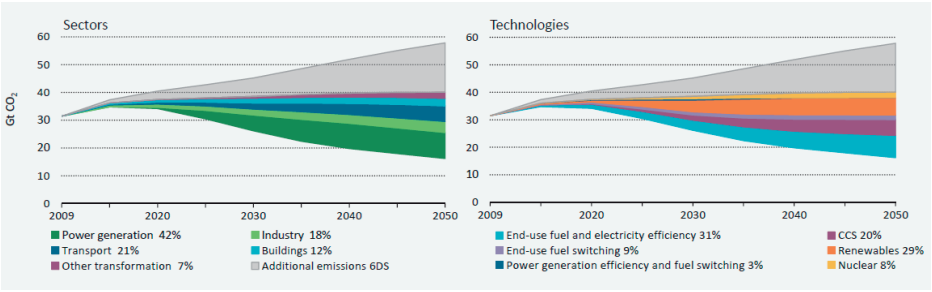

FIGURE 1.4: Key technologies to reduce CO_2 emissions in the 2DS (IEA, 2012).

There is no doubt that meeting the future energy demand while at the same time reducing carbon emissions to a sustainable level is one of our main global

challenges in the years to come. Achieving the 2DS requires a collective effort in every aspect: no single fuel, technology or sector can deliver a dominant proportion of the necessary emission reductions – all are necessary to varying degrees. CCS is however the only option to achieve significant CO_2 emission reductions with the continued use of coal and other fossil fuels.

1.1.3 CCS technology overview

Carbon capture and storage refers to a suite of technologies developed to capture and store CO_2 produced from the use of coal and other fossil fuels or biomass. It consists of the separation of CO_2 from industrial and energy related sources, transport to a storage location and long-term isolation from the atmosphere. The capture step involves separating CO_2 from a gas stream which is diluted by the presence of nitrogen and water vapor, and purifying it to produce a highly concentrated stream of CO_2 that is suitable for storage. After the CO_2 is separated, it is compressed for transport by pipeline or ship to a geological storage site, where it is injected underground (IPCC, 2005).

Carbon capture technology is most suitable for capturing CO_2 from large-point sources such as coal-fired power plants and large energy intensive industries such as cement, steel and oil refining. There are three possible pathways for CO_2 capture: post-combustion, pre-combustion and oxy-fuel capture. Figure 1.5 shows a schematic diagram of the three possible capture technologies.

Post-combustion CO_2 capture (PCC) involves separation of CO_2 from industrial gas streams or flue gas produced by combustion of fossil fuel or biomass in air. The most common technique is chemical solvent scrubbing or absorption where a liquid solvent is utilized to capture the fractions of CO_2 present in the flue gas stream (typically 3 - 15 vol% CO_2) at close to ambient pressure (Wang et al., 2011). The solvent is afterward regenerated by heating to produce a nearly pure gas stream of CO_2, while the regenerated solvent is reused. This is a well known and established technology for the separation of CO_2 that has been used in several decades for different purposes. The separation of CO_2 from raw natural gas is for instance practiced on a large scale, using technologies similar to those of post-combustion capture. The most commonly used solvent is monoethanolamine (MEA); however, a number of alternative solvents has been developed in recent years (Wang et al.,

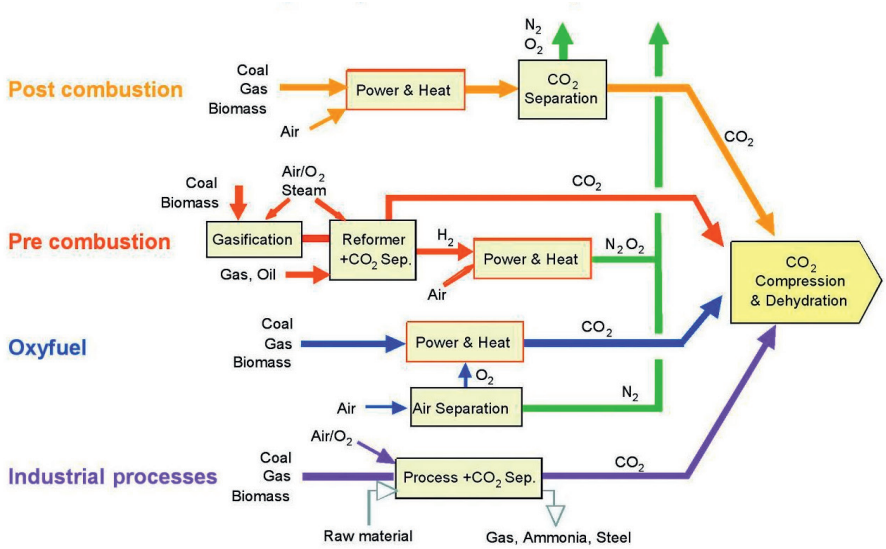

FIGURE 1.5: Schematic representation of CO_2 capture technologies (IPCC, 2005).

2011). Other possible post-combustion technologies are adsorption using solid sorbents and membrane separation of CO_2 (Wang et al., 2011).

In pre-combustion CO_2 capture, the CO_2 is removed prior to the combustion. The fuel is first processed in a reactor with steam and air or oxygen to produce a mixture consisting mainly of carbon monoxide (CO) and hydrogen (H_2), known as "synthesis gas". Additional H_2 together with CO_2 is produced by reacting the CO with steam in a second reactor, called "water-gas shift reactor". The resulting mixture of H_2 and CO_2 is then separated by capturing the CO_2, leaving a carbon-free stream of H_2 that can be combusted to generate heat and/or power. Although the initial fuel conversion steps are more elaborate and costly than in post-combustion systems, the high concentrations of CO_2 produced by the shift reactor (typically 15 to 60% by volume on a dry basis) and the high pressures often encountered in these applications are more favorable for CO_2 separation. Solvent scrubbing or absorption is also a common technique for pre-combustion CO_2 capture. However, due to very different conditions compared to post-combustion systems, other solvents are used in this case. Typically physical solvents are applied in pre-combustion capture, whereas chemical solvents are common in post-combustion capture. Physical solvent scrubbing is already established at large scale for sulfur removal in integrated gasificaton combined cycle (IGCC) plants and CO_2 removal in large-scale production of hydrogen for ammonia and fertilizer manufacturing. However,

demonstration of pre-combustion CO_2 capture by physical absorption has not yet been attempted in a full-scale power plant. Other possible pre-combustion techniques are sorbent enhanced reforming where the water-gas shift reaction is combined with the CO_2 capture step using high-temperature sorbents, or membrane separation of H_2 (IPCC, 2005).

Oxy-fuel combustion systems use oxygen instead of air for combustion of the fuel and the resulting flue gas consists mainly of CO_2 (usually more than 80 vol%) and water vapor. Water is easily separated from CO_2 by condensation. This eliminates the need for solvents and the associated environmental impacts. An upstream air separation unit (ASU) is however required to produce pure oxygen for combustion, which is quite costly and energy intensive. Combustion with pure oxygen also leads to high flue gas temperatures which require selection of special materials. An advanced variant of oxy-combustion is chemical-looping combustion. This technology uses a metal oxygen carrier such as oxides of iron, nickel or copper to transfer the oxygen for combustion of the fuel. The oxygen carrier is reduced during oxidizing of the fuel, and must therefore be transported to a separate reactor for re-oxidizing with air. Oxy-fuel combustion for CO_2 capture is currently only in the demonstration phase (IPCC, 2005).

Various CO_2 capture technologies are already used in several industrial applications. However, the realization of industrial scale CCS has remained limited. Research is being conducted to achieve higher levels of system integration, increased efficiency and reduced cost for industrial scale CCS. The choice of capture technology is determined largely by the process conditions under which it must operate. The main advantage of post-combustion CO_2 capture is that the technology is much more mature than the alternatives of pre-combustion and oxy-fuel combustion CO_2 capture. It has been demonstrated in laboratory and pilot plant scale for many years, and the technology has been proven to work. Further it does not require substantial modifications when applied to power plants and can therefore be easily implemented as retrofit to existing conventional power production units. Recently, a number of full-scale post-combustion CO_2 capture demonstration projects are being developed, and the world's first large-scale power sector CCS project named "Boundary Dam" was commissioned in October 2014 in the Saskatchewan province in Canada. The capture facility is attached to a 110 MW coal fired power unit operated by SaskPower and the captured CO_2 is injected into nearby oilfields to enhance petroleum production (SaskPower, 2015).

The main challenge of the post-combustion technology is the energy intensive CO_2 separation step, which represents about $75 - 80\%$ of the total cost of CCS (Davison, 2007). Research is directed to process optimization and new solvent development in order to improve the process economics.

1.1.4 Dynamic modeling of post-combustion CO_2 capture

Before full-scale post-combustion CO_2 capture is realized it is also essential to have a broad understanding of the operational behavior of the plant, both at steady state conditions and during transient operation. Process modeling is a useful and cost-effective tool for gathering such information and several steady state models of the CO_2 absorption plant have been developed and verified to experimental data. However, in order to predict the transient effects of conditions that are superimposed on the capture plant, a dynamic model is required (Kvamsdal et al., 2009). Power plants might operate in a flexible manner according to varying electricity demand and prices, thus an attached capture plant might be exposed to large and frequent load changes. Knowledge on the transient behavior during these load changes is therefore of great importance for commercializing the CO_2 capture process, and dynamic modeling and simulation can be a useful tool in order to gain understanding of the transient responses and resolve challenges related to these issues. Dynamic simulations will also provide useful information on how the capture process is able to adapt to other possible changes or external disturbances. The flue gas CO_2 concentration might for instance change for different power plant fuel specifications, and possible effects of such changes should be investigated. Proper control systems must also be developed, and a dynamic model can be further utilized in advanced control systems. Start-up and shut-down procedures should be established prior to commercialization, in which dynamic simulators can play an important role. Finally, dynamic simulators can also be used for the training of operating personnel.

1.2 Objectives of the thesis

The objectives of the present thesis are fourfold:

1. Development of a complete dynamic process model for post-combustion CO_2 capture based on chemical absorption.
2. Generation of dynamic pilot plant data for model validation.
3. Steady state and dynamic model validation towards relevant pilot plant data.
4. Application of the developed process model for analyses of important dynamics.

1.3 Outline of the thesis

Chapter 2 presents a detailed process description along with information on the relevant pilot plants used as basis for the model development and validation.

Chapter 3 gives an experimental overview and presents relevant results from the dynamic pilot plant campaign conducted in the Gløshaugen pilot plant.

Chapter 4 describes the development of the dynamic CO_2 capture plant models and presents analyses concerning choice of model complexity and empirical correlations.

Chapter 5 presents the results of dynamic model validation towards collected pilot plant data.

Chapter 6 presents analyses of the CO_2 capture process dynamics using the developed capture plant models.

Finally, conclusions and recommendations for future work are given in Chapter 7.

1.4 Main contributions

This PhD work is mainly performed as part of the BIGCCS project which is among the largest CCS research centers on global scale. A second part of the work is performed as part of the *Octavius* project, which is a FP7 project dedicated to CO_2 capture and storage.

The main contributions of the thesis are:

- **A literature review on dynamic modeling of post-combustion CO_2 capture based on amines.** The review given in Paper A examines the details and complexity of the dynamic models developed at the point. Issues related to transient behavior of the CO_2 capture process and interactions with power plants are summarized, and knowledge gaps and areas that still need more attention are emphasized. A more recent review by Bui et al. (2014) reveals that the activity on dynamic modeling of post-combustion CO_2 capture has increased considerably, but many of the same challenges and questions are still not resolved.

- **Dynamic model development of the post-combustion amine-based CO_2 capture process.** Most research on the CO_2 absorption process has previously been focused on steady state performance, and numerous publications exist on this topic. The recent years have also seen growing attention towards examination of the dynamic behavior of post-combustion CO_2 capture and a considerable effort has been put into the research and model development in dynamic mode. The dynamic process models developed in the present work are implemented using two separate tools for the two different research projects that are covering this work. The process model developed within the BIGCCS project is implemented in MATLAB®, while K-Spice® general dynamic simulation tool is utilized within the *Octavius* project. Paper D and E describes the development and implementation of the K-Spice and MATLAB models, respectively. MEA is the selected amine in the present work, and a complete overview of empirical correlations for heat and mass transfer, column hydraulics and chemical and physical properties that are needed in the model are given as part of this thesis. Many of the dynamic process models that are developed recently include only one single or a few selected process units. Both process models developed in the

present work include all process equipment that are regarded as important for the dynamics. Evaluations of various model complexities are also given as part of the model development. This includes an evaluation of two different set of correlations for estimating mass transfer coefficients and column packing hydraulics, a comparison of the rate-based modeling approach to a simplified equilibrium-stage approach, and an evaluation of two different numerical solution methods for the complete flow sheet model.

- **Generation of relevant pilot plant data for model validation.** The availability of dynamic data for model validation has been mentioned as a challenge by several researchers. This work includes generation of dynamic pilot plant data sets from a specifically designed pilot plant campaign in the Gløshaugen pilot plant. A large range of plant operating conditions and relevant open loop set-point responses are collected, and the data are available on request for anyone who may be interested.

- **Procedures and experiences concerning steady state and dynamic model validation.** Both model implementations are validated against steady state and dynamic pilot plant data. The process model developed in K-Spice is validated against data from the Brindisi pilot plant as part of the *Octavius* project. The results are presented in Paper D. The MATLAB model is validated against data from the Gløshaugen pilot plant (given in Paper E), along with data from two larger pilot plants as presented in Section 5.1.2 and 5.1.3. Experiences and insight into the validation procedures is given.

- **Analysis of the dominating process dynamics.** An investigation of typical time constants at various locations of the process for different operational set-point changes is given in Section 6.1. These measures gives insight into the main inertia of the process. Various process units are accordingly categorized based on their effect on and contribution to the overall dynamic progress. The work will be published as Paper F.

- **Analysis of the transient performance during flexible operation.** An evalutaion of various flexible operation modes based on a simulation study. The results are given in Section 6.2 and will be published as Paper G.

1.4.1 List of publications

First author contributions

(B) N. Enaasen, A. Tobiesen, H. M. Kvamsdal and M. Hillestad, 2013. Dynamic Modeling of the Solvent Regeneration Part of a CO_2 Capture Plant. *Energy Procedia* 37, 2058–2065.

(C) N. Enaasen, A. Tobiesen, H. M. Kvamsdal and M. Hillestad, 2013. A Numerical Solution Strategy for Dynamic Simulation of Post-combustion CO_2 Capture. *Energy Procedia* 37, 1670–1677.

(D) N. Enaasen, L. Zangrilli, A. Mangiaracine, T. Mejdell, H. M. Kvamsdal and M. Hillestad, 2014. Validation of a Dynamic Model of the Brindisi Pilot Plant. *Energy Procedia* 63, 1040–1054.

(E) N. E. Flø, H. Knuutila, H. M. Kvamsdal and M. Hillestad, 2015. Dynamic model validation of the post-combustion CO_2 absorption process. *International Journal of Greenhouse Gas Control 41, 127–141.*

(F) N. E. Flø, H. M. Kvamsdal, M. Hillestad and T. Mejdell, 2015. Dominating Dynamics of the Post-combustion CO_2 Absorption Process. Submitted to *Computers & Chemical Engineering.*

(G) N. E. Flø, H. M. Kvamsdal and M. Hillestad, 2015. Dynamic Simulation of Post-combustion CO_2 Capture for Flexible Operation of the Brindisi Pilot Plant. Submitted to *International Journal of Greenhouse Gas Control.*

Co-author contributions

(A) A. Chikukwa, N. Enaasen, H. M. Kvamsdal and M. Hillestad, 2011. Dynamic Modeling of Post-combustion CO_2 Capture Using Amines – A Review. *Energy Procedia* 23, 82–91.

1.4.2 List of presentations

1. A. Chikukwa, N. Enaasen, H. M. Kvamsdal and M. Hillestad. Dynamic Modeling of Post-combustion CO_2 Capture Using Amines – A Review. TCCS-6, Trondheim, Norway, June 14th - 16th, 2011. (Poster presentation)

2. N. Enaasen, H. M. Kvamsdal and M. Hillestad. Dynamic modeling of post-combustion CO_2 capture. BIGCCS Internal seminar, Trondheim, Norway, December 14th, 2011. (Oral presentation)

3. N. Enaasen, H. M. Kvamsdal and M. Hillestad. Dynamics of the interaction between power generation and capture plant. UTCCS-1, Austin, Texas, USA, January 25th - 27th, 2012. (Oral presentation)

4. N. Enaasen, A. Tobiesen, H. M. Kvamsdal and M. Hillestad. CO2SIM - SOLVit software for simulation of absorption based CO_2 capture. SOLVit Workshop, September 12th - 13th, 2012. (Oral presentation)

5. N. Enaasen, H. M. Kvamsdal and M. Hillestad. Dynamic modeling of post-combustion CO_2 capture. BIGCCS PhD seminar, Trondheim, Norway, September 20th, 2012. (Oral presentation)

6. N. Enaasen, A. Tobiesen, H. M. Kvamsdal and M. Hillestad. Dynamic modeling of the solvent regeneration part of a CO_2 capture plant. GHGT-11, Kyoto, Japan, November 18th - 22th, 2012. (Oral presentation)

7. N. Enaasen, A. Tobiesen, H. M. Kvamsdal and M. Hillestad. A Numerical Solution Strategy for Dynamic Simulation of Post-combustion CO_2 capture. GHGT-11, Kyoto, Japan, November 18th - 22th, 2012. (Poster presentation)

8. N. Enaasen, A. Tobiesen, H. M. Kvamsdal and M. Hillestad. A Numerical Solution Strategy for Dynamic Simulation of Post-combustion CO_2 capture. Joint Research Review Meeting, Kyoto, Japan, November 23th, 2012. (Oral presentation)

9. N. Enaasen, H. M. Kvamsdal and M. Hillestad. Dynamic unit modeling and dynamic process plant modeling for CO_2 capture. Group meeting at UT, Austin, USA, February 20th, 2013. (Oral presentation)

10. N. Enaasen, A. Tobiesen, H. M. Kvamsdal and M. Hillestad. Verification of Basic Control System for Post-combustion CO_2 Capture Based on Power Plant Load Change. TCCS-7, Trondheim, Norway, June 4th - 6th, 2013. (Oral presentation)

11. N. Enaasen, M. Hillestad, H. M. Kvamsdal, T. Mejdell and G. Haugen. Dynamic process model of Brindisi pilot plant. *Octavius* meeting, Brindisi, Italy, September 24th - 25th, 2013. (Oral presentation)

12. N. Enaasen, H. Knuutila, H. M. Kvamsdal and M. Hillestad. Absorption Process Dynamics. UTCCS-2, Austin, USA, January 28th - 30th, 2014. (Oral presentation)

13. N. Enaasen, L. Zangrilli, A. Mangiaracina, T. Mejdell, H. M. Kvamsdal and M. Hillestad. Validation of a Dynamic Model of the Brindisi CO_2 Capture Pilot Plant. GHGT-12, Austin, Japan, October 5th - 9th, 2014. (Oral presentation)

14. N. Enaasen, H. M. Kvamsdal and M. Hillestad. Dominating Dynamics of a Post-combustion CO_2 Capture Plant. GHGT-12, Austin, Texas, USA, October 5th - 9th, 2014. (Poster presentation)

15. N. E. Flø, H. Knuutila, H. M. Kvamsdal and M. Hillestad. Experimental validation of a dynamic model for post-combustion CO_2 Capture. TCCS-8, Trondheim, Norway, June 16th - 18th, 2015. (Oral presentation)

Chapter 2

Post-combustion carbon capture based on chemical absorption

2.1 General process description

Chemical absorption is the most mature and developed technology for post-combustion CO_2 capture. The technique uses a solvent that is able to absorb and react with CO_2 to separate it from the other compounds of the flue gas. The reactions need to be reversible so that the solvent can be regenerated. A strong binding between the solvent molecules and CO_2 offers a fast and effective removal of most of the CO_2 in one stage absorption. However, strong chemical bindings are also the main reason for high regeneration energy requirement and process operating costs.

The process flow diagram of the conventional post-combustion chemical absorption process is displayed in Figure 2.1. Flue gas is usually cooled down and saturated with water in a direct contact cooler before it enters the absorber column where it is contacted counter-currently with the lean solvent. CO_2 is absorbed and reacts with the solvent molecules yielding a solvent rich in CO_2 and a purified gas with a low CO_2 content. The scrubbed gas passes through a water wash section to balance water in the system and remove any solvent droplets or solvent vapor carried over, before the gas is vented to the atmosphere. The lean solvent gradually heats up as it absorbs CO_2 due to exothermic reactions. The temperature inside the absorber is typically 40 - 60°C. The rich solvent is pumped through the cross heat exchanger where heat from the warmer regenerated lean solvent exiting the

reboiler is transferred. The pre-heated rich solvent then enters the the stripper column where the chemical reactions are reversed to desorb CO_2 and regenerate the solvent. Heat is supplied via the reboiler to maintain the regeneration conditions, which means heating up the solvent to stripping temperature, providing the required desorption heat for releasing the chemically bound CO_2 and producing steam which acts as a stripping gas. The regeneration process takes place at elevated temperatures (100°C - 120°C) and slightly higher than atmospheric pressure (1.5 - 2 bara). Steam is recovered in the condenser and fed back to the stripper as condensate, while the gas phase product exiting the condenser contains more than 99% CO_2. The regenerated lean solvent is then pumped back to the absorber via the cross heat exchanger and a lean cooler in order to bring it down to absorber temperature levels (IPCC, 2005).

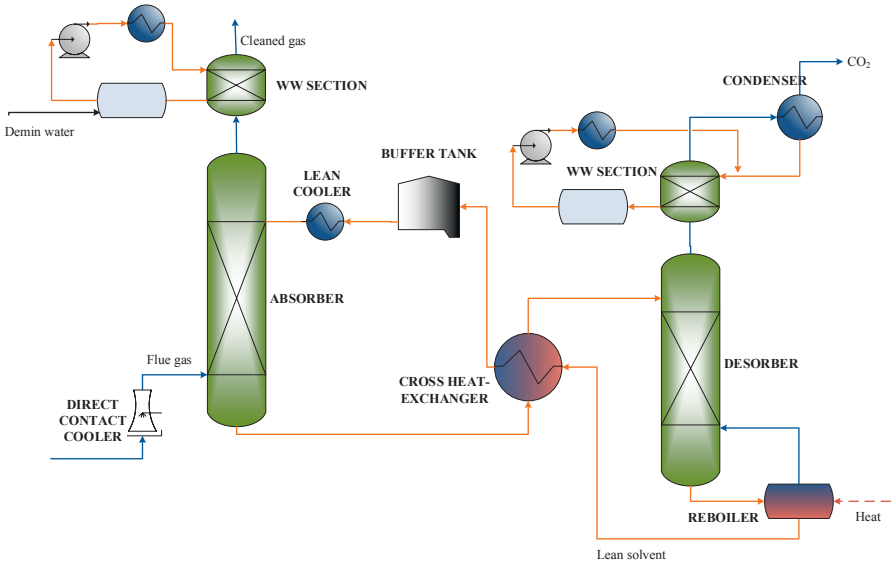

FIGURE 2.1: Process flow diagram for post-combustion CO_2 capture by chemical absorption.

Suitable solvents for chemical absorption are amine-based solvents, ammonia and carbonates. Monoethanolamine (MEA) is the most studied amine-based solvent and is currently considered as the baseline solvent for its high reaction rate with CO_2 and low solvent cost. MEA is a primary amine, and will therefore, in comparison with secondary and tertiary amines, form stable carbamate and react fast with CO_2. The net reaction between CO_2 and primary amines (RNH_2) is as follows

(Xie et al., 2010):

$$CO_2 + 2RNH_2 = RNHCOO^- + RNH_3^+ \tag{2.1}$$

where RNH_3^+ is the protonated amine and $RNHCOO^-$ is the carbamate ion formed from the amine. In the case of MEA, R refers to the alkanol group $OHCH_2CH_2$. The regeneration heat required to release the CO_2 from MEA is, however, relatively high and the chemical absorption is limited by the maximum loading capacity of 0.5 mol CO_2/mol MEA based on stoichiometry, as seen from Equation 2.1. Physical absorption may contribute to a slightly increased CO_2 loading above this theoretical limit. Further, MEA degrades at temperature levels above 120 °C and in the presence of SOx, NOx or oxygen in the flue gas. Amine degradation reduces the CO_2 removal capacity and the degradation products may induce foaming and corrosion. Corrosion reduces the lifespan of the equipment and causes further degradation of the solvent (IPCC, 2005). It is therefore crucial to have a proper flue gas scrubber section before the inlet of the absorber, to remove present contaminants. Nevertheless, it can be difficult to remove all of the flue gas contaminants. Thus solvent reclamation units are often installed to separate the degraded solution (Kohl and Nielsen, 1997).

The key parameters determining the technical and economic operation of CO_2 absorption systems are (IPCC, 2005):

- Flue gas flow rate - determines the size of the absorber which represents a significant contribution to the overall capital cost.
- CO_2 content in the flue gas - determines the choice of solvent. Since flue gas is usually at atmospheric pressure, the partial pressure of CO_2 will be as low as 3-15 kPa, and under these conditions, aqueous amines and amine blends (chemical solvents) are the most suitable absorption solvents (Wang et al., 2011).
- CO_2 removal rate - represent an economic trade-off as a higher recovery will lead to a taller absorption column, higher energy penalties and hence increased capital and operating costs. In practice, typical CO_2 recoveries are between 80% and 95%.
- Solvent flow rate - determines the size of most equipment apart from the absorber. It does also affect the reboiler heating requirement and additional electricity needed for solvent pumping.

- Total energy requirement - determines to a large extent the overall operating costs of the process. Heat is needed to regenerate the solvent, and electrical energy is required for compression of the CO_2 product and to a lesser extent for liquid pumping and operating the flue gas fan.

- Cooling requirement - may represent an additional operating cost depending on its availability. Cooling is needed in order to bring the flue gas and solvent temperatures down to temperature levels required for efficient absorption of CO_2, and for cooling the stripper product gas down to temperatures where water can be separated from CO_2 by condensation.

One of the main factors determining the economic feasibility of CCS is total energy requirement and the resulting efficiency penalty when implemented in power cycles. The cost of electricity generation attributed to post-combustion CO_2 capture increases by 35 - 70% for a natural gas combined cycle plant, 40 - 85% for a new pulverized coal plant and 20 - 55% for an integrated gasification combined cycle plant (IPCC, 2005), where the main contributions relate to solvent regeneration. Figure 2.2 presents the normalized power plant operating cost and CO_2 emissions with and without CO_2 capture. The cost of CO_2 avoided corresponds to the slope of a line connecting any two plants (or points) of interest.

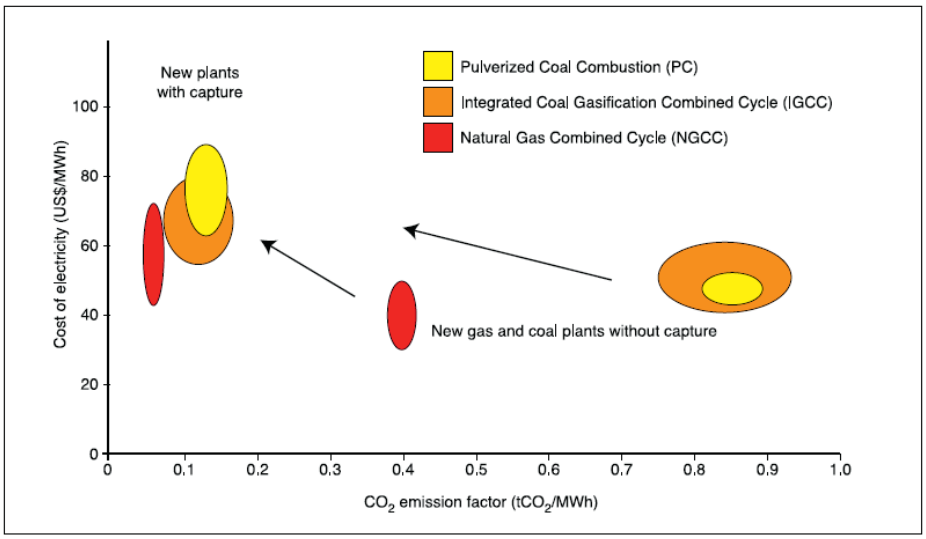

FIGURE 2.2: Cost of electricity (excluding transport and storage costs) compared to CO_2 emission rate for different types of power plants with and without CO_2 capture (IPCC, 2005).

In principle, the thermal energy for the solvent regeneration process can be supplied by an auxiliary boiler in a retrofit situation. The heat requirement is at such levels that low-pressure steam can be used in the reboiler. A more efficient alternative is integration of the absorption process into the power plant, where low or intermediate pressure steam for the reboiler heating is extracted directly from the power plant steam cycle. Some of this heat can be recovered by preheating the boiler feed water. Values for the heat requirement for the leading post-combustion absorption technologies are between 2.7 - 3.3 GJ/tCO_2, depending on the solvent process. Typical values for additional electricity requirement are between 0.06 - 0.11 GJ/tCO_2 for post-combustion capture in coal-fired power plants and 0.21 - 0.33 GJ/tCO_2 for post-combustion capture in natural gas-fired combined cycles. Compression of the CO_2 to 110 bar will require around 0.4 GJ/tCO_2 (IPCC, 2005).

2.2 Pilot plant descriptions

Data from four different pilot plants are used for model equipment sizing, parameter setting and validation in this work. These plants have different configurations, dimensions, capacities and/or operate at different conditions, thus descriptions and process flow sheets of the four different pilot plants are given in the following. Information about relevant pilot plant data used for model validation is also included. To evaluate the pilot plant data, various calculated steady state CO_2 mass balances are compared. Possible deviations in the CO_2 mass balances, that is discrepancies between the different methods, indicate the confidence in the measurements and/or possible leakages. Three different methods are applied for calculation of relative deviation (RD) in the CO_2 mass balances:

1. Absorber:
$$\frac{m^{\mathrm{l}}_{\mathrm{CO_2}} - m^{\mathrm{g}}_{\mathrm{CO_2,abs}}}{AVG(m^{\mathrm{g}}_{\mathrm{CO_2,abs}}, m^{\mathrm{l}}_{\mathrm{CO_2}})} \tag{2.2}$$

2. Desorber:
$$\frac{m^{\mathrm{l}}_{\mathrm{CO_2}} - m^{\mathrm{g}}_{\mathrm{CO_2,des}}}{AVG(m^{\mathrm{g}}_{\mathrm{CO_2,des}}, m^{\mathrm{l}}_{\mathrm{CO_2}})} \tag{2.3}$$

3. Overall process:
$$\frac{m^{\mathrm{g}}_{\mathrm{CO_2,des}} - m^{\mathrm{g}}_{\mathrm{CO_2,abs}}}{AVG(m^{\mathrm{g}}_{\mathrm{CO_2,des}}, m^{\mathrm{g}}_{\mathrm{CO_2,abs}})} \tag{2.4}$$

where $m^{g}_{CO_2,abs}$ is the amount of CO_2 absorbed from gas phase in the absorber, $m^{l}_{CO_2}$ is the amount of CO_2 absorbed in the solvent and $m^{g}_{CO_2,des}$ is the amount of CO_2 released in the CO_2 stripper. AVG denotes the average value of the parameters listed in the subsequent parenthesis.

If mass balance calculations for multiple steady state operating points in the same pilot plant are available, the average relative deviation (ARD) of the estimated mass balances can be calculated as follows:

$$ARD = \frac{1}{N}\sum_{i=1}^{N}|RD_i| \tag{2.5}$$

where N is the number of steady state cases and RD_i is the relative deviation given by Equation 2.2, 2.3 or 2.4.

2.2.1 Gløshaugen CO_2 capture pilot plant

The Gløshaugen pilot plant is a small-scale CO_2 capture pilot plant located in NTNU/ SINTEF's laboratories at Gløshaugen in Trondheim, Norway. A flow sheet of the pilot plant is presented in Figure 2.3.

The pilot plant is usually operated with a flue gas flow rate around 100 m^3/h and the solvent flow rate can be varied between 2 - 6 L/min. The maximum flue gas and solvent capacities are 150 m^3/h and 9 L/min, respectively.

The absorber is a 150 mm diameter column, while the desorber diameter is 100 mm. Both columns contain Sulzer BX structured packing, 4.23 m for the absorber and 3.57 mm for the desorber, respectively. Both columns are equipped with temperature sensors in the packing sections that allow prediction of column temperature profiles. The extra column shown in Figure 2.3 does not contain any packing and is therefore not in operation. However the rich solvent is passed through the extra column sump where the liquid level is controlled by the rich solvent pump P2.

As seen from Figure 2.3, the complete plant is operated as a closed system, thus all stripped CO_2 is transferred back and mixed with the absorber outlet gas prior to entering the absorber column as CO_2 rich gas. The condensate from the condenser is returned to the reboiler in this configuration. The pilot plant also has a lean

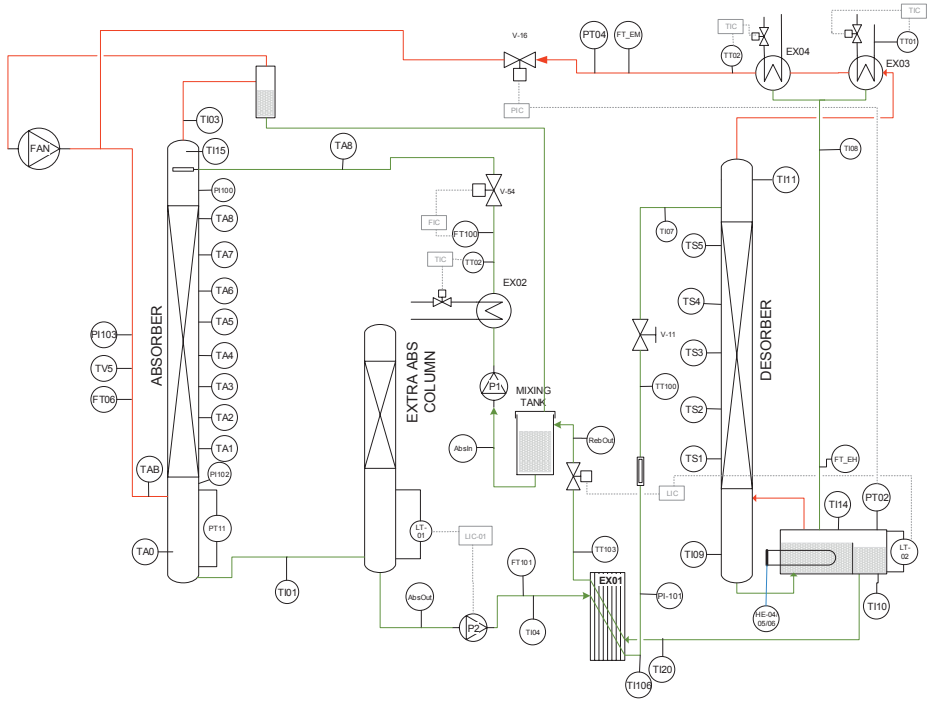

FIGURE 2.3: A schematic overview of the Gløshaugen pilot plant.

solvent mixing tank prior to the lean solvent cooler which acts as a solvent buffer. Make-up MEA and water can be added manually to this tank. The reboiler is electrically heated with a maximum effect of 17.5 kW.

Typical solvent hold-ups and residence times for solvent flow rates of 2.5 - 4.5 L/min are given in Table 2.1.

TABLE 2.1: Solvent hold-ups and residence times in the Gløshaugen pilot plant.

	Solvent hold-up [L]	**Residence time** [min]
Absorber packing	7	1.6 - 2.8
Absorber sump and extra column	20	4.4 - 8
Desorber packing	3	0.7 - 1.2
Desorber sump and reboiler	65	14.4 - 26
Buffer tank	25	5.6 - 10
Cross heat exchanger and piping	40	8.9 - 16
Total	**160**	**35.6 - 64**

Pilot plant data from eight different steady state operating points and logged data from six dynamic runs with set-point changes in solvent circulation rate

and reboiler duty are generated in this work through a dynamic test campaign in the BIGCCS project. A summary of the steady state data and the dynamic experiments is given in Table 3.1 and Figure 3.3 and 3.4 in Chapter 3.

2.2.2 Brindisi CO_2 capture pilot plant

The Brindisi pilot plant is a fully instrumented relatively large post-combustion CO_2 capture pilot plant located in Brindisi, Italy. It is attached to a full scale coal-fired power plant and both units are operated by ENEL. A flow sheet of the plant is presented in Figure 2.4.

The capture plant is designed for 10 000 Nm^3/h exhaust gas (which corresponds to about 0.45% of the total 660 MW power plant exhaust gas), capturing about 2 000 kg/h of CO_2. The pilot plant can handle flue gas flow rates up to 12 000 Nm^3/h and the maximum CO_2 production capacity is 2 500 kg/h. The solvent flow rate can be varied between 20 - 80 m^3/h.

The absorber and desorber diameters are 1.5 m and 1.3 m, respectively. The absorber contain Sulzer Mellapak 250X structured packing of 22 m, while the desorber contain random packing of 11 m.

The Brindisi pilot plant has two 100 m^3 solvent storage tanks (PV-776/777), both situated at the lean solvent side of the process, which act as a solvent storage and inventory buffer. The reboiler is heated by low pressurized steam of 2.5 bara and 130°C.

Typical solvent hold-ups and residence times for solvent flow rates of 30 m^3/h are given in Table 2.2. A minimum solvent storage volume of 28 m^3 is used in these calculations. A larger solvent inventory will naturally increase the buffer tank residence time.

2.2.2.1 Pilot plant data

A pilot plant campaign was conducted in May and June 2013 through the EU project *Octavius* using 30 wt% MEA as solvent. As part of the campaign various transient tests with step-wise changes in different operational parameters such as flue gas flow rate, reboiler duty and solvent flow rate were performed, while

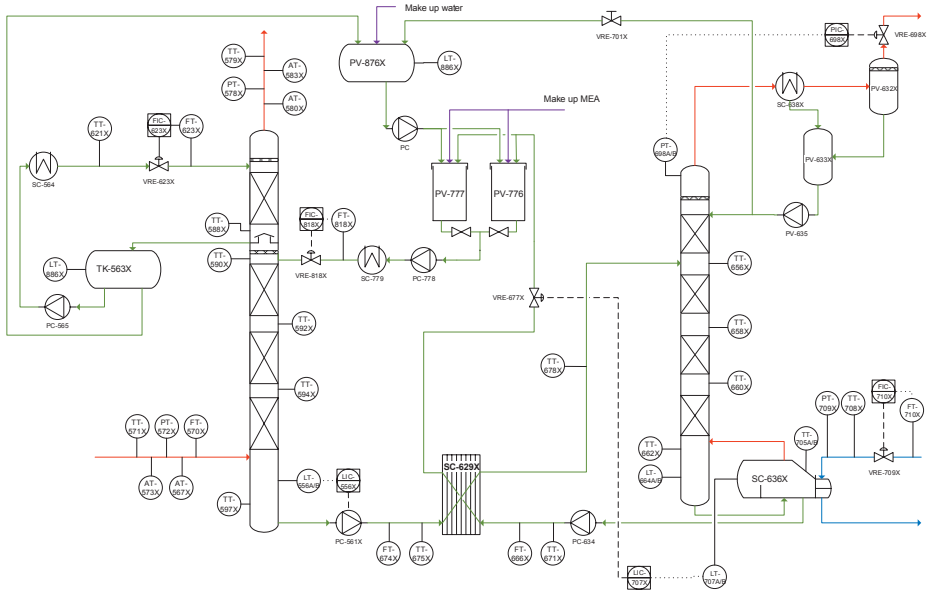

FIGURE 2.4: A schematic overview of the Brindisi pilot plant.

TABLE 2.2: Solvent hold-ups and residence times in the Brindisi pilot plant.

	Solvent hold-up [m^3]	**Residence time** [min]
Absorber	7	14
Absorber sump	3	6
Desorber and reboiler	5	10
Desorber sump and reboiler	8	16
Buffer tank	28	56
Cross heat exchanger and piping	10	20
Total	**61**	**122**

the responses and performance of the capture plant were monitored and logged every minute. The flue gas flow rate was not measured directly, however, it was estimated based on measured pressure drop in the absorber column using the following equation:

$$F_{\text{fluegas}} = 3140.3 \Delta P_{\text{abs}}^{0.4914} \tag{2.6}$$

where F_{fluegas} is the flue gas flow rate given in [Nm^3/h] and ΔP_{abs} is the absorber column pressure drop in [mbar].

Solvent samples were also withdrawn frequently and analyzed in the laboratory to determine the MEA and CO_2 concentrations. The pilot plant was operated with

the minimum total solvent hold-up of about 61 m^3 in order to get quick process responses after step-changes were imposed.

A summary of the steady state pilot plant performance is given in Table 2.3, while the dynamic experiments are presented in Figure 2.5. The steady state data are 30 minute time averaged logged data at stable conditions prior to any step change. At these opearting points, solvent loading and lean MEA wt% are also available through manual solvent analysis, as seen in Table 2.3.

The amount of absorbed and desorbed CO_2 ($m^g_{CO_2,abs}$ and $m^g_{CO_2,des}$) are calculated from the logged pilot plant data and the results are used to estimate the deviation in CO_2 mass balance by Equation 2.4 for each case, which also is reported in Table 2.3. The mass balance calculations indicate a generally lower amount of desorbed CO_2 compared to the estimated amount of absorbed CO_2 for all cases except case 1 where the error is close to zero. The average relative deviation of the overall mass balance calculations is 4.2%. Due to lack of solvent density measurements, the amount of CO_2 absorbed in the solvent ($m^l_{CO_2}$) cannot be estimated, and it is therefore difficult to conclude which of the calculated absorption ($m^g_{CO_2,abs}$) or desorption ($m^g_{CO_2,des}$) rates are more reliable. However, since the flue gas flow rate is not a directly measured variable, but estimated based on other measurements, it is reasonable to assume that $m^g_{CO_2,des}$ is more reliable. This variable is therefore used in the calculated energy performance for each steady state case, which is reported in Table 2.3.

The dynamic cases presented in Figure 2.5 show flue gas, solvent and steam flow rate as functions of time. Case 1 represents multiple step-changes in steam flow rate along with a single step-change in lean solvent flow rate, while case 2 represents a step-change in lean solvent flow rate and case 3 represents step-changes in flue gas flow rate.

TABLE 2.3: Steady state data from the Brindisi pilot plant.

Case		**1**	**2**	**3**	**4**	**5**	**6**	**7**	**8**	**9**	**10**	**11**	**12**
Flue gas flow rate	[Nm^3/h]	9928	9876	9929	9893	9949	9869	9921	9898	9885	11045	9911	8996
Flue gas temperature	[°C]	47.7	46.2	44.8	45.6	44.7	45.9	46.9	49.1	48.2	48.5	48.1	45.6
Flue gas CO_2 concentration	[dry vol%]	11.4	11.0	12.5	12.0	10.4	11.7	11.0	12.8	10.9	11.5	11.6	11.1
Lean solvent flow rate	[kg/h]	30.0	30.0	30.0	30.0	35.0	35.0	35.0	35.6	25.6	28.5	28.5	28.5
Lean solvent solvent temperature	[°C]	47.1	46.9	47.0	47.0	47.0	47.0	47.1	47.0	45.1	46.1	45.1	44.9
Lean solvent MEA concentration	[wt%]	30.5	29.6	30.1	29.8	29.8	30.0	29.7	29.5	29.3	29.1	28.9	28.9
Lean CO_2 loading	[$molCO_2/molMEA$]	0.18	0.196	0.21	0.22	0.23	0.20	0.20	0.21	0.22	0.18	0.18	0.18
Rich CO_2 loading	[$molCO_2/molMEA$]	0.48	0.50	0.48	0.49	0.43	0.44	0.45	0.47	0.47	0.49	0.48	0.46
Steam flow rate to the reboiler	[kg/h]	3150	2851	2700	2401	2800	3150	3326	2907	2907	2708	2707	2707
Stripper pressure	[bar]	1.83	1.84	1.84	1.84	1.84	1.84	1.83	1.84	1.84	1.84	1.84	1.84
Calculated absorbed amount of CO_2													
Absorbed from gas ($m^{g}_{CO_2,abs}$)	[kg/h]	1936	1879	1902	1700	1724	1972	1853	2056	1765	18636	1812	1748
Desorbed ($m^{g}_{CO_2,des}$)	[kg/h]	1953	1815	1772	1654	1712	1912	1838	1871	1721	1704	1714	1650
Relative deviation in steady state CO_2 mass balance													
Overall process	[%]	+0.9	-3.4	-7.1	-2.8	-0.7	-3.1	-0.8	-9.4	-2.5	-8.9	-5.6	-5.8
Energy performance	[$MJ/kgCO_2$]	3.53	3.46	3.36	3.20	3.62	3.64	4.01	3.69	3.64	4.05	3.66	3.61

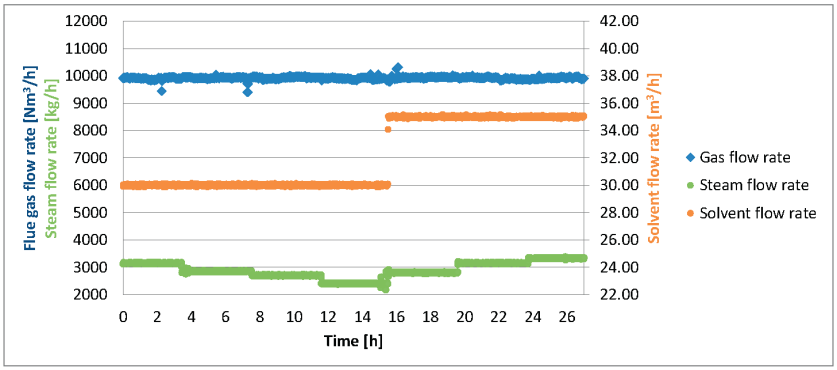

(A) Dynamic case1: Set-point changes in steam flow rate and lean solvent flow rate

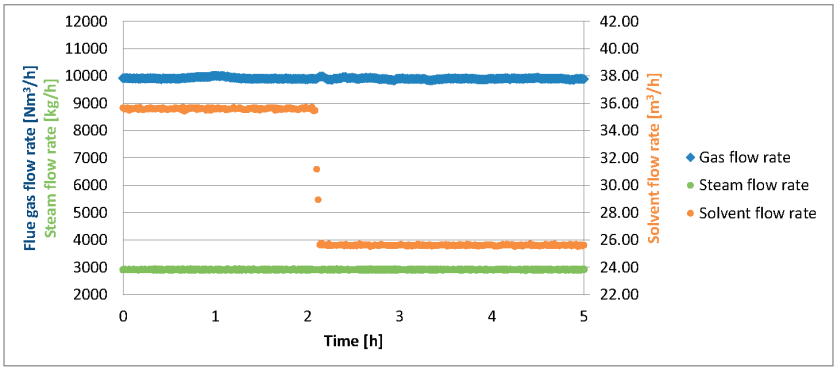

(B) Dynamic case 2: Set-point change in lean solvent flow rate

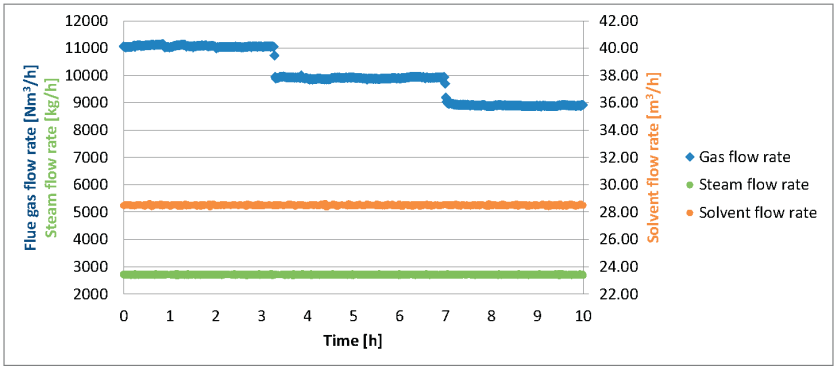

(C) Dynamic case 3: Set-point changes in flue gas flow rate

FIGURE 2.5: Dynamic data from the Brindisi pilot plant.

2.2.3 Tiller CO_2 capture test facility

The Tiller pilot plant is a full column height CO_2 capture plant located in SINTEF's laboratories at Tiller in Trondheim, Norway. A flow sheet of the plant is presented in Figure 2.6.

A propane burner provides flue gas to the absorber. The flue gas fan has a capacity to reach gas velocities above 4 m/s ($\approx$ 450 m^3/h) at the absorber inlet, which is calculated to be around the flooding point. The inlet gas phase CO_2 concentration can be varied between 2 - 14 vol%. The solvent flow rate is adjustable to meet the CO_2 capture requirement, with a maximum flow rate of 20 L/min. An electrically heated reboiler is used to regenerate the solvent, and the reboiler has a maximum duty of 60 kW.

The absorber diameter is 200 mm and the absorber tower contains 19.418 m of packing divided into 4 sections. The desorber column has an inner diameter of 150 mm, and 3 packing sections with a total packing height of 13.78 m. Both columns contain Sulzer Mellapak 2X structured packing.

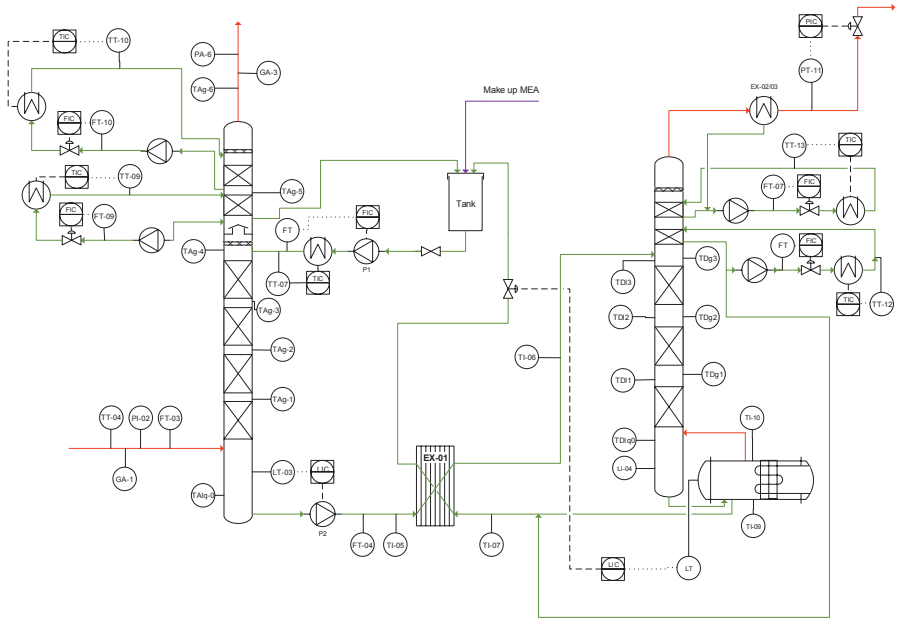

FIGURE 2.6: A schematic overview of the Tiller pilot plant.

Both columns are instrumented with temperature sensors located at every meter of the packing, and pressure sensors below each packing section and above the upper water wash section. The stripper and the reboiler are equipped with a heat tracing system to minimize the heat loss. The heat tracing system consists of two layers of insulation with an aluminum shield and heating tapes in between. Control loops adjust the temperature at the shield to be equal to the temperatures inside the column. With practically no driving forces the heat transport from the column wall to the shield becomes negligible.

The absorber and desorber diameters in the Tiller pilot plant have been dimensioned according to the amount of flue gas available and are quite small. However, the philosophy has been to otherwise design the plant as similar as possible to industrial sized plants. The gas rate (m/s), the liquid load ($m^3/(s\,m^2)$), the packing material and the total packing heights are therefore equivalent to full-scale, such that the conditions for mass and heat transfer from gas to liquid and reaction rates will be very much like in industrial sized plants. Scale-up of column diameters, vessel sizes and gas and liquid flow rates will therefore represent industrial sizes.

The solvent hold-ups and residence times of various units are divided according to the distribution presented in Table 2.4 for solvent flow rates of 3.5 - 7 L/min.

TABLE 2.4: Solvent hold-ups and residence times in the Tiller pilot plant.

	Solvent hold-up [L]	Residence time [min]
Absorber packing	50	7 - 14
Absorber sump	16	2 – 5
Desorber packing	20	3 – 6
Desorber sump and reboiler	280	40 - 80
Buffer tank	57	8 - 16
Cross heat exchanger and piping	92	13 - 26
Total	515	73 - 147

2.2.3.1 Pilot plant data

Two sets of steady state pilot plant data from a Tiller campaign in the *SOLVIT* project are used for model validation. Run 100612 is a natural gas case with 4.2 dry vol% of CO_2 carried out on June 6 2010, while run 100718 is a coal case with 11.6 dry vol% CO_2 carried out on July 18 2010. Additional information about the cases is presented in Table 2.5.

TABLE 2.5: Steady state data from the Tiller pilot plant.

Case		**100612**	**100718**
Flue gas flow rate	[Nm^3/h]	216.4	138.4
Flue gas temperature	[°C]	48.4	44.2
Flue gas CO_2 concentration	[dry vol%]	4.2	11.6
Lean solvent flow rate	[kg/h]	222.0	408.0
Lean solvent solvent temperature	[°C]	41.6	38.0
Lean solvent MEA concentration	[wt%]	27.1	26.7
Lean CO_2 loading	[molCO_2/molMEA]	0.14	0.17
Rich CO_2 loading	[molCO_2/molMEA]	0.48	0.49
Reboiler duty	[kW]	18.5	26.7
Stripper pressure	[bar]	1.80	1.90
Calculated absorbed amount of CO_2			
Absorbed from gas ($m^{g}_{CO_2,abs}$)	[kg/h]	15.3	25.8
Absorbed to solvent ($m^{l}_{CO_2}$)	[kg/h]	14.8	25.1
Desorbed ($m^{g}_{CO_2,des}$)	[kg/h]	14.8	24.4
Relative deviation in steady state CO_2 mass balance			
Absorber	[%]	-3.6	-2.8
Desorber	[%]	+0.2	-3.1
Overall process	[%]	-3.4	-5.8
Energy performance	[MJ/(kgCO_2)]	4.48	3.82

The amount of absorbed CO_2 from gas ($m^{g}_{CO_2,abs}$), absorbed CO_2 in the solvent ($m^{l}_{CO_2}$) and desorbed CO_2 ($m^{g}_{CO_2,des}$) are estimated from the logged pilot plant data and solvent analysis. The results are used to estimate the relative deviations in CO_2 mass balance for the absorber, stripper and overall process according to Equation 2.2, 2.3 and 2.4, respectively. These numbers are also reported in Table 2.5. The mass balance calculations indicate a very good agreement between measured pilot plant data, with a maximum relative deviation of 5.8%.

2.2.4 Technology Centre Mongstad

The CO_2 Technology Centre Mongstad (TCM) has installed an amine-based CO_2 capture pilot plant next to the Statoil refinery at Mongstad, Norway. The size of the facility and its flexibility allows extensive test possibilities, and the information gathered from the plant can be extrapolated for eventually full-scale implementation. Flue gas can be supplied from either the on-site natural gas-fired combined heat and power (CHP) plant or from the Statoil refinery residue fluid catalytic cracker (RFCC). Due to very different conditions of these flue gases (3.5

vol% CO_2 in CHP gas and 13 vol% CO_2 in RFCC gas), different post-absorption process equipment is required. Two different stripper columns are therefore constructed at the site (Hamborg et al., 2014). The data used in this work are from tests performed with the CHP gas, thus the following description will only concern the CHP gas related configuration. A simplified process flow sheet of the TCM plant using CHP gas is presented in Figure 2.7.

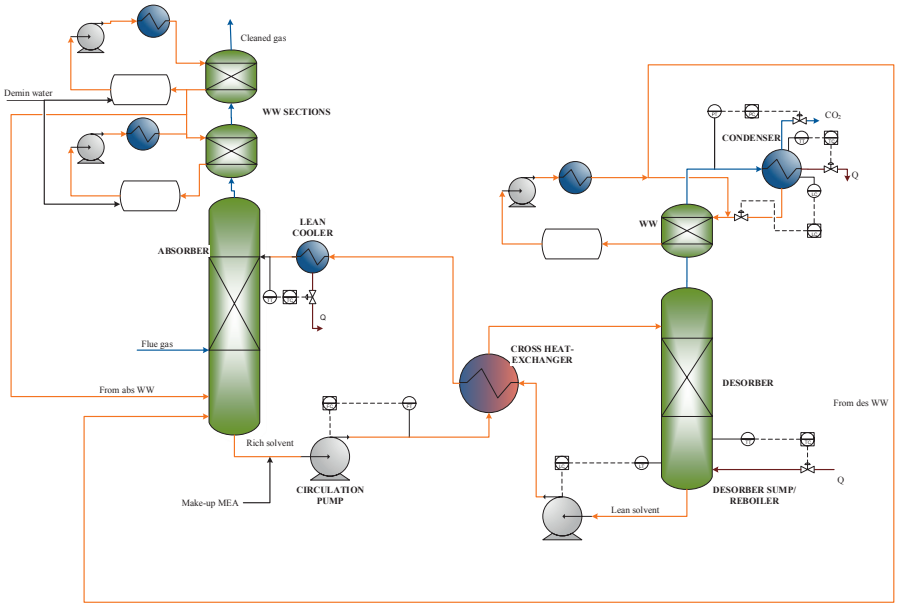

FIGURE 2.7: A schematic overview of the TCM pilot plant.

The TCM test facility can handle CHP gas flow rates in the range of 30 000 - 60 000 Nm^3/h with a capacity of capturing up to 80 t CO_2/d. The solvent flow rate can be varied in the range of 30 - 150 m^3/h. The reboiler is steam heated and the duty can be varied in the range of 2.5 - 6 MW (Brigman et al., 2014).

The absorber is a rectangular cross-section tower with an equivalent circular diameter of 1.5 m. The desorber is a cylindrical tower with a diameter of 1.25 m. The absorber has three packing sections with Koch Glitsch Flexipac 2X structured packing. These are 12, 6, and 6 m high, respectively. The lean solvent can be fed to the absorber at different levels, meaning that the absorber packing height can be chosen to 12, 18 or 24 m. The stripper has one packing section filled with Koch Glitsch Flexipac 2X structured stainless-steel packing that is 8 m high (Hamborg et al., 2014).

Heat is provided to the reboiler by medium pressure (MP) steam in a thermosiphon reboiler. The condenser condensate is returned to the stripper. The TCM process configuration does not include a separate solvent buffer tank as for the previous plants, however, the absorber sump is used for this purpose. Thus rich solvent flow rate is controlled in this plant instead of lean solvent flow rate.

The solvent hold-ups and residence times of various units are divided according to the distribution presented in Table 2.6 for solvent flow rates of 30 - 100 m^3/h.

TABLE 2.6: Solvent hold-ups and residence times in the TCM test facility.

	Solvent hold-up [m^3]	Residence time [min]
Absorber packing	7	4 - 14
Absorber sump	13	8 - 26
Desorber packing	1	1 - 2
Desorber sump and reboiler	5	3 - 10
Cross heat exchanger and piping	24	14 - 48
Total	50	30 - 100

2.2.4.1 Pilot plant data

The TCM data available for model validation are taken from part of an Aker Solutions test period conducted between December 2013 and February 2014. The tests are performed to define energy U-curves (that is energy performance as function of lean loading for a given flue gas flow rate and CO_2 recovery rate) (Brigman et al., 2014). Thus, no specific dynamic tests were performed during the campaign. However, logged data from a number of steady state operating conditions are available including logged transient data when moving between steady state operating points. The establishment of the U-curves is most often done by performing a step-change in solvent flow rate while adjusting the reboiler duty to give the desired capture rate. The flue gas flow rate is also varied in some cases. A solvent system of 30 wt% aqueous MEA was generally applied during the campaign, however, data where the MEA concentration is increased from 30 to 40 wt% are also available, along with a period of operation with 40 wt% MEA.

Specifically, 8 steady state and 4 dynamic cases are extracted from this test period and used for model validation. The selected steady state cases are presented in Table 2.7 while the dynamic cases are presented in Figures 2.8 and 2.9. The presented dynamic data includes the flue gas inlet flow rate, rich solvent flow rate

and the amount of MP steam to the reboiler as functions of time. The dynamic case 3 involves an increase in the solvent MEA concentration, and the logged MEA make-up flow rate and water is presented in Figure 2.9b.

The amount of absorbed CO_2 from the gas ($m^{g}_{CO_2,abs}$), absorbed CO_2 to the solvent ($m^{l}_{CO_2}$) and desorbed CO_2 ($m^{g}_{CO_2,des}$) are estimated from the logged pilot plant data and solvent analysis at steady state condition. The results are further used to estimate the relative deviation in CO_2 mass balance for the absorber, stripper and overall process, according to Equations 2.2 - 2.4 for each steady state case. These results are reported in Table 2.7, and the average relative deviations are 8.6, 5.1 and 9.4%, respectively. The desorber mass balance calculations indicate a good agreement between the calculated amount of absorbed CO_2 in the solvent and desorbed amount of CO_2 in the stripper, except for case 4 and 8. The absorber and overall mass balance calculations show larger deviations which indicate weaknesses in the gas flow measurement or gas phase analysis of CO_2. The desorption rate ($m^{g}_{CO_2,des}$) is therefore utilized in the calculation of energy performance which is given in Table 2.7.

A remark on the online gas phase CO_2 analysis is that one single FTIR instrument is used to analyze absorber inlet gas, absorber outlet gas and desorber outlet gas concentrations. This means that the analyzer is cycled between all three sampling points in a 90 - minute cycle. The CO_2 gas measurements are therefore neither measured simultaneously or continuously during the test period. When the analyzer is switched from one sampling point to another, the last measured composition value is displayed and logged in the plant control system until the next sampling cycle (Hamborg et al., 2014). This may explain the relatively large deviations in absorber and overall CO_2 mass balance. Further, discontinuous CO_2 gas phase measurements are not optimal for dynamic analysis.

Solvent analyses are withdrawn and analyzed in the laboratory twice a day during the MEA campaign. Thus, the transient information about solvent concentrations is also quite limited.

TCM experienced foaming during some parts of the MEA campaign, thus anti-foam solution was added to the solvent for parts of the test period. This concerns the steady state cases 6 and 7.

TABLE 2.7: Steady state data from TCM.

Case		**1**	**2**	**3**	**4**	**5**	**6**	**7**	**8**
Flue gas flow rate	[Nm^3/h]	66634	48315	44757	45222	46484	45899	46028	57891
Flue gas temperature	[°C]	46.8	46.9	25.0	25.0	24.9	24.1	24.9	24.9
Flue gas CO_2 concentration	[dry vol%]	3.15	3.23	3.30	3.34	3.27	3.40	3.45	3.44
Rich solvent flow rate	[kg/h]	53051	43024	57502	80885	42266	42507	82500	71483
Lean solvent MEA concentration	[wt%]	34.4	33.6	34.8	34.6	34.2	34.1	34.3	34.0
Lean CO_2 loading	[molCO_2/molMEA]	0.16	0.15	0.25	0.32	0.19	0.19	0.31	0.26
Rich CO_2 loading	[molCO_2/molMEA]	0.44	0.45	0.49	0.46	0.49	0.48	0.46	0.45
Reboiler duty	[kW]	4901	4249	2939	3148	3500	2792	3097	3477
Stripper pressure	[bar]	1.99	1.99	1.99	2.00	1.99	2.00	1.99	1.99
Calculated absorbed amount of CO_2									
Absorbed from gas ($m^{g}_{CO_2,abs}$)	[kg/h]	2998	2596	2373	2386	2230	2608	2490	2924
Absorbed to solvent ($m^{l}_{CO_2}$)	[kg/h]	3331	2802	2778	2360	2733	2677	2819	2999
Desorbed ($m^{g}_{CO_2,des}$)	[kg/h]	3236	2765	2620	2702	2697	2698	2713	3309
Relative deviation in steady state CO_2 mass balance									
Absorber	[%]	+10.0	+7.4	+14.6	-1.1	+18.4	+2.6	+11.7	+2.5
Desorber	[%]	+2.9	+1.3	+5.7	-14.5	+1.3	-0.8	+3.8	-10.3
Overall process	[%]	+7.3	+6.1	+9.4	+11.7	+17.3	+3.4	+8.2	+11.6
Energy performance	[MJ/kgCO_2]	5.30	5.46	3.81	4.80	4.61	3.75	3.95	4.17

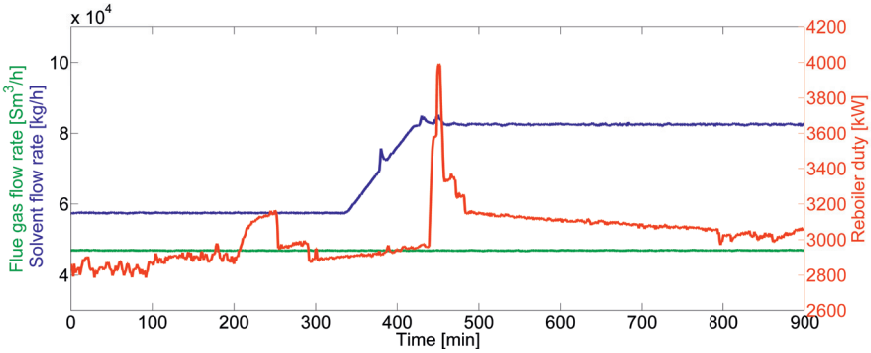

(A) Dynamic case 1: 42% increase in solvent flow rate

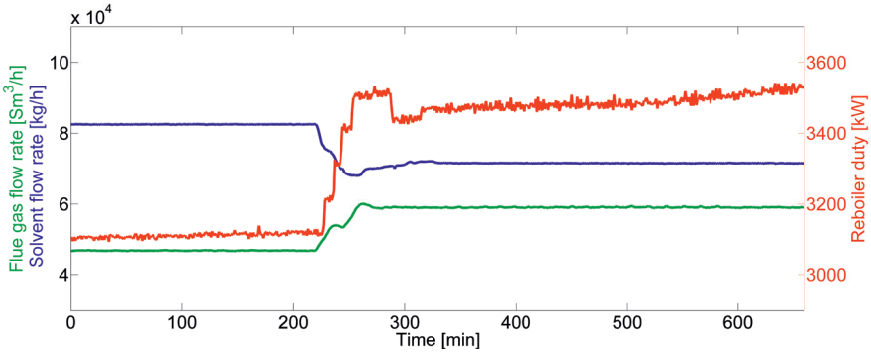

(B) Dynamic case 2: 26% increase in flue gas flow rate and 13% decrease in solvent flow rate

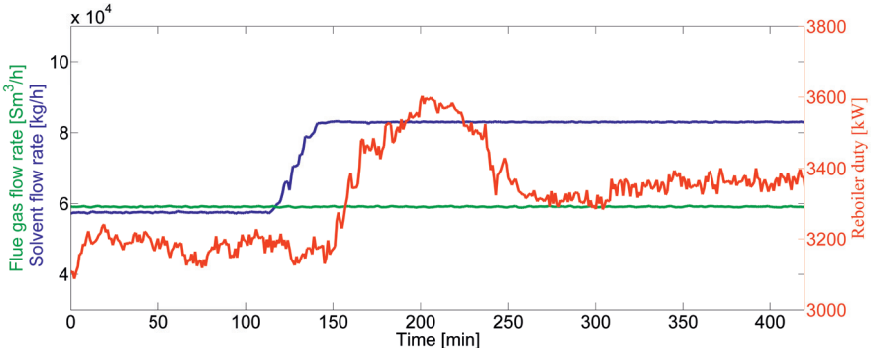

(C) Dynamic case 4: 43% increase in solvent flow rate with 40 wt% MEA

FIGURE 2.8: Dynamic data from the TCM test facility, case 1,2 and 4. (—) Flue gas flow rate, (—) solvent flow rate and (—) reboiler duty.

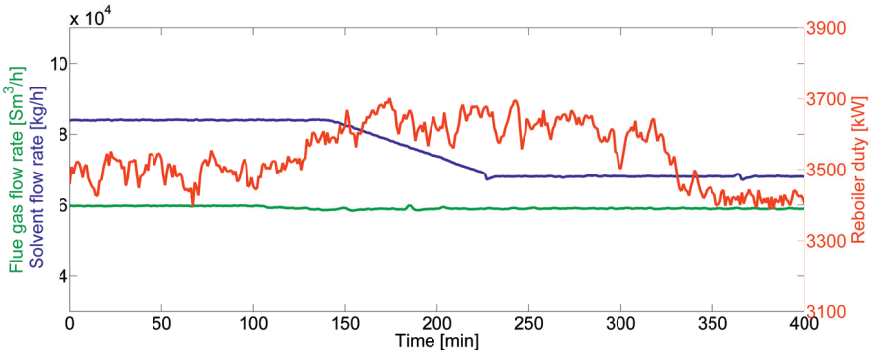

(A) Dynamic case 3: 19% decrease in solvent flow rate. (—) Flue gas flow rate, (—) solvent flow rate and (—) reboiler duty.

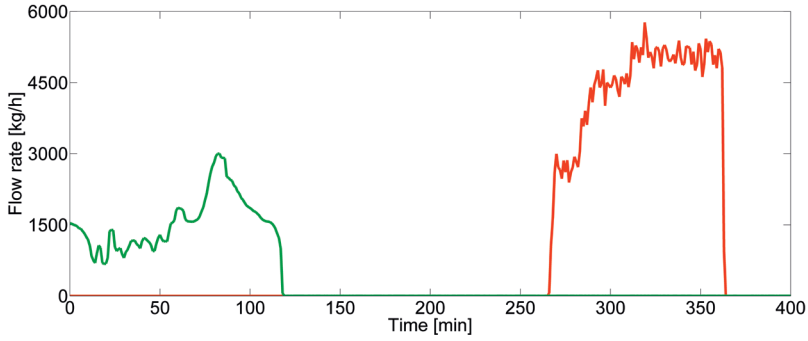

(B) Dynamic case 3: Increase in solvent MEA concentration from approximately 30 wt% to 40 wt%. (—) Water wash bleed and (—) MEA make-up.

FIGURE 2.9: Dynamic data from the TCM pilot plant, case 3.

Chapter 3

Dynamic campaign in the Gløshaugen pilot plant

A pilot plant campaign focused on dynamic testing was planned and executed as part of this work in the BIGCCS project. The campaign was conducted in the Gløshaugen pilot plant from December 2013 to March 2014. The pilot plant description and process flow sheet is given in Section 2.2.1.

3.1 Experimental description and operational procedure

The dynamic experiments were executed by performing set-point changes to the lean solvent flow rate or reboiler duty, starting from steady state conditions. Open loop process responses in gas and liquid flow rates, temperatures and pressures, gas compositions and liquid density of the rich and lean solvent were logged every minute throughout the experiments. Based on previous experience, the pilot plant was left stabilizing for at least 6 hours after a set-point change was introduced (Pinto et al., 2014). No other external impact was imposed on the pilot plant during this period to ensure a steady state starting point for the next dynamic test.

A two-channel IR CO_2 gas analyzer (Rosemount Binos 100) connected to the absorber inlet and outlet gas streams measured the gas phase CO_2 content on

a dry basis. The CO_2 analyzers were calibrated once a day using gas mixtures produced from calibrated mass flow controllers (Bronkhorst Hi-Tec) for CO_2 and N_2. At least 4 - 5 different concentrations were used covering the whole range of relevance.

Solvent samples from three different locations (lean solvent into the absorber (AbsIn), rich solvent out of the absorber (AbsOut) and lean solvent out of the reboiler (RebOut)) were withdrawn throughout the experiments. A set of solvent samples were first collected at steady state conditions before any step change was performed. During transient periods solvent samples at the absorber outlet (AbsOut) and reboiler outlet (RebOut) were withdrawn every 15 minutes during the first hour after a step change. Additionally samples at the absorber inlet (AbsIn) were withdrawn after 30, 45 and 60 minutes. After 60 minutes the pilot started to approach steady state and only slow changes in the density and temperatures were observed. The sampling was therefore stopped.

The absorber sump and reboiler level, lean cooler temperature, condenser temperature and reboiler pressure were controlled at set-point during the experiments.

3.2 Solvent analyses

The solvent samples were analyzed for CO_2 concentration and for total alkalinity which corresponds to the MEA concentration. The CO_2 concentration were analyzed both by using a GC Apollo 9000 Combustion TOC analyzer and manual analysis using the barium chloride method. For the latter method, CO_2 in the sample was precipitated with $BaCl_2$ to form $BaCO_3$. $BaCO_3$ was then separated and dissolved in excess HCl and by back titration the solution with NaOH, the amount of CO_2 was calculated. An automatic titrator (Metrohm 702 SM Titrino) was used for this purpose (Monteiro et al., 2013). Manual analysis of at least one sample from each dynamic run ensures that the analysis results of the instrumental determination with the Apollo 9000 analyzer are correct. The MEA concentration was determined by titration with H_2SO_4 using the Metrohm 702 SM Titrino and standard procedures (Ma'mun et al., 2007).

The mass weight fraction of MEA (w_{MEA}) and CO_2 loading (α) are from the analysis calculated as follows:

$$w_{\mathrm{MEA}} = \frac{\bar{C}_{\mathrm{l,MEA}} \cdot M_{\mathrm{MEA}}}{1000\left(1 - \frac{\bar{C}_{\mathrm{l,CO_2}} \cdot M_{\mathrm{CO_2}}}{1000}\right)} \tag{3.1}$$

$$\alpha = \frac{\bar{C}_{\mathrm{l,CO_2}}}{\bar{C}_{\mathrm{l,MEA}}} \tag{3.2}$$

where $\bar{C}_{\mathrm{l,MEA}}$ and $\bar{C}_{\mathrm{l,CO_2}}$ are the measured solvent MEA and CO_2 molal concentrations respectively in [mol/kg], and M represent the molecular weight.

3.3 Correlation of CO_2 loading to online solvent density measurements

The online solvent density measurements (ρ_{l}) were successfully used to correlate CO_2 loading according to the following equation valid for 30 wt% MEA:

$$\rho_{\mathrm{l}} = \left(1 + 222.25267\frac{\alpha}{T_{\mathrm{l}}} + \frac{2.49573 \cdot 10^5}{T_{\mathrm{l}}^2}\right)\exp\left(-\frac{394.9888}{T_{\mathrm{l}}} + 0.04254\sqrt{\frac{\alpha}{T_{\mathrm{l}}}}\right) \cdot 10^3 \tag{3.3}$$

The results from the CO_2 loading/density correlation are presented in the right-hand side graphs in Figure 3.4 for each dynamic case, and shows a very good agreement to solvent sample analyses.

3.4 Steady state pilot plant results

Eight steady state operating points were established during the campaign based on time-averaged logged data at steady state conditions over a 30-60 min period. A summary of the results is presented in Table 3.1, and a complete overview of time average logged steady state pilot plant data is given in the appendix of Paper E in Appendix C.5.

3.4.1 Steady state mass balance

The collected steady state data are used to check the reliability of the pilot plant data based on different calculations of the amount of absorbed CO_2. Three different methods are used to estimate the CO_2 absorption in [kg/h]; method 1 is estimation of the amount absorbed from gas phase in the absorber, method 2 is estimation of the amount absorbed in the liquid phase, while method 3 is a calculation of the amount desorbed to gas phase in the desorber:

1. Absorbed CO_2 from the flue gas calculated based on the absorber inlet and outlet gas phase CO_2 mole fractions which are measured with IR-analyzers and the gas flow measurement located prior to the absorber ($F_{\text{g,abs,in}}$):

$$m^{\text{g}}_{\text{CO}_2,\text{abs}} = (F_{\text{g,abs,in}} \cdot y_{\text{CO}_2,abs,in} - F_{\text{g,abs,out}} \cdot y_{\text{CO}_2,\text{abs,out}}) \frac{M_{\text{CO}_2}}{3600} \tag{3.4}$$

   $F_{\text{g,abs,out}}$ is the absorber outlet gas flow rate which is estimated based on the assumption of constant flow of inert gas through the column (inert components are assumed not to be absorbed):

$$F_{\text{g,abs,out}} = F_{\text{g,abs,in}} \frac{y_{\text{inert,abs,in}}}{y_{\text{inert,abs,out}}} \tag{3.5}$$

   The mole factions of inert gas is calculated based on the assumption of gas being saturated with water at the absorber inlet and outlet:

$$y_{\text{inert}} = 1 - y_{\text{CO}_2} - y_{\text{H}_2\text{O}} \tag{3.6}$$

   where the absorber inlet and outlet gas phase temperatures determines the H_2O mole fractions.

2. Absorbed CO_2 in the solvent calculated based on analysis of the absorber inlet and outlet solvent CO_2 molal concentrations ($\bar{C}_{\text{l,CO}_2,\text{abs,in}}$ and $\bar{C}_{\text{l,CO}_2,\text{abs,out}}$) and lean and rich solvent mass flow rates ($\bar{F}_{\text{l,lean}}$ and $\bar{F}_{\text{l,rich}}$):

$$m^{\text{l}}_{\text{CO}_2} = (\bar{F}_{\text{l,rich}} \cdot \bar{C}_{\text{l,CO}_2,\text{abs,out}} - \bar{F}_{\text{l,lean}} \cdot \bar{C}_{\text{l,CO}_2,\text{abs,in}}) \frac{M_{\text{CO}_2}}{1000} \tag{3.7}$$

3. Desorbed CO_2 calculated based on the condenser outlet gas flow rate ($\bar{F}_{g,cond,out}$) and CO_2 content ($w_{CO_2,cond,out}$):

$$m^{g}_{CO_2,des} = \bar{F}_{g,cond,out} \cdot w_{CO_2,cond,out} \tag{3.8}$$

where $w_{CO_2,cond,out} = 1 - w_{H_2O,cond,out}$ and $w_{H_2O,cond,out}$ is determined by the condenser temperature.

The CO_2 mass balances are found by comparing the different values of calculated absorbed CO_2, according to Equations 2.2 - 2.4, and these indicate the confidence in the measurements and possible pilot plant leakages. The calculated experimental absorption/desorption rates and relative deviation in calculated steady state mass balances are presented in Table 3.1. The experimental absorption/desorption rates are also presented in parity plots in Figure 3.1.

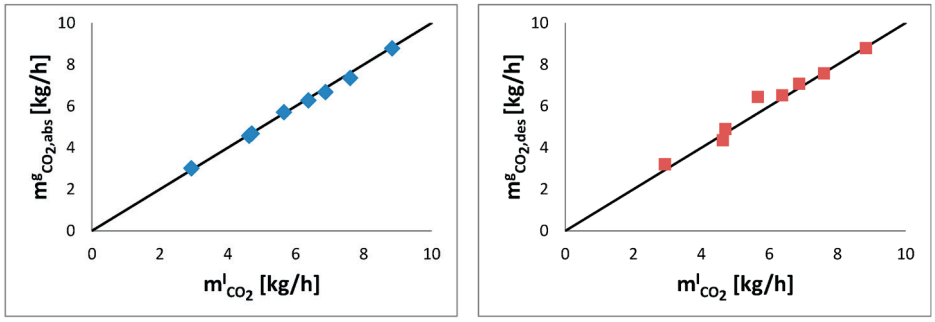

(A) Calculated based on absorber inlet and outlet gas and solvent conditions

(B) Calculated based on desorber outlet gas and inlet and outlet solvent conditions

FIGURE 3.1: Experimental CO_2 absorption and desorption rates for the Gløshaugen pilot plant.

The calculated ARD by Equation 2.5 for the absorber ($m^{g}_{CO_2,abs}$ compared to $m^{l}_{CO_2}$) is 1.8%, with a maximum relative deviation of 3.4%. The small deviations indicate that the logged pilot plant data for these calculations are reliable and that steady state conditions were attained in the start of each experiment. The overall mass balance ($m^{g}_{CO_2,des}$ compared to $m^{l}_{CO_2}$) shows slightly larger relative deviations with an ARD of 5.1% and a maximum of 12.0%. The confidence of the absorption rates calculated by methods 1 and 2 (based on their good agreement), suggests that method 3 ($m^{g}_{CO_2,des}$) is slightly overpredicted in most cases, which is probably caused by a measurement inaccuracy of produced CO_2 gas flow rate. The same trend is also indicated in the dynamic results presented in Figure 3.4

TABLE 3.1: Steady state data from the Gløshaugen pilot plant.

Case		**1**	**2**	**3**	**4**	**5**	**6**	**7**	**8**
Flue gas flow rate	[Nm^3/h]	78.6	75.8	112.2	89.1	109.1	107.6	107.4	105.4
Flue gas temperature	[°C]	42.2	49.2	46.7	41.8	44.4	38.9	39.6	36.6
Flue gas CO_2 concentration	[dry vol%]	3.5	6.8	3.0	3.6	3.9	5.4	4.6	1.6
Lean solvent flow rate	[kg/h]	166.9	172.3	152.1	142.1	240.9	178.7	238.8	239.1
Lean solvent solvent temperature	[°C]	49.1	58.3	58.0	53.5	52.2	46.9	50.0	40.9
Lean MEA concentration	[wt%]	31.0	32.2	31.2	30.4	33.0	29.2	30.3	29.2
Lean CO_2 loading	[$molCO_2/molMEA$]	0.30	0.26	0.22	0.25	0.27	0.34	0.31	0.26
Rich CO_2 loading	[$molCO_2/molMEA$]	0.42	0.45	0.49	0.42	0.41	0.49	0.44	0.32
Reboiler duty	[kW]	6.8	9.2	10.0	8.3	10.4	6.1	8.3	8.3
Stripper pressure	[bar]	1.91	1.91	1.92	1.91	1.91	1.72	1.71	1.71
Calculated absorbed amount of CO_2									
Absorbed from gas ($m^{g}_{CO_2,abs}$)	[kg/h]	4.57	7.35	8.78	5.71	6.67	4.68	6.28	3.01
Absorbed to solvent ($m^{l}_{CO_2}$)	[kg/h]	4.63	7.60	8.84	5.66	6.88	4.71	6.38	2.93
Desorbed ($m^{g}_{CO_2,des}$)	[kg/h]	4.36	7.58	8.79	6.44	7.08	4.89	6.52	3.21
Relative deviation in steady state CO_2 mass balance									
Absorber	[%]	+1.3	+3.4	+0.7	-0.9	+2.9	+0.6	+1.6	-2.6
Desorber	[%]	-8.3	-0.2	-0.6	+12.5	+3.7	+5.9	+0.3	+2.4
Overall process	[%]	-4.7	+3.0	+0.1	+12.1	+5.8	+4.4	+3.8	+6.6
Energy performance	[$MJ/kgCO_2$]	5.30	4.37	4.08	5.28	5.42	4.68	4.70	10.14

later in this chapter, where a larger level of desorbed CO_2 is a general observation. It is therefore concluded that the CO_2 absorption rates estimated by methods 1 and 2 are most reliable.

3.4.2 Energy performance

Two other campaigns with 30 wt% MEA have been performed over the years in the same pilot plant. Figure 3.2 is collected from Paper E in Appendix C.5 and shows a comparison of the specific reboiler duty (SRD) as a function of rich loading at steady state in all the three campaigns. The specific reboiler duty in [$MJ/kgCO_2$] is calculated by:

$$SRD = \frac{Q_{reb}}{m_{CO_2}} \frac{3600}{1000} \tag{3.9}$$

where Q_{reb} is the reboiler duty in [kW], and m_{CO_2} is the amount of absorbed CO_2 in [kg/h]. $m^l_{CO_2}$ estimated by Equation 3.7 was used in these calculations.

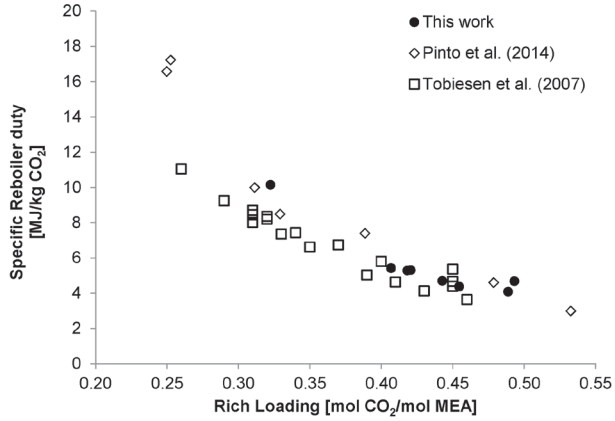

FIGURE 3.2: Specific reboiler duty as a function of rich loading for the Gløshaugen pilot plant.

Slightly higher values of the specific reboiler duty were estimated in the campaign by Pinto et al. (2014) and in paper E in Appendix C.5 compared to Tobiesen et al. (2007). The difference is not very large and can most likely be explained by the change of packing material and packing height in the stripper. In Tobiesen et al. (2007), Mellapak 250Y was used in the stripper and the packing height was 4.1

m, whereas Sulzer BX of packing height 3.57 m was used during the campaigns presented in Pinto et al. (2014) and paper E in Appendix C.5. Overall it is clear that the pilot plant data gathered in the present work is in good agreement with data from Pinto et al. (2014) and Tobiesen et al. (2007).

3.5 Dynamic pilot plant results

Six different dynamic runs were successfully executed in the Gløshaugen pilot plant campaign with step changes in the lean solvent flow rate and reboiler duty. Due to the configuration of the Gløshaugen pilot plant with direct recirculation of CO_2 released in the desorber to the absorber inlet gas, any step change in solvent flow rate or reboiler duty will consequently affect the CO_2 content of the absorber inlet gas. These variations serve as an additional disturbance to the system.

The flue gas flow rate, flue gas CO_2 content, solvent flow rate and reboiler duty of the six different dynamic runs are presented graphically in Figure 3.3. Additional information about the steady state starting points is given in Table 3.1. The logged responses in absorbed and desorbed CO_2 and solvent CO_2 loading are presented in Figure 3.4.

The dynamic results for absorption and desorption rates show quite fast dynamics and transient dependency between the two sections of the plant, as the responses are very similar and only a minor delay is observed from the absorber to the desorber. A small stationary deviation is observed, as the estimated desorption rate is slightly larger than the absorption rate in most cases. This is related to the deviations in CO_2 mass balance at steady state which was discussed in Section 3.4.1. Some instabilities are observed for some of the cases, especially for absorption rate after the set-point change in case 6. This result from variations in the CO_2 product flow rate, due to fluctuations in the stripper pressure. The produced CO_2 is mixed with the absorber outlet gas and fed back to the absorber as inlet gas. Variations in the CO_2 product flow rate will therefore cause disruptions in the flow rate and composition of the absorber inlet gas, which again causes fluctuations in the absorber outlet gas. These variations are amplified in the absorption rate calculated by Equation 3.4, since this relation is based on both absorber inlet and outlet gas flow rates and CO_2 concentrations, which both fluctuate only slightly shifted in time. A better time dependent prediction of the absorption rate in cases

with fluctuating gas flow rates and concentrations could have been provided using the lean and rich solvent flow rates and CO_2 concentrations. However, the rich solvent flow rate did also fluctuate significantly during most of the experiments due to flashing in the cross heat exchanger, thus this variable is only suited for steady state calculations where it can be time-averaged.

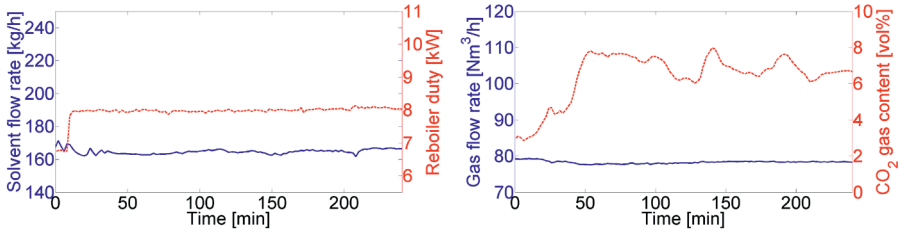

(A) Case 1: +17.0% set-point change in reboiler duty

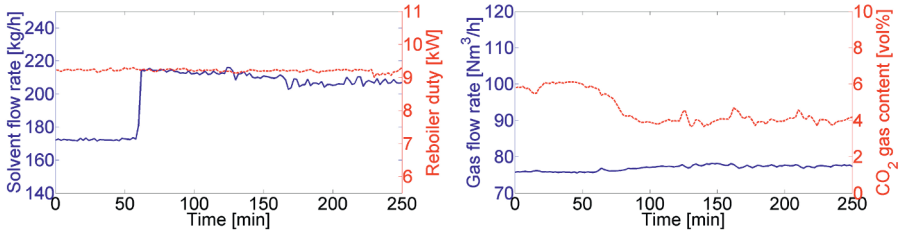

(B) Case 2: +21.8% set-point change in solvent flow rate

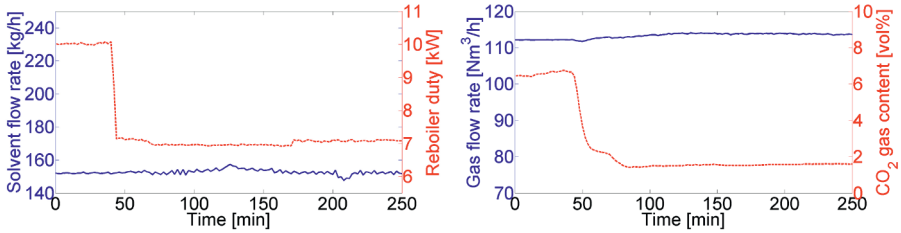

(C) Case 3: -29.6% set-point change in reboiler duty

FIGURE 3.3: Dynamic test campaign in the Gløshaugen pilot plant. Graphs to the left: (—) solvent flow rate and (---) reboiler duty. Graphs to the right: (—) flue gas flow rate and (---) flue gas CO_2 content.
(Continues next page)

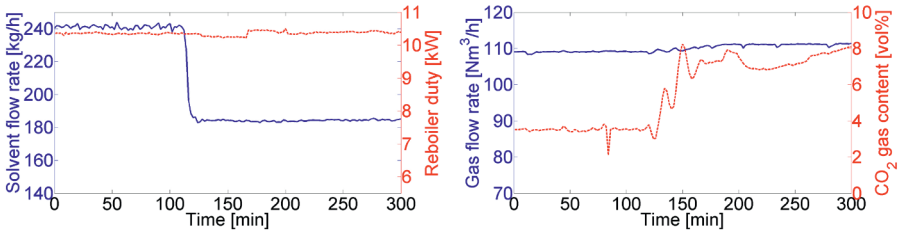

(D) Case 5: -23.5% set-point change in solvent flow rate

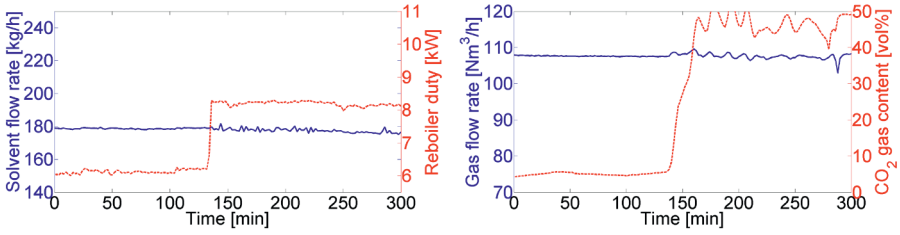

(E) Case 6: +33.3% set-point change in reboiler duty

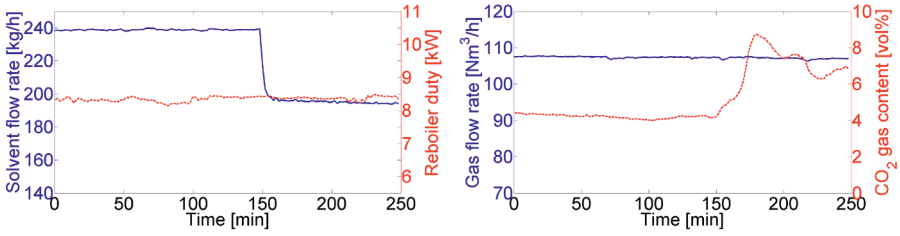

(F) Case 7: -18.0% set-point change in solvent flow rate

FIGURE 3.3: Dynamic test campaign in the Gløshaugen pilot plant. Graphs to the left: (—) solvent flow rate and (---) reboiler duty. Graphs to the right: (—) flue gas flow rate and (---) flue gas CO_2 content. (Continued from previous page)

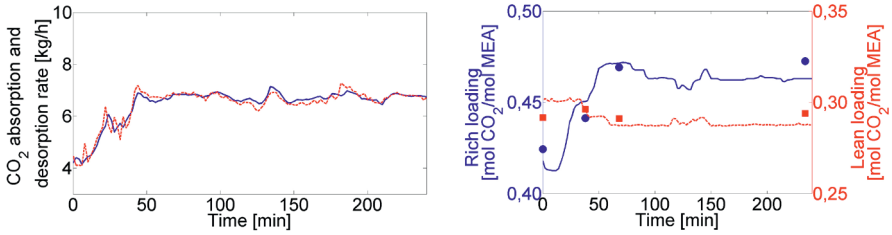

(A) Case 1: +17.0% set-point change in reboiler duty

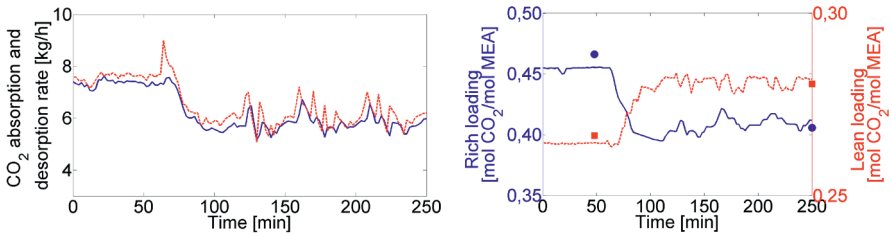

(B) Case 2: +21.8% set-point change in solvent flow rate

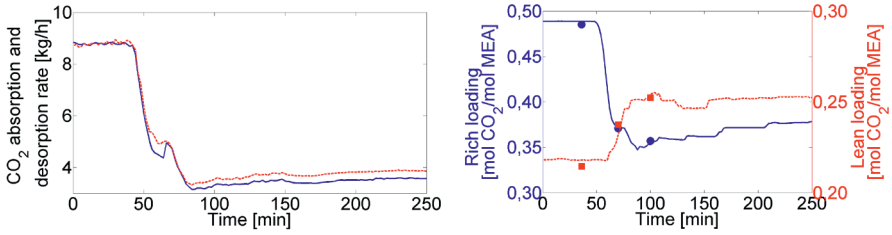

(C) Case 3: -29.6% set-point change in reboiler duty

FIGURE 3.4: Results from the dynamic test campaign in the Gløshaugen pilot plant. Graphs to the left: (—) absorbed CO_2 ($m^g_{CO_2,abs}$), (---) desorbed CO_2 ($m^g_{CO_2,des}$). Graphs to the right: (—) rich CO_2 loading (density), (●) rich CO_2 loading (analysis), (---) lean CO_2 loading (density) and (■) lean CO_2 loading (analysis).
(Continues next page)

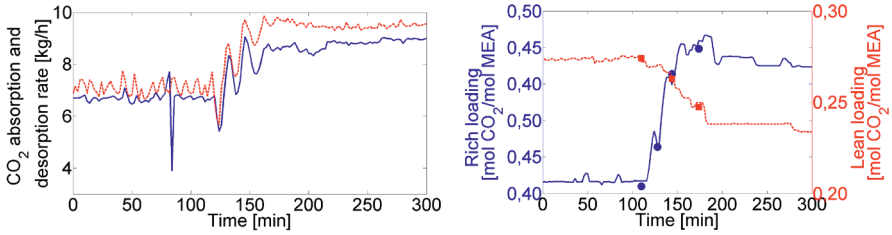

(D) Case 5: -23.5% set-point change in solvent flow rate

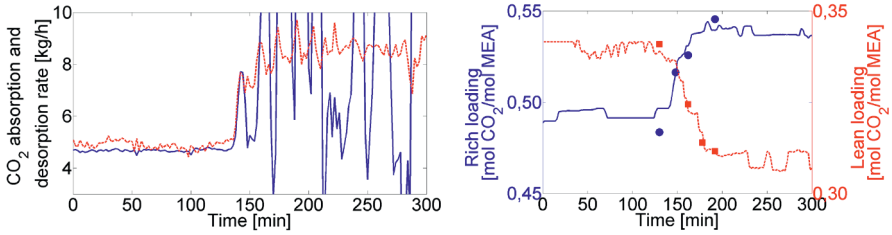

(E) Case 6: +33.3% set-point change in reboiler duty

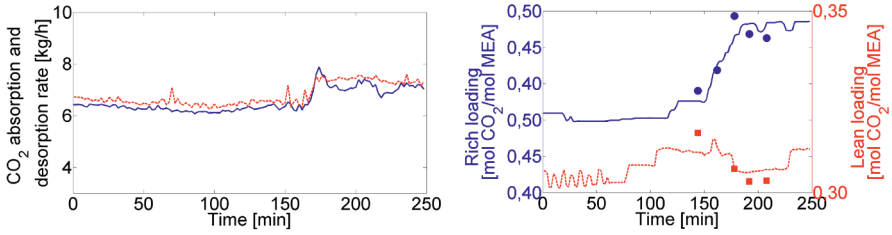

(F) Case 7: -18.0% set-point change in solvent flow rate

FIGURE 3.4: Results from the dynamic test campaign in the Gløshaugen pilot plant. Graphs to the left: (—) absorbed CO_2 ($m^{g}_{CO_2,abs}$), (---) desorbed CO_2 ($m^{g}_{CO_2,des}$). Graphs to the right: (—) rich CO_2 loading (density), (●) rich CO_2 loading (analysis), (---) lean CO_2 loading (density) and (■) lean CO_2 loading (analysis).
(Continued from previous page)

Chapter 4

Dynamic process model development

4.1 Introduction to dynamic process modeling

There are various approaches to dynamic process modeling. One distinction is made for empirical vs mechanistic models. Empirical models are simply derived by fitting data and are therefore only local representations of the process. Empirical models can therefore not be extrapolated outside the range of data used for fitting. Mechanistic models rely on our understanding of the process and are derived from first principle balances or fundamental conservation laws, which make them rigorous and useful for simulation and exploration of new operating conditions (Hangos and Cameron, 2001).

The development of a dynamic model from first principles leads in general to a mixed set of partial differential and algebraic equations (PDAEs), i.e.,

$$G(t, z, x(t,z), y(t,z), \frac{\partial y(t,z)}{\partial t}, \frac{\partial y(t,z)}{\partial z}, v(x,y)) = 0 \tag{4.1}$$

where t and z are independent variables, y is a set of dependent variables for which partial derivatives are defined, x is a set of dependent variables for which no partial derivatives are defined, and v are additional parameters calculated from dependent variables.

Partial differential equations (PDEs) typically arise from the conservation of fundamental quantities, while algebraic equations (AEs) result from processes where accumulation is not considered important or transients are assumed to occur instantaneously, as well as from the introduction of other auxiliary relationships among variables.

A PDAE system can be reduced to a system of differential-algebraic equations (DAEs) in the form of:

$$H(t, x(t), y(t), \frac{\partial y(t)}{\partial t}) = 0 \tag{4.2}$$

This can be achieved by discretization of partial derivatives. The system can further be simplified by differentiation of the algebraic equations. The DAE system is then transformed to an ordinary differential equation (ODE) system which makes the problem easier to solve. A disadvantage is that the link to physical representation is lost after the algebraic equations are differentiated.

Models may further be divided into lumped parameter and distributed parameter models. The distributed parameters are functions of spacial location such as a series of compartments or stages, while the lumped parameters are assumed to be independent of location and can therefore be regarded as a single compartment or a stage. Dynamic lumped parameter models result typically in ODEs, while distributed parameter models will lead to PDEs (Hangos and Cameron, 2001). Discretization is normally required for the latter in order to solve the model numerically as a set of ODEs. Orthogonal collocation is a useful method for discretization, which uses the roots of orthogonal polynomials to transform the PDEs to ODEs. The approximation of the first and second order derivatives and integral term at the ith collocation point are shown below (Arora et al., 2005):

$$\left(\frac{\partial y}{\partial z}\right)_{z=z_i} = \sum_{j=1}^{N+2} A_{i,j} y_j \tag{4.3}$$

$$\left(\frac{\partial^2 y}{\partial z^2}\right)_{z=z_i} = \sum_{j=1}^{N+2} B_{i,j} y_j \tag{4.4}$$

$$\left(\int_{z=z_1}^{z=z_{N+2}} y(z)dz\right)_{z=z_i} = \sum_{j=1}^{N+2} Q_{i,j} y_j \tag{4.5}$$

where N is the number of internal collocation points, A is the matrix of first derivative weights, B is the matrix of second derivative weights and Q is the matrix of quadrature weights.

For solution of the equation system, a distinction can be made between the simultaneous equation-based and modular integration approaches. In the simultaneous equation-based approach the system is modeled as a whole, meaning that all model equations are implemented in a single routine and solved simultaneously (Westerberg and Piela, 1994). The advantage of this method is that information between connecting units is handled directly (Vegeais and Stadtherr, 1992), which is especially beneficial in the case of process recirculation loops. However, it can be cumbersome to modify a simultaneous model for different process configurations.

In the sequential modular approach the model is decomposed into sub-systems or modules which typically represent separate pieces of process equipment. Each module is solved individually and the output of every module is computed as a function of inputs and internal variables (Westerberg and Piela, 1994). Modules are characterized either as a storage (pressure) module or a resistive (flow) module. A module in which the conserved variables are accumulated is called a storage module and is characterized by dynamic conservation laws in the form of:

$$\frac{dP(t)}{dt} \propto F(t) \tag{4.6}$$

This type of module calculates the pressure ($P(t)$) based on input and output mass flows ($F(t)$). In resistive modules the accumulation of conserved variables is neglected, which results in algebraic equations in the form of:

$$F(t) \propto P(t) \tag{4.7}$$

The mass flow is here calculated based on upstream and downstream pressures. To keep causality, storage and resistive modules must be connected in series, as shown in Figure 4.1.

The sequential modular-based method requires additional coordination algorithms to handle information flow between connecting units (Westerberg and Piela, 1994). The co-ordination algorithm should also keep the various process units synchronized in time, and it should be able to handle process recirculation loops which

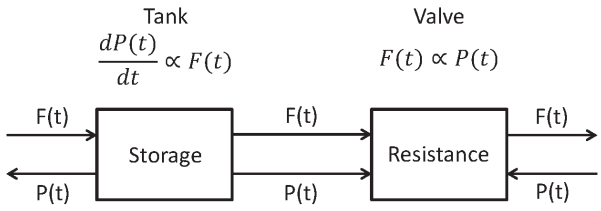

FIGURE 4.1: The principle of the sequential modular approach.

must be solved by iteration since each module is solved individually. The coordination algorithm will treat each process unit as a "black box" that produces output given input. Since outlet flow from a process unit is pressure driven, the downstream pressures must also be provided to each unit. Hence, pressure-flow interaction loops exist between connecting process units. These loops may be solved by an iterative procedure on the modular integration level. Alternatively, by decoupling the problem in two levels (one for fast pressure dynamics and one for slow dynamics) the loops can be solved by a pressure-flow interaction algorithm (P-F network solver) on flow sheet level without or with minimum iteration. Pressure predictions will subsequently be used as input to the modular integration level. Further, the total simulation window is divided into time intervals where couplings between units occur only at the end of each time interval. The units' external variables (input from connecting units) need to be described as functions of time, i.e. as polynomials.

The sequential modular-based method offers the possibility of computational speed through parallel processing of the individual process units. An additional advantage is the possibility of tailoring the integration algorithm to each process unit and its dynamic behavior, which offers desirable convergence and stability properties (Vegeais and Stadtherr, 1992). Specifying initial conditions that satisfy the system of equations for each process unit is also easier compared to specifying consistent initial conditions for the simultaneously solved complete process model. The modular approach would be more preferable for complex equation systems since it enables the user to increase the level of complexity where necessary and re-use existing model components.

Model variables are also classified into different groups. Independent variables require specification by the user and represent extra degrees of freedom. The

independent variables in dynamic simulations are typically time (t), and an additionally direction (z) in the case of distributed parameter models. Dependent variables are calculated from the solution of the model equations. Typical examples are temperatures and mole fractions. Parameters, such as densities or rate constants, are variables calculated from the dependent variables.

In order to run a model and simulate a process, various parameters, constants, initial conditions for dependent variables and system boundaries must be specified as model input variables.

4.2 Dynamic modeling of post-combustion CO_2 capture units

4.2.1 Approaches for interface mass transfer modeling

The packed columns in the post-combustion CO_2 capture process are the most complex process units to model. Two different approaches are commonly used for modeling interface mass and heat transfer, that is the equilibrium-stage (EQ) approach and the non-equilibrium (NEQ) or rate-based approach (Peng et al., 2002). An overview is illustrated in Figure 4.2.

The equilibrium stage approach (bottom illustrations in Figure 4.2) assumes theoretical ideal stages in which liquid and vapor phases attain equilibrium. This has been the traditional method due to its simplicity (Taylor and Krishna, 1993). These models may assume that chemical reactions are at equilibrium or may consider the reaction kinetics. Recently, the rate-based approach (upper illustrations in Figure 4.2), where actual mass and heat transfer rates are considered to estimate fluxes across the interface has earned increasing attention (Peng et al., 2002). This is a more appropriate method for modeling reactive absorption processes since phase equilibrium is hardly attained in practice. The rate-based approach assumes that the vapor-liquid equilibrium occurs only at the interface which gives a more consistent method of modeling (Afkhamipour and Mofarahi, 2013). At its lowest level of complexity, the chemical reactions of the rate-based model are assumed to be at equilibrium (upper left illustration in Figure 4.2). A more rigorous approach involves the inclusion of an enhancement factor to estimate actual absorption rates

with chemical reactions from known physical absorption rates (upper middle illustration in Figure 4.2). At the highest level of complexity, reaction kinetics are modeled directly (upper right illustration in Figure 4.2), that is reaction rates are implemented directly into the transport and balance equations in the film and the bulk of the fluid.

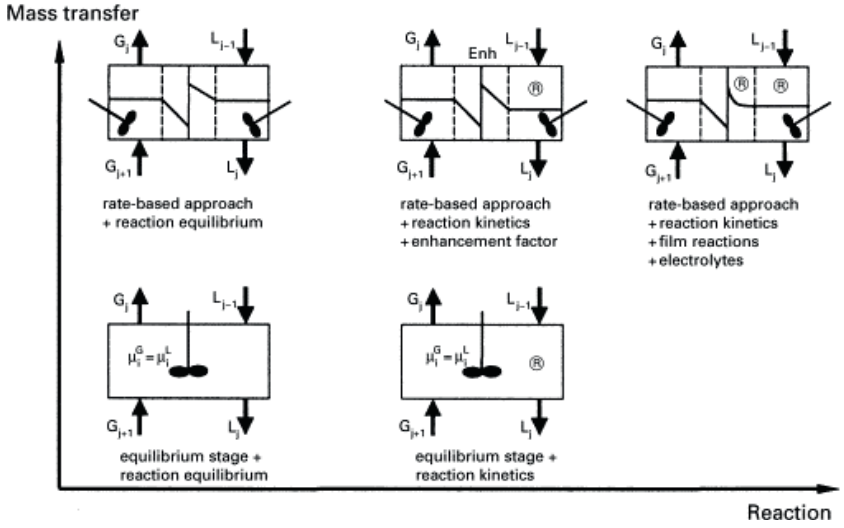

FIGURE 4.2: Different levels of reactive absorption model complexity (Kenig et al., 2001).

4.2.2 Literature review

A literature review on the state-of-the-art of dynamic process modeling of post-combustion CO_2 capture using amines is found in Paper A in Appendix C.1. Since 2011, a considerable effort has been put into the research and model development on this topic. The recent contribution of Bui et al. (2014) provides an updated examination of the dynamic modeling activity reported in the literature, along with a thorough discussion of key areas that need to be addressed in future dynamic process models.

The first dynamic models were simplified and consisted only of one section of the PCC process, that is the absorber (Gáspár and Cormoş, 2011, 2012, Jayarathna et al., 2011, 2013a, Kvamsdal et al., 2009, Lawal et al., 2009a,b, Mac Dowell et al., 2013, Posch and Haider, 2013), the desorber (Gáspár and Cormoş, 2011, Greer et al., 2010, Ziaii et al., 2009) or the reboiler (Arce et al., 2012) only. Recently,

more complex and extensive process models are developed where several units are included and connected to each other. Some of these process models does only concern the connected absorber and desorber columns and possibly the reboiler, which means that other units such as the column sumps and cross heat exchanger are neglected. However, the additional units does also store accumulated solvent and may therefore represent important dynamics that should be included in the process model in order to improve the overall dynamic representation of the plant.

A variety of commercially available modeling tools have been used for dynamic process simulation of the PCC process. Some of these are limited to specific model complexities, such as Aspen Dynamics which only allows equilibrium-based models in dynamic mode. MATLAB® and gPROMS® does however provide desirable flexibility for the choice of model complexity according to the specific model applications. These tools give the user full insight into the structure and content of the process model and underlying sub-models, along with greater influence and opportunities to modify the model and its complexity and accuracy for specific applications.

Comparison of simulation results to experimental observations is important in order to ensure that the developed models predict realistic results. A general lack of proper data for dynamic model validation has been reported by several authors in the literature (Biliyok et al., 2012, Bui et al., 2014, Kvamsdal et al., 2009), and consequently most of the developed models are only validated for steady state conditions, if validated at all. This issue will be further elaborated in Chapter 5.

Table 4.1 gives a summary of main findings in the literature on dynamic process modeling of post-combustion CO_2 capture.

TABLE 4.1: Summary of dynamic modeling on post-combustion CO_2 capture using amines.

Reference	**Simulation tool**	**Model complexity**	**Model validation**	**Description and model application**
Lawal et al. (2010)	gPROMS and Aspen Properties	Rate based mass transfer and chemical equilibrium	Steady state validation using data from the SRP pilot plant (Dugas, 2006)	Steady state model validation and dynamic analysis of step-changes in water balance control, flue gas flow rate and reboiler duty
Lawal et al. (2011)	gPROMS and Aspen Properties	Rate based mass transfer and chemical equilibrium. Process model previously presented in (Lawal et al., 2010).	Steady state validation using data from the SRP pilot plant (Dugas, 2006) previously presented in (Lawal et al., 2010)	Investigation of dynamic behavior of PCC in an enhanced O_2 coal combustion power plant
Lawal et al. (2012)	gPROMS and Aspen Properties	Rate based mass transfer and chemical equilibrium. Scale-up of process model presented in (Lawal et al., 2010), and integration to a power plant model.	Steady state validation using data from the SRP pilot plant (Dugas, 2006) previously presented in (Lawal et al., 2010)	Development of a power plant model linked to a full-scale PCC model, and investigation of plant performance with different absorber column heights, different concentrations of MEA, reducing power plant output and increasing capture level set-point
Biliyok et al. (2012)	gPROMS and Aspen Properties	Rate based mass transfer and chemical equilibrium. Process model previously presented in (Lawal et al., 2010).	Steady state validation using data from the SRP pilot plant (Dugas, 2006) presented in (Lawal et al., 2010) and dynamic validation using logged data from the SRP pilot plant	Dynamic model validation and investigation of dynamic effects of increasing inlet flue gas moisture and impacts of absorber inter-cooling
Panahi and Skogestad (2012)	UniSim			Evaluation of control structures

TABLE 4.1: Summary of dynamic modeling on post-combustion CO_2 capture using amines (continued from previous page)

Reference	**Simulation tool**	**Model complexity**	**Model validation**	**Description and model application**
Karimi et al. (2012)	Unisim Design	Rate based mass transfer	Steady state validation using data from the SRP pilot plant (Dugas, 2006)	Evaluation of various stripper configurations
Harun et al. (2012)	gPROMS	Rate based mass transfer and enhancement factor	Steady state validation using Aspen Plus simulation results and data from the SRP pilot plant (Dugas, 2006)	Investigation of transient responses to changes in the flue gas flow rate and the reboiler heat duty
Nittaya et al. (2014a)	gPROMS	Rate based mass transfer and enhancement factor. Process model based on Harun et al. (2012) with inclusion of condenser, absorber sump and reboiler	Steady state validation using data from the SRP pilot plant (Dugas, 2006) previously resented in Harun et al. (2012)	Investigation of control structures
Nittaya et al. (2014b)	gPROMS	Rate based mass transfer and enhancement factor. Process model previously presented in Nittaya et al. (2014a)	Steady state validation using data from the SRP pilot plant (Dugas, 2006) previously resented in Harun et al. (2012)	Process scale-up and investigation of the effects of absorber height, changes in flue gas flow rate, changes in CO_2 capture level set-point and flue gas composition
Jayarathna et al. (2013c)	MATLAB	Rate based mass transfer and enhancement factor. Cross heat-exchanger, lean cooler, column sumps and buffer tank are not included	Steady state validation using data from the SRP pilot plant (Dugas, 2006)	Investigation of process dynamics for changes in flue gas flow rate and reboiler vapor fraction

TABLE 4.1: Summary of dynamic modeling on post-combustion CO_2 capture using amines (continued from previous page)

Reference	Simulation tool	Model complexity	Model validation	Description and model application
Jayarathna et al. (2013b)	MATLAB	Rate based mass transfer and enhancement factor. Improvement of the previously presented process model in Jayarathna et al. (2013c) by inclusion of heat-exchangers and buffer tank tank	Steady state validation using data from the SRP pilot plant (Dugas, 2006)	Investigation of process dynamics for changes in flue gas flow rate, solvent flow rate and evaporation fraction in the reboiler
Prölß et al. (2011)	Dymola/ Modelica	Rate based mass transfer and chemical equilibrium		Model reduction and comparison of simplified and rigorous models
Åkesson et al. (2012)	Dymola/ Modelica	Rate based mass transfer and chemical equilibrium. Process model previously presented in Prölß et al. (2011)	Dynamic validation using data from the Esbjerg pilot plant (Faber et al., 2011)	Dynamic model validation and and model reduction for demonstration of NMPC
Garðarsdóttir et al. (2015)	Dymola/ Modelica	Rate based mass transfer and chemical equilibrium. Process model is based on the model previously presented in Åkesson et al. (2012) with inclusion of power plant steam extraction	Dynamic validation using data from the Esbjerg pilot plant (Faber et al., 2011) previously presented in Åkesson et al. (2012)	Power plant steam extraction is modeled and included in a scale-up of the previously developed PCC model. Control strategies are developed and the transient behavior of the absorption system during power plant load changes is investigated.

TABLE 4.1: Summary of dynamic modeling on post-combustion CO_2 capture using amines (continued from previous page)

Reference	**Simulation tool**	**Model complexity**	**Model validation**	**Description and model application**
Ziaii et al. (2011)	Aspen Custom Modeller	Rate based mass transfer. Steady state heat exchangers, CO_2 compressors and steam turbine		Development of dynamic absorber and desorber models integrated with steady state approximated steam turbines and CO_2 compression.
Léonard et al. (2013)	Aspen Plus Dynamics	Equilibrium-stage		Investigation of water balance control strategies
Dietl et al. (2012)	Modelica	Rate based mass transfer and chemical equilibrium		Evaluation of control structures
Lin et al. (2011)	Aspen Dynamics	Equilibrium-stage and chemical equilibrium		Evaluation of control structure for various disturbances
Lin et al. (2012)	Aspen Dynamics	Equilibrium-stage and chemical equilibrium		Development of a power plant model and evaluation of control structures for flexible operation
Mac Dowell and Shah (2015)	gPROMS	Rate based mass transfer and chemical equilibrium		Power plant model development and evaluation of flexible operation modes: load following, solvent storage, exhaust gas by-pass and time-varying solvent regeneration
Enaasen et al. (2014) (paper D in Appendix C.4)	K-Spice	Rate based mass transfer and enhancement factor	Validation using data from the Brindisi plant	Dynamic model validation
Flø et al. (2015) (paper E in Appendix C.5)	MATLAB	Rate based mass transfer and enhancement factor	Validation using data from the Gløshaugen pilot plant	Dynamic model validation

4.3 Development of the MATLAB model

4.3.1 Overall flow sheet modeling

The amine-based CO_2 capture process is relatively complex with many different unit operations and process control units. For the present dynamic models, the process configurations are simplified by only taking the major and most important process units and controllers into account. Process scheme simplifications and flow sheets of the modeled processes are given in present section, while the different process unit models and approaches for modeling of heat and mass transfer, column hydrodynamics and physical properties are described in the subsequent sections.

The process model developed in MATLAB® consist of dynamic unit models representing each piece of process equipment: absorber, desorber, absorber sump, reboiler, condenser, cross heat exchanger, lean cooler and buffer tank. All process unit models are mechanistic and are developed from first principle conservation laws. The absorber, desorber, cross heat exchanger and lean cooler models are distributed parameter models, while the other units are lumped models where perfect mixing is assumed. This leads to a set of PDAEs as will be presented in Section 4.3.2.

The desorber sump model is typically lumped into the reboiler and the piping is lumped into the cross heat exchanger model in the present work. The water wash sections usually connected to the absorber and desorber sections are not considered in the MATLAB model. The purpose of these sections is to remove MEA droplets and water vapor from the outlet gas. The omission of these sections can therefore lead to a higher loss of MEA and water through the absorber outlet gas, causing a higher make-up requirement. However, the uncertainties of MEA carry-over is large and dependent on external factors like particles and contaminants present in the flue gas, which are not considered in the model. Such phenomena will also have limited effect on the process dynamics, and are therefore not considered important for the dynamic process model. Make-up water must however be provided in dynamic simulations over longer periods to maintain the water-balance.

Basic control systems are also implemented with level controllers for main vessels, a pressure controller for the desorber and temperature controllers in the condenser and lean cooler. P- or PI-controllers are implemented for this purpose, and the

use of PI-controllers will additionally introduce an integral equation as described in Appendix A.5.

The various units of the overall process model developed in MATLAB are indicated in Figure 4.3 along with their respective set of dependent variables. The system boundary is indicated by the green dashed line around the process in Figure 4.3. For the open-loop process model, a minimum of seven different feed points or model inputs are present as indicated by red arrows and text in Figure 4.3:

1. Flue gas flow rate and condition (temperature and composition)
2. Absorber gas outlet pressure
3. Solvent flow rate
4. Lean solvent cooling duty, or controller set-point
5. Reboiler duty, or controller set-point
6. Condenser cooling duty, or controller set-point
7. CO_2 outlet pressure

In addition make-up water and amine are system feed points which also must be provided if applied. Other input parameters that require specification are process parameters such as equipment sizes and specifications, control parameters and set-points and initial conditions. The main process sinks or outputs are purified flue gas and CO_2 product gas as indicated by blue arrows and text in Figure 4.3.

The dependent variables for each process unit are also indicated in Figure 4.3. The absorber model has 11 dependent variables for each collocation point (4 gas mole fractions, 3 solvent mole fractions, gas and liquid temperature and gas and liquid molar flux). The desorber column has 10 dependent variables for each collocation point (3 gas mole fractions, 3 solvent mole fractions, gas and liquid temperature and gas and liquid molar flux). The general heat exchanger model has 10 dependent variables for each collocation point , 5 on each of the cold and hot side (3 solvent mole fractions, liquid temperature and liquid molar flux). The lean solvent cooler does only have one single liquid component on the cooling water side, thus the number of dependent variables is reduced to 7 for each collocation point. The flash tank model has 8 dependent variables (3 component molar hold-ups for

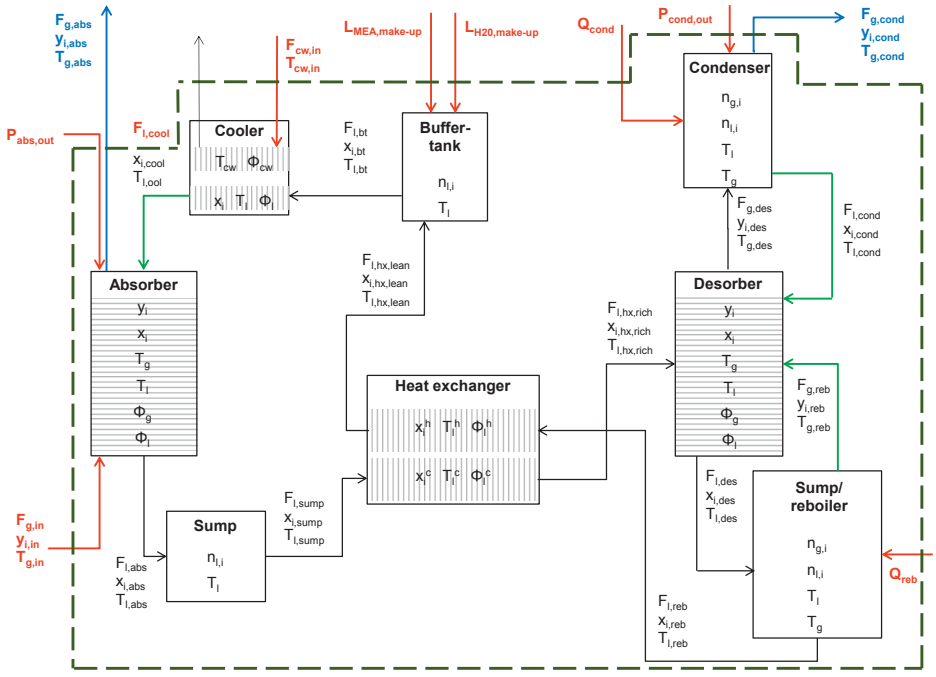

FIGURE 4.3: System boundary and connections between units in the post-combustion CO_2 capture process. The dependent variables are indicated for each process unit, where x and y are liquid and gas mole fractions, n is molar hold-up, T is temperature and Φ is mass flux. i indicates different components, CO_2, H_2O and MEA for the general case and additionally inert for the absorber gas phase. Process input variables are indicated with red arrows and text, while output variables are indicated with blue arrows and text.

gas phase, 3 component molar hold-ups for liquid phase, along with gas and liquid temperatures), and the mixing tank has 4 dependent variables (3 component molar hold-ups for liquid phase and liquid temperatures). All PI-controllers will also contribute with an additional dependent variable, according to Equation A.81 in Appendix A.5. A system consisting of an absorber, desorber, cross heat exchanger, lean cooler, reboiler, condenser, absorber sump and buffer tank, with 30 collocation points in the absorber, 20 in the desorber and 10 in the heat exchanger and lean cooler, along with PI controllers for level in absorber sump, reboiler and condenser, temperature in lean cooler and condenser and pressure in the desorber will consequently have a total of 730 dependent variables and dynamic model equations, as shown in Table 4.2.

The MATLAB model is adapted for three different pilot plant configurations which

TABLE 4.2: Number of dependent variables in the dynamic MATLAB model.

Absorber column	(30 x 11)	330
Absorber sump		4
Cross heat exchanger	(10 x 10)	100
Desorber column	(20 x 10)	200
Reboiler		8
Condenser		8
Buffer tank		4
Lean cooler	(10 x 7)	70
Controllers		6
Overall model		730

are illustrated in Figures 4.4 - 4.6. The CO_2 recirculation from condenser gas outlet to absorber inlet is Gløshaugen pilot plant is not considered in the model, and the absorber inlet gas is defined as a model input. The model of the Tiller pilot plant has included a level controller and a MEA concentration controller in the buffer tank for simulation purposes which will be described in Section 6.1.

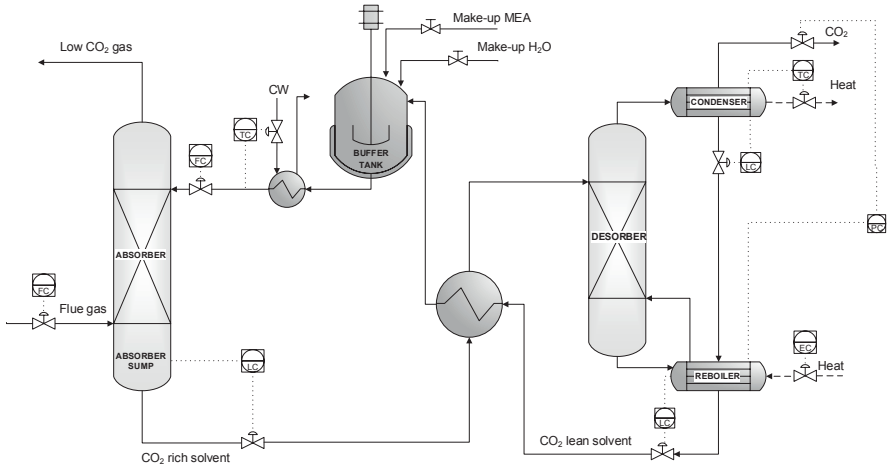

FIGURE 4.4: MATLAB model of the Gløshaugen pilot plant corresponding to process flow sheet in Figure 2.3.

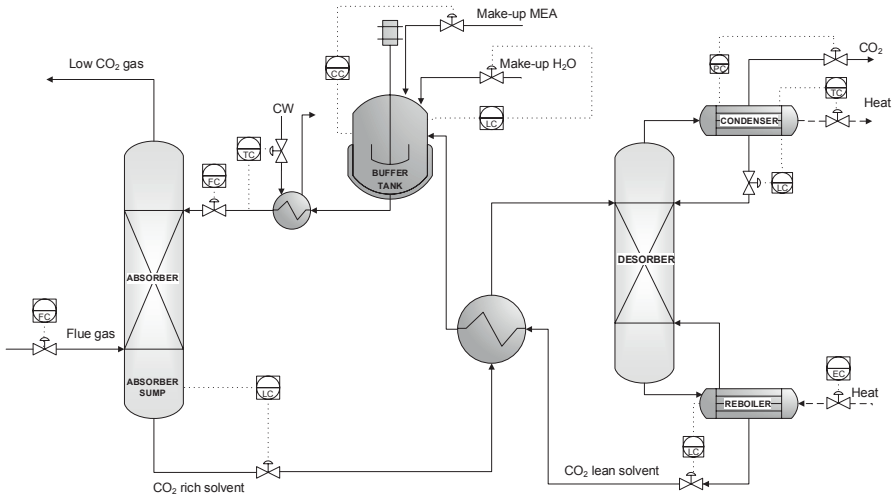

FIGURE 4.5: MATLAB model of the Tiller pilot plant corresponding to process flow sheet in Figure 2.6.

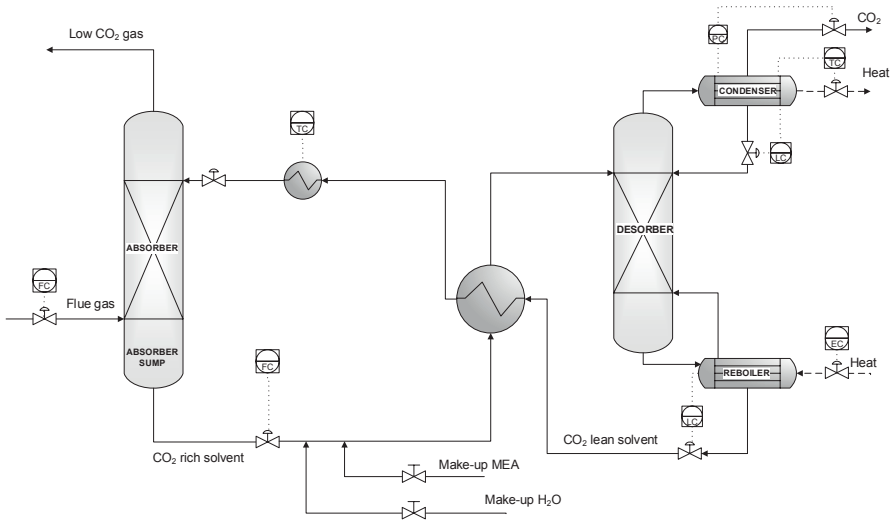

FIGURE 4.6: MATLAB model of the TCM pilot plant corresponding to process flow sheet in Figure 2.7.

4.3.2 Process units models and control equations

The various process units of the CO_2 capture process are modeled by the following four general unit models: mixing tank, flash tank, packed column and counter-current heat exchanger.

4.3.2.1 General mixing tank

The derivation of model equations for the general mixing tank is given along with a model illustration in Appendix A.1. The model is summarized in the following.

The mixing tank material balance for component i is given by:

$$\frac{dN_{\mathrm{l},i}}{dt} = F_{\mathrm{l,in}}x_{i,\mathrm{in}} - F_{\mathrm{l}}x_i \tag{4.8}$$

while the mixing tank energy balance is:

$$N_{\mathrm{l,tot}}C_{p,\mathrm{l}}\frac{dT_{\mathrm{l}}}{dt} = F_{\mathrm{l,in}}C_{\mathrm{p,l}}(T_{\mathrm{l,in}} - T_{\mathrm{l}}) - A_{\mathrm{sur}}\hat{h}_{\mathrm{sur}}(T_{\mathrm{l}} - T_{\mathrm{sur}}) \tag{4.9}$$

4.3.2.2 General flash tank

The model of the general flash tank illustrated in Figure A.2 is derived in Appendix A.2. A summary is given in the following.

The flash tank material balances for component i in liquid and gas phase, respectively, are:

$$\frac{dN_{\mathrm{l},i}}{dt} = F_{\mathrm{l,in}}x_{i,\mathrm{in}} - F_{\mathrm{l}}x_i + A_{\mathrm{g/l}}J_{\mathrm{g/l},i} \tag{4.10}$$

$$\frac{dN_{\mathrm{g},i}}{dt} = F_{\mathrm{g,in}}y_{i,\mathrm{in}} - F_{\mathrm{g}}y_i - A_{\mathrm{g/l}}J_{\mathrm{g/l},i} \tag{4.11}$$

The flash tank energy balances for liquid and gas phase, respectively are:

$$\begin{aligned} N_{\mathrm{l,tot}}C_{\mathrm{p,l}}\frac{dT_{\mathrm{l}}}{dt} = {} & F_{\mathrm{l,in}}C_{\mathrm{p,l}}(T_{\mathrm{l,in}} - T_{\mathrm{l}}) + A_{\mathrm{g/l}}\Delta h^{\mathrm{abs}}_{\mathrm{CO_2}}J_{\mathrm{g/l,CO_2}} \\ & + A_{\mathrm{g/l}}\Delta h^{\mathrm{vap}}_{\mathrm{H_2O}}J_{\mathrm{g/l,H_2O}} + A_{\mathrm{g/l}}\Delta h^{\mathrm{vap}}_{\mathrm{MEA}}J_{\mathrm{g/l,MEA}} \\ & - A_{\mathrm{g/l}}\hat{h}_{\mathrm{g/l}}(T_{\mathrm{l}} - T_{\mathrm{g}}) - A_{\mathrm{sur}}\hat{h}_{\mathrm{sur}}(T_{\mathrm{l}} - T_{\mathrm{sur}}) + \dot{Q}_{\mathrm{ex}} \end{aligned} \tag{4.12}$$

$$N_{\mathrm{g,tot}}C_{\mathrm{v,g}}\frac{dT_{\mathrm{g}}}{dt} = F_{\mathrm{g,in}}C_{\mathrm{p,g}}(T_{\mathrm{g,in}} - T_{\mathrm{g}}) + RT_{\mathrm{g}}(F_{\mathrm{g,in}} - F_{\mathrm{g}} - A_{\mathrm{g/l}}\sum_{k=1}^{\mathrm{nc}} J_{\mathrm{g/l},k}) + A_{\mathrm{g/l}}\hat{h}_{\mathrm{g/l}}(T_{\mathrm{l}} - T_{\mathrm{g}}) - A_{\mathrm{sur}}\hat{h}_{\mathrm{sur}}(T_{\mathrm{g}} - T_{\mathrm{sur}}) + \dot{Q}_{\mathrm{ex}} \tag{4.13}$$

4.3.2.3 General packed column

The general packed column is illustrated in Figure A.3. The model equation derivation is shown in Appendix A.3 and a summary is given in the following.

The general column overall material balances for liquid and gas phase, respectively are given by:

$$0 = \frac{\partial G_{\mathrm{l}}}{\partial z} + a_{\mathrm{g/l}}\sum_{k=1}^{\mathrm{nc}} J_{\mathrm{g/l},k} \tag{4.14}$$

$$0 = -\frac{\partial G_{\mathrm{g}}}{\partial z} + \varepsilon_{\mathrm{g}}\frac{C_{\mathrm{g,tot}}}{T_{\mathrm{g}}}\frac{\partial T_{\mathrm{g}}}{\partial t} - a_{\mathrm{g/l}}\sum_{k=1}^{\mathrm{nc}} J_{\mathrm{g/l},k} \tag{4.15}$$

The general column component material balances for liquid and gas phase, respectively, are:

$$\varepsilon_{\mathrm{l}}C_{\mathrm{l,tot}}\frac{\partial x_i}{\partial t} = G_{\mathrm{l}}\frac{\partial x_i}{\partial z} - x_i a_{\mathrm{g/l}}\sum_{k=1}^{\mathrm{nc}} J_{\mathrm{g/l},k} + a_{\mathrm{g/l}}J_{\mathrm{g/l},i} \tag{4.16}$$

$$\varepsilon_{\mathrm{g}}C_{\mathrm{g,tot}}\frac{\partial y_i}{\partial t} = -G_{\mathrm{g}}\frac{\partial y_i}{\partial z} + y_i a_{\mathrm{g/l}}\sum_{k=1}^{\mathrm{nc}} J_{\mathrm{g/l},k} - a_{\mathrm{g/l}}J_{\mathrm{g/l},i} \tag{4.17}$$

The general column energy balances for liquid and gas phase, respectively are given by:

$$\varepsilon_{\mathrm{l}}C_{\mathrm{tot,l}}C_{p,l}\frac{dT_l}{dt} = G_{\mathrm{l}}C_{p,l}\frac{dT_l}{dz} + a_{\mathrm{g/l}}J_{\mathrm{g/l,H_2O}}\Delta h^{\mathrm{vap}}_{\mathrm{H_2O}} + a_{\mathrm{g/l}}J_{\mathrm{g/l,MEA}}\Delta h^{\mathrm{vap}}_{\mathrm{MEA}} + a_{\mathrm{g/l}}J_{\mathrm{g/l,MEA}}\Delta h^{\mathrm{abs}}_{\mathrm{CO_2}} - a_{\mathrm{g/l}}\hat{h}_{\mathrm{g/l}}(T_{\mathrm{l}} - T_{\mathrm{g}}) - a_{\mathrm{sur}}\hat{h}_{\mathrm{sur}}(T_{\mathrm{l}} - T_{\mathrm{sur}}) \tag{4.18}$$

$$C_{\mathrm{tot,g}}C_{\mathrm{v,g}}\frac{dT_{\mathrm{g}}}{dt} = -G_{\mathrm{g}}C_{\mathrm{p,g}}\frac{T_g}{dz} + a_{\mathrm{g/l}}\hat{h}_{\mathrm{g/l}}(T_{\mathrm{l}} - T_{\mathrm{g}}) - a_{\mathrm{sur}}\hat{h}_{\mathrm{sur}}(T_{\mathrm{g}} - T_{\mathrm{sur}}) \tag{4.19}$$

4.3.2.4 Counter-current heat exchanger

The counter-current heat exchanger is illustrated in Figure A.4. The model equations are derived in Appendix A.4 and a summary is given here.

The overall material balances for the hot and cold sides, respectively:

$$0 = \frac{\partial G_{\mathrm{l}}^{\mathrm{h}}}{\partial z} \tag{4.20}$$

$$0 = -\frac{\partial G_{\mathrm{l}}^{\mathrm{c}}}{\partial z} \tag{4.21}$$

The component material balances for the hot and cold sides, respectively are given by:

$$C_{\mathrm{l,tot}}^{\mathrm{h}} \frac{\partial x_i^{\mathrm{h}}}{\partial t} = G_{\mathrm{l}}^{\mathrm{h}} \frac{\partial x_i^{\mathrm{h}}}{\partial z} \tag{4.22}$$

$$C_{\mathrm{l,tot}}^{\mathrm{c}} \frac{\partial x_i^{\mathrm{c}}}{\partial t} = -G_{\mathrm{l}}^{\mathrm{c}} \frac{\partial x_i^{\mathrm{c}}}{\partial z} \tag{4.23}$$

The energy balances for the hot and cold sides, respectively are:

$$C_{\mathrm{l,tot}}^{\mathrm{h}} C_{\mathrm{p,l}}^{\mathrm{h}} \frac{\partial T_{\mathrm{l}}^{\mathrm{h}}}{\partial t} = G_{l}^{\mathrm{h}} C_{\mathrm{p,l}}^{\mathrm{h}} \frac{\partial T_{\mathrm{l}}^{\mathrm{h}}}{\partial z} - a_{\mathrm{hx}}^{\mathrm{h}} \hat{h}_{\mathrm{hx}} (T_{\mathrm{l}}^{\mathrm{h}} - T_{\mathrm{l}}^{\mathrm{c}}) \tag{4.24}$$

$$C_{\mathrm{l,tot}}^{\mathrm{c}} C_{\mathrm{p,l}}^{\mathrm{c}} \frac{\partial T_{\mathrm{l}}^{\mathrm{c}}}{\partial t} = -G_{\mathrm{l}}^{\mathrm{c}} C_{\mathrm{p,l}}^{\mathrm{c}} \frac{\partial T_{\mathrm{l}}^{\mathrm{c}}}{\partial z} + a_{\mathrm{hx}}^{\mathrm{c}} \hat{h}_{\mathrm{hx}} (T_{\mathrm{l}}^{\mathrm{h}} - T_{\mathrm{l}}^{\mathrm{c}}) \tag{4.25}$$

4.3.2.5 Control equations

Mixing tanks and flash tanks are equipped with level controllers (LC). The controller error is in this case $e(t) = H_{\mathrm{l}}^{\mathrm{sp}} - H_{\mathrm{l}}$, where H_{l} and $H_{\mathrm{l}}^{\mathrm{sp}}$ are the actual level and set-point level, respectively, typically measured in pressure difference [mbar]. The manipulated variable ($u(t)$) controls the outlet liquid flow rate (F_{l}), which is given by the general flow equation:

$$F_{\mathrm{l}} = K_{\mathrm{L}} u(t) \sqrt{\Delta P} \tag{4.26}$$

where K_{L} is the valve constant and ΔP is the driving force over the valve. $u(t)$ is given by Equation A.80 or A.79 for P-control and PI-control, respectively.

The regeneration section has a pressure controller where the error is $e(t) = P^{sp} - P$, measured in [bar]. The manipulated variable ($u(t)$) controls the outlet gas flow according to the following relation:

$$F_{\mathrm{g}} = K_{\mathrm{V}} u(t) \sqrt{\Delta P} \tag{4.27}$$

where K_{V} is the valve constant and ΔP is the driving force over the valve. $u(t)$ is given by Equation A.80 or A.79 for P-control and PI-control, respectively.

The temperature controller error is $e(t) = T^{sp} - T$. The temperature controller for the condenser is modeled as follows:

$$Q = K_{\mathrm{Q}} u(t) \tag{4.28}$$

where Q is the heat and K_{Q} is a valve constant. The temperature controller for the lean cooler is modeled as follows:

$$F_{\mathrm{cw,in}} = K_{\mathrm{cw}} u(t) \sqrt{\Delta P} \tag{4.29}$$

where K_{cw} is the valve constant. $u(t)$ is in both cases as previously given by Equation A.80 or A.79 for P-control and PI-control, respectively.

4.3.3 Heat and mass transfer modeling

The concept of interface heat and mass transfer is used to describe the transfer of thermal energy and molecules between the phases of a vapor-liquid system. This phenomenon depends on the existence of a driving force between the separate phases. The driving force is a measure of how far the phases are from equilibrium.

Typically a temperature gradient is required for heat transfer, while a chemical potential gradient will allow mass transfer (Dutta, 2009). In practice, concentration gradients for mass transfer are used as driving forces in the present models.

Interface mass transfer involves three sequential transfer steps (Dutta, 2009):

1. The transfer of a component from the bulk phase to the interface
2. The transfer across the interface
3. The transfer from the interface to the other bulk phase

Whitman (1923) first proposed the "two-film theory" for gas absorption which has been shown to be appropriate for many interphase mass transfer problems. The general theory has two principal assumptions:

1. The rate of mass transfer between the phases is controlled by the rates of diffusion on each side of the interface.
2. The rate of mass diffusion across the interface is instantaneous, and therefore equilibrium at the interface is maintained at all times.

This means that while the main bulk of the gas and liquid phases are assumed to be well-mixed and homogeneous, two stagnant films exist on either side of the interface where mass and heat are allowed to transfer in sequence, by pure molecular diffusion. This idea is similar to the stagnant film theory described in heat transfer (Dutta, 2009). Even though more sophisticated models for mass transfer are developed (i.e. penetration theory and surface renewal theory (Cussler, 2009)), the simplicity of the two-film theory has proven to be extremely useful in mass transfer modeling (Dutta, 2009).

The molar flux of component i through gas and liquid films is illustrated in Figure 4.7 and described mathematically by (Dutta, 2009):

$$\begin{aligned} J_{\mathrm{g/l},i} &= k_{\mathrm{g},i}(C_{\mathrm{g},i,\mathrm{b}} - C_{\mathrm{g},i,\mathrm{if}}) = \frac{k_{\mathrm{g},i}}{RT_g}(P_{i,\mathrm{b}} - P_{i,\mathrm{if}}) \\ &= k_{\mathrm{l},i}(C_{\mathrm{l},i,\mathrm{if}} - C_{\mathrm{l},i,\mathrm{b}}) \end{aligned} \tag{4.30}$$

where k_{g} and k_{l} are gas and liquid film mass transfer coefficients, respectively, P_i and $C_{\mathrm{l},i}$ are partial pressure and concentration of component i in gas and liquid

phase, respectively, and subscript b and if represent bulk phase and interface, respectively. Interface concentrations are not directly measurable quantities, and cannot be specified as such in a practical problem. However, by assuming equilibrium at the interface $P_{i,\mathrm{if}} = P_{i,\mathrm{if}}^{\mathrm{eq}^*}$ and $C_{\mathrm{l},i,\mathrm{if}} = C_{\mathrm{l},i,\mathrm{if}}^{\mathrm{eq}^*}$, and an equilibrium relation ($P_i^{\mathrm{eq}^*} = \phi(C_{\mathrm{l},i}^{\mathrm{eq}^*})$) is used to relate these quantities (Dutta, 2009).

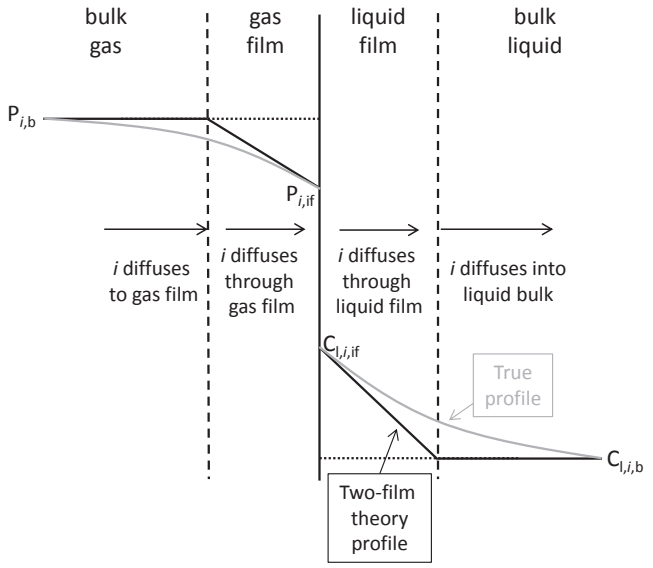

FIGURE 4.7: Illustration of the two-film theory principle.

Equilibrium data for non-ideal gas-liquid systems of low concentrations can be expressed by Henry's law (Dutta, 2009):

$$P_i^{\mathrm{eq}^*} = He_i C_{\mathrm{l},i}^{\mathrm{eq}^*} \tag{4.31}$$

where He_i is Henry's law constant.

By using this equilibrium relation, the interfacial concentrations can be eliminated by a combination of the gas film and liquid film flux equations,

$$\begin{aligned} \frac{J_{\mathrm{g/l},i}}{\frac{k_{\mathrm{g},i}}{RT_g}} &= (P_{i,\mathrm{b}} - P_{i,\mathrm{if}}^{\mathrm{eq}^*}) \\ \frac{J_{\mathrm{g/l},i}}{\frac{k_{\mathrm{l},i}}{He_i}} &= (P_{i,\mathrm{if}}^{\mathrm{eq}^*} - P_{i,\mathrm{b}}^{\mathrm{eq}^*}) \end{aligned} \tag{4.32}$$

yielding:

$$J_{\mathrm{g/l},i} = K_{\mathrm{tot},i}(P_{i,\mathrm{b}} - P_i^{\mathrm{eq}^*}) \tag{4.33}$$

where $K_{\mathrm{tot},i} = \frac{1}{\frac{RT_g}{k_{\mathrm{g},i}} + \frac{He_i}{k_{\mathrm{l},i}}}$ is the overall mass transfer coefficient.

The liquid film mass transfer resistance for water and MEA is neglected, thus the total mass transfer coefficient $K_{\mathrm{tot},i}$ for these components is given by:

$$K_{\mathrm{tot},i} = \frac{k_{\mathrm{g},i}}{RT_{\mathrm{g}}} \tag{4.34}$$

In the case when chemical reactions are occurring in the liquid film, mass transfer is enhanced. This is the case for CO_2 which is reacting with MEA in the liquid film. The effect of chemical reactions on the rate of mass transfer is usually expressed as an enhancement factor (E), which is defined as the ratio of the rate of absorption with chemical reaction to the rate of purely physical absorption (Equation 4.45).

The interfacial flux is in this case given by:

$$\begin{aligned} J_{\mathrm{g/l,CO_2}} &= \frac{k_{\mathrm{g,CO_2}}}{RT_g}(P_{\mathrm{CO_2,b}} - P_{\mathrm{CO_2,if}}) = Ek_{\mathrm{l,CO_2}}(C_{\mathrm{l,CO_2,if}} - C_{\mathrm{l,CO_2,b}}) \\ &= K_{\mathrm{tot,CO_2}}(P_{\mathrm{CO_2,b}} - P_{\mathrm{CO_2}}^{\mathrm{eq}^*}) \end{aligned} \tag{4.35}$$

where $P_{\mathrm{CO_2}}^{\mathrm{eq}^*}$ is the partial pressure of of CO_2 of gas in chemical equilibrium with the bulk liquid phase which is given by Henry's law (Equation 4.31).

This leads to an overall mass transfer coefficient $K_{\mathrm{tot,CO_2}}$ of:

$$K_{\mathrm{tot,CO_2}} = \frac{1}{\frac{RT_g}{k_{\mathrm{g,CO_2}}} + \frac{He_{\mathrm{CO_2}}}{Ek_{\mathrm{l,CO_2}}}} \tag{4.36}$$

Similarly, just as mass transfer is mass in transit due to a concentration difference, heat transfer is thermal energy in transit due to a temperature difference. This is called the heat and mass transfer analogy, and the equivalent expression for heat flux is therefore given by (Lienhard V and Lienhard IV, 2011):

$$\dot{q}_{\mathrm{g/l}} = \hat{h}_{\mathrm{tot}}(T_{\mathrm{g}} - T_{\mathrm{l}}) \tag{4.37}$$

where $\hat{h}_{\mathrm{tot}}$ is the overall heat transfer coefficient.

4.3.3.1 Local mass transfer coefficients

Several authors have developed correlations predicting local mass transfer coefficients (k_{g} and k_{l}). Billet and Schultes (1999) developed the following relations based on results from a large number of experiments in absorber columns with both dumped and arranged packings:

$$k_{\mathrm{g},i} = C_{\mathrm{g}} D_{\mathrm{g},i} \frac{1}{(\varepsilon_{\mathrm{void}} - \varepsilon_{\mathrm{l}})^{1/2}} \left(\frac{a}{d_{\mathrm{h}}}\right)^{1/2} \left(\frac{u_{\mathrm{g}}\rho_{\mathrm{g}}}{a\mu_{\mathrm{g}}}\right)^{3/4} \left(\frac{\mu_{\mathrm{g}}}{D_{\mathrm{g},i}\rho_{\mathrm{g}}}\right)^{1/3} \tag{4.38}$$

$$k_{\mathrm{l},i} = C_{\mathrm{l}} 12^{1/6} \bar{u}_{\mathrm{l}}^{1/2} \left(\frac{D_{\mathrm{l},i}}{d_{\mathrm{h}}}\right)^{1/2} \tag{4.39}$$

$\bar{u}_{\mathrm{l}}$ is the mean effective liquid velocity which below the loading point ($u_{\mathrm{g}} \leq u_{\mathrm{g,s}}$) is given by:

$$\bar{u}_{\mathrm{l}} = \frac{u_{\mathrm{l}}}{\varepsilon_{\mathrm{l}}} \tag{4.40}$$

while above the loading point ($u_{\mathrm{g,s}} \leq u_{\mathrm{g}} \leq u_{\mathrm{g,fl}}$) it is given as:

$$\bar{u}_{\mathrm{l}} = \left(\frac{g\rho_{\mathrm{g}}^2 u_{\mathrm{g}}^2}{12\mu_{\mathrm{l}} a^2 \rho_{\mathrm{l}}^2}\right)^{1/3} \left(\frac{L}{G}\right)^{2/3} \left(1 - \left(\frac{u_{\mathrm{g}} - u_{\mathrm{g,s}}}{u_{\mathrm{g,fl}} - u_{\mathrm{g,s}}}\right)^2\right) \tag{4.41}$$

Rocha et al. (1996) presented the following correlations for gas and liquid film mass transfer coefficients based on experiments with structured packings:

$$k_{\mathrm{g},i} = \frac{0.054 D_{\mathrm{g},i}}{S} \left(\frac{(u_{\mathrm{g,e}} + u_{\mathrm{l,e}})\rho_{\mathrm{g}} S}{\mu_{\mathrm{g}}}\right)^{0.8} \left(\frac{\mu_{\mathrm{g}}}{D_{\mathrm{g},i}\rho_{\mathrm{g}}}\right)^{0.33} \tag{4.42}$$

$$k_{\mathrm{l},i} = 2\left(\frac{D_{\mathrm{l},i} C_E u_{\mathrm{l,e}}}{\pi S}\right)^{1/2} \tag{4.43}$$

where $u_{\mathrm{g,e}} = \frac{u_{\mathrm{g}}}{\varepsilon_{\mathrm{void}}(1-\varepsilon_{\mathrm{l}})\sin\beta}$ and $u_{\mathrm{l,e}} = \frac{u_{\mathrm{l}}}{\varepsilon_{\mathrm{void}}\varepsilon_{\mathrm{l}}\sin\beta}$

4.3.3.2 Heat transfer coefficient

The heat transfer coefficient correlation is taken from Geankoplis (2003) and modified with a sensitivity factor of 0.1 based on experiments by Freguia (2002) (Kvamsdal and Hillestad, 2012):

$$h_{\mathrm{g/l}} = 0.1 \cdot 1000 \cdot 4.05 \cdot 10^{-3}\left(\frac{\rho_{\mathrm{g}} u_{\mathrm{g}}}{d_{\mathrm{h}}}\right)^{0.5} C_{\mathrm{p,g}}^{0.33} \tag{4.44}$$

4.3.3.3 Enhancement factor

It is customary to treat gas-liquid reactions as absorption accompanied by chemical reaction. Chemical reactions lower the resistance of the liquid film, and the effect is accelerated absorption rate for the gas phase component. An enhancement factor (E) is commonly used to correct the liquid film mass transfer rate. E is therefore always equal to or greater than 1, where 1 basically means no enhancement.

The exact numerical enhancement factor is defined as the ratio of the absorption rate in the presence of a chemical reaction to the absorption rate of purely physical absorption in the absence of chemical reaction (Dutta, 2009):

$$E = \frac{J_{\mathrm{chemical}}}{J_{\mathrm{physical}}} \tag{4.45}$$

The effect of chemical reaction on mass transfer will depend on the reaction regime. The Hatta modulus (Ha) and the infinite enhancement factor (E_∞) are often used to analyze reaction regimes (Gavhane, 2009). Ha^2 is defined as the maximum possible conversion in the film compared to maximum possible diffusion through the film (Kumar et al., 2003). Ha is therefore given as:

$$Ha = \frac{\sqrt{k_{\mathrm{rx}} D_{\mathrm{l,CO_2}} C_{Am,\mathrm{b}}}}{k_{\mathrm{l,CO_2}}} \tag{4.46}$$

The asymptotic infinite enhancement factor for an irreversible reaction is defined as (Kumar et al., 2003):

$$E_\infty = \left(1 + \frac{D_{Am}}{D_{\mathrm{CO}_2}} \frac{C_{Am,\mathrm{b}}}{\nu_{Am} C_{\mathrm{CO}_2,\mathrm{l,if}}}\right)\left(\frac{D_{\mathrm{CO}_2}}{D_{Am}}\right)^q \tag{4.47}$$

Where $q = 0$ in the film model and $q = 1/2$ in the penetration model and ν_{Am} is the stoichiometric coefficient of amine in the reaction with CO_2.

The various regimes and enhancement factors are listed in Table 4.3. In the case of very slow reactions, all reaction takes place in the bulk of the liquid and the diffusional processes are so fast compared to the reaction rate that no concentration gradients occur in the liquid film. The overall mass transfer rate is governed by the reaction rate alone and no enhancement is seen.

For slow reactions, reaction occurs uniformly throughout the liquid, and the liquid film offers some resistance to transfer of the gas phase component into the main body of the liquid. Practically no visible enhancement is seen due to slow reactions, and the concentration gradient in the film is linear.

For fast reactions the chemical reaction will only occur in the film. The gas-phase component concentration is therefore zero in the liquid bulk. A nonlinear concentration gradient is seen in the liquid film, leading to mass transfer enhancement. In this region assumption of a pseudo 1st order reaction regime is accepted, which in general is valid when the concentration of free MEA is high and more or less constant throughout the reaction zone. If the concentration of amine is so high that it can be assumed to be constant, it can be included in the expression for k_{rx} and the film reaction is assumed to be a pseudo 1st order reaction ($r = k_{rx} C_{\mathrm{CO}_2} C_{Am} = k^*_{rx} C_{\mathrm{CO}_2}$) as described in Section 4.3.5.6.

In the infinitely fast (or instantaneous) reaction regime, the reactions are so fast that the solute and reactant cannot coexist. Chemical reactions will only occur in the reaction zone of the liquid film, and a reaction plane is formed. The mass transfer is therefore governed by the diffusion rates of the gas phase component and solvent into the reaction plane of the liquid film.

For transition regions, the enhancement factor needs to be calculated numerically. The explicit approximation by DeCoursey (1982) is however a common approach:

TABLE 4.3: Selection of enhancement factor models (continues next page).

Reaction regime	Hatta modulus	Enhancement factor	Concentration profile
Very slow	$Ha < 0.3$	$E = 1$	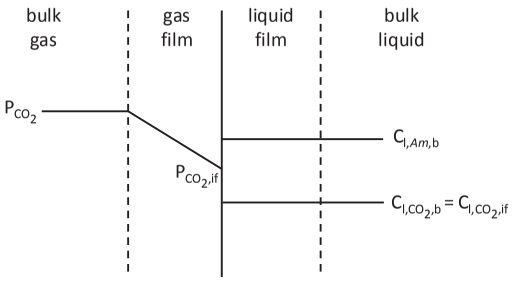
Slow	$Ha < 0.3$	$E = 1$	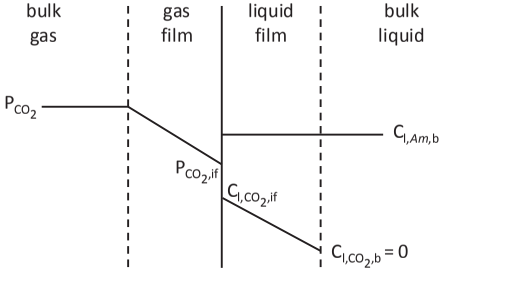

TABLE 4.3: Selection of enhancement factor models (continued from previous page).

Reaction regime	Hatta modulus	Enhancement factor	Concentration profile
Fast	$3 < Ha < \frac{E_\infty}{5}$	$E = Ha$	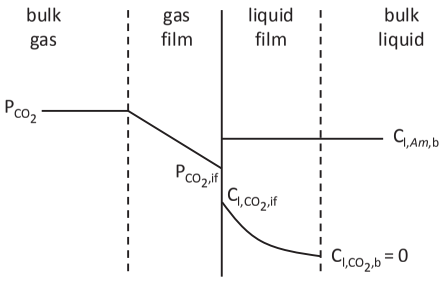
Instantaneous	$Ha > 5E_\infty$	$E = E_\infty$	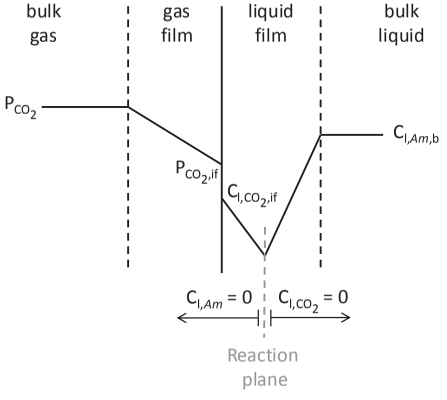

$$E_{\mathrm{DC}} = \frac{-Ha^2}{2(E_\infty - 1)} + \sqrt{\frac{Ha^4}{4(E_\infty - 1)^2} + \frac{E_\infty Ha^2}{(E_\infty - 1)} + 1} \tag{4.48}$$

4.3.4 Modeling of column hydrodynamics

The column hydrodynamics will affect the CO_2 absorption and desorption rates. These parameters are introduced as mechanistic models for effective interface area, liquid hold-up and pressure drop.

4.3.4.1 Effective interface area

The effective interface area or wetted area (a_e) is of great importance for the mass and heat transfer between gas and liquid phases in packed columns. It is usually represented by a wetting factor ($\frac{a_{e,s}}{a}$) and the specific interface area (a) of the specific packing material:

$$a_e = \left(\frac{a_{e,s}}{a}\right) a \tag{4.49}$$

Billet and Schultes (1999) proposed an equation set to predict the wetting factor for various conditions or operating zones. Equation 4.50 applies to load conditions up to the loading point, i.e. $u_g \leq u_{g,s}$:

$$\frac{a_{e,s}}{a} = 1.5\,(a d_h)^{-0.5} \left(\frac{u_l d_h \rho_l}{\mu_l}\right)^{-0.2} \left(\frac{u_l^2 \rho_l d_h}{\sigma_l}\right)^{0.75} \left(\frac{u_l^2}{g d_h}\right)^{-0.45} \tag{4.50}$$

where the hydraulic diameter (d_h) is given by:

$$d_h = 4\frac{\varepsilon_{void}}{a} \tag{4.51}$$

Above the loading point ($u_g > u_{g,s}$), the shear stress of the counter-current gas is large enough to dam up the falling film so that the column hold-up and the size of the wetted interface increase, while the effective flow velocity of the falling film decreases. For these conditions the wetted factor is predicted by Equation 4.52:

$$\frac{a_e}{a} = \frac{a_{e,s}}{a} + \left(\frac{a_{e,fl}}{a} - \frac{a_{e,s}}{a}\right)\left(\frac{u_g}{u_{g,fl}}\right)^{13} \tag{4.52}$$

where $\frac{a_{e,s}}{a}$ is the wetting factor at and below the loading point given in Equation 4.50 and $\frac{a_{e,fl}}{a}$ is the wetting factor at flooding point given by:

$$\frac{a_{e,fl}}{a} = 10.5\left(\frac{\sigma_l}{\sigma_w}\right)^{0.56}(ad_h)^{-0.5}\left(\frac{u_l d_h \rho_l}{\mu_l}\right)^{-0.2}\left(\frac{u_l^2 \rho_l d_h}{\sigma_l}\right)^{0.75}\left(\frac{u_l^2}{g d_h}\right)^{-0.45} \tag{4.53}$$

Relations for prediction of the loading point ($u_{g,s}$) and flooding point ($u_{g,fl}$) are given by Billet and Schultes (1999).

Rocha et al. (1996) presented the following relation to estimate the effective interface area (a_e) for a wide range of conditions:

$$a_e = F_{SE} F_t a \tag{4.54}$$

where F_{SE} is a factor for surface enhancement given for the packing material and F_t is a dimensionless correction factor for total hold up due to effective wetted area defined by:

$$F_t = \frac{29.12(We_l Fr_l)^{0.15} S^{0.359}}{Re_l^{0.2}\varepsilon^{0.6}(1 - 0.93\cos\gamma)(sin\beta)^{0.3}} \tag{4.55}$$

4.3.4.2 Liquid hold-up

The liquid hold-up of the column is defined as the ratio of volume occupied by the solvent to the total volume of the column ($\varepsilon_l = \frac{V_l}{V_{tot}}$). Billet and Schultes (1999) proposed the following correlation of liquid hold-up at and below the loading point ($u_g \leq u_{g,s}$):

$$\varepsilon_l = \left(12\frac{1}{g}\frac{\mu_l}{\rho_l}u_l a^2\right)^{1/3} \tag{4.56}$$

Above the loading point ($u_{g,s} < u_g \leq u_{g,fl}$), the liquid hold-up will increase due to the friction of gas causing reduced velocity of the falling film, and Equation 4.57 should be applied.

$$\varepsilon_l = \varepsilon_{l,s} + (\varepsilon_{l,fl} - \varepsilon_{l,s})\left(\frac{u_g}{u_{g,fl}}\right)^{13} \tag{4.57}$$

where the hold-up at flooding is given by:

$$\varepsilon_{\mathrm{l,fl}}^3 \left(3\varepsilon_{\mathrm{l,fl}} - \varepsilon_{\mathrm{void}}\right) = \frac{6}{g} a^2 \varepsilon_{\mathrm{void}} \frac{\mu_{\mathrm{l}}}{\rho_{\mathrm{l}}} \frac{L}{G} \frac{\rho_{\mathrm{g}}}{\rho_{\mathrm{l}}} u_{\mathrm{g,fl}} \tag{4.58}$$

Rocha et al. (1993) presented the following equation set to predict solvent hold-up.

$$\varepsilon_{\mathrm{l}} = \left(4\frac{F_t}{S}\right)^{2/3} \left(\frac{3\mu_{\mathrm{l}} u_{\mathrm{l}}}{\rho_{\mathrm{l}}(sin\beta)\varepsilon_{\mathrm{void}} g_{\mathrm{e}}}\right)^{1/3} \tag{4.59}$$

$$g_{\mathrm{e}} = g\left(\frac{\rho_{\mathrm{l}} - \rho_{\mathrm{g}}}{\rho_{\mathrm{l}}}\right)\left(1 - \frac{\frac{\Delta P}{\Delta z}}{(\frac{\Delta P}{\Delta z})_{\mathrm{flood}}}\right) \tag{4.60}$$

4.3.4.3 Pressure drop

Billet and Schultes (1999) presented the following correlations for pressure drop in units [Pa/m]:

$$\frac{\Delta P}{\Delta z} = \Psi_{\mathrm{l}} \frac{a}{(\varepsilon_{\mathrm{void}} - \varepsilon_{\mathrm{l}})^3} \frac{F_{\mathrm{v}}^2}{2} \frac{1}{K} \tag{4.61}$$

$$\Psi_{\mathrm{l}} = C_0 \left(\frac{64}{Re_{\mathrm{g}}} + \frac{1.8}{Re_{\mathrm{g}}^{0.8}}\right)\left(\frac{\varepsilon_{\mathrm{void}} - \varepsilon_{\mathrm{l}}}{\varepsilon_{\mathrm{void}}}\right)^{1.5} \left(\frac{\varepsilon_{\mathrm{l}}}{\varepsilon_{\mathrm{L,s}}}\right)^{0.3} \exp(C_1\sqrt{Fr_{\mathrm{l}}}) \tag{4.62}$$

$$\frac{1}{K} = 1 + \frac{2}{3}\left(\frac{1}{1 - \varepsilon_{\mathrm{void}}}\right)\frac{d_{\mathrm{p}}}{D_{col}} \tag{4.63}$$

where C_0 is a packing specific constant, $C_1 = \frac{13300}{a^{3/2}}$, $F_{\mathrm{v}} = u_{\mathrm{g}}\sqrt{\rho_{\mathrm{g}}}$ is the gas load factor, $d_{\mathrm{p}} = 6\frac{1-\varepsilon_{\mathrm{void}}}{a}\rho_{\mathrm{g}}$ is the nominal packing diameter, Re_{g} is the gas stream Reynolds number and Fr_{l} is the liquid Froude number.

The pressure drop correlation proposed by Rocha et al. (1993) is given in units [Pa/m] by the following equations:

$$\frac{\Delta P}{\Delta z} = \left(\frac{\Delta P}{\Delta z}\right)_{dry} \left(\frac{1}{1 - K_2\varepsilon_{\mathrm{l}}}\right)^5 \tag{4.64}$$

$$\left(\frac{\Delta P}{\Delta z}\right)_{\mathrm{dry}} = \frac{0.177\rho_{\mathrm{g}}}{S\varepsilon^2(\sin\beta)^2} u_{\mathrm{g}}^2 + \frac{88.774\mu_{\mathrm{g}}}{S^2\varepsilon\sin\beta} u_{\mathrm{g}} \tag{4.65}$$

$$\left(\frac{\Delta P}{\Delta z}\right)_{\text{flood}} = 1025 \tag{4.66}$$

where $K_2 = 0.614 + 71.35S$.

4.3.5 Modeling of physical, chemical and thermodynamic properties

4.3.5.1 Density

The density of unloaded solution in units [kg/m^3] is proposed by Cheng et al. (1996) as follows:

$$\begin{aligned}\rho_{\text{l,unloaded}} &= (1 - w_{\text{MEA}})\rho_{\text{l,H}_2\text{O}} + w_{\text{MEA}}\rho_{\text{l,MEA}} \\ &+ w_{\text{MEA}}(1 - w_{\text{MEA}})\left(5.8430 + 0.3139\bar{T} + \frac{510.6409 w_{\text{MEA}}}{\bar{T}^{0.45}}\right)\end{aligned} \tag{4.67}$$

where $\bar{T}$ is the temperature in [°C]. The density of pure water and MEA is given by:

$$\rho_{l,\text{H}_2\text{O}} = 1002.30 - 0.1321\bar{T} - 0.00308\bar{T}^2 \tag{4.68}$$

$$\rho_{l,\text{MEA}} = 1023.75 - 0.5575\bar{T} - 0.00187\bar{T}^2 \tag{4.69}$$

Based on this the component and total molar concentrations in [kmol/m^3] are calculated as follows:

$$C_{\text{l,MEA}} = \frac{w_{\text{MEA}}\rho_{\text{l,unloaded}}}{M_{\text{MEA}}} \tag{4.70}$$

$$C_{\text{l,H}_2\text{O}} = (1 - w_{\text{MEA}})\frac{\rho_{\text{l,unloaded}}}{M_{\text{H}_2\text{O}}} \tag{4.71}$$

$$C_{\text{l,CO}_2} = \alpha C_{\text{l,MEA}} \tag{4.72}$$

$$C_{\text{l,tot}} = C_{\text{l,CO}_2} + C_{\text{l,H}_2\text{O}} + C_{\text{l,MEA}} \tag{4.73}$$

The density of loaded solution in [kg/m^3] is now given by:

$$\rho_{\text{l,loaded}} = C_{\text{l,tot}} \sum_{i=1}^{i=nc} M_i x_i \tag{4.74}$$

A correlation proposed by Hartono et al. (2014) is using excess molar volume to predict the density of unloaded solution in [kg/m^3]:

$$\rho_{\mathrm{l,unloaded}} = \frac{x^{\mathrm{sol}}_{\mathrm{H_2O}} M_{\mathrm{H_2O}} + x^{\mathrm{sol}}_{\mathrm{MEA}} M_{\mathrm{MEA}}}{V^{\mathrm{E}} + \left(\frac{x_{\mathrm{H_2O}} M_{\mathrm{H_2O}}}{\rho_{\mathrm{l,H_2O}}} + \frac{x_{\mathrm{MEA}} M_{\mathrm{MEA}}}{\rho_{\mathrm{l,MEA}}}\right)} \tag{4.75}$$

where x_i^{sol} represent the mole fraction of component i in unloaded solution and $\rho_{\mathrm{l},i}$ is the density of pure component i. V^{E} is the excess molar volume given by:

$$V^{\mathrm{E}} = (k_1 + k_2 T_c + k_3 x^{sol}_{\mathrm{MEA}} + k_4 (x^{\mathrm{sol}}_{\mathrm{MEA}})^2) x^{\mathrm{sol}}_{\mathrm{H_2O}} x^{\mathrm{sol}}_{\mathrm{MEA}} \cdot 10^{-3} \tag{4.76}$$

The density of pure water and MEA in [kg/m^3] is in this case given by:

$$\rho_{\mathrm{l,H_2O}} = (-5.3270 \cdot 10^{-07} \bar{T}^2 - 7.4762 \cdot 10^{-04} \bar{T} + 1.0308) \cdot 10^3 \tag{4.77}$$

$$\rho_{\mathrm{l,MEA}} = (-2.5598 \cdot 10^{-06} \bar{T}^2 - 1.9691 \cdot 10^{-04} \bar{T} + 1.0040) \cdot 10^3 \tag{4.78}$$

The parameter values in Equation 4.76 given in Hartono et al. (2013) are: $k_1 = -1.9210$, $k_2 = 1.6792 \cdot 10^{-3}$, $k_3 = -3.0951$ and $k_4 = 3.4412$.

The density of loaded solution in [kg/m^3] is given by the following relation by Hartono et al. (2014):

$$\rho_{\mathrm{l,loaded}} = \frac{\rho_{\mathrm{l,unloaded}}}{1 - w_{\mathrm{CO_2,added}}(1 - \Phi^3)} \tag{4.79}$$

where $w_{\mathrm{CO_2,added}}$ is the amount of CO_2 added to the solution on a mass basis:

$$w_{\mathrm{CO_2,added}} = \frac{\alpha x^{sol}_{\mathrm{MEA}} M_{\mathrm{CO_2}}}{x^{sol}_{\mathrm{MEA}} M_{\mathrm{MEA}} + (1 - x^{sol}_{\mathrm{MEA}} - \alpha x^{sol}_{\mathrm{MEA}}) M_{\mathrm{H_2O}} + \alpha x^{sol}_{\mathrm{MEA}} M_{\mathrm{CO_2}}} \tag{4.80}$$

and Φ is the volume expansion caused by the CO_2 addition:

$$\Phi = \frac{a_1 \alpha x^{sol}_{\mathrm{MEA}} + a_2 x^{sol}_{\mathrm{MEA}}}{a_3 + x^{sol}_{\mathrm{MEA}}} \tag{4.81}$$

where the parameter values given in Hartono et al. (2014) are as follows: $a_1 = 0.29$, $a_2 = 0.18$ and $a_3 = 0.66$.

The total gas concentration and density are given by the ideal gas law:

$$C_{\mathrm{g,tot}} = \frac{P}{RT_{\mathrm{g}}} \tag{4.82}$$

$$\rho_{\mathrm{g,tot}} = C_{\mathrm{g,tot}} \sum_{i=1}^{i=nc} M_i y_i \tag{4.83}$$

4.3.5.2 Solvent viscosity

The viscosity of unloaded solution in [Pa s] is proposed by Hartono et al. (2014) as the sum of an "'ideal"' viscosity based on the weighted sum of the solution component's pure viscosities (η_i) and a viscosity deviation (η_y):

$$\ln(\eta_{\mathrm{unloaded}}) = x_{\mathrm{MEA}} \ln(\eta_{\mathrm{MEA}}) + x_{\mathrm{H_2O}} \ln(\eta_{\mathrm{H_2O}}) + \ln(\eta_y) \tag{4.84}$$

The viscosity deviation is given by:

$$\ln(\eta_y) = (l_1 + l_2\bar{T}_{\mathrm{l}} + t_3\bar{T}_{\mathrm{l}}^2 + l_4 x_{\mathrm{MEA}}) x_{\mathrm{MEA}} x_{\mathrm{H_2O}} \tag{4.85}$$

where $\bar{T}$ is the temperature measured in [°C] and the correlation parameters are: $l_1 = 8.36$, $l_2 = -4.664 \cdot 10^{-2}$, $l_3 = 1.6 \cdot 10^{-4}$ and $l_4 = -4.14$.

$\eta_{\mathrm{H_2O}}$ and η_{MEA} are given in [Pa s] by

$$\eta_{\mathrm{H_2O}} = \exp\left(2.303 \frac{1.3272(293.0 - T_{\mathrm{l}}) - 0.001053(T_{\mathrm{l}} - 293.0)^2}{(T_{\mathrm{l}} - 168.0)}\right) \cdot 1.002 \cdot 10^{-3} \tag{4.86}$$

$$\eta_{\mathrm{MEA}} = \exp\left(-3.9356 + \frac{1010.8}{T_{\mathrm{l}} - 151.17}\right) \cdot 10^{-3} \tag{4.87}$$

The viscosity of water is taken from Lide (1985), while the viscosity of MEA is taken from DiGuilio et al. (1992).

The viscosity of loaded solution in [Pa s] is further given by Hartono et al. (2014) as a function of the unloaded viscosity and a new deviation (η_y^*) representing the deviation from unloaded solution:

$$\ln(\eta_{\text{loaded}}) = (1 - x_{\text{CO}_2}) \ln(\eta_{\text{unloaded}}) + x_{\text{CO}_2} \ln(\eta_y^*) \tag{4.88}$$

where

$$\ln(10^{-3} \cdot \eta_y^*) = \frac{6.98 x_{\text{MEA}} + 10.48 \alpha x_{\text{MEA}}}{0.049 + x_{\text{MEA}}} \tag{4.89}$$

4.3.5.3 Diffusivity

The mass diffusivity or diffusion coefficient is a proportionality constant between the molar flux due to molecular diffusion and the driving force for diffusion. Due to chemical reactions between CO_2 and amines, it is not possible to measure the free molecular diffusivity directly. The N_2O analogy has been frequently used to estimate the diffusivity of CO_2 in amine solutions, as suggested by Sada et al. (1978).

$$D_{\text{l,CO}_2} = D_{\text{l,N}_2\text{O}} \left(\frac{D_{\text{l,CO}_2\text{–H}_2\text{O}}}{D_{\text{l,N}_2\text{O–H}_2\text{O}}} \right) \tag{4.90}$$

Versteeg and van Swaaij (1988) proposed that the diffusivity of N_2O in an aqueous MEA solution in [m^2/s] can be estimated by a modified Stokes-Einstein relation:

$$D_{\text{l,N}_2\text{O}} = D_{\text{l,N}_2\text{O–H}_2\text{O}} \left(\frac{\mu_{\text{H}_2\text{O}}}{\mu_{\text{MEA}}} \right)^{0.8} \tag{4.91}$$

Versteeg and van Swaaij (1988) proposed the following diffusivities of CO_2 and N_2O in H_2O:

$$D_{\text{l,CO}_2\text{–H}_2\text{O}} = 2.35 \cdot 10^{-6} \cdot \exp\left(\frac{-2119}{T_{\text{l}}} \right) \tag{4.92}$$

$$D_{\text{l,N}_2\text{O–H}_2\text{O}} = 5.07 \cdot 10^{-6} \cdot \exp\left(\frac{-2371}{T_{\text{l}}} \right) \tag{4.93}$$

Ko et al. (2000) subsequently provided a correlation for $D_{\mathrm{l,N_2O\text{–}H_2O}}$ using experimental data:

$$D_{\mathrm{l,N_2O\text{–}H_2O}} = \left(5.07 \cdot 10^{-6} + 8.65 \cdot 10^{-7} C_{\mathrm{l,MEA}} + 2.78 \cdot 10^{-7} C_{\mathrm{l,MEA}}^2\right) \cdot \exp\left(\frac{-2371 - 93.4 C_{\mathrm{l,MEA}}}{T_\mathrm{l}}\right) \tag{4.94}$$

Gas phase diffusivities in [m^2/s] are taken from (Reid et al., 1987):

$$D_{\mathrm{g,CO_2}} = 7.907 \cdot 10^{-8} \left(\frac{T_\mathrm{g}^{1.75}}{P}\right) \tag{4.95}$$

$$D_{\mathrm{g,H_2O}} = 1.26 \cdot 10^{-7} \left(\frac{T_\mathrm{g}^{1.75}}{P}\right) \tag{4.96}$$

$$D_{\mathrm{g,MEA}} = 1 \cdot 10^{-6} \tag{4.97}$$

4.3.5.4 Physical solubility

The physical solubility of CO_2 in loaded solution is frequently estimated using the N_2O analogy by the following relation in [kPa m^3/mol] (Hartono et al., 2013, 2014):

$$\frac{(He_{\mathrm{CO_2,loaded}})}{(H_{\mathrm{N_2O,loaded}})} = \frac{H_{\mathrm{CO_2\text{–}H_2O}}}{H_{\mathrm{N_2O\text{–}H_2O}}} \tag{4.98}$$

where

$$He_{\mathrm{CO_2\text{–}H_2O}} = \exp(-212.73 + \frac{2078.17}{T_\mathrm{l}} + 40.90 \ln T_\mathrm{l} - 0.09 T_\mathrm{l}) \tag{4.99}$$

and

$$\ln(He_{\mathrm{N_2O\text{–}H_2O}}) = -700.65 + \frac{14905.50}{T_\mathrm{l}} + 126.35 \ln(T_\mathrm{l}) - 0.23 T_\mathrm{l} \tag{4.100}$$

The physical solubility of N_2O in loaded solution in [kPa m^3/mol] is further proposed by Hartono et al. (2014):

$$\ln(He_{\mathrm{N_2O,loaded}}) = \ln(He_{\mathrm{N_2O,unloaded}}) + \ln(\Delta He_{\mathrm{N_2O,loaded}}) \tag{4.101}$$

where

$$\ln(\Delta He_{\mathrm{N_2O,loaded}}) = 0.77x_{\mathrm{MEA}} + 0.033x_{\mathrm{MEA}}\alpha T_{\mathrm{l}} \tag{4.102}$$

The physical solubility of N_2O in unloaded solution, given as an apparent Henry's constant in [kPa m^3/mol] is proposed by Hartono et al. (2014) as a weighted sum of N_2O's solubility in pure solutions ($He_{\mathrm{N_2O-H_2O}}$ and $He_{\mathrm{N_2O-MEA}}$) and an apparent Henry's constant deviation ($\Delta He_{\mathrm{N_2O,unloaded}}$):

$$\begin{aligned}\ln(He_{\mathrm{N_2O,unloaded}}) =& \phi_{\mathrm{H_2O}} \ln(He_{\mathrm{N_2O-H_2O}}) + \phi_{\mathrm{MEA}} \ln(He_{\mathrm{N_2O-MEA}}) \\ &+ \ln(\Delta He_{\mathrm{N_2O,unloaded}})\end{aligned} \tag{4.103}$$

where

$$\ln(\Delta He_{\mathrm{N_2O},unloaded}) = -10^6 V^E \sqrt{(1-\phi^2_{\mathrm{MEA}})} \tag{4.104}$$

$$\phi_{MEA} = \frac{\frac{x^{\mathrm{sol}}_{\mathrm{MEA}} M_{\mathrm{MEA}}}{\rho_{\mathrm{MEA}}}}{\frac{x^{\mathrm{sol}}_{\mathrm{H_2O}} M_{\mathrm{H_2O}}}{\rho_{\mathrm{H_2O}}} + \frac{x^{\mathrm{sol}}_{\mathrm{MEA}} M_{\mathrm{MEA}}}{\rho_{\mathrm{MEA}}}} \tag{4.105}$$

$$\phi_{\mathrm{H_2O}} = \frac{\frac{x^{\mathrm{sol}}_{\mathrm{H_2O}} M_{\mathrm{H_2O}}}{\rho_{\mathrm{H_2O}}}}{\frac{x^{\mathrm{sol}}_{\mathrm{H_2O}} M_{\mathrm{H_2O}}}{\rho_{\mathrm{H_2O}}} + \frac{x^{\mathrm{sol}}_{\mathrm{MEA}} M_{\mathrm{MEA}}}{\rho_{\mathrm{MEA}}}} \tag{4.106}$$

$$\ln(He_{\mathrm{N_2O-MEA}}) = 3.95 - \frac{589.94}{T_{\mathrm{l}}} - 99.04 \tag{4.107}$$

4.3.5.5 Vapor-liquid equilibrium

The CO_2 equilibrium pressure in [kPa] for 30 wt% MEA solution is correlated with loading and temperature based on experimental data obtained at NTNU and SINTEF (Ugochukwu et al., 2011). A soft model is developed by SINTEF based on these data, and the correlation and a graphical representation is presented in Equation 4.108 and Figure 4.8.

$$P_{CO_2} = \exp\left(1.8\ln(\alpha) + k_1 + \frac{10}{1 + k_2 \exp\left(-k_3 \ln(\alpha)\right)}\right) \tag{4.108}$$

where $k_1 = -9155.955T_l + 28.027$, $k_2 = \exp(-6146.180T_l + 14.999)$ and $k_3 = 7527.038T_l - 16.942$.

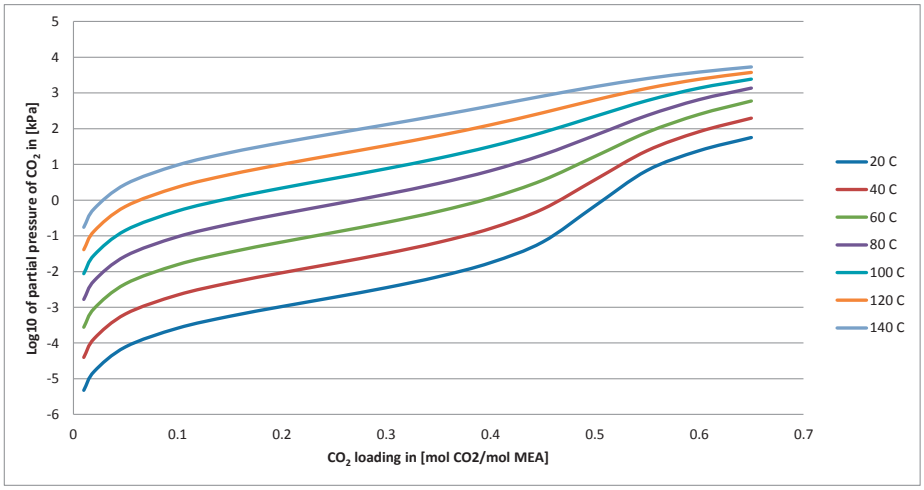

FIGURE 4.8: VLE as function of solvent CO_2 loading and temperature.

4.3.5.6 Chemical reactions and reaction kinetics

Reactions occurring in the vapor phase in the CO_2 absorption plant are generally considered negligible. Based on that assumption, species generation is considered to take place in the liquid phase only.

Possible reaction mechanisms for the CO_2-MEA-H_2O system are presented in the literature, however the net reaction is given in Equation 2.1. Reaction rates are commonly described as functions of the concentration of the reacting species. The CO_2-MEA reaction is normally considered to be first order in CO_2 and MEA, which leads to the following expression of the forward CO_2-MEA reaction (Monteiro, 2014):

$$-r_{CO_2} = k_2[CO_2][MEA] \tag{4.109}$$

For the pseudo-first order assumption, MEA is assumed to be constant and can be regarded as a part of the rate constant k_{app} , yielding:

$$-r_{CO_2} = k_{\text{app}}[CO_2] \tag{4.110}$$

Reactions between CO_2 and water also occur, and the experimentally measured rate constant (k_{obs}) is in reality a contribution from all reactions taking place in the system. Two different kinetic mechanisms are suggested in order to interpret the k_{app} into kinetic rate constants. One is the zwitterion model proposed by Caplow (1968) and Danckwerts (1979), as shown in Equation 4.111, while the other is the direct (termolecular) model proposed by Crooks and Donnellan (1989) as shown in Equation 4.112.

The zwitterion mechanism consists of the formation of a complex called a zwitterion, followed by the deprotonation of the zwitterion by a base. The general rate of reaction of CO_2 with MEA via the zwitterion mechanism could be described as:

$$-r_{CO_2} = \frac{k_2[\text{MEA}]}{1 + \frac{k_{-1}}{\sum k_b[B]}}[CO_2] = \frac{k_{\text{app}}}{1 + \frac{k_{-1}}{\sum k_b[B]}}[CO_2] \tag{4.111}$$

where $\sum k_b[B]$ indicates the contribution to proton transfer by all bases present in the solution.

The termolecular or direct mechanism assumes that the reaction is a single-step between CO_2 and MEA where the initial product is not a zwitterion. The rate of reaction of CO_2 with MEA is described as:

$$-r_{CO_2} = \{k^T_{\text{MEA}}[\text{MEA}] + k^T_{H_2O}[\text{MEA}]\}[\text{MEA}][CO_2] \tag{4.112}$$

For the latter, Luo et al. (2015) have developed the following expressions for the parameters k^T_{MEA} and $k^T_{H_2O}$:

$$\begin{aligned} k^T_{\text{MEA}} &= 2.003 \cdot 10^{10} \exp\left(\frac{-4742}{T_1}\right) \\ k^T_{H_2O} &= 4.147 \cdot 10^{6} \exp\left(\frac{-3110}{T_1}\right) \end{aligned} \tag{4.113}$$

4.3.5.7 Specific heat capacity

Solvent heat capacity in units [kJ °C/kg] is given as a weighted function of component heat capacities:

$$\begin{aligned} C_{\mathrm{p,l}} = & w_{\mathrm{H_2O}} C_{\mathrm{p,l,H_2O}} + w_{\mathrm{MEA}} C_{\mathrm{p,l,MEA}} \\ & + w_{\mathrm{H_2O}} w_{\mathrm{MEA}} \left(-0.9198 + 0.01369 \bar{T}_{\mathrm{l}} + \frac{69.6243 w_{\mathrm{MEA}}}{\bar{T}_{\mathrm{l}}^{1.5859}} \right) \end{aligned} \tag{4.114}$$

where the component heat capacities are given as follows:

$$\begin{aligned} C_{\mathrm{p,l,H_2O}} &= 4.1908 + 6.620 \cdot 10^{-4} \bar{T}_{\mathrm{l}} + 9.14 \cdot 10^{-6} \bar{T}_{\mathrm{l}}^2 \\ C_{\mathrm{p,l,MEA}} &= 2.5749 + 6.612 \cdot 10^{-3} \bar{T}_{\mathrm{l}} + 1.90 \cdot 10^{-5} \bar{T}_{\mathrm{l}}^2 \end{aligned} \tag{4.115}$$

The gas heat capacity is given in units [kJ °C/kg] by Reid et al. (1987) as:

$$C_{\mathrm{p,g}} = \sum_i C_{\mathrm{p,g},i} \frac{y_i}{M_i}; \tag{4.116}$$

where the gas component heat capacities in units [kJ °C/kmol] are as follows:

$$\begin{aligned} C_{\mathrm{p,g,CO_2}} &= 19.80 + 7.344 \cdot 10^{-2} T_{\mathrm{g}} - 5.602 \cdot 10^{-5} T_{\mathrm{g}}^2 + 1.715 \cdot 10^{-8} T_{\mathrm{g}}^3 \\ C_{\mathrm{p,g,H_2O}} &= 32.24 + 1.924 \cdot 10^{-3} T_{\mathrm{g}} + 1.055 \cdot 10^{-5} T_{\mathrm{g}}^2 - 3.596 \cdot 10^{-9} T_{\mathrm{g}}^3 \\ C_{\mathrm{p,g,MEA}} &= 9.311 + 3.009 \cdot 10^{-1} T_{\mathrm{g}} - 1.818 \cdot 10^{-4} T_{\mathrm{g}}^2 + 4.656 \cdot 10^{-8} T_{\mathrm{g}}^3 \\ C_{\mathrm{p,g,N_2}} &= 31.15 - 1.357 \cdot 10^{-2} T_{\mathrm{g}} + 2.680 \cdot 10^{-5} T_{\mathrm{g}}^2 - 1.168 \cdot 10^{-8} T_{\mathrm{g}}^3 \\ C_{\mathrm{p,g,O_2}} &= 28.11 - 3.680 \cdot 10^{-6} T_{\mathrm{g}} + 1.746 \cdot 10^{-5} T_{\mathrm{g}}^2 - 1.065 \cdot 10^{-8} T_{\mathrm{g}}^3 \end{aligned} \tag{4.117}$$

4.3.5.8 Heat of vaporization

Gáspár and Cormoş (2011) presented the following correlations for prediction of heat of vaporization of MEA and water in [kJ/kmol]:

$$\Delta h_{vap,\mathrm{MEA}} = (-1.447 T_{\mathrm{l}} + 1077.6) \cdot M_{\mathrm{MEA}} \tag{4.118}$$

$$\Delta h_{vap,\mathrm{H_2O}} = (6.5737 P_{\mathrm{H_2O}}^2 - 73.173 P_{\mathrm{H_2O}} + 2322.1) \cdot M_{\mathrm{H_2O}} \tag{4.119}$$

4.3.5.9 Heat of absorption

The heat of absorption of CO_2 is commonly used to combine heat of reaction with MEA and heat of solution of CO_2 in an MEA solution. This property will be dependent on both temperature and CO_2 loading (Kim et al., 2014), and is a very important term in the liquid phase energy balance.

Kohl and Nielsen (1997) presented a correlation for heat of absorption in [kJ/kmol] as a function of CO_2 loading for $\alpha_{CO_2} < 0.55$:

$$\begin{aligned}\Delta h_{\text{abs},CO_2} =& (-2.798\alpha^5 + 1.6545\alpha^4 - 0.1686\alpha^3 - 0.04535\alpha^2 \\ &+ 0.00839\alpha + 0.085017) \cdot 10^6\end{aligned} \tag{4.120}$$

The heat of absorption for CO_2 absorbed in 30 wt% aqueous MEA was measured by Kim et al. (2014) for temperatures of 40, 80 and 120 °C and various loadings. A loading dependence similar to the one described by Equation 4.120 is observed, but a dependency in temperature is also observed. Data from Mathonat et al. (1998) reveal the same trend. Kim et al. (2014) notes that significant uncertainty remains with regard to the temperature effects in the heat of absorption, especially for higher temperatures, and a linear dependency of heat of absorption with temperature is more probable. The experimental data of Kim et al. (2014) for 40 and 80 °C are therefore used to generate a linear prediction of heat of absorption with temperature at low loadings. This relation is afterward combined with Equation 4.120 to create the following general relation for heat of absorption in [kJ/kmol] as a function of both loading and temperature:

$$\begin{aligned}\Delta h_{\text{abs},CO_2} =& (-2.798\alpha^5 + 1.6545\alpha^4 - 0.1686\alpha^3 - 0.04535\alpha^2 \\ &+ 0.00839\alpha + (\frac{0.085375T_l + 58.746}{1000})) \cdot 10^6\end{aligned} \tag{4.121}$$

Figure 4.9 shows the results of Kim et al. (2014) together with the developed soft-model (Equation 4.121).

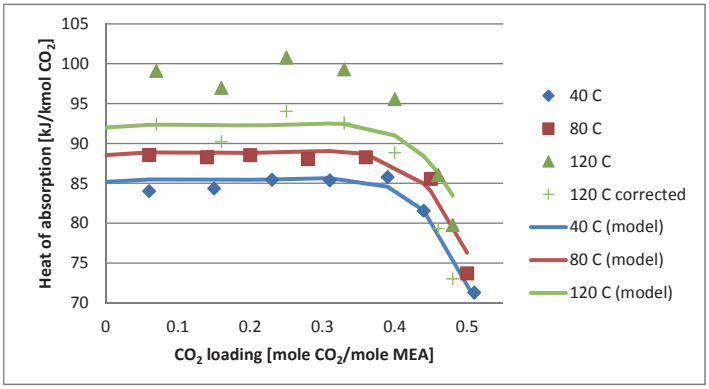

FIGURE 4.9: Heat of absorption of CO_2 for 30 wt% MEA solution at 40, 80 and 120 °C (Kim et al., 2014).

4.4 Implementation of the MATLAB model

The developed mathematical process unit models and control equations described in Section 4.3.2, the mass and heat transfer models described in Section 4.3.3 and the thermodynamic and physical and chemical property sub-models described in Section 4.3.5 are implemented in MATLAB. As previously explained, this result in a set of integral, partial differntial and algebraic equations (IPDAEs), thus numerical methods are required in order to solve the equation systems. The collocation method described in Section 4.1 is applied to discretize the spatial partial derivatives of the distributed parameter models and handle integral equations according to Equations 4.3 - 4.5. This will reduce the IPDAE system into a system of DAEs which is solvable by ode-solvers in MATLAB. ode15s is used for this purpose.

The process model can be adapted to various process configurations through manipulation of unit connections in a separate file where connection between units are configured. Sizing of equipment can be adjusted in the unit input files. The model can also easily be adapted to handle different packing types by providing the correct packing parameters in the respective absorber and desorber input files. Specification of various empirical correlation methods is also performed in the model input. The number of collocation points for the distributed parameter unit models (absorber, desorber, cross heat exchanger and lean cooler) can also be modified.

Initial conditions are loaded from previously stored steady state conditions for the system given the current boundary conditions. System boundary conditions are either specified directly in MATLAB, or alternatively, experimentally logged values stored in Excel-files can be loaded before the simulation is started. The logged data may be dynamic, however, they are not continuous since they are logged with a certain frequency (e.g. every minute) and come with time stamps. ode15s does not handle discontinuities well. Thus, interpolation methods are required in order to convert the time-dependent logged pilot plant data into continuous boundary conditions for the model, which gives better convergence properties. The function *interp1* and method *cubic* are used for this purpose.

4.4.1 Sequential modular vs simultaneous equation-based method

Paper C in Appendix C.3 presents an evaluation of the sequential modular-based numerical solution strategy described in Section 4.1 for the CO_2 capture process model.

The process model used for this investigation consists of an absorber unit model and a unit model representing the regeneration section of the plant, where essentially the desorber, reboiler and condenser are solved in a simultaneous manner, as described in Paper B in Appendix C.2. This means that each process unit (that is the absorber and the regeneration section in this case) is modeled and integrated individually, while a co-ordination algorithm is developed in order to synchronize the process units in time and provide input information between them. The simulation window is divided into time intervals with a certain time step t_h, and couplings between the units are only allowed at the end of each time interval. This means that unit input variables such as inlet flow rate, pressure, temperature and composition are updated at the end of each time step as a function of time based on their respective gradients during the current time interval. Recirculation loops are also iterated at the end of each time step, and a direct substitution method is used for this purpose.

A pressure-flow interaction algorithm (P-F network solver) is developed in order to provide estimates of the downstream pressures for each unit, which is required in order to calculate the outlet flows. The P-F network solver minimizes the need

for iteration on the pressure loops by providing proper predictions of downstream pressures. An illustration of the developed P-F network solver is presented in Figure 4.10, where F_{ij} represent a mass flow rate from unit i to unit j and P_j is the current pressure of unit j which is downstream from unit i. The flow between two units is modeled by a typical valve equation similar to Equation 4.26:

$$F_{ij} = K_L u(t)\sqrt{P_i - P_j} \tag{4.122}$$

while the pressure change in unit i is given by:

$$\frac{\mathrm{d}P_i}{\mathrm{d}t} = \frac{1}{\tau_i}\sum_{j}^{\mathrm{N}} \delta_{ij} F_{ij} \tag{4.123}$$

δ takes care of directionality; δ = +1 when directed to node i, -1 when directed from node i, and otherwise 0. The parameter τ is given by

$$\tau_i = V_i \frac{\partial \rho_i}{\partial P_i} \tag{4.124}$$

and can be considered a constant in this context.

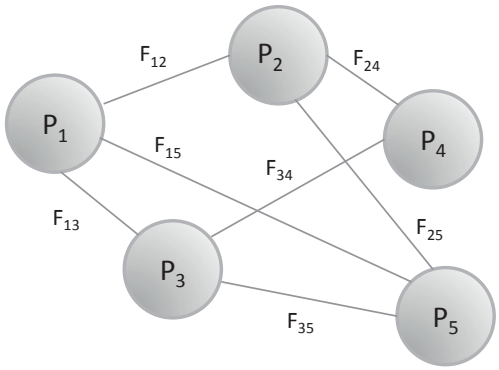

FIGURE 4.10: Illustration of units and connections in the P-F network solver.

Based on the present situation of mass flow rates, it is desired to predict how the pressure will evolve in each unit. To do so, a linearizing of the pressure model Equation 4.123 around time t_k is performed:

$$\begin{aligned}\frac{\mathrm{d}P_i}{\mathrm{d}t} =& \frac{1}{\tau_i}\sum_j^{\mathrm{N}} \delta_{ij} F_{ij}^k + \frac{1}{\tau_i}\sum_j^{\mathrm{N}} \delta_{ij}\left(\frac{\mathrm{d}F_{ij}}{\mathrm{d}P_i}\right)_{P_j} \frac{\mathrm{d}P_i}{\mathrm{d}t}\,(t-t_k) \\ &+ \frac{1}{\tau_i}\sum_j^{\mathrm{N}} \delta_{ij}\left(\frac{\mathrm{d}F_{ij}}{\mathrm{d}P_j}\right)_{P_i} \frac{\mathrm{d}P_j}{\mathrm{d}t}\,(t-t_k)\end{aligned} \tag{4.125}$$

Applying the time horizon concept, introducing a global time step $t_h = t_{k+1} - t_k$ and converting to matrix form yields:

$$[\mathrm{I} - t_h \mathrm{J}_k]\frac{\mathrm{dP}}{\mathrm{d}t} = \begin{pmatrix} \frac{1}{\tau_1}\sum_j^{\mathrm{N}} \delta_{1j} F_{1j}^k \\ \vdots \\ \frac{1}{\tau_N}\sum_j^{\mathrm{N}} \delta_{Nj} F_{Nj}^k \end{pmatrix} \tag{4.126}$$

Equation 4.126 can by implicit Euler integration be transformed into:

$$\mathrm{P}_{k+1} - \mathrm{P}_k = t_h\,[\mathrm{I} - t_h \mathrm{J}_k]^{-1} \begin{pmatrix} \frac{1}{\tau_1}\sum_j^{\mathrm{N}} \delta_{1j} F_{1j}^k \\ \vdots \\ \frac{1}{\tau_N}\sum_j^{\mathrm{N}} \delta_{Nj} F_{Nj}^k \end{pmatrix} \tag{4.127}$$

which is solved as a linear system without iterations.

It was concluded in Paper C in Appendix C.3 that the sequential modular-based method proves to offer desirable convergence and stability properties for a simplified plant model consisting of an absorber and a regeneration unit. However, due to the recirculation loop of lean solvent it has later been discovered that the simultaneous equation-based method provides substantial improvements in computational speed compared to the modular-based method. The simultaneous equation-based method avoids the need for iteration on tear streams since all connections between units are handled directly at each time step, whereas the modular-based method requires iteration on selected tear streams for recirculation loops after each time step. Depending on the tolerance specified for the recirculation loop iteration, the simulation time increases up to 30 - 50% using the modular-based method compared to the equation-based method in this case. Also, if the whole process plant is divided into modules representing each piece of process equipment, as it should be to enable the advantage of tailoring integration routines to each unit model, three recirculation loops are identified in this process that must be handled by iteration on flowsheet level in the modular-based method. That is lean

solvent to the absorber column, reboiler vapor to the desorber column and condenser water condensate to the desorber column, as indicated by green arrows in Figure 4.3. Performing iterations on all these three tear streams will increase the computational requirements and simulation time even more.

Modification and reuse of existing code has been mentioned as an advantage of the sequential modular approach compared to the simultaneous equation-based method. However, this has been quite simply resolved for the CO_2 capture process model through clever design of program code. A separate process plant configuration file is called by ode15s where all unit models again are called from their respective model files. In this way code is easily reused with only minor modifications for the individual process units.

Proper initialization is however very important in order to obtain convergence using the equation-based method, thus routines are developed to handle this issue. The specific process model is basically run until steady state conditions are reached for a given set of boundary conditions. When the process conditions have stabilized at a satisfactory level, the final conditions are stored, before they are reloaded as initial conditions for the subsequent dynamic simulations. One limitation with this method is that the simulations always must be started from steady state process conditions, and actual pilot plant conditions therefore cannot be loaded as initial conditions to the model. Nevertheless, providing actual measurements as initial conditions seems like an impossible task since quite a number of the initial conditions are unknown (not measured) in the pilot plant. These include for instance column concentrations as functions of the axial direction for the absorber and desorber.

A top level representation of the execution path for the simultaneous equation-based model is presented in Figure 4.11. A representation of the modular-based execution path for the overall process model is also included in Figure 4.12 for comparison. It should be noted that a simplified version of the latter model outline was investigated in Paper C in Appendix C.3, since only the absorber unit and a complete regeneration unit (consisting of the reboiler, condenser and desorber) were applied in this case. Thus, only one tear stream was considered in the simplified case, that being the lean solvent to the absorber inlet.

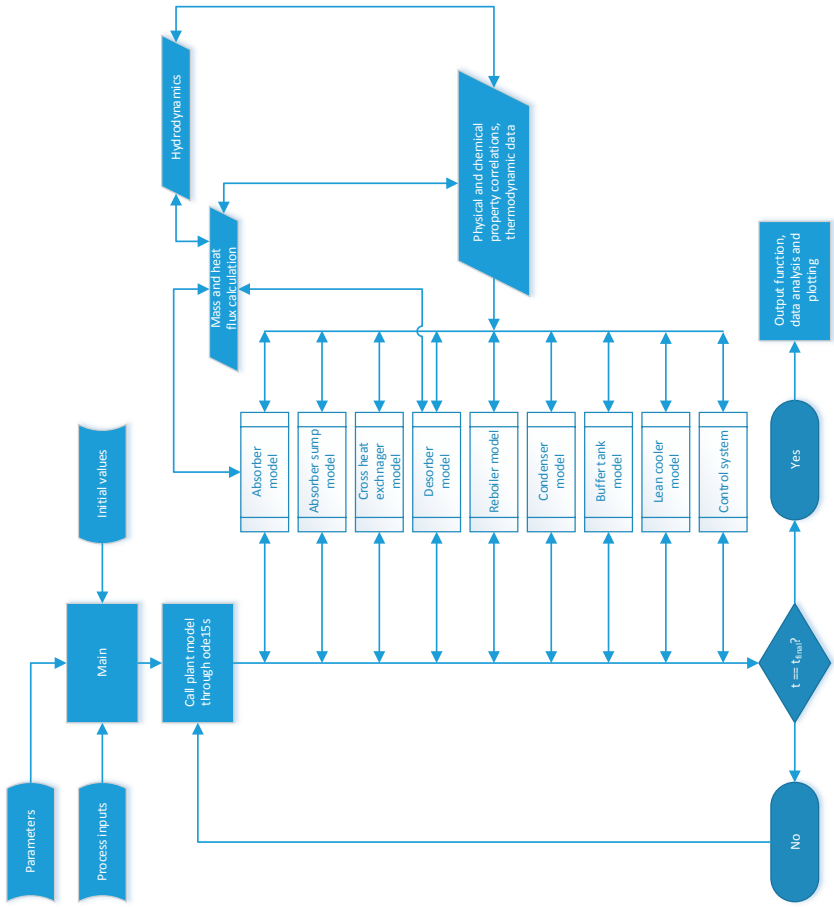

FIGURE 4.11: Flow sheet of the simultaneous equation-based model execution.

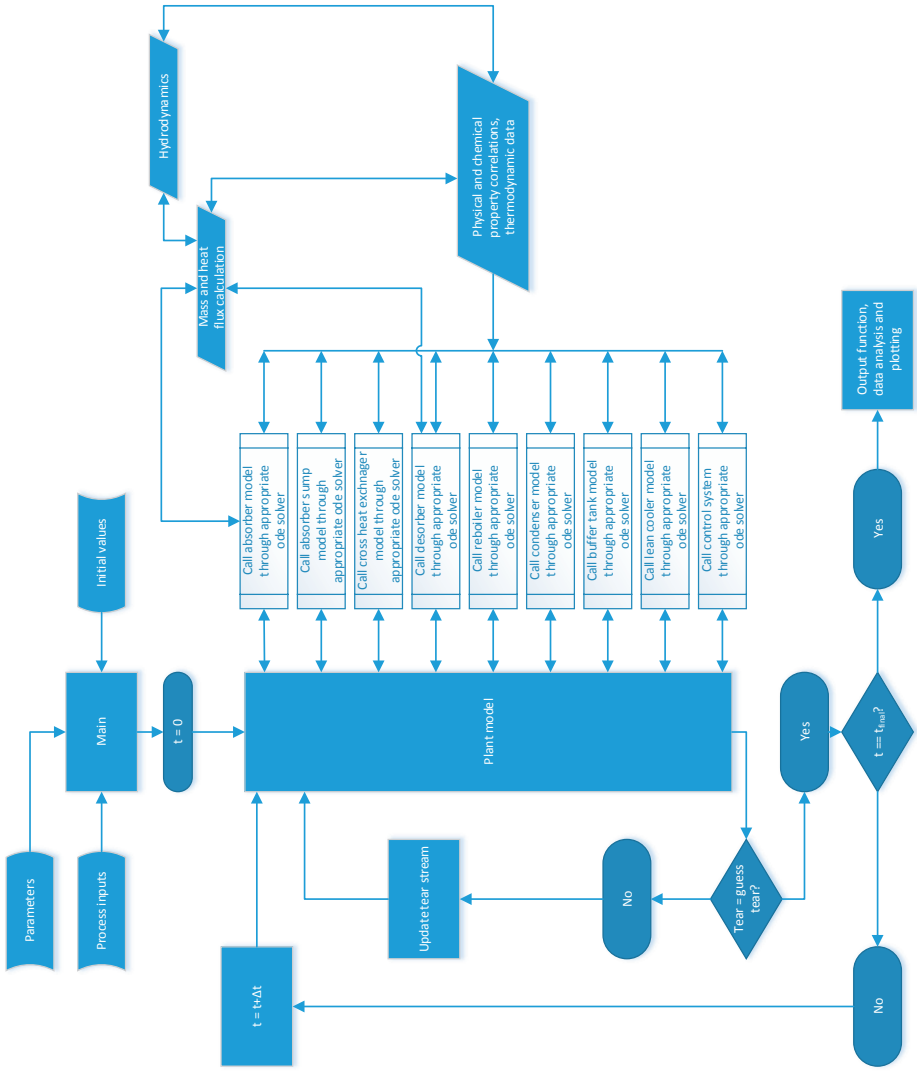

FIGURE 4.12: Flow sheet of the sequential modular-based model execution.

4.5 Analysis of degree of model complexity

4.5.1 Choice of enhancement factor models

The rate-based approach of mass transfer using various models of the enhancement factor is evaluated in this section. The DeCoursey relation given by Equation 4.48 is regarded as a general term for the enhancement factor. It is however common to approximate the enhancement factor by the Hatta modulus (pseudo-first order assumption) for absorber column conditions (Tobiesen et al., 2007). For stripper conditions, is is common to assume reversible instantaneous reaction due to the high temperatures in the desorber column which means that equilibrium prevails in the liquid phase (Tobiesen et al., 2008). Equations 4.46 and 4.47 are applied for absorber and stripper conditions, respectively, in this case.

E_∞ and thereby E_{DC} requires iteration on the interface concentration of CO_2 as seen in Equation 4.47 ($E_\infty = f(C_{\mathrm{l,CO_2,if}})$). $C_{\mathrm{l,CO_2,if}}$ can be back-calculated from the molar interface flux of CO_2 ($J_{\mathrm{g/l,CO_2}}$) according to Equation 4.128. However, $J_{\mathrm{g/l,CO_2}}$ is again dependent on the enhancement factor.

$$J_{\mathrm{g/l,CO_2}} = k_{\mathrm{l,CO_2}}(C_{\mathrm{l,CO_2,if}} - C_{\mathrm{l,CO_2,b}}) \tag{4.128}$$

Iterations are rather impractical in dynamic simulations, due to increased calculation time. A comparison of simulation results using various expressions for the enhancement factor in the MATLAB model of the Tiller pilot plant is therefore given in the following. The two steady state cases in the Tiller pilot plant presented in Table 2.5 are used as basis for the simulations, and the Rocha correlations are applied for prediction of mass transfer and column hydraulics. Steady state column temperature profiles, solvent CO_2 loading, and total CO_2 absorption/desorption rates are compared for the different estimations of the enhancement factor in Figures 4.13 and 4.14 and Table 4.4. The pilot plant data are also included and the relative deviation between the simulated and pilot plant results are given in parenthesis in Table 4.4.

Assuming $E = Ha$ for absorber conditions seems like a perfectly valid assumption for the two cases studied according to these results. The CO_2 absorption and rich CO_2 loading does not seem to improve much using the more advanced

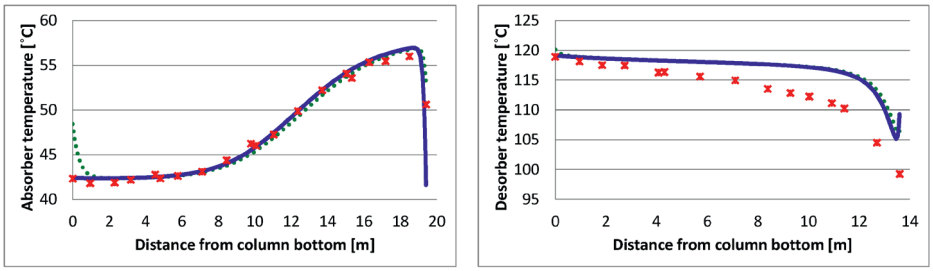

(A) $E = Ha$ for both columns

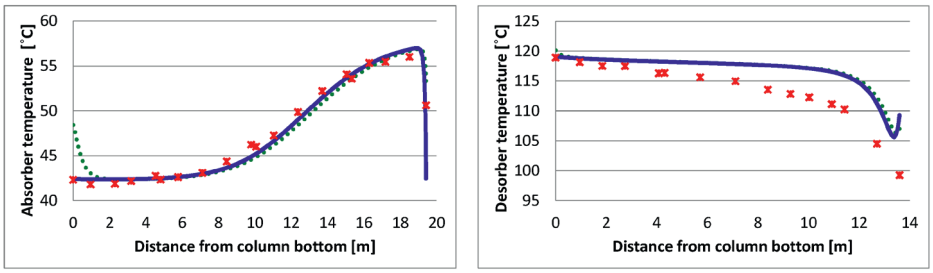

(B) $E = Ha$ for absorber, $E = E_\infty$ for desorber

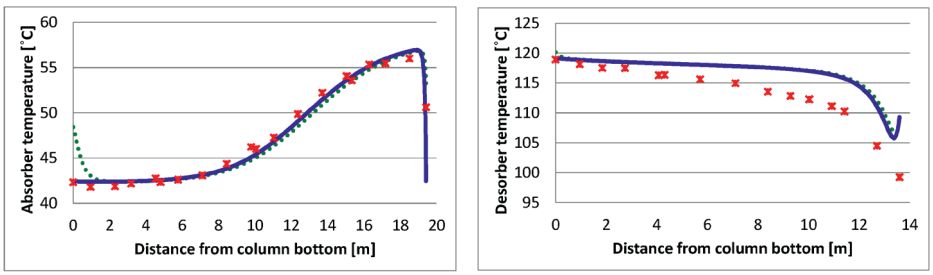

(C) $E = E_{DC}$ for both columns

FIGURE 4.13: Steady state absorber and desorber temperature profiles for various alternatives of enhancement factor models for case 100612 in the Tiller pilot plant. (—) Model (solvent), (---) Model (gas), (✱) Pilot plant.

enhancement factor model and the absorber temperature profiles are very similar for both cases. Assuming $E = E_\infty$ for stripper conditions seems to estimate conditions slightly closer to equilibrium compared to the more advanced model, when comparing the temperature profiles. However, the differences in desorber temperature profiles are very small in both cases, thus the effect is regarded as minimal. The absorption rates are also very similar for both cases, but the lean CO_2 loading values are slightly improved using the DeCoursey model. Assuming $E = E_{DC}$ therefore does not seem to improve the simulation results much, as the

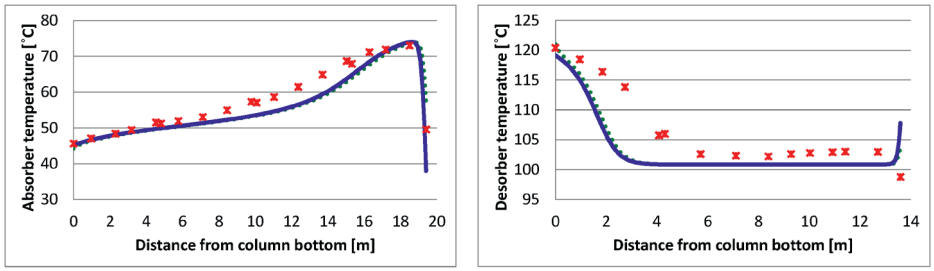

(A) $E = Ha$ for both columns

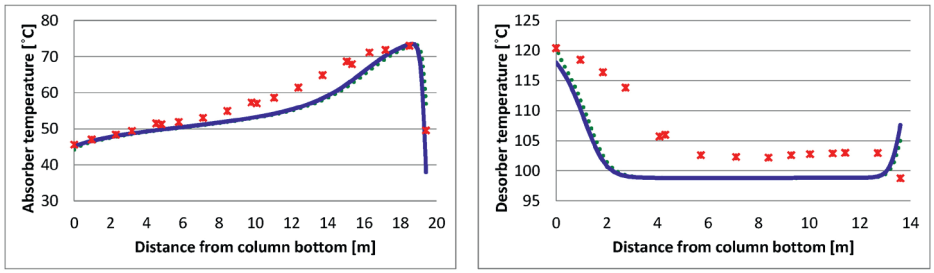

(B) $E = Ha$ for absorber, $E = E_\infty$ for desorber

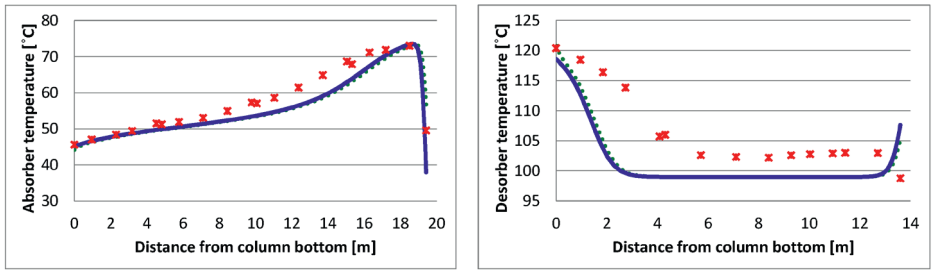

(C) $E = E_{DC}$ for both columns

FIGURE 4.14: Steady state absorber and desorber temperature profiles for various alternatives of enhancement factor models for case 100718 in the Tiller pilot plant. (—) Model (solvent), (---) Model (gas), (✱) Pilot plant.

absorption and desorption rates and CO_2 loadings are only slightly improved or similar, and the absorber and desorber temperature profiles also look very similar. In fact assuming $E = Ha$ for both columns gives also very similar results, and even slightly improved results for the absorption/desorption rates and lean CO_2 loading in case 100718. A comparison of the estimated Ha, E_∞ and E_{DC} is given for the absorber and desorber for both cases in Figure 4.15. These results support the validity of assuming $E = Ha$ for absorber conditions since the contribution from E_∞ is very limited and the estimated E_{DC} more or less equals Ha. Also for

TABLE 4.4: Comparison of the Tiller pilot plant data for cases 100612 and 100718 to steady state simulation results for various alternatives of enhancement factor models. The relative deviations from pilot plant data are given in parenthesis.

Case 100612	**Absorbed CO_2** [kg/h]	**Desorbed CO_2** [kg/h]	**Rich CO_2 loading** [molCO_2/molMEA]	**Lean CO_2 loading** [molCO_2/molMEA]
Pilot	15.31	14.80	0.48	0.14
E=Ha	15.20 (-0.8%)	15.20 (+2.7%)	0.48 (+1.2%)	0.12 (-12.1%)
$E = Ha/E_\infty$	15.22 (-0.6%)	15.22 (+2.8%)	0.48 (+1.2%)	0.12 (-12.5%)
$E = E_{DC}$	15.17 (-0.9%)	15.17 (+2.5%)	0.48 (+1.2%)	0.12 (-11.9%)
Case 100718	**Absorbed CO_2** [kg/h]	**Desorbed CO_2** [kg/h]	**Rich CO_2 loading** [molCO_2/molMEA]	**Lean CO_2 loading** [molCO_2/molMEA]
Pilot	25.84	24.38	0.49	0.17
E=Ha	24.65 (-4.6%)	24.65 (+1.1%)	0.50 (+2.0%)	0.17 (+0.7%)
$E = Ha/E_\infty$	23.66 (-8.5%)	23.66 (-3.0%)	0.50 (+2.0%)	0.18 (+8.2%)
$E = E_{DC}$	23.65 (-8.5%)	23.65 (-3.0%)	0.50 (+1.8%)	0.18 (+7.6%)

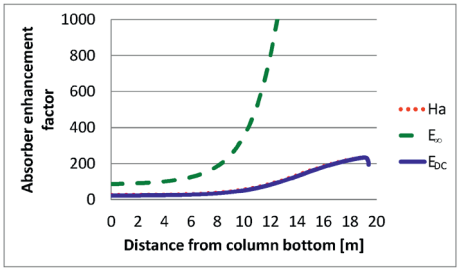

(A) Case 100612 absorber enhancement factor

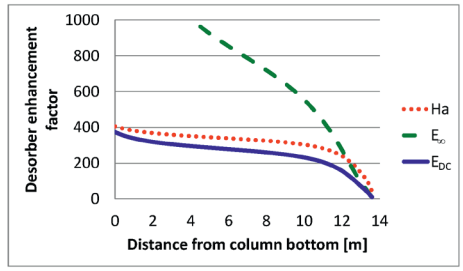

(B) Case 100612 desorber enhancement factor

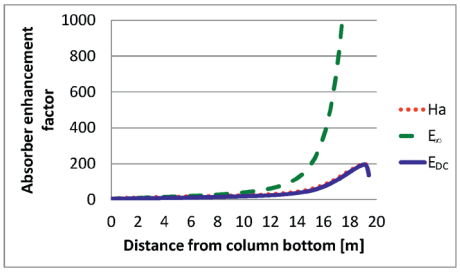

(C) Case 100718 absorber enhancement factor

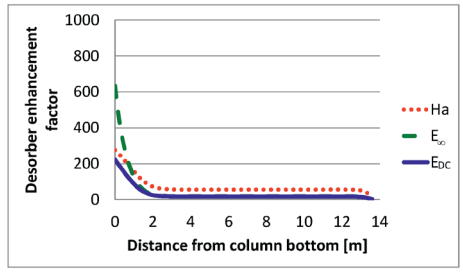

(D) Case 100718 desorber enhancement factor

FIGURE 4.15: Contributions to E_{DC}

desorber conditions the estimated E_{DC} is close to Ha, especially for case 100612 where E_∞ is much larger in most parts of the column. For case 100718, the predicted E_{DC} is closer to E_∞ for most parts of the desorber, however, the difference from Ha is not very large either, especially for the lower part of the column where most of the mass transfer is actually taking place. For practical reasons it

is therefore considered accepted to use the Hatta modulus in both absorber and stripper conditions to avoid computationally intensive iterations in the dynamic simulations. The consequence is simulation results that are slightly shifted towards equilibrium for desorber conditions in cases where the Hatta modulus is larger than E_{DC}.

4.5.2 Equilibrium-stage vs rate-based approach for mass transfer

A comparison of the equilibrium-stage and rate-based approaches of modeling mass transfer in the absorption and desorption towers is performed in this section. This means that the bottom left modeling approach shown in Figure 4.2 in Section 4.2 is compared to the modeling approach shown in the upper middle illustration in the same figure.

Cases 100612 and 100718 in the Tiller pilot plant are used as basis for the comparison, and the Rocha mass transfer and hydrodynamic correlations are applied for the rate-based calculations. In order to compare the equilibrium-stage model to the corresponding rate-based model, the number of theoretical stages are chosen such that the solvent CO_2 loadings and overall CO_2 capture rate are close to those measured experimentally. The simulated amount of absorbed/desorbed CO_2 and solvent CO_2 loadings corresponding to experimental cases 100612 and 100718 are presented in Table 4.5. The simulated temperature profiles using the equilibrium-stage model are presented in Figures 4.16 and 4.17. Correspondingly, the temperature profiles using the rate-based approach are presented in Figures 4.13 and 4.14 for comparison.

The equilibrium-stage model can be tuned to predict output values that are reasonable compared to the pilot plant results. The rate-based approach gives however slightly better estimation of CO_2 capture performance, and far better predictions of absorber column temperature profiles. The equilibrium model, on the other hand, gives a slightly better fit for the desorber temperature profile, especially for case 100718, which suggests that the rate-based mass transfer rates for desorber conditions are slightly overpredicted by the applied correlations as will be discussed further in Sections 5.1.1 and 5.1.2. However, a similar tuning routine can be performed for the rate-based modeling approach by adjusting the mass transfer

TABLE 4.5: Comparison of the Tiller pilot plant data for cases 100612 and 100718 to steady state simulation results for the equilibrium-stage and rate-based modeling approach. The relative deviations from pilot plant data are given in parenthesis.

Case 100612	**Absorbed CO_2** [kg/h]	**Desorbed CO_2** [kg/h]	**Rich CO_2 loading** [$molCO_2/molMEA$]	**Lean CO_2 loading** [$molCO_2/molMEA$]
Pilot	15.31	14.80	0.48	0.14
E=Ha	15.20 (-0.8%)	15.20 (+2.7%)	0.48 (+1.2%)	0.12 (-12.1%)
EQ	15.06 (-1.6%)	15.06 (+1.7%)	0.48 (+1.0%)	0.12 (-10.5%)
Case 100718	**Absorbed CO_2** [kg/h]	**Desorbed CO_2** [kg/h]	**Rich CO_2 loading** [$molCO_2/molMEA$]	**Lean CO_2 loading** [$molCO_2/molMEA$]
Pilot	25.84	24.38	0.49	0.17
E=Ha	24.65 (-4.6%)	24.65 (+1.1%)	0.50 (+2.0%)	0.17 (+0.7%)
EQ	25.53 (-1.2%)	25.53 (+4.7%)	0.50 (+2.2%)	0.16 (-4.6%)

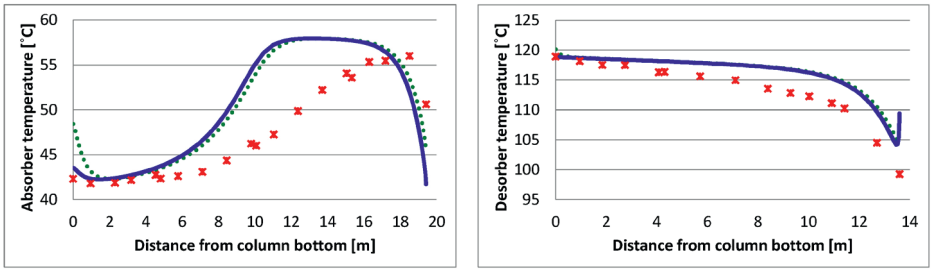

(A) Stage equilibrium for both columns

FIGURE 4.16: Steady state absorber and desorber temperature profiles for the equilibrium-stage model for case 100612 in the Tiller pilot plant. (—) Model (solvent), (---) Model (gas), (✱) Pilot plant.

coefficients to yield an equally improved fit of the desorber column temperature profiles. It should also be noted that the desorber temperature predictions using the equilibrium-stage approach for case 100612 give quite similar results compared to the rate-based approach with probable overpredicted mass transfer rates. This suggest that the selected number of equilibrium stages fits better for case 100718, and is slightly too high for case 100612, which is reasonable since the solvent flow rate is lower and the solvent residence time of the desorber is believed to be higher in case 100612. An improved and more sophisticated fitting procedure for the number of equilibrium stages depending on the solvent hold-up and desorber L/G is therefore believed to give improved predictions of the desorber temperature profile using the equilibrium-stage model.

A previous study presented by Lawal et al. (2009a) shows similar simulation results for the absorber column when comparing the equilibrium-stage model to the rate-based approach. Lawal et al. (2009a) concluded that the rate-based model gives better predictions of the absorber performance and temperature profile compared

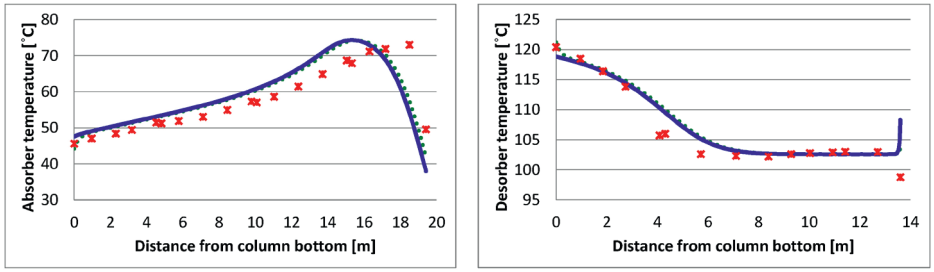

(A) Stage equilibrium for both columns

FIGURE 4.17: Steady state absorber and desorber temperature profiles for the equilibrium-stage model for case 100718 in the Tiller pilot plant. (—) Model (solvent), (---) Model (gas), (✱) Pilot plant.

to the equilibrium-stage model. However, Peng et al. (2003) suggest that the equilibrium-stage model is sufficient for dynamic modeling, since the dynamic responses using the rate-based and equilibrium-stage approaches are similar, even though the steady state results may differ. The comparison by Peng et al. (2003) was performed with another system, that being the production of tert-amyl methyl ether (TAME). The dynamic results may differ for the amine-based CO_2 capture process. This will depend on the nature of the system, that is the magnitude of the actual mass transfer and chemical reaction rates compared to gas and liquid absorber flow rates, which determines the distance from equilibrium. A dynamic simulation using the Gløshaugen pilot plant model applying the equilibrium-stage model for both the absorber and desorber columns is therefore performed and compared to results using the rate-based approach and dynamic pilot plant data. The equilibrium-stage results are presented in Figure B.1 in Appendix B.1, and show in fact very similar transient behavior in good agreement with the pilot plant results and rate-based simulation results presented in Figures 4.22 and 4.23. This will be elaborated in Section 5.1.1.

It is concluded that the choice of mass transfer model approach depends on the application of the model, as in many cases the equilibrium-stage approach might be sufficient for predicting dynamic responses. However, a more detailed dynamic model is required for other purposes where accurate results at both steady state and dynamic conditions are required with particular interest in the absorber performance.

4.6 Sensitivity to choice of empirical correlations

Two different empirical correlations for gas and liquid mass transfer coefficients and column hydraulics are tested through dynamic simulation. The Billet correlations (Billet and Schultes, 1999) are applied in a validation study of the MATLAB model using data from the Gløshaugen pilot plant, where the results are presented in Paper E in Appendix C.5. The correlations suggested by Rocha (Rocha et al., 1993, 1996) are later applied in a model with the same process configuration and the same simulated cases for comparison, and the results are given in the following.

The CO_2 absorption rate using the Billet correlations were initially underpredicted. The effective interface area of the absorber and desorber packing was therefore corrected by a factor of 2.25 in order to give a better fit to steady state pilot plant data. The Rocha correlations were applied without any adjustments or parameter fitting.

Steady state simulation results using the two different empirical correlations for mass transfer coefficients and column hydraulics are given in Table 4.6. Predicted steady state absorber and desorber temperature profiles are presented in Figures 4.20 and 4.21. From Table 4.6 it is seen that both correlations generate reasonable simulation results in good agreement with the pilot plant measurements. All absorption rates are within ±10% relative deviation compared to experimental values, except $m^g_{CO_2,des}$ which has slightly larger errors, probably due to measurement uncertainties as explained in Section 3.4.1. With the exception of lean loading estimation in cases 4 and 7, the relative deviation between modeled and measured CO_2 loading results are also within ±10%, and most of them are even within ±5%.

The prediction of solvent-hold up, effective interface area and gas and liquid film mass transfer coefficient for CO_2 is however very different for the two investigated correlations. The correlations by Billet in general predict lower solvent hold-up and effective interface area (wetting factor), while the mass transfer coefficients are larger. All these factors contribute to the overall CO_2 absorption rate, thus the net effect is similar and both correlations seem to work well. However, as previously mentioned the effective interface area predicted by the Billet correlation was corrected by a factor of 2.25 in order to meet the observed absorption rates. This means that the actual predicted effective interface area is even smaller for the Billet correlation. The predicted wetting factors for the corrected case is in the

range of 0.54 - 0.73 using the Billet correlation as seen in Figures 4.18 and 4.19, which corresponds to wetting factors of 0.24 - 0.32 for the unfitted case. For the Rocha correlations a wetting factor in the range of 0.67 - 0.90 is predicted for all cases (without adjustments), which seems more realistic. It is therefore reasonable to assume that the Rocha correlations give more reliable predictions of the wetting factor.

Similar results are reported by Razi et al. (2012), where design correlations for CO_2 absorption with MEA is reviewed. The study does not concern the Rocha correlations, however it is concluded by comparison of simulation results using various other correlations that the Billet model predicts a general lower solvent hold-up and effective interface area and higher mass transfer coefficients than most other correlations. Tobiesen et al. (2007) also compared various correlations for hydrodynamics of the very same pilot plant, and concluded that the correlations from Billet gave an unreasonably low effective interface area.

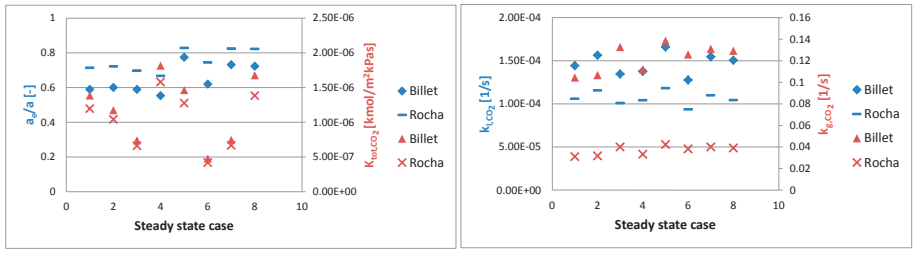

(A) Calculated wetting factor and overall mass transfer coefficient for the absorber

(B) Calculated gas and liquid film mass transfer coefficients for the absorber

FIGURE 4.18: Parameter estimation using the Billet and Rocha correlations for the absorber.

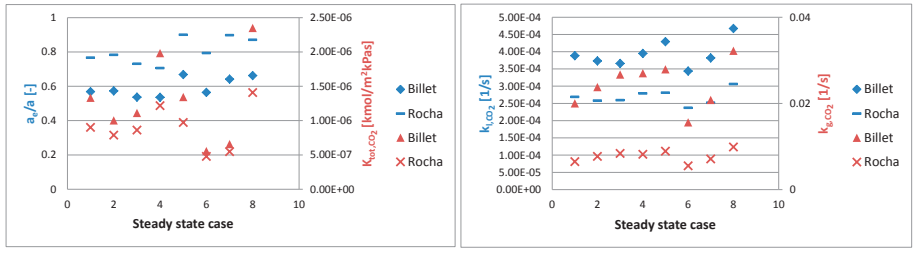

(A) Calculated wetting factor and overall mass transfer coefficient for the desorber

(B) Calculated gas and liquid film mass transfer coefficients for the desorber

FIGURE 4.19: Parameter estimation using the Billet and Rocha correlations for the desorber.

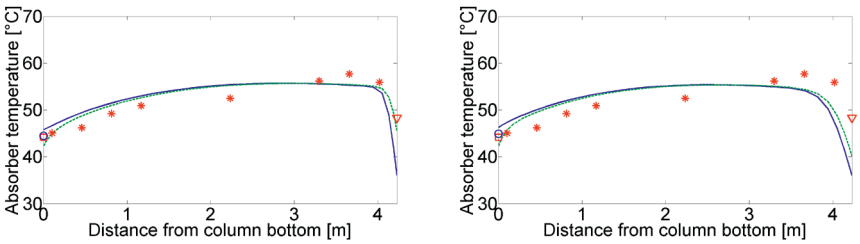

(A) Case 1: Billet correlations in the left figure, Rocha correlations to the right

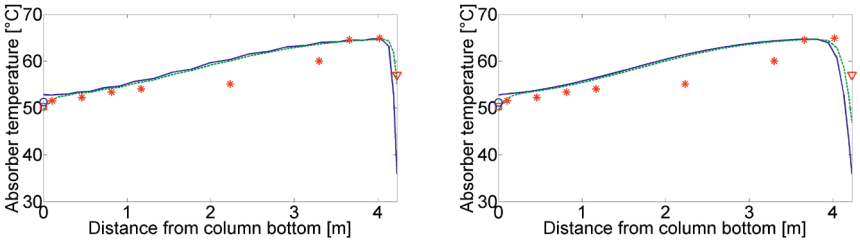

(B) Case 2: Billet correlations in the left figure, Rocha correlations to the right

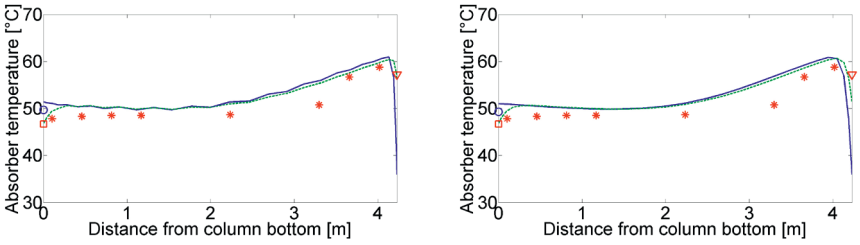

(C) Case 3: Billet correlations in the left figure, Rocha correlations to the right

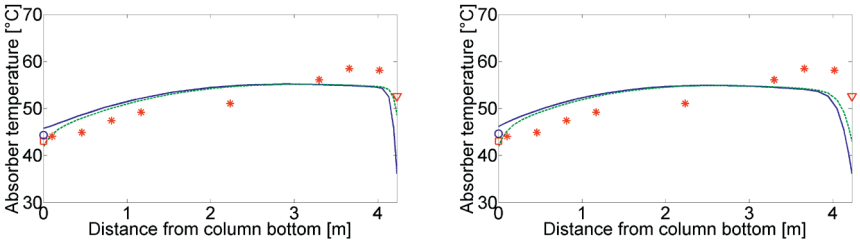

(D) Case 4: Billet correlations in the left figure, Rocha correlations to the right

FIGURE 4.20: Steady state absorber temperature profiles in the Gløshaugen pilot plant. (—) Model (solvent), (---) Model (gas), (○) Model (absorber sump), (✱) Pilot (packing), (□) Pilot (absorber sump) and (▽) Pilot (outlet gas). (Continues next page).

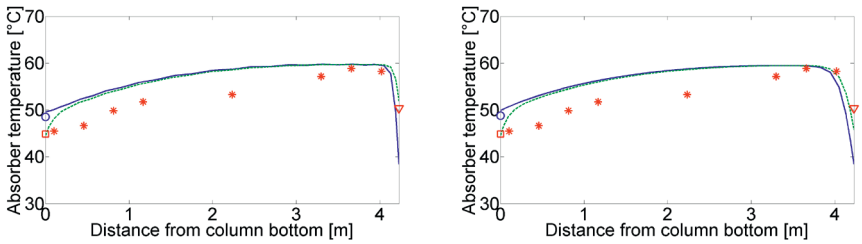

(E) Case 5: Billet correlations in the left figure, Rocha correlations to the right

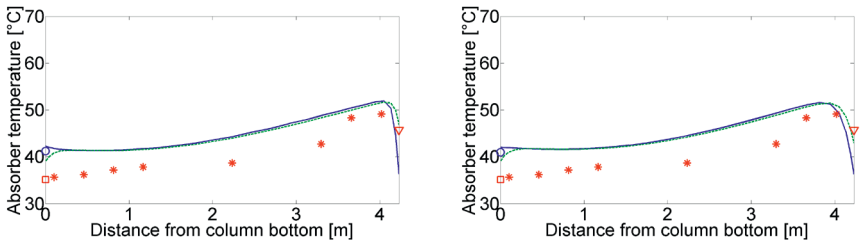

(F) Case 6: Billet correlations in the left figure, Rocha correlations to the right

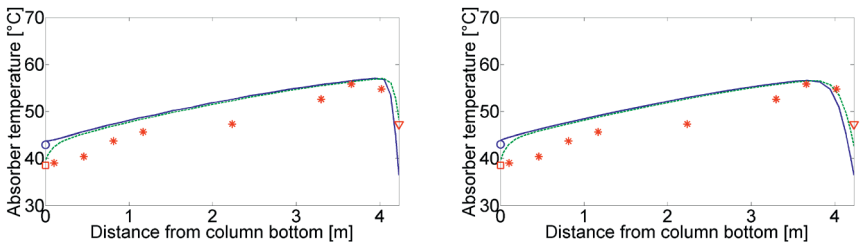

(G) Case 7: Billet correlations in the left figure, Rocha correlations to the right

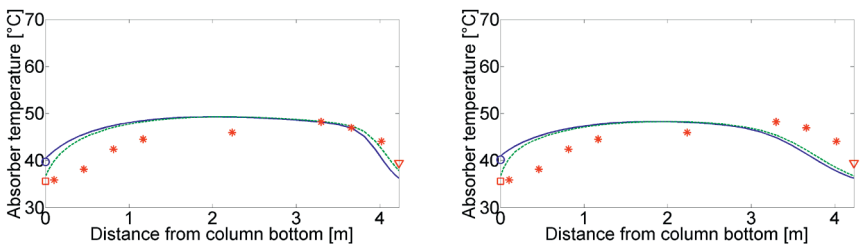

(H) Case 8: Billet correlations in the left figure, Rocha correlations to the right

FIGURE 4.20: Steady state absorber temperature profiles in the Gløshaugen pilot plant. (—) Model (solvent), (---) Model (gas), (○) Model (absorber sump), (✱) Pilot (packing), (□) Pilot (absorber sump) and (▽) Pilot (outlet gas). (Continued from previous page).

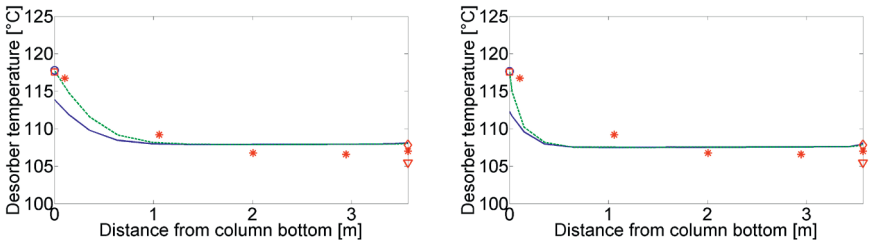

(A) Case 1: Billet correlations in the left figure, Rocha correlations to the right

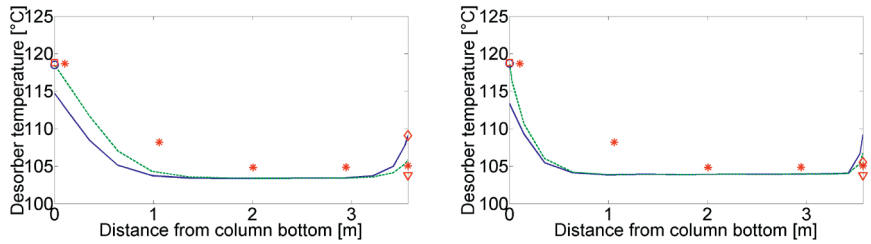

(B) Case 2: Billet correlations in the left figure, Rocha correlations to the right

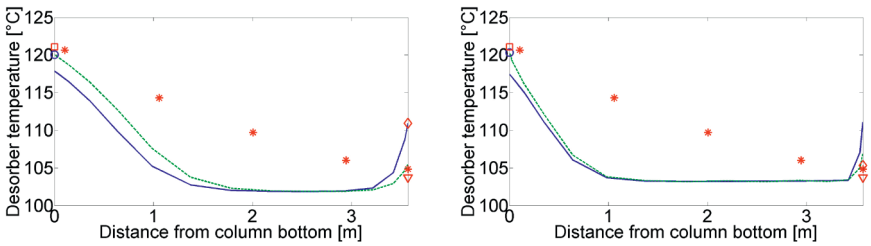

(C) Case 3: Billet correlations in the left figure, Rocha correlations to the right

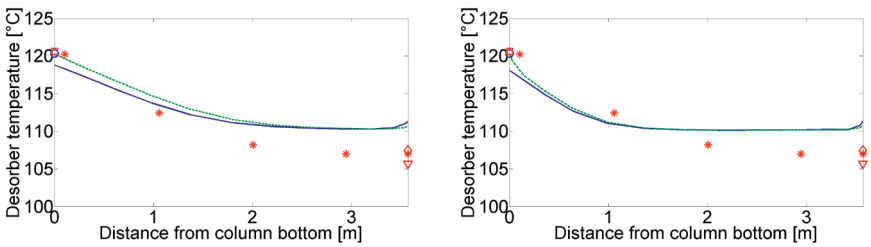

(D) Case 4: Billet correlations in the left figure, Rocha correlations to the right

FIGURE 4.21: Steady state desorber temperature profiles in the Gløshaugen pilot plant. (—) Model (solvent), (---) Model (gas), (○) Model (reboiler), (✱) Pilot (packing), (□) Pilot (reboiler), (◇) Pilot (inlet solvent) and (▽) Pilot (outlet gas). (Continues next page).

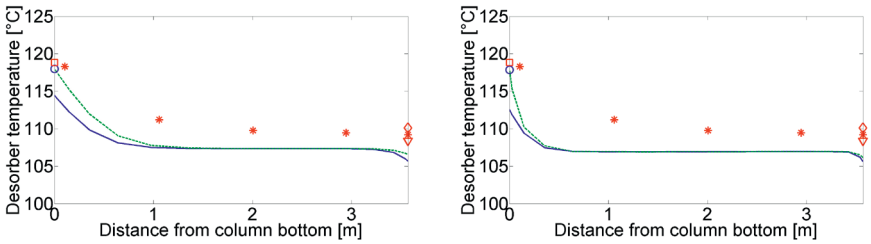

(E) Case 5: Billet correlations in the left figure, Rocha correlations to the right

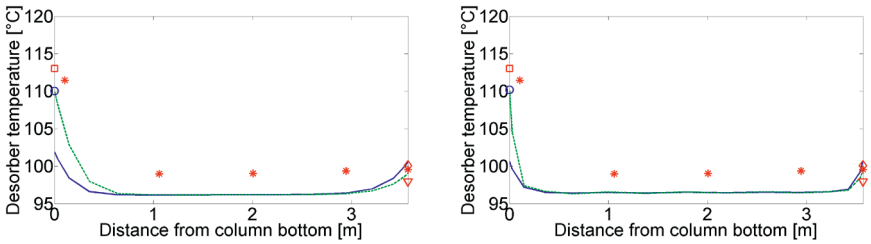

(F) Case 6: Billet correlations in the left figure, Rocha correlations to the right

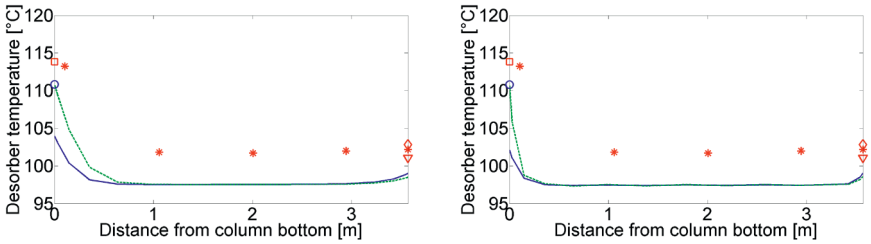

(G) Case 7: Billet correlations in the left figure, Rocha correlations to the right

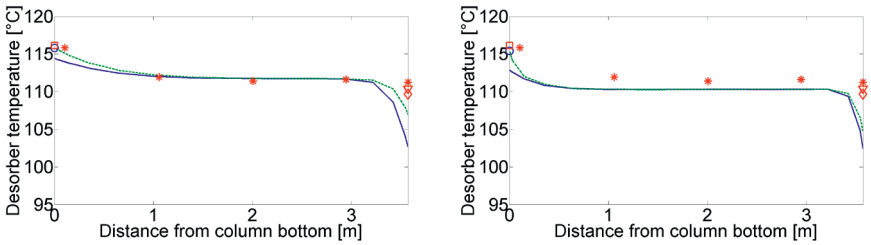

(H) Case 8: Billet correlations in the left figure, Rocha correlations to the right

FIGURE 4.21: Steady state desorber temperature profiles in the Gløshaugen pilot plant. (—) Model (solvent), (---) Model (gas), (○) Model (reboiler), (✱) Pilot (packing), (□) Pilot (reboiler), (◇) Pilot (inlet solvent) and (▽) Pilot (outlet gas). (Continued from previews page).

TABLE 4.6: Steady state simulation results of the Gløshaugen pilot plant.

	Correlation		**1**	**2**	**3**	**4**	**5**	**6**	**7**	**8**	**ARD** [%]
Absorbed CO_2	Billet	[kg/h]	4.60	7.68	8.78	5.50	6.78	4.75	5.85	2.87	
		$m^g_{CO_2,abs}$ RD [%]	+0.7	+4.5	+0.0	-3.6	+1.6	+1.6	-6.8	-4.7	2.9
		$m^l_{CO_2}$ RD [%]	-0.6	+1.0	-0.7	-2.7	-1.4	+1.0	-8.2	-2.2	2.2
		$m^g_{CO_2,des}$ RD [%]	+5.5	+1.4	-0.1	-14.5	-4.2	-2.8	-10.3	-10.8	6.2
	Rocha	[kg/h]	4.60	7.74	8.95	5.47	6.63	4.80	5.79	2.82	
		$m^g_{CO_2,abs}$ RD [%]	+0.7	+5.3	+1.9	-4.1	-0.6	+2.7	-7.7	-6.2	3.6
		$m^l_{CO_2}$ RD [%]	-0.6	+1.7	+1.2	-3.2	-3.5	+2.0	-9.1	-3.7	3.1
		$m^g_{CO_2,des}$ RD [%]	+5.6	+2.1	+1.8	-15.0	-6.3	-1.8	-11.2	-12.2	7.0
Lean CO_2 loading	Billet	[molCO$_2$/molMEA]	0.28	0.26	0.22	0.20	0.28	0.35	0.35	0.25	
		RD [%]	-8.4	-0.6	-0.5	-18.0	+1.0	+4.1	+12.6	-4.5	6.2
	Rocha	[molCO$_2$/molMEA]	0.28	0.26	0.21	0.20	0.28	0.35	0.35	0.26	
		RD [%]	-7.6	-2.1	-4.7	-18.0	+2.0	+3.5	+12.7	0.0	6.3
Rich CO_2 loading	Billet	[molCO$_2$/molMEA]	0.40	0.46	0.48	0.38	0.40	0.49	0.46	0.30	
		RD [%]	-4.9	+0.9	-1.7	-8.7	-2.4	-1.3	+4.4	-6.2	3.8
	Rocha	[molCO$_2$/molMEA]	0.41	0.46	0.48	0.38	0.40	0.49	0.46	0.31	
		RD [%]	-3.6	+1.5	-1.5	-8.1	-1.6	-1.0	+5.0	-2.5	3.1

The absorber temperature profiles show a very good agreement to pilot plant data for all simulated cases, and the predictions using the Billet and Rocha correlations are very similar. The temperature profile in the upper part of the absorber packing is slightly steeper using the Billet correlations compared to the Rocha correlations. This is probably caused by higher predicted mass transfer coefficients using Billet, causing increased mass transfer, reaction and generation of heat in this part of the packing. The temperature profile is consequently steeper, which is in agreement with the pilot plant observations. However, the difference between the correlations is very small and both correlations are considered adequate for prediction of absorber temperatures. The desorber temperature profiles differ slightly from pilot plant measurements, especially in cases 2, 3, 6 and 7; however, the predictions by Billet and Rocha correlations are quite similar. For the simulations presented in Paper E in Appendix C.5 where the Billet correlations were applied, the desorber effective interface area was corrected by a factor of 0.5. In this case the desorber temperatures gave a better fit to the experimental measurements, however, a very small interface area (0.12 - 0.17) was assumed in this case. This seems rather unrealistic, and there is therefore reason to believe that the overall mass transfer coefficient for desorber conditions is overpredicted (as mentioned in Section 4.5.1) and should have been adjusted instead. The net effect is however the same, and it is not expected to affect the dynamic responses at all. A fitting procedure to reduce the desorber mass transfer coefficients could therefore have been applied in order to improve the simulated desorber temperature profiles using both the Billet and Rocha correlations. Similar results would have been expected using both correlations.

A comparison of dynamic simulation results using the two sets of correlations for mass transfer and column hydraulics, is presented in Figures 4.22 and 4.23. The related pilot plant measurements are also included. The same fitting factor of the Billet interface area correlation of 2.25 is utilized, while the Rocha correlation is applied as is. Very similar dynamic behavior is observed, and it is observed that the main differences between the correlations seems to lie in stationary deviation.

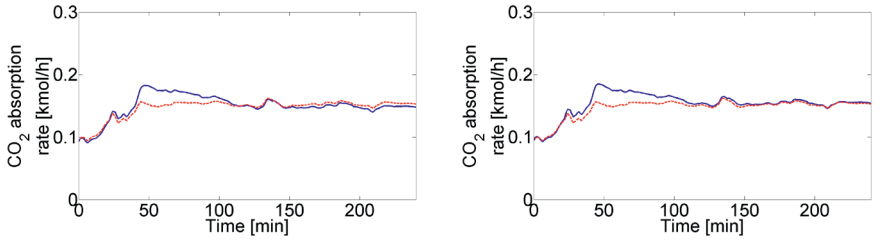

(A) Case 1: Billet correlations in the left figure, Rocha correlations to the right

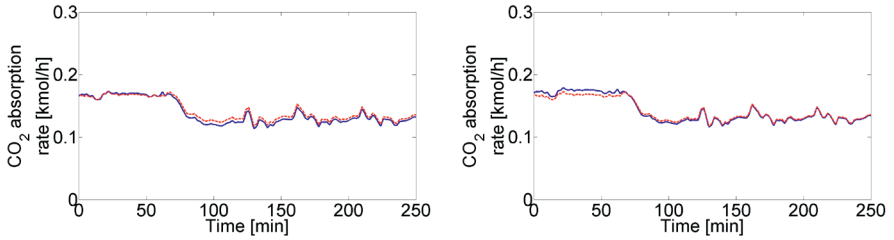

(B) Case 2: Billet correlations in the left figure, Rocha correlations to the right

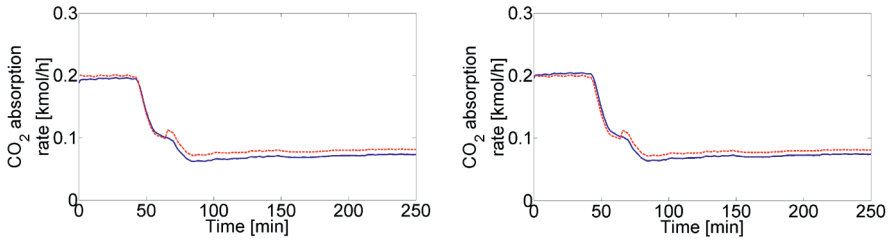

(C) Case 3: Billet correlations in the left figure, Rocha correlations to the right

FIGURE 4.22: Dynamic responses for CO_2 absorption in the Gløshaugen pilot plant. (—) Model, (---) Pilot plant. (Continues next page).

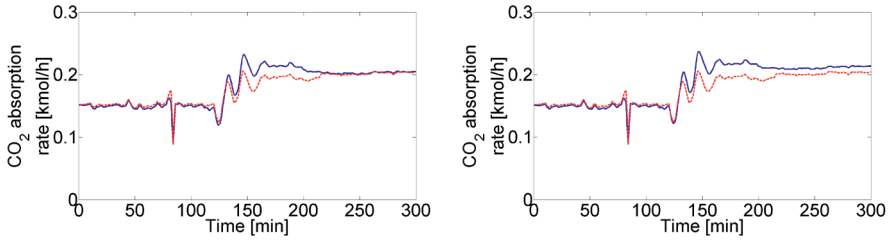

(D) Case 5: Billet correlations in the left figure, Rocha correlations to the right

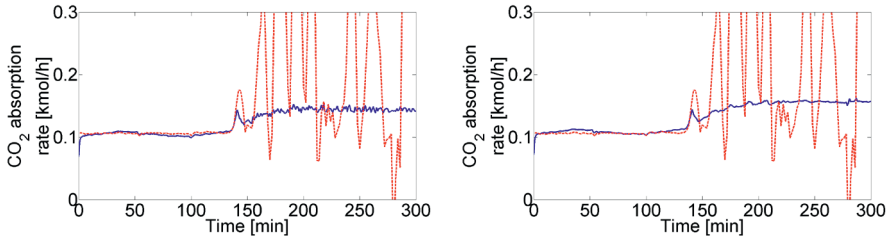

(E) Case 6: Billet correlations in the left figure, Rocha correlations to the right

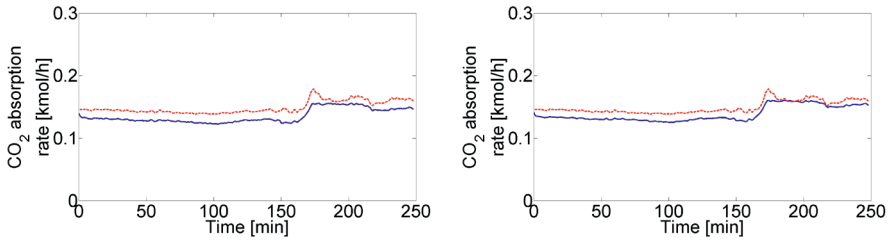

(F) Case 7: Billet correlations in the left figure, Rocha correlations to the right

FIGURE 4.22: Dynamic responses for CO_2 absorption in the Gløshaugen pilot plant. (—) Model, (---) Pilot plant. (continued from previous page).

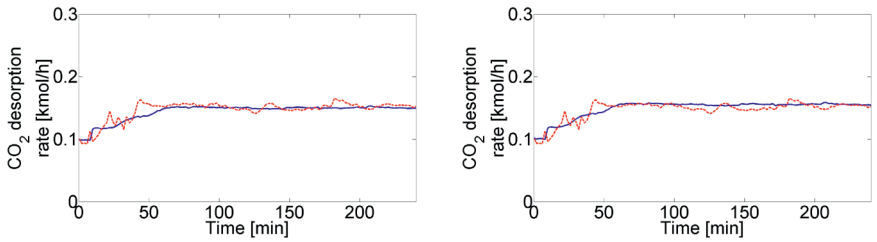

(A) Case 1: Billet correlations in the left figure, Rocha correlations to the right

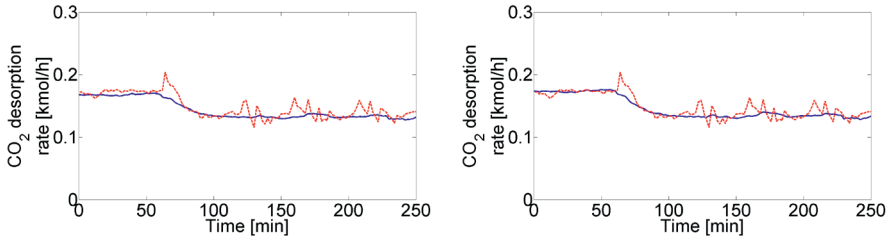

(B) Case 2: Billet correlations in the left figure, Rocha correlations to the right

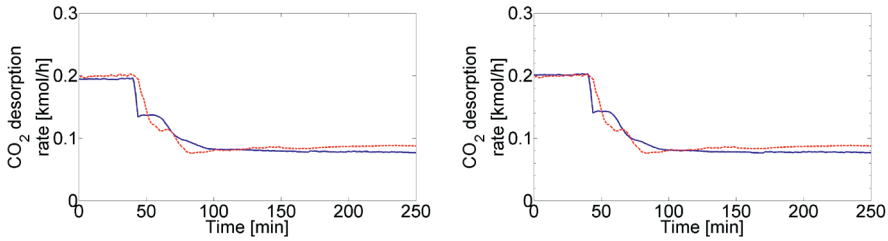

(C) Case 3: Billet correlations in the left figure, Rocha correlations to the right

FIGURE 4.23: Dynamic responses for CO_2 desorption in the Gløshaugen pilot plant. (—) Model, (---) Pilot plant. (Continues next page).

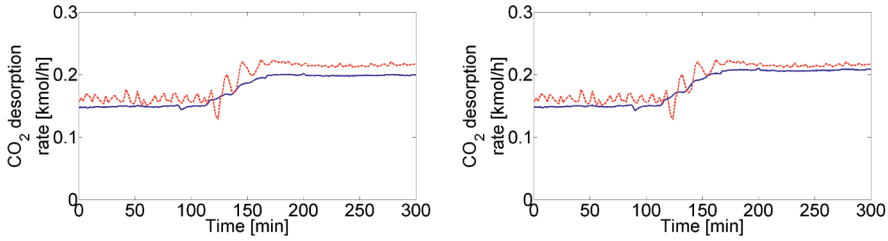

(D) Case 5: Billet correlations in the left figure, Rocha correlations to the right

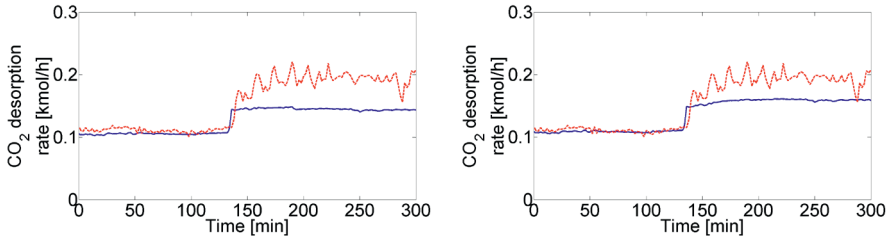

(E) Case 6: Billet correlations in the left figure, Rocha correlations to the right

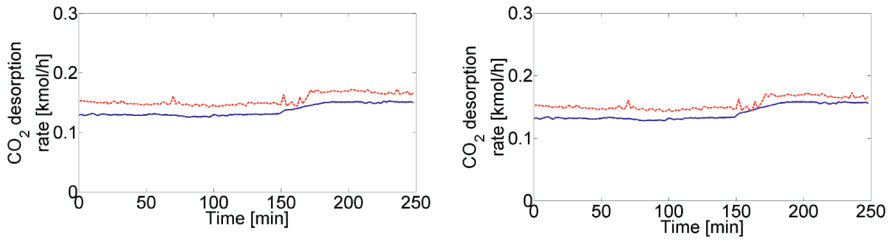

(F) Case 7: Billet correlations in the left figure, Rocha correlations to the right

FIGURE 4.23: Dynamic responses for CO_2 desorption in the Gløshaugen pilot plant. (—) Model, (---) Pilot plant. (continued from previous page).

4.7 Development of the K-Spice model

The CO_2 absorption process is also implemented in K-spice® general dynamic simulation tool as part of the *Octavius* project. K-spice is an advanced and flexible dynamic process simulator developed by Kongsberg Oil & Gas Technologies. It has mainly been used for modeling and simulation of oil and gas processes including natural gas treatment. The software uses an intuitive graphical user interface which allows the user to configure process models by drawing the process P&ID using a library of symbols representing process units. Each unit is configured according to the desired specification and connected to other units by flow lines. Specific StreamBoundary modules represent the system boundary feed points which have to be specified by the user. The library also contains necessary instrumentation and various process controllers.

Robust equation-solving and implicit integration methods are used to solve the resulting process system. The solution methods are based on the modular integration approach (described in Section 4.1) and uses a pressure-flow network solver to predict downstream pressures. Recirculation loops are handled by configuration algorithms. The execution order and integration step size can be specified by the user, and the simulation speed can be adjusted as desired with a maximum speed determined by the complexity of the overall process model and the selected integration step size.

Running the model is very intuitive by pressing a play button, and it can be paused or stopped anytime. While running the model it is possible to perform changes in the StreamBoundaries in order to simulate process disturbances or operational load changes, and/or changes in controller set-points in order to simulate internal operational changes.

4.7.1 Process equipment, instrumentation and control system

K-Spice has embedded a powerful library of process units such as mixing tanks, heat exchangers, absorption column sections as well as piping, pumps and valves. The library also contains basic instrumentation and control units.

Columns are modeled either as set of trays or packing sections. They are all equilibrium-based by default, but obtain a rate-based approach by applying an add-on reaction set module as will be described in Section 4.7.3. The stage calculation for both trays and packed sections are modeled as a flash operation, where the equilibrium between the phases at the interphase is calculated. The adjustable parameters to a stage are the rate of hold-up and gas and liquid flow and mixing rates into the interface flash calculation. A non-equilibrium stage can therefore be modeled by adjusting the parameters describing the flow into the flash.

The following correlations calculate the column pressure drop (ΔP) in [Pa] and solvent hold-up (ε_l) in [$\mathrm{m^3/m^3}$]:

$$\Delta P = C_2 \cdot 10^{C_3 u_\mathrm{l}} \rho_\mathrm{g} u_\mathrm{g}^2 h \tag{4.129}$$

$$\varepsilon_\mathrm{l} = B_\mathrm{p} \varepsilon_\mathrm{o} + \varepsilon_\mathrm{static} \tag{4.130}$$

where $\varepsilon_\mathrm{static}$ is the static hold-up set constant for each packing type and ε_o is the operating hold-up defined by:

$$\varepsilon_\mathrm{o} = 2.2 \left(\frac{\mu_\mathrm{l} u_\mathrm{l}}{g \rho_\mathrm{l} d_\mathrm{p}^2} \right)^{1/3} + 1.8 \left(\frac{u_\mathrm{l}^2}{g d_\mathrm{p}} \right) \tag{4.131}$$

u_g and u_l are gas and liquid superficial velocities in [m/s], ρ_g and ρ_l are gas and liquid densities in [$\mathrm{kg/m^3}$], μ_l is the liquid viscosity in [Pa/s], h is the height of the packing stage in [m], d_p is the nominal packing size in [m] and C_2, C_3 and B_p are constants provided for the packing at each stage.

4.7.2 Thermodynamic methods

Process simulations require thermodynamic methods for calculation of thermodynamic properties and phase equilibrium. In order to enhance calculation speed, K-Spice has an in-built thermopackage that interpolates thermodynamic data based on table look-ups. Thermodynamic tables are generated by MultiFlash™ provided by InfoChem ltd for the specific system in study. The thermodynamic tables are

only valid for physical equilibrium between gas and liquid phases, and are therefore not configured for chemical equilibrium with reactions. This is resolved by the introduction of the ChemAbsorption module which is described in the next section. Another limitation is that the tables are generated for a specific composition. However several tables can be used in the K-Spice model, tuned for specific conditions.

4.7.3 Chemical absorption module

K-Spice supports simulation of chemical absorption processes by using the ChemAbsorption module. The add-on reaction set in this module compensate for the chemical reactions which are not accounted for in the thermodynamic tables and acts as a secondary look-up table for the equilibrium. The chemistry of the absorption process must be configured separately within this module. A single gas component is configured with a single absorbent, and the module contains correlations that calculate mass transfer and interface mass fluxes with enhancement factor for chemical reaction. This corresponds to a rate-based approach for calculation of mass transfer. The ChemAbsorption module provides information about interface mass flux once it is connected to the individual packing sections in the absorber and desorber columns.

The mass transfer of a single gas component being absorbed is characterized by the following properties:

- VLE data
- Heat of reaction
- Gas and liquid phase mass transfer coefficients
- Enhancement factor

Information about these properties must be provided as tables in the ChemAbsorption module for various temperatures and absorbent loadings. Mass transfer coefficients and enhancement factor are also functions of gas and liquid column mass fluxes ($\bar{G}_\mathrm{g}$ and $\bar{G}_\mathrm{l}$ in $[\mathrm{kg\,m^2/s}]$). The abovementioned properties are calculated from the correlations given below:

$$k_{\mathrm{l}}a = tab_{k_{\mathrm{l}}a}(\alpha, T_{\mathrm{l}}) \cdot (a_0 + a_1 \bar{G}_{\mathrm{g}}^{a_2} \bar{G}_{\mathrm{l}}^{a_3}) \tag{4.132}$$

$$k_{\mathrm{g}}a = (b_0 + b_1 T_{\mathrm{l}}) \bar{G}_{\mathrm{g}}^{b_2} \bar{G}_{\mathrm{l}}^{b_3} \tag{4.133}$$

$$E = 1 + tab_E(\alpha, T_{\mathrm{l}}) \cdot \frac{c_0}{(c_1 + c_2 \bar{G}_{\mathrm{g}} + c_3 \bar{G}_{\mathrm{l}})} \tag{4.134}$$

tab are table values dependent on CO_2 loading and temperature, while a_0, a_1, a_2, a_3, b_0, b_1, b_2, b_3, c_0, c_1, c_2 and c_3 are correlation parameters.

4.7.4 Modeling the Brindisi pilot plant in K-Spice

A system of process units representing the Brindisi pilot plant is implemented in K-Spice, and each process unit is sized according to the Brindisi pilot plant dimensions. A control scheme corresponding to the control structure found in the Brindisi pilot plant is also applied. A screen shot of the graphical representation of the model is presented in Figure 4.24.

A set of packing sections interfaced with the ChemAbsorption module configured for 30 wt% MEA as solvent is used to model the absorber and stripper columns. The absorber and desorber water-wash sections are also implemented as packing sections, however, assuming equilibrium conditions. Drums are utilized to model absorber and desorber sump, reboiler, condenser and buffer tank. All vessels are given the correct dimensions according to the Brindisi pilot plant and provided with level controllers to ensure correct solvent hold-up. A pressure controller regulate the stripper pressure, and temperature controllers regulates the condener and lean cooler temperatures.

Tables for the VLE, heat of reaction, enhancement factor and gas and liquid mass transfer coefficients are generated from the MATLAB model and SINTEF's CO2SIM software. So are correlation constants required in Equations 4.129 -4.134. The chemical equilibrium and heat of reaction models are equivalent to the soft models implemented in MATLAB which is presented graphically in Figures 4.8 and 4.9, respectively.

A total of three thermodynamic tables were generated by Multiflash and imported in K-Spice. This includes separate tables for the solvent system tuned for both absorber and desorber conditions, along with a water/steam table for the reboiler.

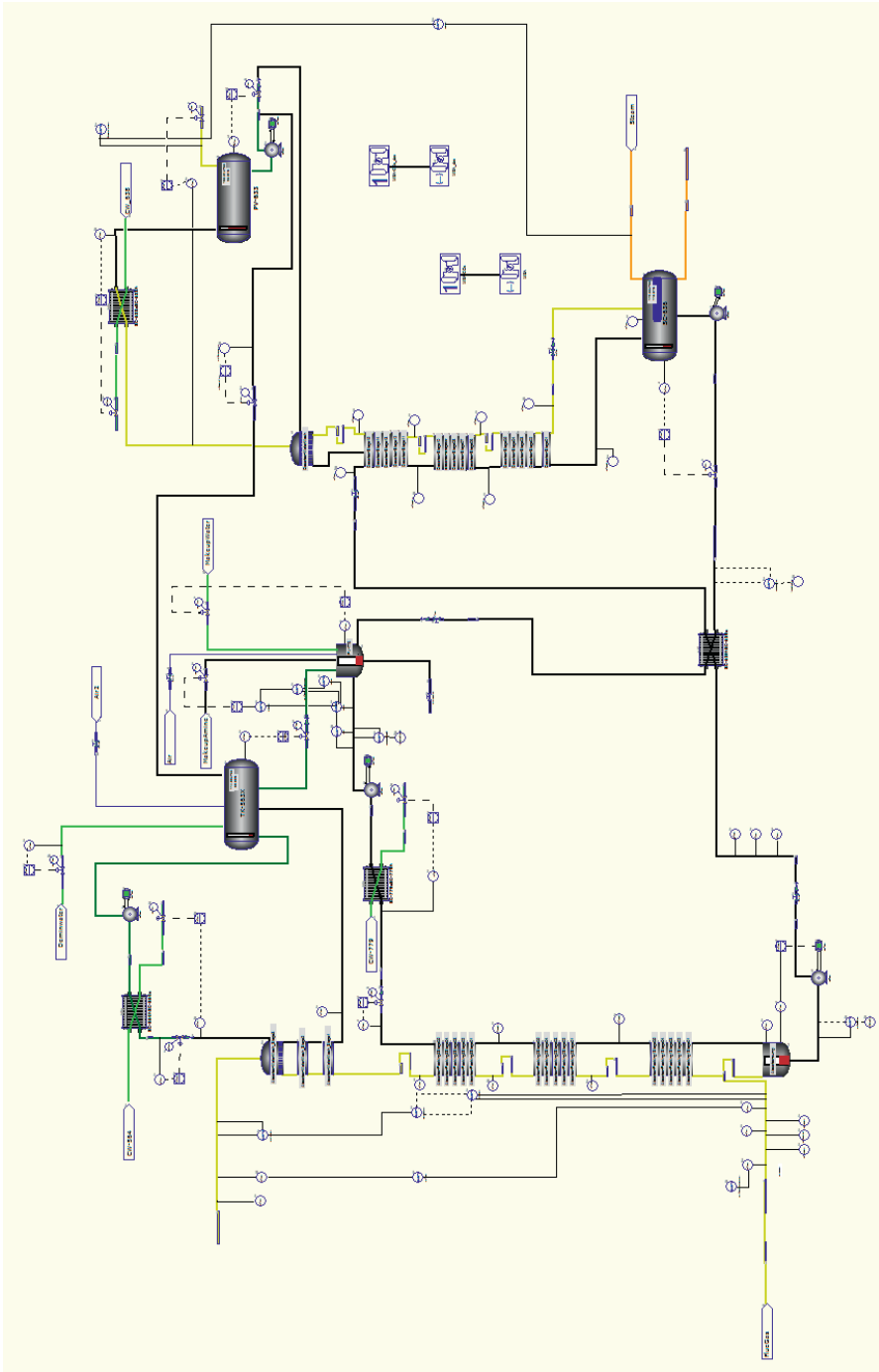

FIGURE 4.24: K-Spice model of the Brindisi pilot plant corresponding to process flow sheet in Figure 2.4.

Chapter 5

Model validation

Model validation is a key step in the model development procedure demonstrating the agreement between simulation results and experimental data of the system modeled. In order to ensure general validity of the model it is important to perform validation against data from several plants and preferably for a variety of process conditions and operational changes or process disturbances. Pilot plant data from several plants and various process conditions are therefore used to validate the process model in this work, both at steady state and dynamic mode.

Model validation is carried out by using certain logged data from pilot experiments as model input, comparing simulated process responses to the related logged pilot plant data. Model inputs are typically those indicated by red arrows and text in Figure 4.3, while the responses are process outputs indicated by blue arrows and text in Figure 4.3 along with any internal variable or calculated parameter that is logged during the experiments, such as column temperatures or CO_2 solvent loading. The relative deviation (RD) and average relative deviation (ARD) are used to evaluate the difference between simulation results and experimental values:

$$RD = \frac{y_{model} - y_{pilot}}{y_{pilot}} \tag{5.1}$$

$$ARD = \frac{1}{n}\sum_{i=1}^{n}|RD_i| \tag{5.2}$$

The process model is first validated at steady state mode to fit unknown parameters such as heat loss or unknown packing coefficients or perform other parameter

adjustments to improve the fit to experimental data. Afterward, dynamic model validation is carried out in order to ensure that the transient behavior of the model is reliable.

As dynamic pilot plant data available in the literature are very scarce, only a few models have been validated against dynamic data previously as indicated in the review summary in Table 4.1. Several models have however been validated using steady state pilot plant data or other simulation tools (Gáspár and Cormoş, 2011, Harun et al., 2011, Jayarathna et al., 2011, Kvamsdal et al., 2009, Lawal et al., 2010). However, it should be emphasized that data from specifically designed dynamic experiments with proper step changes in relevant operating parameters that enforce desired dynamic behavior should be used for model validation. Validation using only logged pilot plant data, where the pilot plant not necessarily is operated in a transient manner, will not give the same confidence in the developed model.

5.1 Validation of the MATLAB model

5.1.1 Gløshaugen pilot plant

The MATLAB model has been validated against the steady state and dynamic pilot plant data from the Gløshaugen pilot plant, that is presented in Table 3.1 and Figure 3.3. The following variables are used as model boundary condition inputs:

- absorber inlet gas conditions (flow rate, temperature and composition)
- lean solvent flow rate
- reboiler duty
- absorber outlet pressure
- condenser outlet pressure

The controllers indicated in Figure 4.4 are also specified with parameters and set-points from the pilot plant, and other input parameters like equipment sizes and packing parameters are given as input data. Simulation results using the

Billet mass transfer and column hydraulics models are presented in Paper E in Appendix C.5, while updated simulation results using both the Billet and Rocha correlations are compared in Section 4.6.

5.1.1.1 Steady state validation

The MATLAB model of the Gløshaugen pilot plant was first validated at steady state conditions to determine heat loss in the absorber and desorber columns and the reboiler, and to estimate the cross-heat exchanger heat transfer area. Heat loss from other units is neglected. The predicted effective interface area of the absorber packing using the Billet correlation was initially unrealistically low and had to be adjusted by a factor of 2.25 in order to meet the absorption rates observed at steady state in the pilot experiments. The Rocha correlations were able to predict reasonable absorption rates without any adjustments, as explained in Section 4.6. Thus, the model parameters that are fitted to the data are absorber, desorber and reboiler heat loss and cross-heat exchanger area, and additionally the absorber effective interface area when using the Billet correlation.

Steady state simulation results for CO_2 absorption/desorption rates and solvent CO_2 loadings are presented and compared to pilot plant observations in Table 4.6. Both correlations used in the simulations are able to predict satisfactorily steady state results, with ARDs for CO_2 absorption rates ($m^l_{CO_2}$) of 2.2% and 3.1% for the Billet and Rocha correlations, respectively. The deviations observed at steady state conditions are believed to be caused by uncertainties in the pilot plant measurements and uncertainties in modeled mass transfer coefficients and effective mass transfer area correlations. These parameters are compared for the two correlations used in the simulations in Figures 4.18 and 4.19, respectively, and a general trend of a higher predicted wetting factor and lower values for the overall mass transfer coefficients is observed for the Rocha correlation compared to the Billet correlation. The high mass transfer coefficients estimated by the Billet correlation are caused by higher predicted gas and liquid film mass transfer coefficients as seen in Figures 4.18b and 4.19b. These observations are in agreement with Razi et al. (2012), where it was observed that the Billet predictions in general are located in the lower range for effective packing surface area and solvent hold-up and in the upper range for mass transfer coefficients, compared to other correlations. Since all these factors contribute to the overall CO_2 absorption rate, the net effect on

absorption is similar for both correlations in the present study. However, as previously mentioned the effective interface area predicted by the Billet correlation was adjusted by a factor of 2.25 in order to meet the observed absorption rates, which means that the actual predicted effective interface area is even smaller for the Billet correlation. The uncorrected wetting factors were in the range of 0.24 - 0.32 using the Billet correlation. For the Rocha correlation a wetting factor in the range of 0.67 - 0.90 is predicted, which seems more realistic.

When comparing the temperature profiles in Figures 4.20 and 4.21, both correlations show similar results. The simulated absorber temperature profiles are in agreement with the experimental measurements for all cases, and the temperature bulge is well located. However, the desorber temperature profiles show somewhat larger deviations compared to the pilot plant measurements. A steeper simulated temperature profile in the lower part of the desorber is seen in cases 2, 3, 6 and 7, before the profile flattens out through the rest of the column. The reason for the deviation is believed to be related to an overestimation of the overall mass transfer rate, probably due to overprediction of gas and/or liquid film mass transfer coefficients for desorber conditions. Simulated desorption are therefore predicted to occur in a narrower area of the desorber column, more specifically in the bottom part, right after reboiler gas is fed to the column. According to the pilot measurements, the desorption occurs in a larger part of the packing, indicated by not so steep temperature profiles. It is therefore believed that gas and/or liquid mass transfer rates are overpredicted for desorber conditions, possibly due to elevated temperatures. In fact, the simulations performed in Paper E in Appendix C.5 showed a better fit for the desorber temperature profile, after adjustment of the effective interface area (and thereby the desorption rate) for the desorber packing by a factor of 0.5. This adjustment is at a later stage believed to be incorrect due to the unreasonable low resulting value for the effective interface area or wetting factor. However, a correction of the overall mass transfer coefficient would have given the exact same results, since the mass flux depends proportionally on both these parameters.

The inlet desober temperature is also deviating in some cases, and a steep decline in desorber temperature just after solvent inlet is seen in case 2, 3, 6 and 7. The reason for this deviation is believed to be caused by flashing on the rich side of the cross heat exchanger prior to the desorber inlet. The model assumes no phase change in the cross heat exchanger, thus the solvent enters the desorber column

as liquid phase only. However, flashing is commonly observed in the cross heat exchanger during pilot experiments, which means that part of the desorption is already occurring prior to the desorber column and the experimental temperature is therefore expected to be lower than the simulated temperature. Due to the model assumption of no flashing in the heat exchanger, the desorber inlet temperature predicted by the model is higher compared to pilot measurements and the flashing will consequently occur instantaneously when the solvent enters the desorber. This effect is especially evident in cases with high rich loadings, where heat exchanger flashing is likely to occur. This is in fact the case for steady state case 2, 3, 6 and 7, which according to Table 3.1 has high rich loadings. Similar trends has also been observed previously (Tobiesen et al., 2008).

5.1.1.2 Dynamic validation

The dynamic responses in CO_2 absorption and desorption rates using the Billet and Rocha correlations are presented Figure 4.22 and 4.23. The responses in CO_2 absorption shows a very good agreement to the pilot plant observations for both correlations used in the simulations. Some fluctuations are, however, observed in the experimental desorption rates which are not captured by the model. These are related to variations in desorber pressure, possibly caused by flashing in the cross heat exchanger. A comparison of the experimentally measured and simulated lean and rich CO_2 loadings are presented in Figure 5.1. The Rocha correlations are applied in this comparison.

The general agreement is considered adequate also for CO_2 loadings, however slightly larger deviations are observed for this process output. One reason for the deviations is possible variations in MEA concentration during the experiment, due to water vaporization. Make-up of MEA or water is not performed during the experiment, nor in the simulations; however, small temperature differences between the simulated and measured absorber outlet gas may cause deviations in gas water content and consequently deviations in the process water balance. Further it must be noted that comparing small numbers like CO_2 loadings might make possible deviations seem larger. This concerns lean CO_2 loadings in particular, and the effect is also reflected by the relative steady state deviations for lean CO_2 loading reported in Table 4.6. These deviations are relatively large in most cases, even

though the rich loadings and absorption rates seem reasonable. It is however concluded that the process model is able to describe the dynamic behavior for the cases that are simulated, regardless of the choice of correlations for mass transfer coefficients and column hydraulics.

As seen in Section 4.5.2, the equilibrium-stage approach was also utilized for steady state simulations of the Tiller pilot plant. Clear deviations in the local absorber temperature profiles were observed; however, the overall process performance was similar to that predicted by the more rigorous rate-based model. It is suggested in the literature that the equilibrium-stage model is sufficient for prediction of dynamic responses, as they are not expected to differ much from those predicted by the rate-based model. To check this statement, the dynamic simulations of the Gløshaugen pilot plant experiments are repeated using the equilibrium-stage approach. The results for CO_2 absorption and desorption rates are presented in Figure B.1 in Appendix B.1. When compared to the simulation results using the rate-based approach in Figures 4.22 and 4.23, the dynamic responses are in fact very similar and there is therefore reason to believe that the mass transfer rate does not contribute to dominating dynamic effects. However, it must be emphasized that the rate-based approach gives a far better representation of steady state absorber conditions as discussed in Section 4.5.2.

5.1.1.3 Verification of the control system

To verify the performance of the control system, simulated and experimental control variables and manipulated variables for case 2 and 5 are presented in Figure 5.2 and 5.3, respectively. The absorber sump and reboiler level is controlled at setpoint for both cases, and the simulation results are very similar to the observations both in terms of liquid level presented in the figures to the left, and actual control action presented in the figures to the right. The reboiler level control valve fluctuates quite a lot in the pilot plant, while it is more tightly controlled in the model. This is probably related to fluctuations in the measured reboiler pressure which are quite obvious in Figures 5.2e and 5.3e. The model predicts a more tight control of reboiler pressure, and the deviation is probably related to process delay in the measurement it self, delay in the control signal and/or delay in the control valve action, that is not included in the model. The modeled controller does therefore seem idealized compared to the real case.

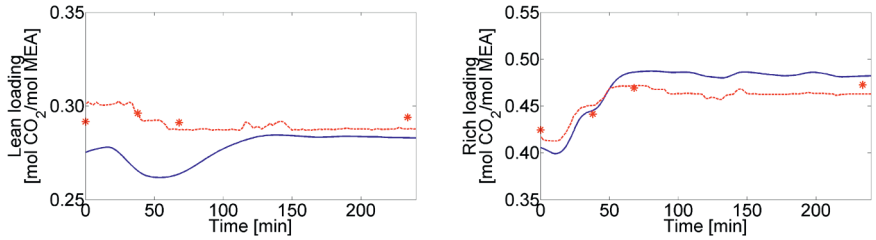

(A) Case 1: Lean loading to the left, rich to the right

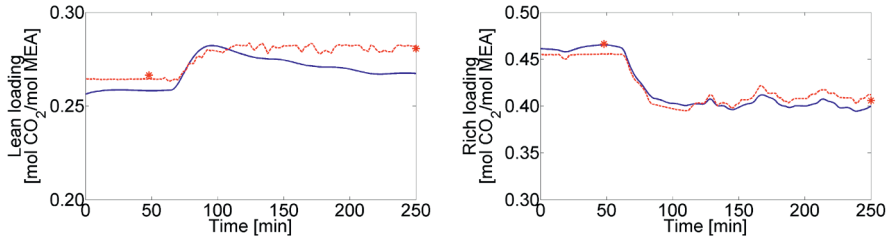

(B) Case 2: Lean loading to the left, rich to the right

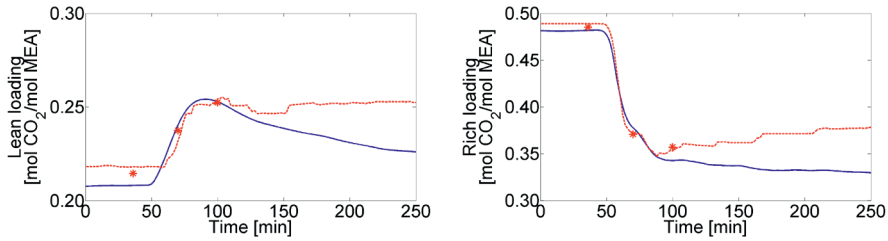

(C) Case 3: Lean loading to the left, rich to the right

FIGURE 5.1: Dynamic responses for lean and rich CO_2 loading in the Gløshaugen pilot plant. (—) Model, (---) Pilot (density), (✱) Pilot (analysis). (Continues next page).

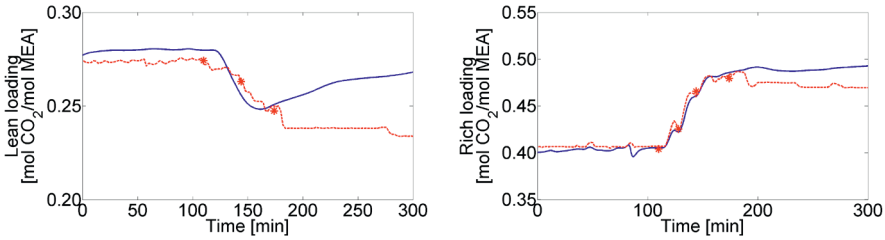

(D) Case 5: Lean loading to the left, rich to the right

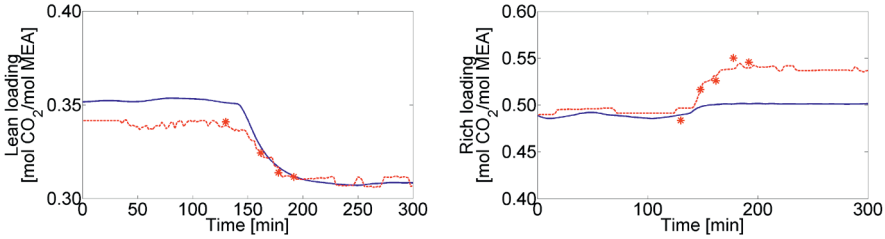

(E) Case 6: Lean loading to the left, rich to the right

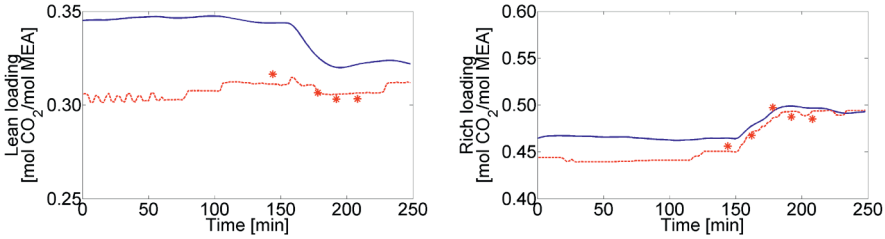

(F) Case 7: Lean loading to the left, rich to the right

FIGURE 5.1: Dynamic responses for lean and rich CO_2 loadings in the Gløshaugen pilot plant. (—) Model, (---) Pilot (density), (✱) Pilot (analysis). (continued from previous page).

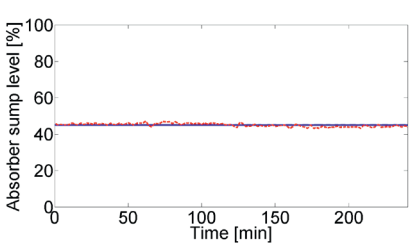

(A) Absorber sump level control variable

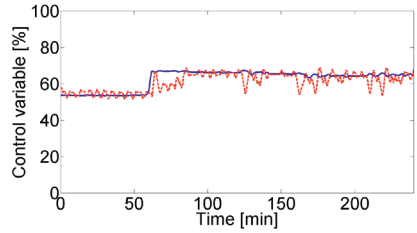

(B) Absorber sump level manipulated variable

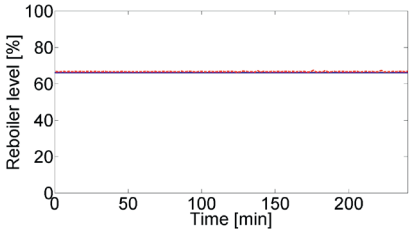

(C) Reboiler level control variable

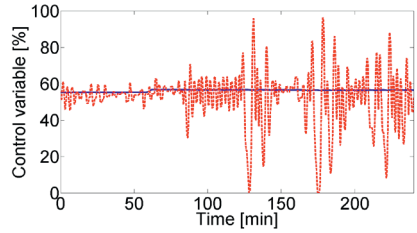

(D) Reboiler level manipulated variable

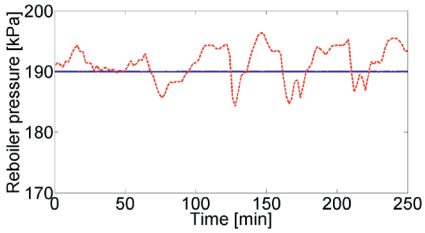

(E) Reboiler pressure control variable

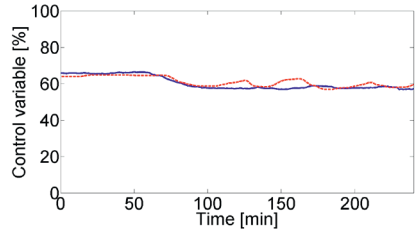

(F) Reboiler pressure manipulated variable

FIGURE 5.2: Dynamic results for the control variables and manipulated variables in the Gløshaugen pilot plant, case 2. (—) Model and (---) Pilot results.

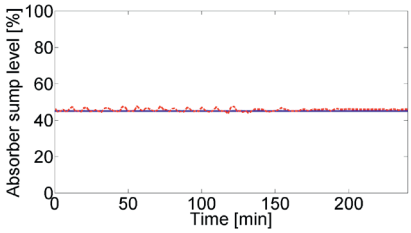

(A) Absorber sump level control variable

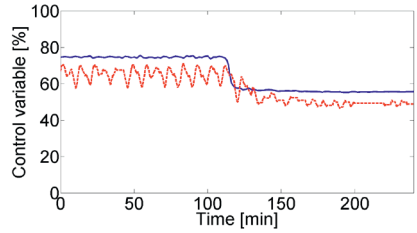

(B) Absorber sump level manipulated variable

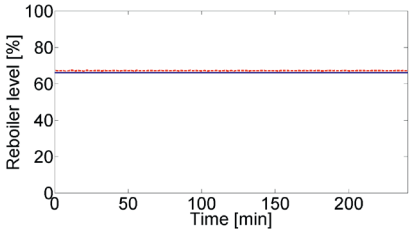

(C) Reboiler level control variable

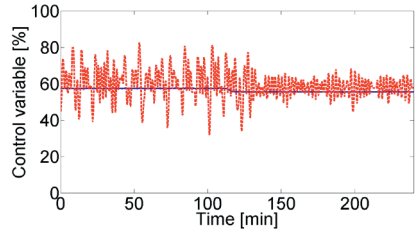

(D) Reboiler level manipulated variable

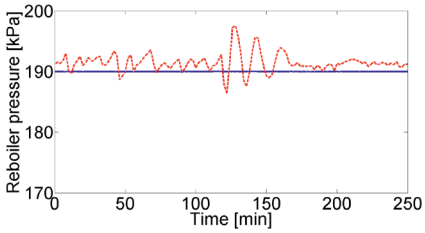

(E) Reboiler pressure control variable

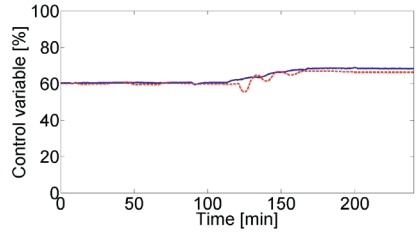

(F) Reboiler pressure manipulated variable

FIGURE 5.3: Dynamic results for the control variables and manipulated variables in the Gløshaugen pilot plant, case 5. (—) Model and (---) Pilot results.

5.1.2 Tiller pilot plant

The MATLAB model has also been validated against two sets of steady state data collected in the Tiller pilot plant. The first case (100612) represents a natural gas based flue gas with 3.9% CO_2, while the second (100718) represents a coal based flue gas with 10.9% CO_2, as described in Table 2.5. The following parameters are provided to the model as system boundary condition input data:

- absorber inlet gas conditions (flow rate, temperature and composition)
- lean solvent flow rate
- reboiler duty
- absorber outlet pressure
- condenser outlet pressure

The controllers indicated in Figure 4.5 are also specified with parameters and set-points from the pilot plant. Other input parameters like equipment sizes and packing parameters are also given as input data. The heat exchanger heat transfer area was adjusted to fit the outlet solvent temperatures, and heat loss was neglected. The simulation results are presented in Sections 4.5.2 and 4.5.1, using the equilibrium-stage approach and rate-based approach with enhancement factor, respectively. The Rocha correlations are applied in the rate-based approach. Thus, the only model parameter that is fitted to the pilot plant data in the rate based model is the heat-exchanger area. For the equilibrium-stage model, the total number of stages is also adjusted to pilot plant observations.

Similar results of total absorbed and desorbed CO_2 and solvent loadings are observed for the equilibrium-stage and rate-based approach. However. the rate-based model gives improved absorber temperature profiles as seen in Figures 4.16 and 4.17 compared to Figures 4.13 and 4.14, respectively. The choice of enhancement factor model, however, did not seem to affect the results significantly, and it was concluded that the assumption of $E = Ha$ is considered adequate for both the absorber and desorber columns.

The absorber temperature profile are well predicted using the rate-based approach, while the desorber profiles show larger deviations. Some general remarks can be

made regarding the desorber temperature profiles in Figures 4.13 and 4.14. Similar to the simulation results of the Gløshaugen pilot plant, the solvent temperature decreases sharply right after the desorber solvent inlet in both cases. This effect is not observed in the pilot experiments. Cross-heat exchanger flashing is commonly observed in pilot experiments, which means that part of the desorption is already occurring prior to the desorber column, while this effect is neglected in the model. The experimental temperature is therefore expected to be lower than the simulated temperature, and the model will predict instantaneous flashing of the solvent when entering the desorber, due to its condition. A second remark about the simulated desorber temperature profiles is that the desorption seems to occur in a narrower area of the column, as indicated by steeper temperature profiles compared to temperature measurements. This is especially evident in case 100718, and was also observed in the simulations of the Gløshaugen pilot plant. The modeled desorption is therefore predicted to occur in the bottom part of the desorber packing, right after reboiler gas is fed to the column, while the desorption in the pilot occurs in a larger part of the packing. It is therefore believed that gas and/or liquid mass transfer rates are overpredicted for desorber conditions, possibly due to elevated temperatures.

Dynamic data from the Tiller pilot plant are unfortunately not available for model validation. However, the two steady state cases simulated here has very different flue gas conditions (natural gas for case 100612 and coal for case 100718). The rate-based model assuming $E = Ha$ is able to predict absorption within a $\pm$ 5% deviation compared to pilot plant results for both cases, which gives high confidence in the model. The error in pilot plant CO_2 mass balance is also $\pm$ 5%, thus a better fit between model and pilot results cannot be expected.

5.1.3 TCM

The MATLAB model is finally validated towards data from the relatively large-scale CO_2 capture pilot plant at TCM. The steady state and dynamic input data are in this case given in Table 2.7 and Figures 2.8 and 2.9. The following parameters are provided to the model as system boundary condition input data:

- absorber inlet gas conditions (flow rate, temperature and composition)
- rich solvent flow rate
- reboiler duty
- absorber outlet pressure
- condenser outlet pressure

The controllers indicated in Figure 4.6 are also specified with parameters and set-points from the pilot plant, and other input parameters like equipment sizes and packing parameters are also given as input data. Both the Billet and the Rocha mass transfer and column hydraulic correlations are applied in the steady state simulations, while the Billet correlations are chosen for simulation of the dynamic cases.

5.1.3.1 Experimental data and measurement accuracy

The control system logs CO_2 concentrations of both the absorber inlet and outlet gas. However, the given data have some weaknesses because the measurements are not performed simultaneously due to lack of equipment. One single FTIR instrument is used to analyze absorber inlet gas, absorber outlet gas and desorber outlet gas concentrations. The analyzer is therefore cycled between all three sampling points as described in Section 2.2.4.1, and the last measured composition value for a given sampling point is displayed and logged in the plant control system when the analyzer is switched to the next sampling point. To illustrate the issue, typical absorber inlet and outlet CO_2 gas phase concentration measurements are shown in Figure 5.4 as functions of time.

The gas phase CO_2 concentration data are therefore not measured continuously which make them less suited for studying process dynamics. This can therefore

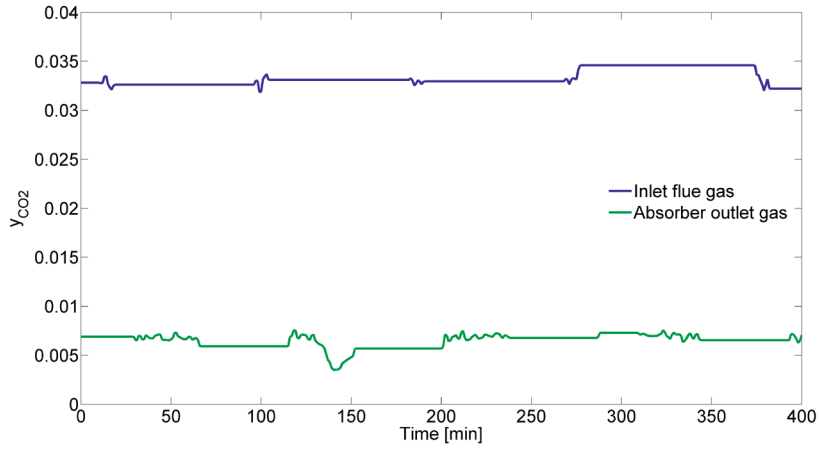

FIGURE 5.4: Typical time-dependent measurement of the gas phase CO_2 content in the TCM plant.

lead to inaccurate comparisons between the responses estimated by the model and the experimental data. Further it may also lead to inaccurate specification of the flue gas boundary condition, and resultingly simulation errors as this variable is used as input to the model. Lastly, since the inlet and outlet absorber gas concentrations are never measured simultaneously, the data are not considered a sufficient basis for estimation of absorption rate from the gas ($m^{g}_{CO_2,abs}$). The inlet CO_2 concentration keeps fairly stable around 3.5% during most of the periods, however, sudden disturbances might not be registered. The time periods where the absorber outlet gas concentrations are measured give therefore the best most reliable representation of $m^{g}_{CO_2,abs}$. However, the estimated desorption $m^{g}_{CO_2,des}$ is based on continuous measurements and is therefore used for validation instead.

The flue gas flow rate is measured by three different flow indicators. Based on experience the ultrasonic flow meter gives the most reliable measurements (Hamborg et al., 2014) and is therefore the selected flow measurement used as model input in the present model validation.

The MP-steam mass flow rate through the reboiler is provided in the dynamic data from TCM. The process model requires a reboiler heat duty input in [kW], thus the equivalent effect of the MP-steam flow rate must be calculated. The steam might be superheated, thus the total released heat in the reboiler is given by:

$$Q_{reb} = F_{steam}\left(\Delta h_{vap,\mathrm{H_2O}} + (T_{steam} - T_{b,\mathrm{H_2O}})C_{p,g,\mathrm{H_2O}}\right) \tag{5.3}$$

where $C_{\mathrm{p,g,H_2O}}$ is the steam heat capacity, $\Delta h_{vap,\mathrm{H_2O}}$ is the heat of vaporization and $T_{b,\mathrm{H_2O}}$ is boiling temperature of water at the given pressure.

5.1.3.2 Steady state validation

The eight different steady state operating points presented in Table 2.7 are simulated with the MATLAB model and compared to pilot plant results. Both the Billet and Rocha models for mass transfer and column hydraulics were applied in the simulations and the results are presented in Table 5.1. The heat exchanger heat transfer area was adjusted to fit the outlet solvent temperatures, and heat loss was neglected in this model. Again a very low wetting factor was observed using the Billet correlation, thus a factor of 2.5 was multiplied in the effective specific packing area for this correlation. The Rocha model was applied as is, without any adjustments. No other parameters are fitted to the data.

The simulated absorption/desorption rates are compared to experimentally estimated $m^l_{\mathrm{CO_2}}$ and $m^g_{\mathrm{CO_2},des}$ with average relative deviations of 4.6% using both the Billet and Rocha models. Both correlations give satisfactory steady state results compared to experimental measurements, and the agreement between model and pilot plant data is in general quite good since all cases show RDs within ±11% for the CO_2 absorption rates. The average relative deviation between simulated and measured rich CO_2 loadings are 5.5% and 4.4% for the Billet model and the Rocha model, respectively. The simulated lean CO_2 loadings, however, show a larger deviation with 16.8% and 12.0% for the Billet and Rocha models, respectively. However, as discussed previously, the relative deviations get larger when comparing small numbers.

As previously observed in the simulations of the Gløshaugen pilot plant, the two correlations predict similar liquid hold-ups, where the hold-up predictions by the Billet correlation are only slightly lower than for the Rocha correlations. The mass transfer rates are however predicted higher by the Billet correlations, and the effective interface area seems more realistic for the Rocha correlations. The net effect on mass transfer rates is however expected to be the same.

The simulated steady state absorber and desorber temperature profiles using the Billet correlation are presented and compared to experimental measurements in Figures 5.5 and 5.6. The absorber temperatures seem to be well predicted by the model in most cases. Some significant deviations are however observed in case 1, 2 and 5, where the simulated temperature bulge is located near the middle of the packing, while the temperature bulge observed in the pilot plant is located closer to the top of the absorber. Several factors may contribute to these deviations, but the main reason is assumed to be associated with errors in the predicted heat content in the gas and liquid phases. That might for instance be condensation/vaporization of water, which may affect the location of the temperature bulge significantly (Kvamsdal and Rochelle, 2008).

The desorber temperature profiles presented in Figure 5.6 show significant differences in simulated and experimentally measured values. The predictions in case 1, 2, 4 and 7 seem to correspond adequately given the scatter of measured temperatures. Similar trends as previously discussed for the Gløshaugen and Tiller pilot plants are observed, with sharp profiles both close to the top and bottom of the desorber, due to instantaneous solvent flashing in the top, and overpredicted mass transfer coefficients.

It should be noted that extensive foaming was experienced in the desorber section at TCM during parts of the campaign. Foaming resulted in steam channeling in the desorber, and the desorber temperature profile was therefore not clearly defined as observed in steady state cases 1 - 5 in Figure 5.6. As a consequence, an anti-foam solution was added to the solvent, which has a clear effect on desorber temperature profiles as seen for cases 6 - 8 in Figure 5.6. The anti-foam solution reduced the steam channeling behavior and the radial difference in desorber temperatures became less smaller.

TABLE 5.1: Steady state simulation results of the TCM pilot plant.

	Correlation		**1**	**2**	**3**	**4**	**5**	**6**	**7**	**8**	**ARD** [%]
Absorbed CO_2	Billet	[kg/h]	3471.4	2835.6	2662.5	2574.5	2797.1	2603.2	2531.5	3090.4	
		$m^l_{CO_2}$ RD [%]	+4.2	+1.2	-4.2	+9.1	+2.4	-2.8	-10.2	+3.1	4.6
		$m^g_{CO_2,des}$ RD [%]	+7.3	+2.6	+1.6	-4.7	+3.7	-3.5	-6.7	-6.6	4.6
	Rocha	[kg/h]	3463.5	2836.5	2641.5	2553.6	2830.5	2665.9	2517.9	3058.2	
		$m^l_{CO_2}$ RD [%]	+4.0	+1.2	-4.9	+8.2	+3.6	-0.4	-10.7	+2.0	4.6
		$m^g_{CO_2,des}$ RD [%]	+7.0	+2.6	+0.8	-5.5	+4.9	-1.2	-7.2	-7.5	4.6
Lean CO_2 loading	Billet	[molCO$_2$/molMEA]	0.12	0.11	0.28	0.33	0.13	0.22	0.34	0.30	
		RD [%]	-24.5	-26.2	+10.2	+1.6	-33.2	+15.4	+8.7	+14.9	16.8
	Rocha	[molCO$_2$/molMEA]	0.12	0.12	0.26	0.32	0.13	0.20	0.33	0.28	
		RD [%]	-21.3	-22.1	+2.8	-1.9	-28.9	+5.3	+5.8	+8.0	12.0
Rich CO_2 loading	Billet	[molCO$_2$/molMEA]	0.41	0.41	0.49	0.47	0.43	0.50	0.48	0.49	
		RD [%]	-6.6	-8.5	+0.4	+1.5	-12.0	+4.0	+2.4	+8.4	5.5
	Rocha	[molCO$_2$/molMEA]	0.42	0.42	0.47	0.46	0.43	0.49	0.47	0.48	
		RD [%]	-5.7	-7.3	-2.9	-1.1	-10.5	+1.9	+0.2	+5.8	4.4

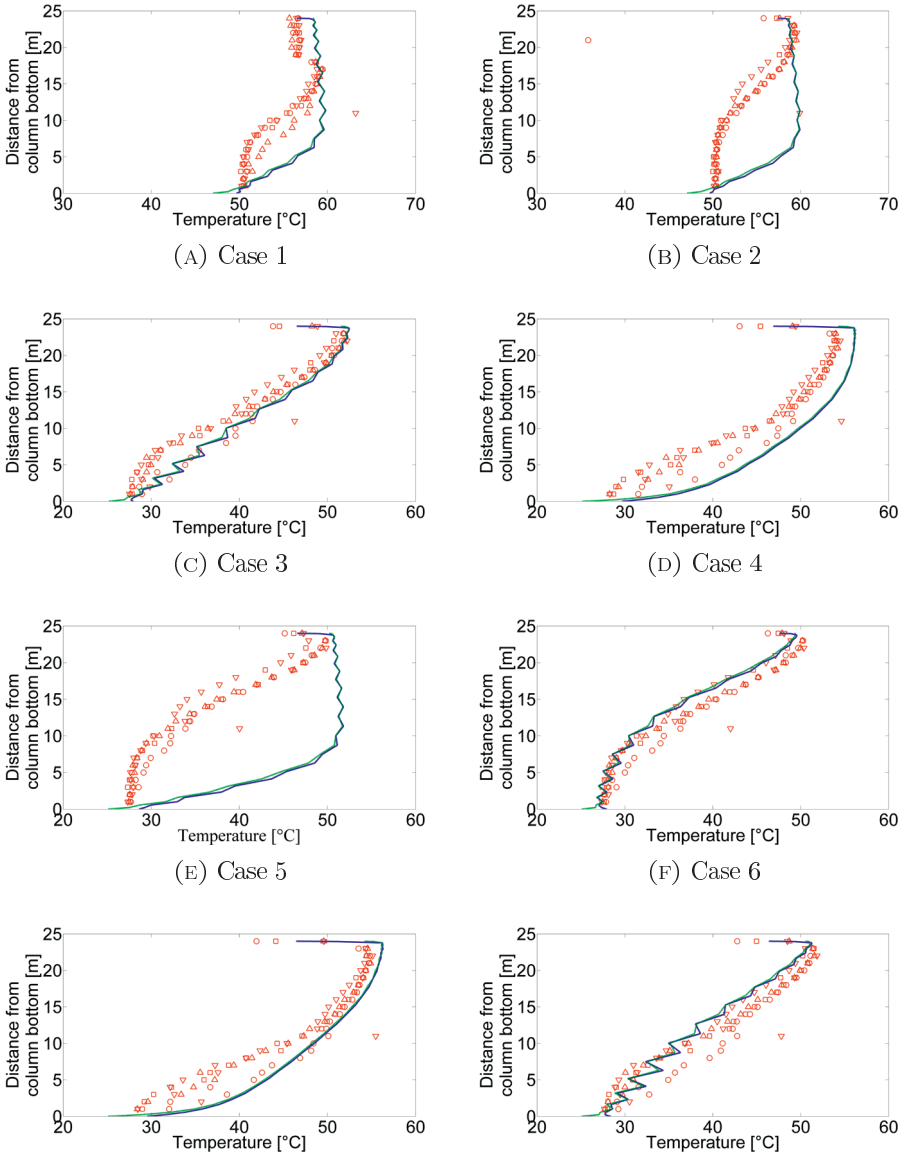

(A) Case 1 (B) Case 2

(C) Case 3 (D) Case 4

(E) Case 5 (F) Case 6

(G) Case 7 (H) Case 8

FIGURE 5.5: Steady state absorber temperature profiles in the TCM plant. (—) Model (solvent), (---) Model (gas), (□ ▽ △ ○) Pilot plant.

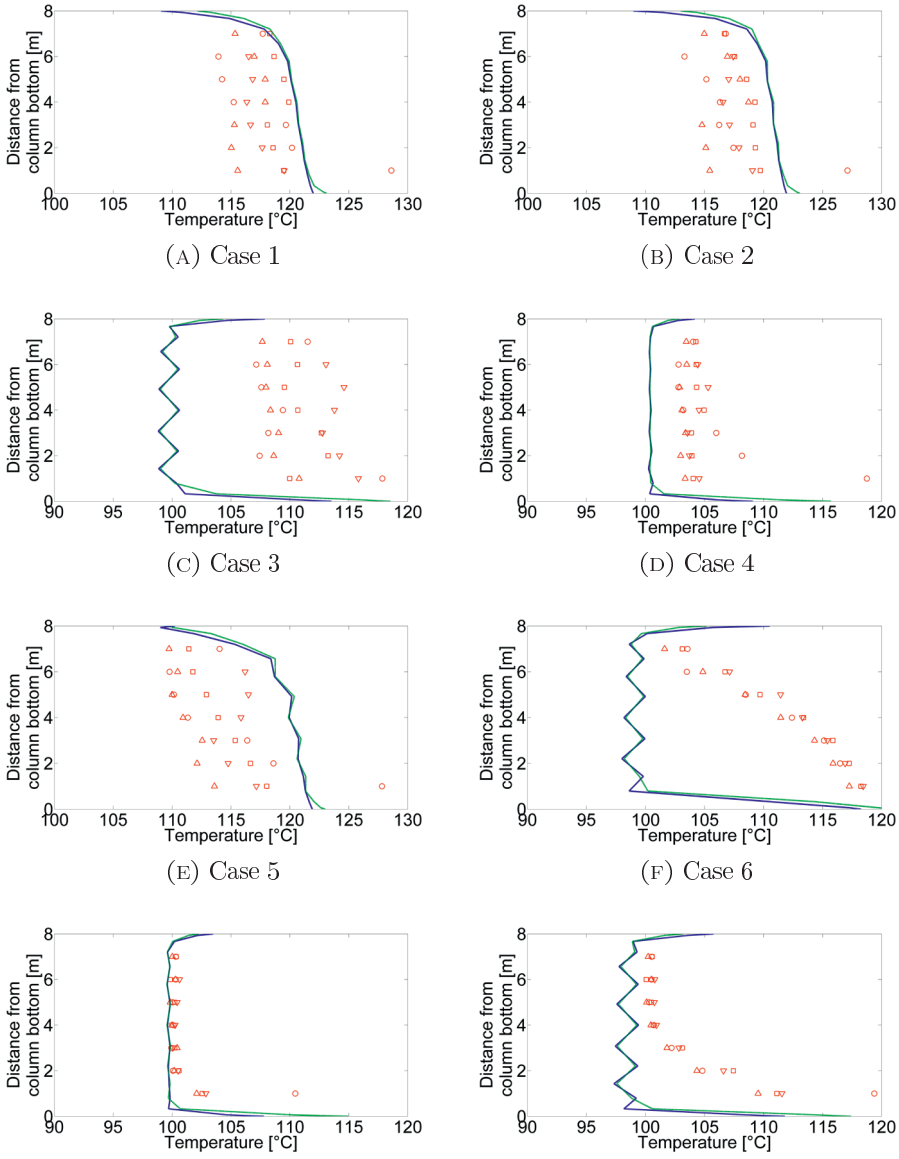

(A) Case 1 (B) Case 2

(C) Case 3 (D) Case 4

(E) Case 5 (F) Case 6

(G) Case 7 (H) Case 8

FIGURE 5.6: Steady state desorber temperature profiles in the TCM plant. (—) Model (solvent), (---) Model (gas), (□ ▽ △ ○) Pilot plant.

5.1.3.3 Dynamic validation

The four different dynamic cases presented in Figures 2.8 and 2.9 are used as model inputs for dynamic simulations of the TCM pilot plant. The resulting simulated responses are compared to logged pilot plant data for the same periods, and the results are presented in Figure 5.7 - 5.9.

The rich solvent flow rate is changed according to the green graph in Figure 5.7. This variable is used as input in the model, and the response in lean solvent flow rate is compared to pilot plant measurements in the same figure, indicated by the blue solid and red dashed line respectively. The simulated and measured lean flow rates have the same magnitude which indicates that the process configuration is correctly implemented in MATLAB and the transient behavior shows good agreement which indicates that the different solvent hold-up and level controllers in the process units are correctly implemented. A small deviation is seen in the dead time for the response in lean solvent flow rate especially in cases 2 and 4, were the modeled response is faster than what is observed in the pilot plant data. This might relate to possible lag in data logging (data updates in the control system) or it may be caused by time delays in the controller or valve actions. However the agreement is better for cases 1 and 3. The process time constants are also very similar for all cases.

The simulated absorption and desorption rates are presented in Figure 5.8 and compared to pilot plant estimations. As previously mentioned, the estimated experimental desorption rate is a better basis for dynamic validation than the absorption rate, since the latter is not based on continuous measurements. However, the inlet absorber CO_2 concentration is more or less stable during the experiments, thus the estimated absorption rates for the short periods where the absorber outlet gas concentration is measured gives an indication about the absorber performance. The model gives very similar transient responses for desorbed CO_2 to those estimated by the pilot plant data. The transient response in the absorbed CO_2 is also similar, even though the discontinuous pilot plant measurement make this a less suited basis for comparison. Some stationary deviations are however seen in some cases for both adsorption and desorption rates, as was also observed in the validation at steady state conditions.

The resulting lean and rich CO_2 loadings are compared to pilot plant results in Figure 5.9. As seen in these figures, the solvent samples are very scarce as they are

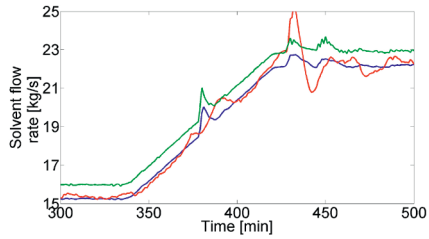

(A) Case 1: Increase in solvent flow rate

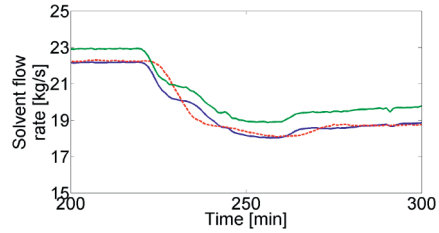

(B) Case 2: Increase in flue gas flow rate and decrease in solvent flow rate

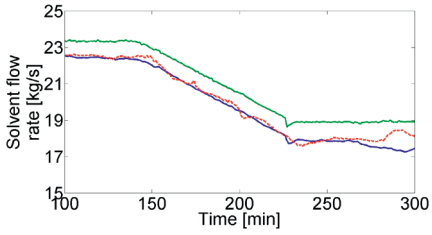

(C) Case 3: Increase in MEA concentration and decrease in solvent flow rate

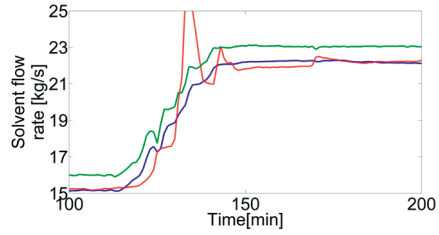

(D) Case 4: Increase in solvent flow rate with 40 wt% MEA

FIGURE 5.7: Dynamic responses for lean solvent flow rate after set-point change in rich solvent flow rate for the TCM plant. (—) rich solvent flow rate, (—) lean solvent flow rate (pilot) and (—) lean solvent flow rate (model).

only withdrawn at steady state conditions in order to generate operating points in energy performance U-curves. The measured and logged solvent densities and related solvent temperatures are however used to correlate the lean and rich CO_2 loadings assuming constant wt% MEA. The density correlation described by Cheng et al. (1996) in Section 4.3.5.1 is used for this purpose. For case 3 where the MEA-concentration is increased it is not possible to predict the CO_2 loading from densities as the experimental transient MEA concentration is unknown. However, the agreement between simulated and estimated CO_2 loadings based on logged solvent densities and temperatures are much better compared to the CO_2 loadings calculated based on analysis of the solvent samples. Due to very good experience with experimental loading/density correlation in previous experiments in the Gløshaugen pilot plant and the good agreement between experimentally correlated loadings and simulations for the TCM data in the present study, it is suggested that there might be significant uncertainties in the solvent sampling or analysis. The steady state validation results for CO_2 loadings might therefore be improved to what is indicated in Table 5.1.

The MEA concentration is increased from about 30 to 40 wt% by adding MEA

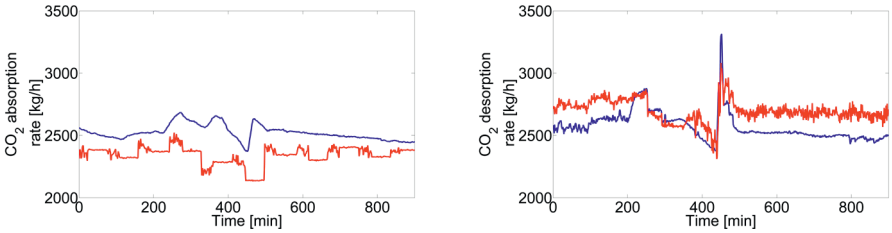

(A) Case 1: Increase in solvent flow rate

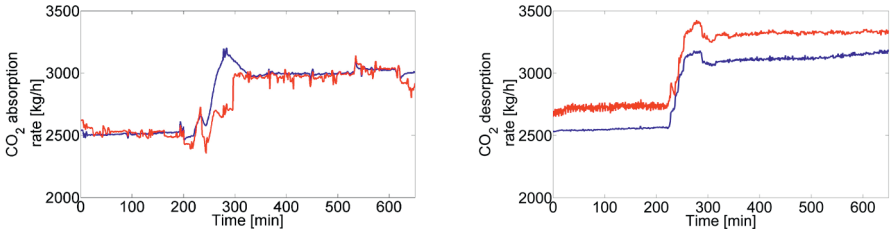

(B) Case 2: Increase in flue gas flow rate and decrease in solvent flow rate

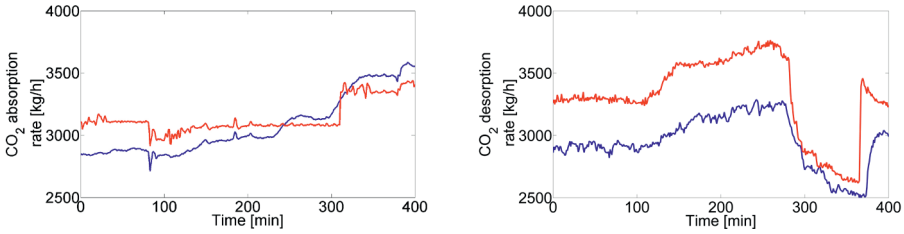

(C) Case 3: Increase in MEA concentration and decrease in solvent flow rate

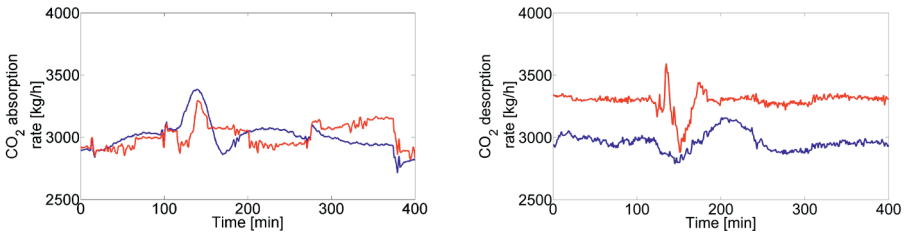

(D) Case 4: Increase in solvent flow rate with 40 wt% MEA

FIGURE 5.8: Dynamic responses for CO_2 absorption and desorption in the TCM plant. (—) Model, (—) Pilot results.

make-up in case 3, as illustrated in Figure 2.9b. Case 4 is operated with 40 wt% MEA. The simulation results in these cases will therefore indicate how the model is able to perform at different MEA concentrations. It should be noted that most of the chemical and physical property correlations are valid for various MEA concentrations (for instance solvent density), however, some are only developed

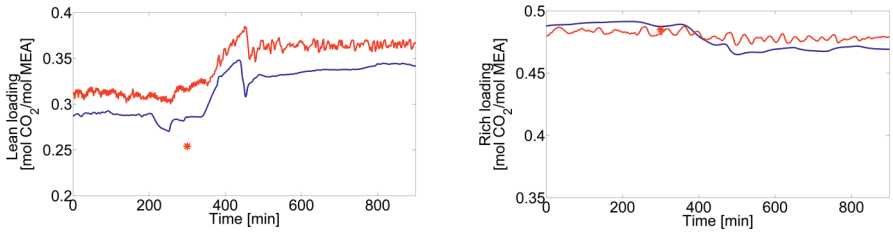

(A) Case 1: Increase in solvent flow rate

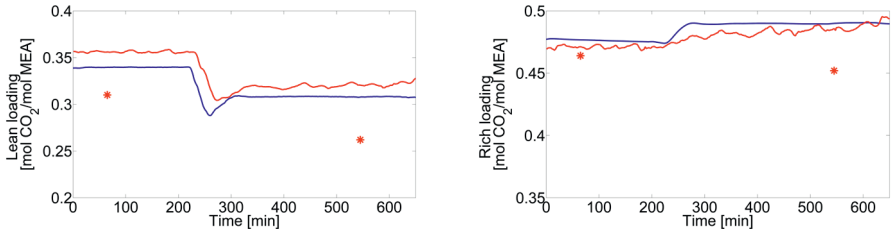

(B) Case 2: Increase in flue gas flow rate and decrease in solvent flow rate

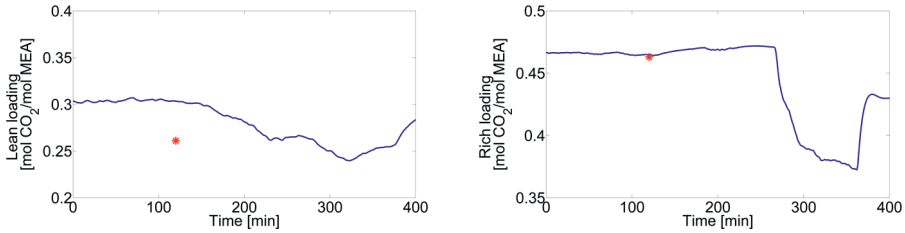

(C) Case 3: Increase in MEA concentration and decrease in solvent flow rate

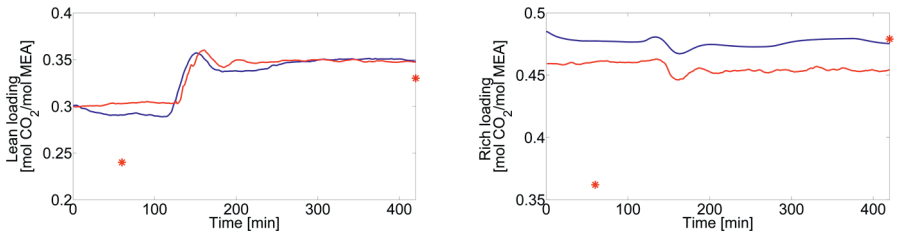

(D) Case 4: Increase in solvent flow rate with 40 wt% MEA

FIGURE 5.9: Dynamic responses for lean and rich CO_2 loadings in the TCM plant. (–) Model, (–) Pilot results (density) and (*) Pilot (analysis).

for 30 wt% MEA, which is regarded as the baseline. This concerns for instance the VLE soft model described in Section 4.3.5.5.

5.2 Validation of the K-Spice model

The K-spice model is validated using data collected from the Brindisi pilot plant as part of the *Octavius* project. The results are presented in Paper D in Appendix C.4. A summary is given here, and for additional results the reader is referred to the published paper.

The data presented in Figure 2.5 are used as input for the three simulated dynamic cases in this validation study. This includes flue gas flow rate, lean solvent flow rate and steam flow rate to the reboiler. Additionally flue gas temperature and composition is also given as model input, but these variables remained more or less constant. As mentioned in Section 2.2.2, it is believed that the desorption rate ($m^{\mathrm{g}}_{\mathrm{CO_2,des}}$) forms the best foundation for model validation, as $m^{\mathrm{l}}_{\mathrm{CO_2}}$ cannot be estimated and $m^{\mathrm{g}}_{\mathrm{CO_2,abs}}$ is uncertain. The simulated desorption rate is compared to $m^{\mathrm{g}}_{\mathrm{CO_2,des}}$ in Figure 5.10. The model follows the transient behavior observed in the pilot plant fairly well. However, some stationary deviations are observed. The model predicts in general a slightly lower desorption rate than what is observed in the pilot experiments.

The simulated desorption rate is compared to $m^{\mathrm{g}}_{\mathrm{CO_2,des}}$ in Figure 5.10. Simulation results of lean and rich loadings and CO_2 capture rate are presented and compared to pilot plant observations in Figures 5.11 and 5.12. The model follows the transient behavior for observed desorption rate in the pilot plant fairly well. However, some stationary deviations are observed, likely to be caused by pilot plant measurements uncertainties or uncertainties in mass transfer correlations. The model predicts in general a slightly lower desorption rate than what is observed in the pilot experiments. The step changes in solvent flow rate and flue gas flow rate in case 2 and 3 does hardly not affect the desorption rate at all, most likely because the solvent has already reached its capacity and obtained maximum rich loading as seen in Figures 5.11b and 5.11c. However, the CO_2 capture rate is increasing as the flue gas flow rate and solvent flow rate are decreased as seen in Figures 5.12b and 5.12c, and the agreement to pilot plant observations of CO_2 capture rate is very good, especially for case 3.

The model seems to overpredict both the lean and rich loading slightly. However, it can be seen that the model predicts a similar transient behavior to what is observed in the pilot plant.

It is concluded that the model shows good transient agreement to the experimental results, and the model is therefore able to capture the main process dynamics. An offset is observed in some cases, especially during the initial simulation time. This is most likely caused by the fact that the model was given a steady state starting point, while the pilot plant was not necessarily completely at steady state when the step change was introduced.

It is emphasized that providing a reasonable starting point for the model before a step change is simulated may be challenging. If actual initial state conditions (given by pilot data) cannot be loaded to initialize the model, the best way is to run the model until steady state conditions and start the dynamic simulation with the calculated states at stable conditions. However, it is challenging to ensure steady state conditions prior to dynamic tests in a pilot plant due to flue gas disturbances in composition, flow rate and temperature, reboiler duty or steam quality and flow rate disturbances or other external disturbances that are not measured. This is highly relevant for processes attached to a real power production unit, such as the Brindisi pilot plant, or other upstream industrial processes. Even when the pilot plant seems to be stable it might still not be at steady state due to slow transients in solvent dynamics which takes hours to adjust. These effects are more significant for larger relative solvent hold-ups, where the overall solvent retention time is higher. The solvent retention time might be about 2-3 hours depending on the individual configuration, and as previously mentioned the actual stabilization time might be even longer due to recirculation of the solvent. CO_2 loadings and other solvent variables will therefore adjust very slowly compared to absorber outlet gas parameters such as temperature and composition, and the pilot plant might therefore not be at steady state even when parameters seem stable.

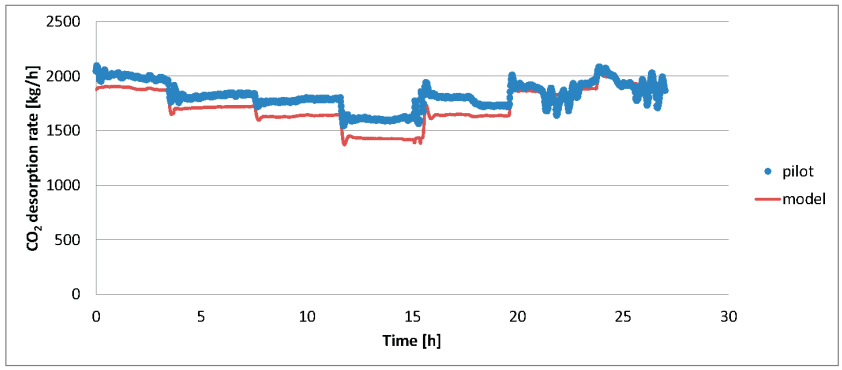

(A) Dynamic case1: Set-point changes in steam flow rate

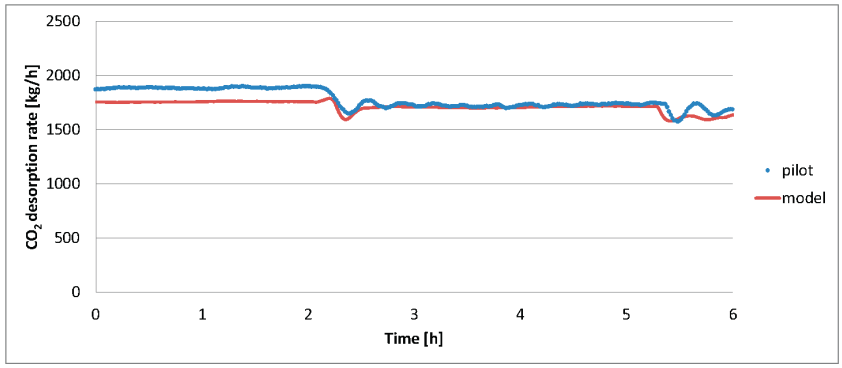

(B) Dynamic case 2: Set-point change in lean solvent flow rate

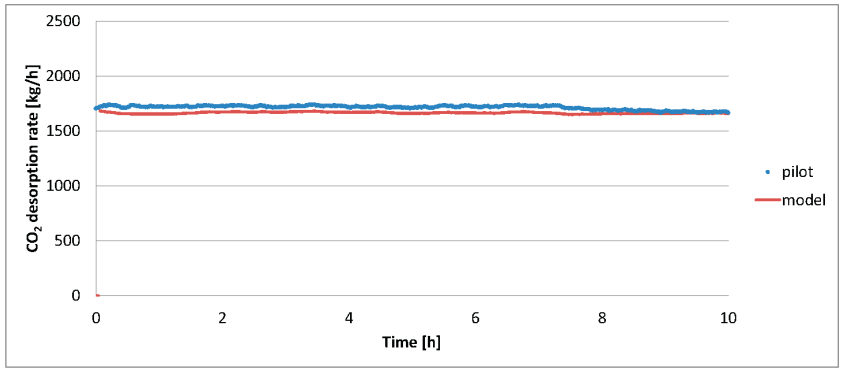

(C) Dynamic case 3: Set-point changes in flue gas flow rate

FIGURE 5.10: Dynamic responses for CO_2 desorption in the Brindisi pilot plant.

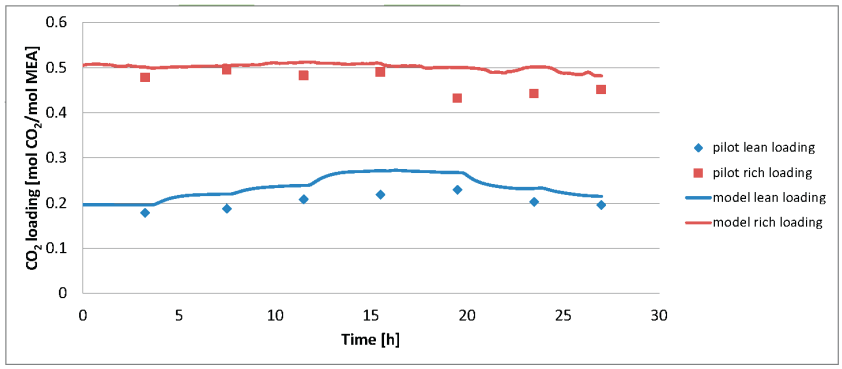

(A) Dynamic case1: Set-point changes in steam flow rate

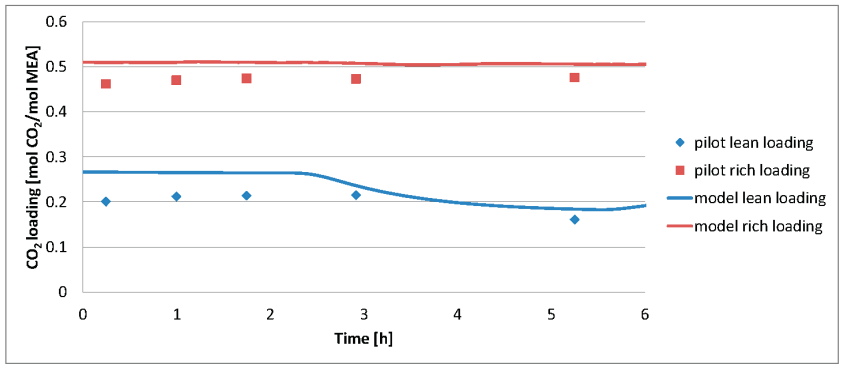

(B) Dynamic case 2: Set-point change in lean solvent flow rate

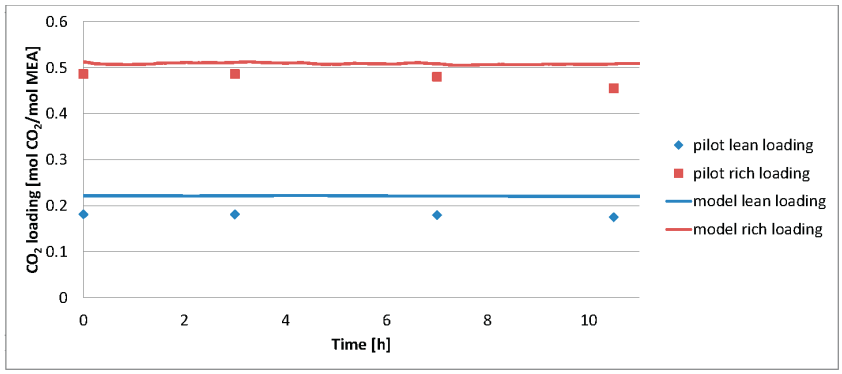

(C) Dynamic case 3: Set-point changes in flue gas flow rate

FIGURE 5.11: Dynamic responses for lean and rich CO_2 loading in the Brindisi pilot plant.

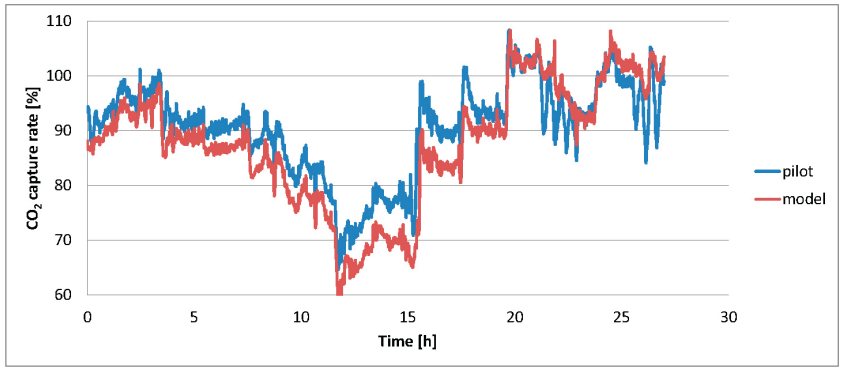

(A) Dynamic case1: Set-point changes in steam flow rate

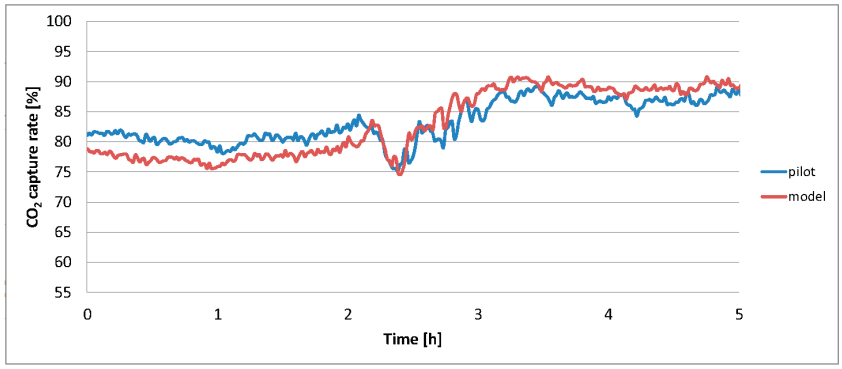

(B) Dynamic case 2: Set-point change in lean solvent flow rate

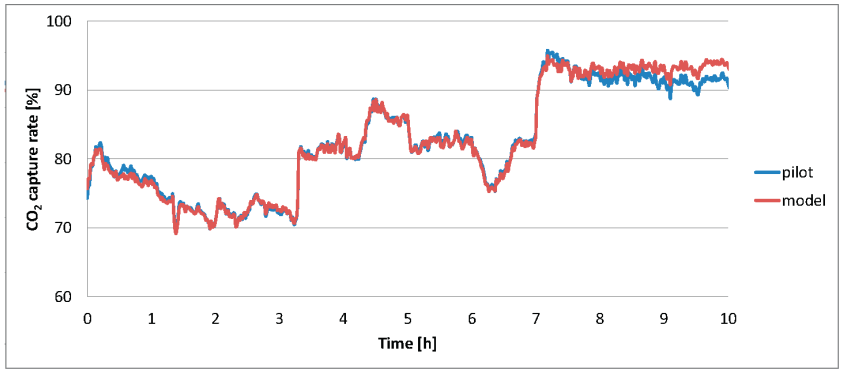

(C) Dynamic case 3: Set-point changes in flue gas flow rate

FIGURE 5.12: Dynamic responses for CO_2 capture rate in the Brindisi pilot plant.

5.3 General remarks

It is important to note that the process model is only validated for the specific pilot plant in study, thus it must be compared to several plants and various conditions in order to ensure general validity. The MATLAB model is here validated using data from three quite different pilot plants and conditions. The model is able to describe the dynamic behavior of both the small-scale Gløshaugen pilot plant and relatively large-scale TCM pilot plant. It is therefore believed that the developed set of unit model equations may be applied in a general manner to other systems, provided correct equipment sizing and parameters. However, the empirical parameter correlations used in the model are limited to their specific range of development, thus care must be taken when applying such correlations for other processes, systems or for new operating conditions without verification to experimental data.

It is also important to consider measurement accuracy and to know which measurements to trust and which are less reliable when analyzing an experimental data set. If the model is fitted to misleading measurements it may not predict reliable responses. For the Gløshaugen pilot plant, three different methods for estimating experimental CO_2 absorption rates were used (Equations 3.4 - 3.8) and the mass balance calculations in Table 3.1 indicated that the two first methods ($m^{g}_{CO_2,abs}$ and $m^{l}_{CO_2}$) were most reliable based on their satisfactory agreement for all cases. The simulated CO_2 absorption rates for the same cases are presented in Table 4.6, and the ARD calculations indicate a better agreement to pilot plant $m^{g}_{CO_2,abs}$ and $m^{l}_{CO_2}$ than to $m^{g}_{CO_2,des}$. The deviation between simulated and observed $m^{g}_{CO_2,abs}$ and $m^{l}_{CO_2}$ are in fact 3.6% and 3.1% using the Rocha calculation, while it is 7.0% for $m^{g}_{CO_2,des}$. For the Brindisi pilot plant, however, $m^{g}_{CO_2,des}$ is considered the most reliable method.

Further, it is emphasized that the nature of the process design with solvent recirculated in a closed loop makes modeling and validation of the CO_2 absorption process challenging. Any error or inaccuracy in the desorption section of the model may affect the performance of the modeled absorption section, and vice versa. Errors might therefore easily evolve and propagate through the system. One should therefore take care ensuring that each section of the model is able to estimate reasonable results and act as a realistic boundary to the connecting units.

Chapter 6

Model application

6.1 Investigation of the dominating process dynamics

An investigation of the dominating process dynamics of the CO_2 capture plants is presented in Paper F in Appendix C.6. The MATLAB model of the Tiller pilot plant is used in the study where dynamic responses after set-point changes in flue gas flow rate, reboiler duty and solvent flow rate are compared to detect stabilization time at various locations in the process. These measures are further used to determine the main inertia of the process and various process units are categorized according to their effect on and contribution to the overall dynamic progress. The design of the Tiller pilot plant resembles full-scale design with full column height, and similar gas velocities (m/s) and solvent loads ($m^3\,m^2/s$), such that scale up of column diameters, vessel sizes and gas and liquid flow rates will give comparable residence times. It is therefore believed that the reported dead times and time constants also will reflect the dynamics of an industrial plant.

The stabilization time of output dynamic responses ($y(t)$) is characterized by the dead time (θ) and time constant (t) when a change in process input ($u(t)$) is introduced to the system. The dead time describes how long time it takes before a process begins to respond when a disturbance is introduced, while a time constant describes how fast the process responds once it has started to react to the change. For complex (higher-order) systems, like the CO_2 absorption process, the dynamic responses may show complex behavior and an analytic expression for the overall

time response of an process output can be impossible to find. One widely used measure is the settling time (t_s) which is defined as the time it takes to reach and stay within a certain relative level of the final value (Singh, 2009), as indicated in Figure 6.1. The 90% settling time is used in the present study, which corresponds to the time it takes for the process output to settle within ±10% of the final value compared to the starting point, that is $y_\infty - 0.1\Delta y < y < y_\infty + 0.1\Delta y$.

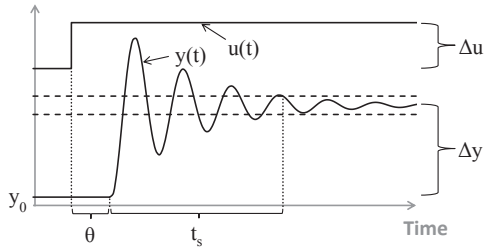

FIGURE 6.1: Dead time (θ) and settling time (t_s) for a higher order process step response.

A case with 216.4 Nm^3/h of flue gas containing 3.9 vol% of CO_2 with the optimal solvent flow rate of 213.1 kg/h and reboiler duty of 15.5 kW to reach 90% capture rate is used as basis for the dynamic simulations. Set-point changes in flue gas flow rate, solvent flow rate or reboiler duty are introduced to the process at initially steady state condition in order to create dynamic responses and compare typical settling times and dead times of the process.

The data input to the different units does not act as step changes in this case because propagation through the process changes the response and thereby affects the input profiles. The dead time will naturally increase and the profile is smoothing out as the disturbance propagates through the process. However, by comparing a units input and output response profile, an image of how the unit contributes to changed dead time and/or time constant of the overall system can be drawn.

6.1.1 Changes in solvent flow rate

Various ramp changes in solvent flow rate (-20%, -10%, +10% and +20%) are simulated. The changes are introduced after 10 minutes and 1 minute is allowed to reach the final value. The simulations are continued for 18 hours to ensure that

a new steady state condition is observed. The flue gas conditions and reboiler duty are kept constant during the whole simulation time. The dead times (θ) and settling times (t_s) for different responses in the process are calculated and compared in Table 6.1, and the results are presented in Figures 6.2- 6.4.

A minimal or no dead time for solvent flow rate is observed for all units, according to Table 6.1. Plug flow models like the cross heat exchanger show no dead time, since the absorber sump outlet and desorber inlet dead times are equal. So are the reboiler outlet and buffer tank inlet dead times. This means that the changes in solvent flow rate are instantaneous for units modeled as plug flow with incompressible fluids. The absorber and desorber columns are also modeled as plug flow, however, the solvent hold-up might change in these units according to disruptions in column hydraulics. Very small dead-times of 3.6 and 1.2 seconds are therefore observed for absorber and desorber, respectively. Plug flow models will not result in any additional settling time as the inlet and outlet flow rates shows exactly the same profile (no change in inlet and outlet settling time). The same yields for the heat exchanger and desorber. The response profile of mixing model units will however change due to mixing effects. The response is smoothing out as it propagates through the mixing units. These units will therefore introduce inertia as settling time, especially the reboiler which has the largest solvent hold-up. The level controllers react however quite fast and are able to adjust very quickly to the new conditions. The flow rates reach a new stable level after about 2 minutes, according to Table 6.1.

The effects of plug flow transport, mass- and heat transfer and chemical reaction in the absorber and desorber packing are observed as shown in Figures 6.4a and 6.4b. The response in rich CO_2 loading at the absorber outlet is slower compared to the response in solvent flow rate, also indicated by increased dead time and settling time. This is due to the effects of plug flow transport, possible changes in solvent hold-up in the packing material and mass transfer and chemical reaction rates which adds inertia to the process. The absorber sump and cross heat exchanger add more transport delay, in terms of dead time. However, while the mixing effects of the absorber sump results in a smoother loading profile at the absorber sump outlet, the heat exchanger causes a simple transport delay as the settling times in and out are more or less identical. The same effects are observed for the lean CO_2 loading, where plug flow models represent transport delay and mixing models smoothens out the profile with additional settling times. 13-20 minutes dead time

for the cold side and 9-14 minutes for the hot side of the cross heat exchanger is observed depending on solvent flow rate. The observed dead time equals the residence time for heat exchanger and piping.

Inverse responses in rich CO_2 loading are observed in Figure 6.4a. This is caused by an initial decrease/increase in rich CO_2 loading as the lean solvent flow rate is increased/decreased. However, once the change in solvent flow rate reaches the regeneration section, the lean solvent loading will start to increase/decrease as presented in Figure 6.4b. This will again cause the rich solvent loading to increase/decrease and therefore change in the opposite direction of the initial change. The dynamic profile will therefore switch, before it stabilizes at a level close to the initial. The overall change in rich loading is very small as seen in Figure 6.4a.

The settling time for absorbed CO_2 is 216-359 minutes for the simulated cases. An inverse response is also seen for the absorbed CO_2 in Figure 6.2, as it first increases/decreases for increased/decreased solvent flow rate, before it start to decrease/increase when the changes in lean loading (seen in Figure 6.4b) reaches the absorber. The response in desorbed CO_2 in Figure 6.3 adjusts faster to a new steady state condition, compared to the absorbed CO_2. The settling times in this case are 11-20 minutes for decreased solvent flow rate and 98-136 minutes for increased flow rate.

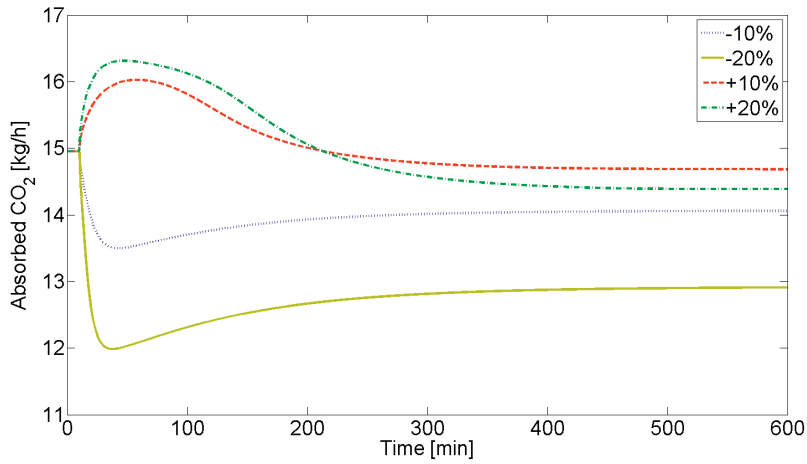

FIGURE 6.2: Responses in absorbed CO_2 for set-point changes in solvent flow rate.

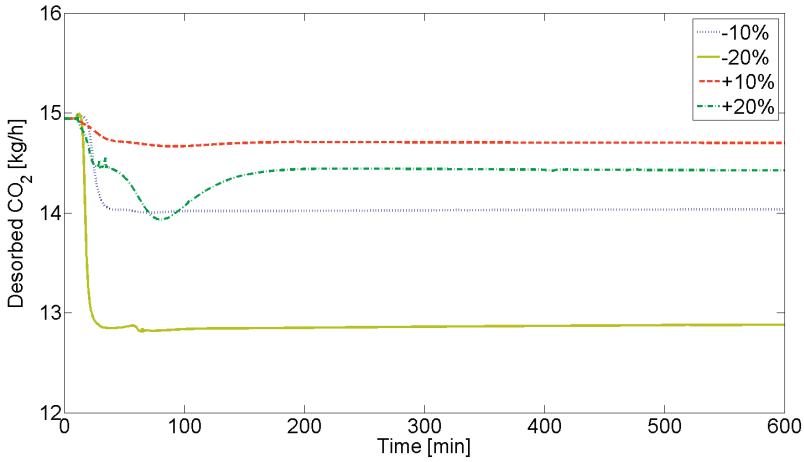

FIGURE 6.3: Responses in desorbed CO_2 for set-point changes in solvent flow rate.

TABLE 6.1: Calculated dead times (θ) and settling times (t_s) for set-point changes in solvent flow rate.

	Dead time (θ) [min]				Settling time (t_s) [min]			
Solvent flow rate	+20%	+10%	-10%	-20%	+20%	+10%	-10%	-20%
Performance								
CO_2 absorbed	0.07	0.07	0.07	0.07	355.36	359.35	237.16	216.35
CO_2 desorbed	0.07	0.10	0.10	0.07	136.37	97.90	20.40	11.26
Rich CO_2 loading								
absorber outlet	0.60	0.38	0.25	0.35	498.68	492.45	160.78	69.20
asorber sump outlet	2.43	1.40	0.55	0.65	500.92	495.90	166.05	76.17
desorber inlet	15.48	16.30	18.50	20.60	500.59	495.18	166.03	76.17
Lean CO_2 loading								
reboiler outlet	0.95	0.75	0.30	0.20	184.92	183.67	214.53	238.45
buffer tank inlet	10.10	10.75	12.68	14.07	185.02	183.73	214.54	238.45
buffer tank outlet	19.80	12.67	13.83	15.00	185.73	192.36	224.87	251.00
Flow rate								
absorber inlet	0.00	0.00	0.00	0.00	0.80	0.80	0.80	0.80
absorber outlet	0.06	0.06	0.06	0.06	0.67	0.67	0.69	0.69
asorber sump outlet	0.07	0.07	0.07	0.07	0.75	0.75	0.75	0.75
desorber inlet	0.07	0.07	0.07	0.07	0.75	0.75	0.75	0.75
desorber outlet	0.09	0.10	0.09	0.10	0.76	0.75	0.74	0.72
reboiler outlet	0.15	0.17	0.09	0.10	1.83	1.83	1.74	1.72
buffer tank inlet	0.15	0.17	0.09	0.10	1.83	1.83	1.74	1.72

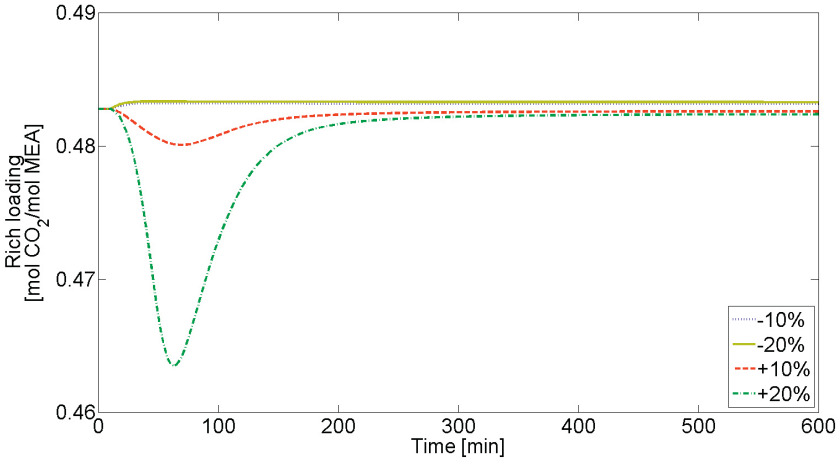

(A)

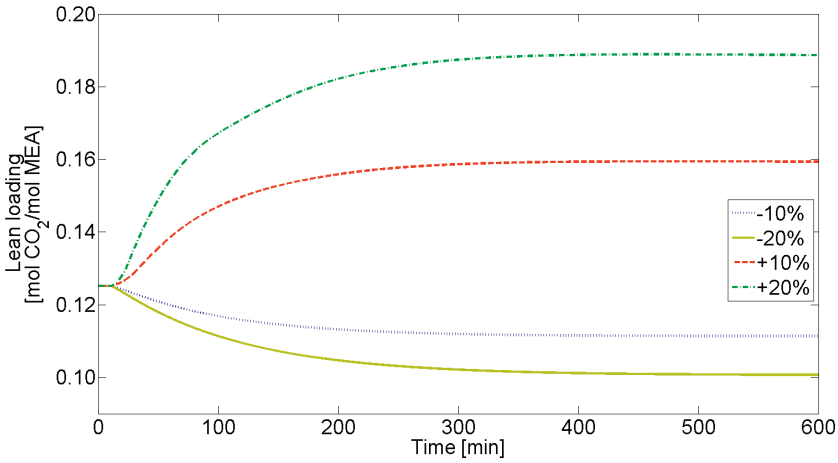

(B)

FIGURE 6.4: Responses in (a) rich CO_2 loadings and (b) lean CO_2 loadings for set-point changes in solvent flow rate.

6.1.2 Changes in reboiler duty

Four simulations with set-point changes in reboiler duty (-20% to +20%) are also performed, while the flue gas conditions and solvent flow rate are kept constant. The set-point changes are introduced as ramp changes after 10 minutes, and 1 minute is allowed to reach the final input value. The simulations are then continued for 18 hours to ensure that a new steady state condition is observed. The results are presented in Figures 6.5-6.7 and the calculated dead times (θ) and settling times (t_s) are presented in Table 6.2.

The settling time for absorbed CO_2 is 219-242 minutes for the simulated cases. For desorbed CO_2 it is only 1 minute for decreased reboiler duty and 18-27 minutes for increased reboiler duty. For the case of increased reboiler duty, the response in desorbed CO_2 has an overshoot as seen in Figure 6.6. The rich CO_2 loadings need longer time to stabilize, as the settling time for the absorber outlet is 248-368 minutes, according to Table 6.2. However, it should be noted that the changes in rich CO_2 loading are very small for all cases, as seen in Figure 6.7a.

Again, the effect of plug flow transportation is observed as the settling time for the response in outlet absorber sump and inlet desorber are identical, which corresponds to the cold side of the heat exchanger including piping. The same yield for the response in reboiler outlet and buffer tank inlet, which corresponds to the hot side of the heat exchanger including piping. The dead time is however, 11 and 17 minutes for the hot and cold sides, respectively, which corresponds to the residence time of these parts of the process given the current flow rate.

TABLE 6.2: Calculated dead times (θ) and settling times (t_s) for set-point changes in reboiler duty.

	Dead time (θ) [min]				Settling time (t_s) [min]			
Reboiler duty	+20%	+10%	-10%	-20%	+20%	+10%	-10%	-20%
Performance								
CO_2 absorbed	22.57	27.20	25.85	23.47	242.41	233.97	218.78	224.43
CO_2 desorbed	0.05	0.05	0.05	0.05	18.47	27.40	1.08	1.08
Rich CO_2 loading								
absorber outlet	31.03	32.73	40.53	39.12	353.59	313.84	248.30	368.05
asorber sump outlet	34.83	38.90	44.95	43.60	355.35	313.75	249.13	368.72
desorber inlet	51.75	56.45	61.77	60.37	355.37	313.80	249.13	368.75
Lean CO_2 loading								
reboiler outlet	0.55	0.55	0.60	0.65	194.48	195.22	195.68	194.28
buffer tank inlet	11.55	11.57	11.65	11.65	194.52	195.20	195.72	194.38
buffer tank outlet	13.80	14.10	15.05	14.23	205.88	205.73	204.62	206.94

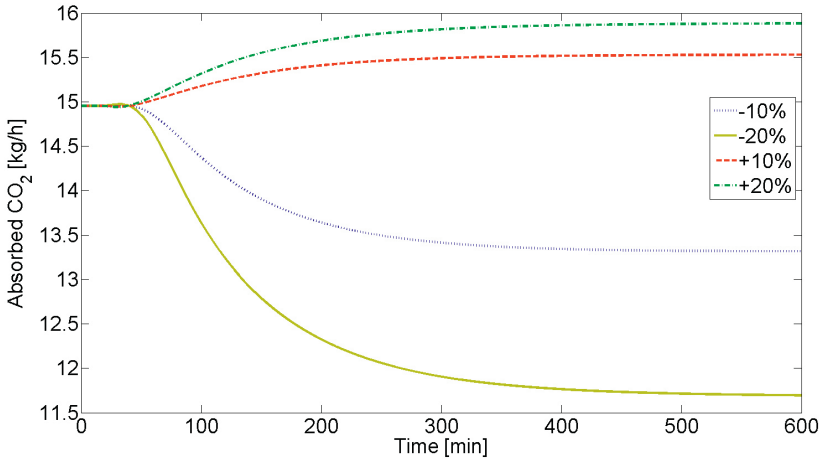

FIGURE 6.5: Responses in absorbed CO_2 for set-point changes in reboiler duty.

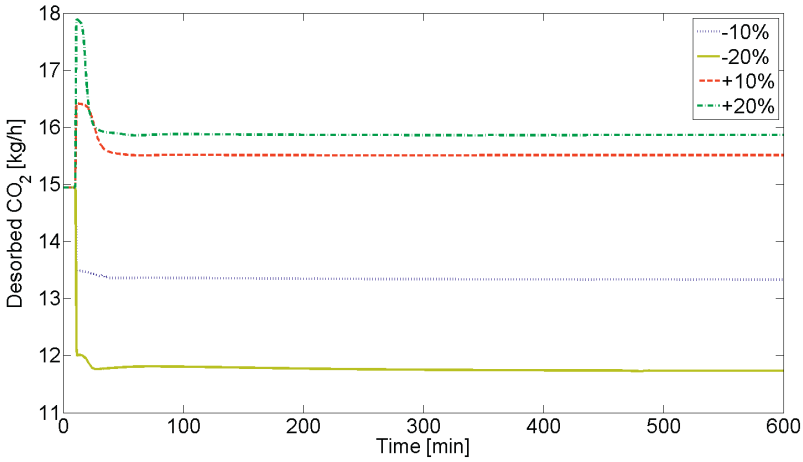

FIGURE 6.6: Responses in desorbed CO_2 for set-point changes in reboiler duty.

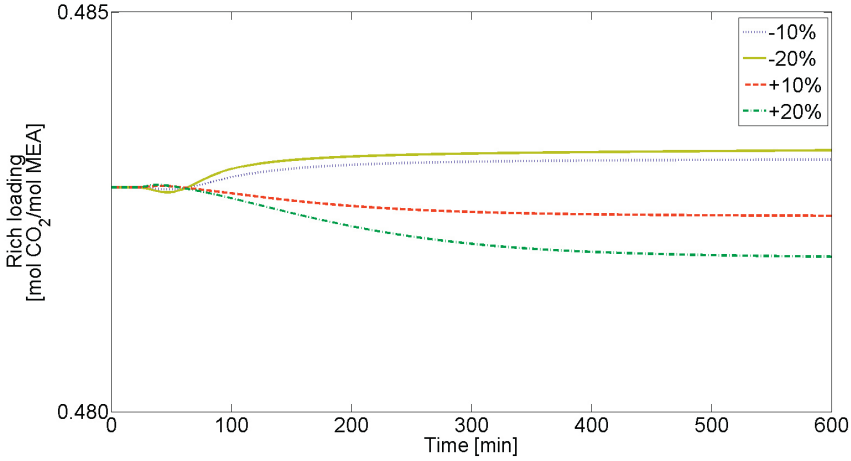

(A)

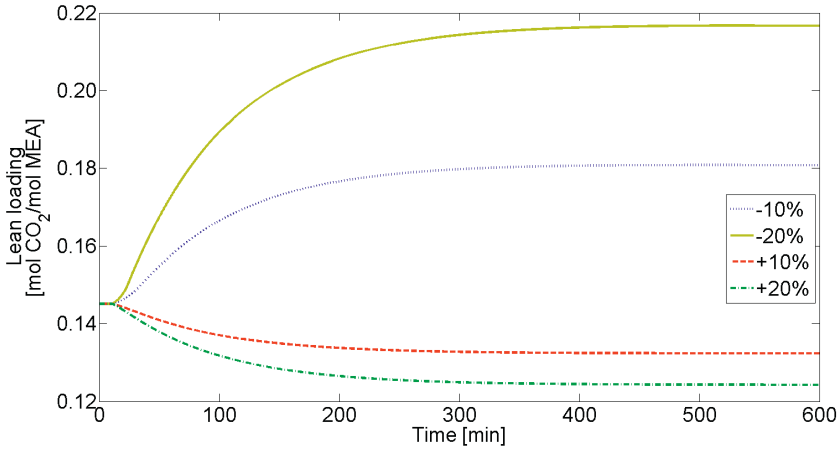

(B)

FIGURE 6.7: Responses in (a) rich CO_2 loadings and (b) lean CO_2 loadings for set-point changes in reboiler duty.

6.1.3 Changes in flue gas flow rate

Four simulations with set-point changes in flue gas flow rate from -20% to +20% are also performed, while the lean solvent flow rate and reboiler duty are kept constant. The changes are as previously introduced as ramp changes after 10 minutes, where 1 minute is allowed to reach the final value. The simulations are continued for 18 hours to ensure a new steady state condition. The results are presented in Figures 6.8-6.11 and calculated dead times and settling times are presented in Table 6.3.

The absorbed CO_2 shown in Figure 6.8 stabilizes very fast at a new steady state level. For increased flue gas flow rate, the final value is very close to the initial since the solvent loading capacity already is close to the limit. Thus almost no more CO_2 is absorbed after the set-point increase. The same results are also seen for desorbed CO_2 in Figure 6.9 and for CO_2 loadings in Figure 6.11, where the response profiles for +10% and +20% set-point change stay more or less constant. The CO_2 capture rate will naturally decrease for increased flue gas flow rate as seen in Figure 6.10. The settling times are 17 and 13 minutes for +20% and +10% set-point change, respectively. The residence time of the gas in the absorber column is less than 1 minute, while for solvent it is about 14 minutes. The effect of mass transfer and chemical reaction rates are therefore believed to be very limited.

For decreased flue gas flow rate a decline in absorbed and desorbed CO_2 is observed, according to Figures 6.8 and 6.9. The CO_2 capture rate will however increase as seen in Figure 6.10, and the estimated settling times are 53 and 13 minutes for -10% and -20% set-point changes, respectively.

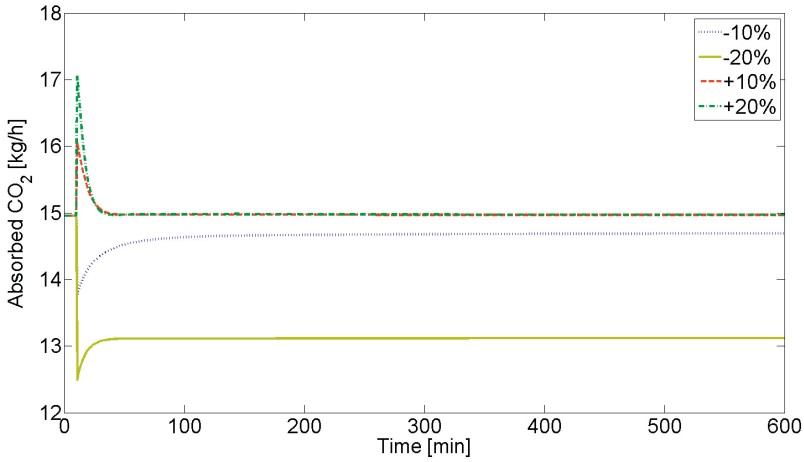

FIGURE 6.8: Responses in absorbed CO_2 for set-point changes in flue gas flow rate.

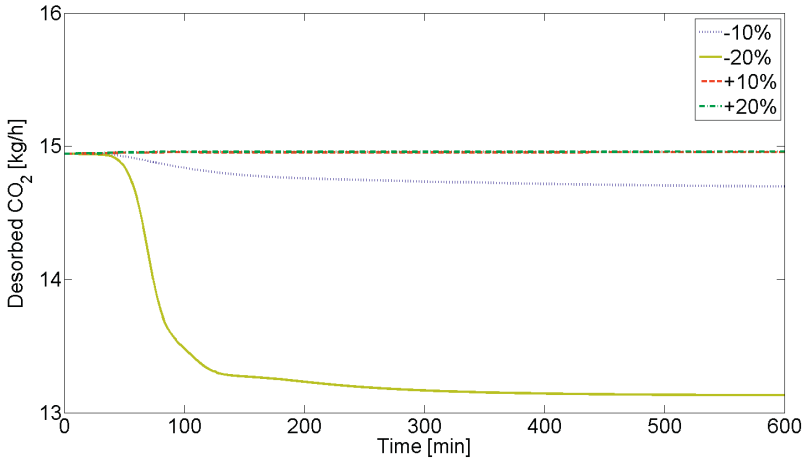

FIGURE 6.9: Responses in desorbed CO_2 for set-point changes in flue gas flow rate.

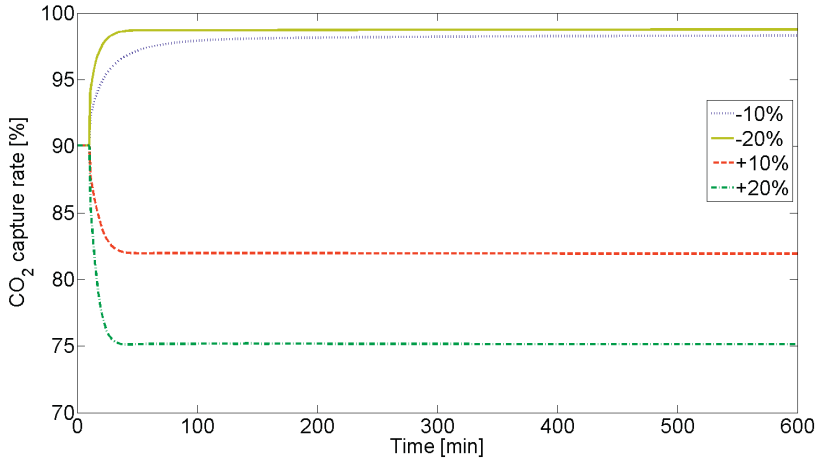

FIGURE 6.10: Responses in CO_2 capture rate for set-point changes in flue gas flow rate.

TABLE 6.3: Calculated dead times (θ) and settling times (t_s) for set-point changes in flue gas flow rate.

	Dead time (θ) [min]				Settling time (t_s) [min]			
Reboiler duty	+20%	+10%	-10%	-20%	+20%	+10%	-10%	-20%
Performance								
CO_2 capture rate	0.02	0.02	0.02	0.02	12.75	16.73	52.65	13.25
CO_2 absorbed			0.02	0.02			183.03	9.70
CO_2 desorbed			1.22	1.32			414.30	115.20
Rich CO_2 loading								
absorber outlet			0.78	2.03			335.24	54.35
asorber sump outlet			3.22	5.18			337.93	58.44
desorber inlet			19.63	21.82			338.15	58.61
Lean CO_2 loading								
reboiler outlet			1.27	0.95			606.26	438.35
buffer tank inlet			11.87	11.80			605.05	436.75
buffer tank outlet			13.00	13.63			639.93	544.44

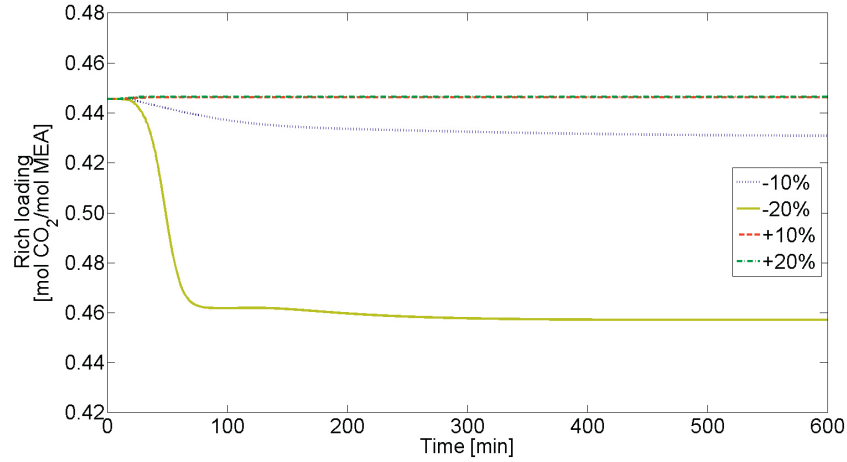

(A)

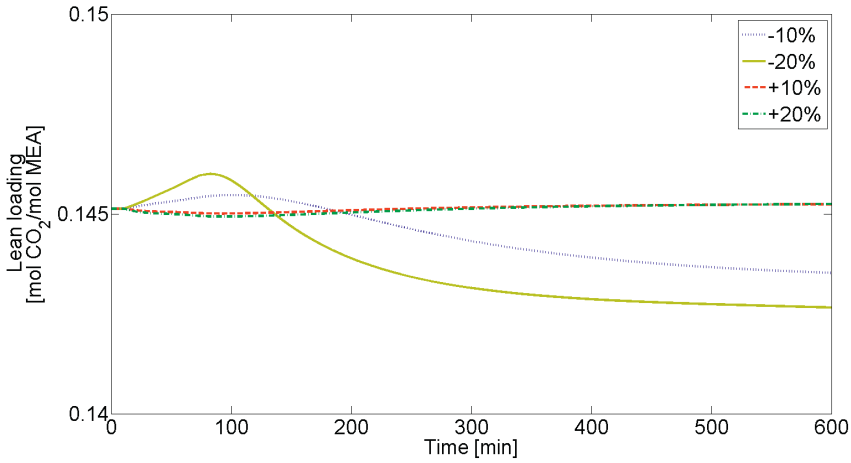

(B)

FIGURE 6.11: Responses in (a) rich CO_2 loadings and (b) lean CO_2 loadings for set-point changes in flue gas flow rate.

6.1.4 Summary

Solvent flow rates adjust very fast due to plug flow of incompressible fluids along with level control for all vessels. The stabilization time for flow rates are therefore within a couple of minutes. Concentrations are more dependent on plug flow transport (which represents dead time), along with mass transfer and chemical reactions in column packing sections and will therefore need more time to stabilize. The stabilization time for CO_2 loadings is up to 8 hours depending on the disturbance introduced. This is mostly caused by mixing effects of large vessels, and larger solvent hold-ups will consequently demand longer stabilization time. However, the changes in rich CO_2 loading are in general very small.

As expected, mixing models like the absorber sump and reboiler will introduce time constants that affect the dynamic response profiles, while plug flow models like the cross heat exchanger causes pure transport delays and no additional settling time. Mass transfer and chemical reaction rates cause some process inertia, but it is relatively small compared to the inertia of larger mixing vessels like the absorber sump, reboiler and buffer tank and transport delay caused by plug flow. Overall, it seems like set-point changes in flue gas flow rate stabilize very fast as it does not disrupt the solvent dynamics significantly. Changes in reboiler duty also allows faster stabilization than changes in flow rate. Even though the flow rates are able to adjust to the new condition very fast, this acts as a larger disturbance to the system.

The overall residence time of the system affects the stabilization time, but the fact that the process has recirculation of solvent will increase the time needed for stabilization even more. The overall residence is only 2 - 3 hours, but it is here proven that stabilization in CO_2 capture rate will require up to 6 hours, that is 2 - 3 times longer than the solvent residence time.

The simulations with set-point changes in flue gas flow rate shows a settling time of 13-53 minutes for the CO_2 capture rate. Increasing the flue gas flow rate does not cause significant disturbances of the solvent as the lean and rich solvent loadings stays stable, and the estimated settling time is in this case 13 - 17 minutes. The stabilization time is similar to the absorber residence time, thus the effect of mass and heat transfer and chemical reaction rates is very limited.

6.2 Dynamic simulations of flexible operation

Results from a simulation study on flexible operation of the CO_2 capture unit according to power plant load changes and varying electricity prices is presented in Paper G in Appendix C.7. By applying flexible CO_2 capture, the CO_2 capture rate can be manipulated to maximize operating profits based on the trade-off between CO_2 emission cost and the current electricity price. The goal for all cases studied is to still maintain a time average capture rate of 90%.

Several techno-economic studies consider possible improvement of operational economics by allowing flexible operation of CCS and exploiting the variations in electricity demand and prices (Chalmers et al., 2012, Cohen et al., 2010, Wiley et al., 2011). However, such analyses typically ignore operating dynamics and transient performance of the CCS plant. For instance it is suggested that the capture unit can be completely switched off during peak electricity price periods, and later switched on when prices are normalized in a cyclic manner (Cohen et al., 2010, Wiley et al., 2011). However, simulations or experimental experience with frequent process start-ups and shut downs and analysis of the related system response times are barely reported in the literature. On/off operation of the regeneration section may be challenging in practice, especially in a frequent manner. In the paper by Mangiaracina et al. (2014) on/off operation is demonstrated as part of a pilot plant campaign considering flexibility in the Brindisi pilot plant. The results show in fact that a significant amount of time is required for the regeneration part of the process to re-pressurize and stabilize after start-up.

The K-Spice model of the Brindisi pilot plant is used to investigate the plant performance during flexible operation in this study, and four different flexible operating modes are evaluated from an operational and dynamic performance perspective.

6.2.1 Flexible operating modes

A power station might undergo frequent load changes as a result of shifting energy demands. The electricity market may also vary quite significantly during a day, week, season or year, which motivates flexible operating modes in an attempt to reduce the time average energy penalty.

In the case of varying electricity generation, a power station will operate at varying loads, which the capture plant will need to follow. This type of operation is referred to as load following. A hypothetical scenario where the power station is ramped down to 70% load during 3 hours at night according to Figure 6.12a is investigated. The load change is done gradually, where the ramping down is started at 10 p.m., 70% load is reached at 2 a.m. and continued until 5 a.m. Ramping up is started at 5 a.m., reaching full load again at 7 a.m.

In the case of varying electricity prices, flexible operation of the capture unit can be beneficial in order to manipulate the economic penalty of carbon capture. During peak electricity price periods it could be economical to utilize more steam for power generation and less on CO_2 capture, while spending more on CCS during off-peak electricity price periods. In this case a power plant operating at full load is considered, while the capture plant is ramped up and down according to a hypothetical daily electricity price profile as illustrated in Figure 6.12b. The simulated ramping rate is in this case 2% per min, and the electricity price intensive periods lasts for 3 hours in the evening and 2 hours in the morning.

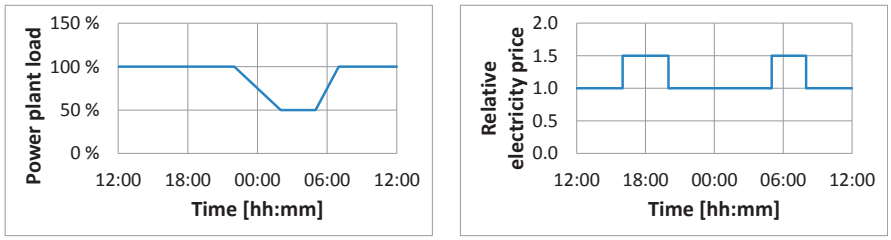

(A) Hypothetical power plant load factor during part load operation

(B) Hypothetical daily variations in electricity price

FIGURE 6.12: Motivation for flexible operating modes.

Three different operating modes are considered in a varying electricity market in order to assess the possibilities of increasing the overall profit of the process. In the following simulations, a constant total amount of steam for regeneration is provided in the three cases. However, the distribution in time is varied in order to reduce the steam consumption in electricity price intensive periods. The following modes are considered:

- Exhaust gas venting, where a fraction of the power station exhaust gas is vented during peak electricity price periods, allowing a momentary CO_2 capture rate below 90%. The CO_2 capture must catch up during off-peak

periods by operating the plant at conditions which increases the capture rates above 90%, to maintain a time average capture rate of 90%..

- Varying degree of solvent regeneration, where the steam rate utilized for solvent regeneration is decreased during peak electricity price periods. CO_2 is allowed to accumulate in the solvent during these hours, while the solvent will be regenerated more deeply when the electricity prices normalize. The momentary CO_2 capture rate will decrease below 90% during peak price periods, which means that the steam rate must be increased during off-peak periods to maintain a time average capture rate of 90%.
- Solvent storage or intermittent stripping, where a rich solvent tank is utilized to store fractions of the solvent during peak electricity price periods, while regenerating at a later stage when electricity is less expensive. This operating mode will also require a lean solvent tank to store the regenerated solvent which will be utilized in peak electricity price periods.

Details about the load following mode and the three other flexible modes of operation related to variations in the electricity price market are presented in Figure 6.13. As seen in Figure 6.13, the load following mode (a) has variable flue gas flow rate, solvent flow rate and steam rate. It is expected that the the rate of produced CO_2 will follow the load, and the capture rate and lean and rich loadings will remain more or less constant. The mode of exhaust gas venting (b) will have a variable flue gas flow rate, solvent flow rate and steam rate. It is expected that the lean and rich CO_2 loadings will remain more or less constant, but the capture rate will depend on the vent fraction. It will be less than 90% in peak electricity price periods, and consequently higher than 90% in off-peak electricity price periods with a time average capture rate of 90%. The rate of produced CO_2 will follow the capture rate. The mode of varying solvent regeneration (c) will have constant flue gas and solvent flow rates. Only the steam rate to the reboiler will be varied, and consequently the lean and rich CO_2 loadings will vary. This will keep the absorber hydraulics constant. It is expected that the CO_2 capture rate and rate of produced CO_2 will follow the steam rate. The mode of solvent storage (d) will have constant flue gas and lean solvent flow rate. The rich solvent flow rate and steam rate to the reboiler will however vary. It is expected that the lean and rich CO_2 loadings will remain constant along with the CO_2 capture rate. The rate of produced CO_2 will however vary according to the steam rate, and is therefore decoupled from the CO_2 capture rate.

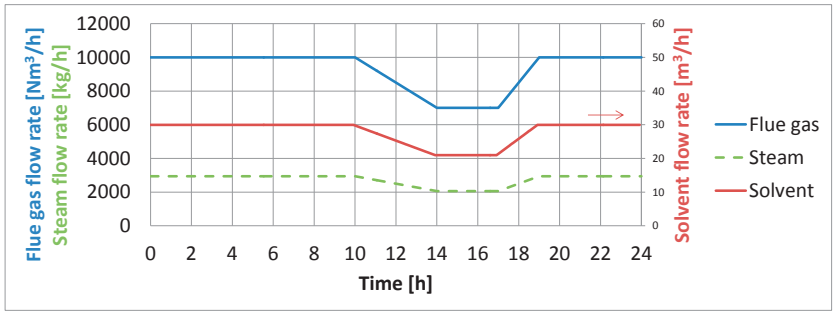

(A) Load following

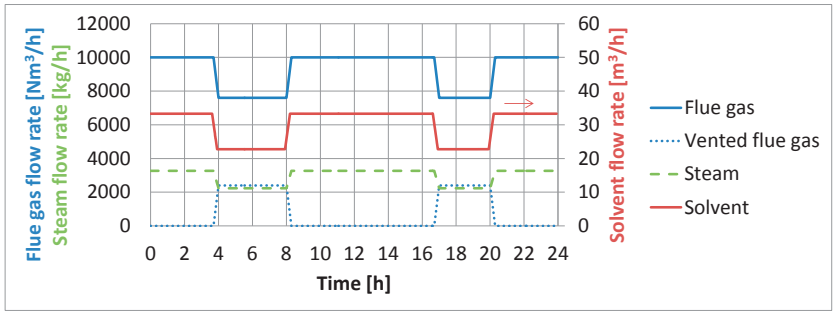

(B) Exhaust gas venting

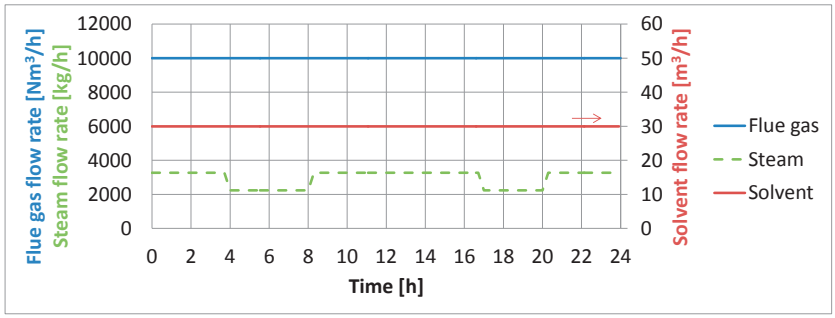

(C) Varying solvent regeneration

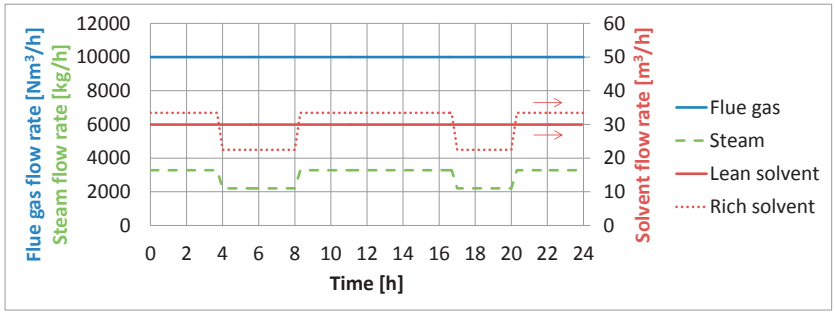

(D) Solvent storage

FIGURE 6.13: Operation plans for various flexible operating modes.

6.2.2 Base case

A steady state base case of 90% capture rate at design-point conditions is established for comparison reference for flexible operating modes. The conditions given in Table 6.4 correspond to the optimal (square) point in Figure 6.14 which gives the minimum energy requirement of 3.68 MJ/kg CO_2.

TABLE 6.4: Brindisi pilot plant - base case simulations

Flue gas flow rate	10 000	Nm^3/h
CO_2 inlet concentration	11.4	dry vol%
Solvent flow rate	30	m^3/h
MEA concentration	30	wt%
Steam flow rate	2941.6	kg/h

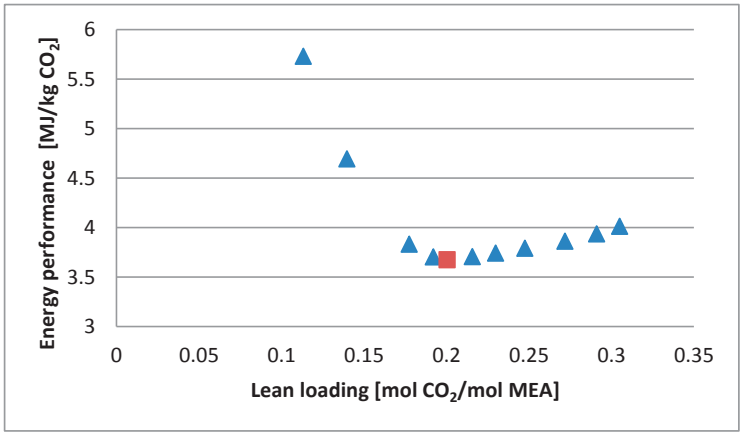

FIGURE 6.14: Energy performance as function of operating point with 90% capture rate for the Brindisi pilot plant.

6.2.3 Load following

A scenario of load following capture plant operation according to Figure 6.12a where the solvent flow rate is controlled proportionally according to the flue gas flow rate and the steam flow rate is controlled proportionally according to the solvent flow rate is simulated. The proposed operation plan is illustrated in Figure 6.13a, and the simulation results are presented in Figure 6.15.

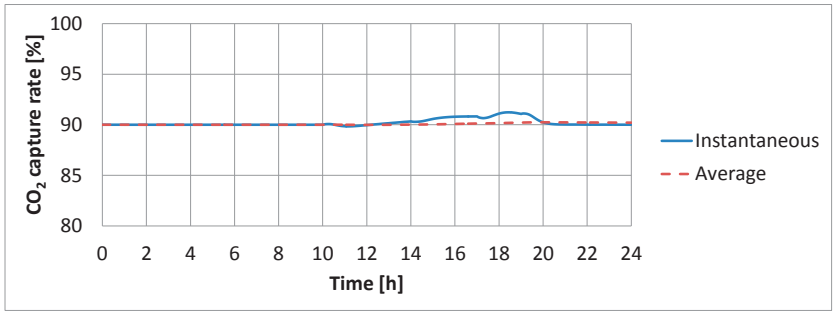

(A) CO_2 capture rate

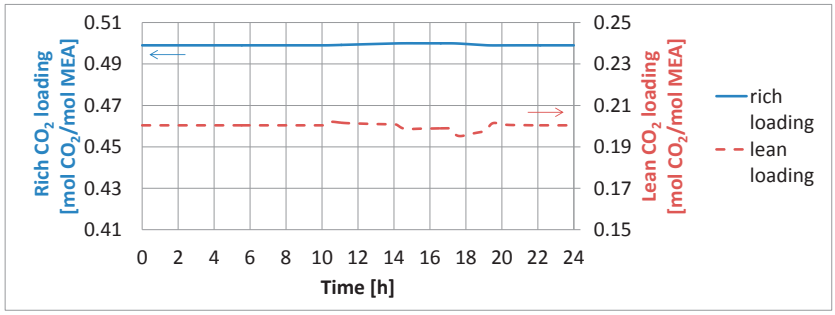

(B) CO_2 loading

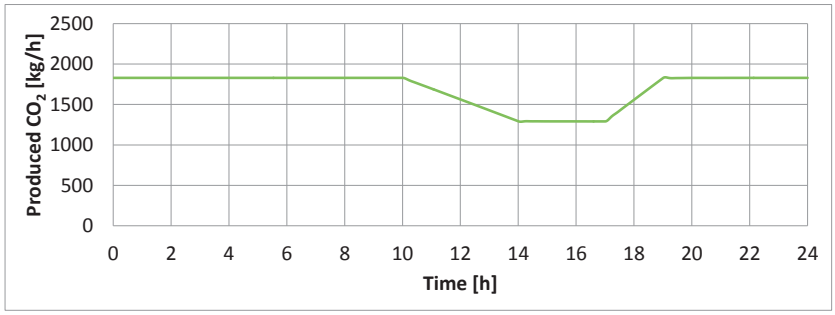

(C) Produced CO_2

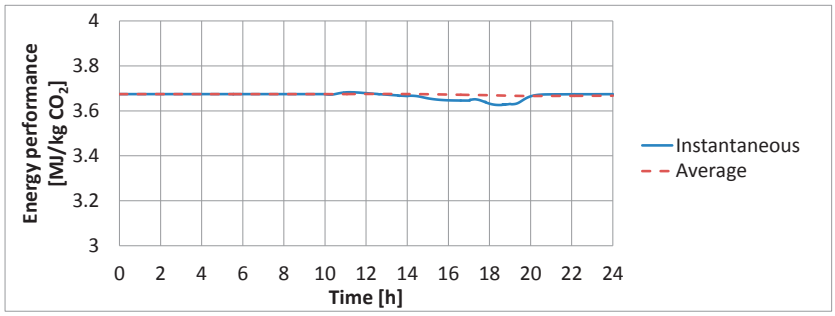

(D) Energy performance

FIGURE 6.15: Simulation results for the load following operating mode.

The instantaneous and time average capture rate is presented in Figure 6.15a. The instantaneous capture rate is maintained more or less constant during the whole period, with a small increase during part load operation. The 24 hour average CO_2 capture rate is therefore 90.2%. The slightly higher capture rate at part load operation is caused by increased residence time and heat transfer in the cross heat exchanger.

A slightly lower lean loading and higher rich loading is seen at part load operation in Figure 6.15b. This is caused by increased heat transfer in the cross heat exchanger and longer solvent residence time in the absorber column. The produced CO_2 illustrated in Figure 6.15c shows a response according to the amount of steam provided to the reboiler. The response is fast and the process is able to stabilize at both part and full load operation.

The overall energy performance is illustrated in Figure 6.15d and the 24 hour average energy consumption is 3.67 MJ/kg CO_2. This is slightly lower than base case caused by the slightly increased capture rate at part load operation.

6.2.4 Exhaust gas venting

Exhaust gas venting, where a fraction of the power station exhaust gas is vented during peak electricity price periods, according to Figure 6.12b has the proposed production plan presented in Figure 6.13b. A vent fraction of 24% is used in the peak electricity price periods, which means that the solvent flow rate and reboiler duty also is reduced by 24%. All the flue gas is directed through the absorber when the electricity price normalizes, and the solvent flow rate and reboiler duty has to be increased to 111% to maintain an average of 90% capture rate. This scenario is simulated and the results are presented in Figure 6.16.

The CO_2 capture rate presented in Figure 6.16a shows a 24 hour average of 89.5%, which is slightly lower than 90% due to partly off-design operation. Only small changes in lean and rich CO_2 loadings is seen in Figure 6.16b. The rich loading is slightly higher in peak hours due to part load absorber operation which causes increased solvent residence time in the packing.

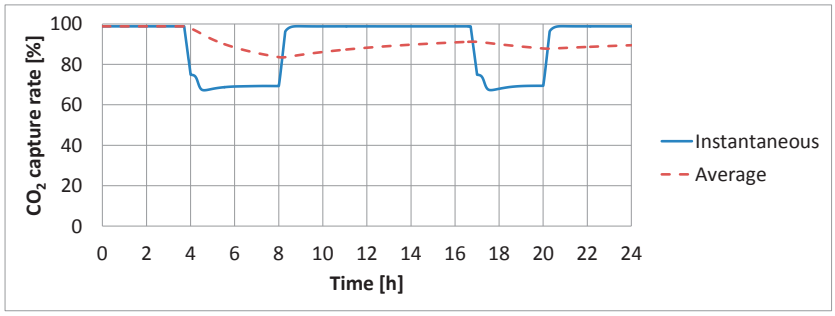

(A) CO_2 capture rate

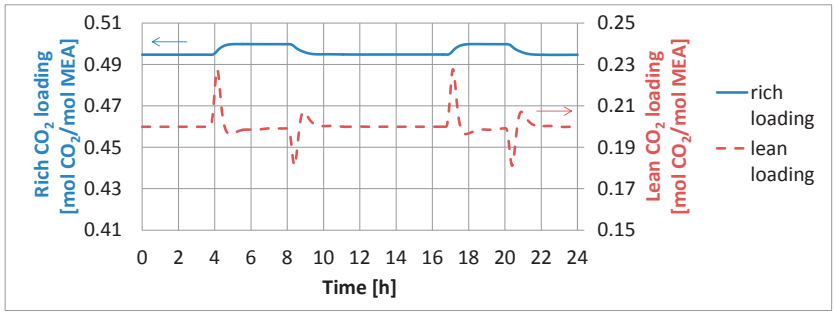

(B) CO_2 loading

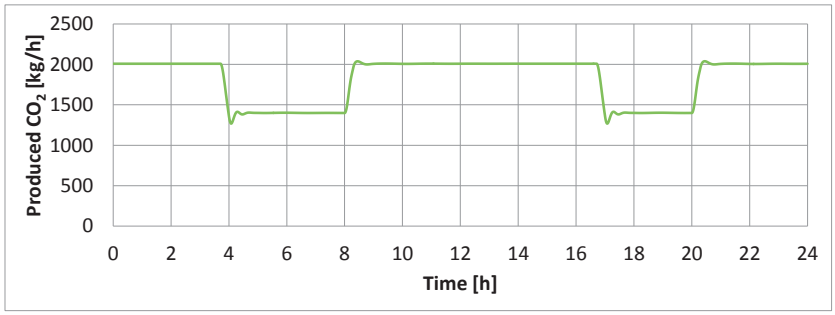

(C) Produced CO_2

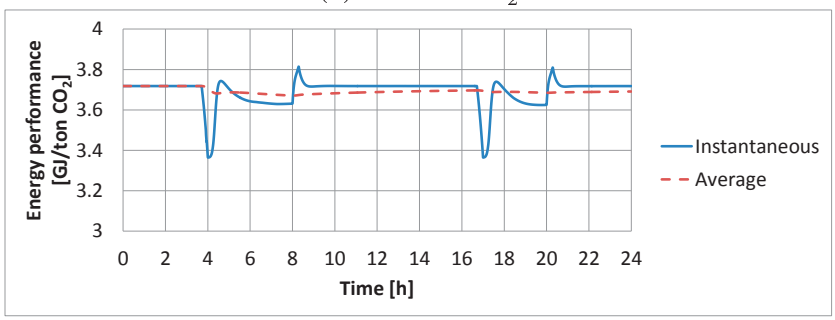

(D) Energy performance

FIGURE 6.16: Simulation results for the operating mode of exhaust gas venting.

The produced CO_2 illustrated in Figure 6.16c follows the amount of steam provided to the reboiler. Small inverse responses are observed just at the time of change in reboiler duty. The desorber gas flow changes instantaneously when the reboiler duty is changed, and it takes some time before the desorber L/G will adjust. This however does not seem to cause operational problems.

The 24 hour average energy consumption is 3.69 MJ/kg CO_2 as indicated in Figure 6.16d, which is only slightly higher than base case. The total amount of steam saved during peak electricity price periods is, however, 4950 kg which corresponds to 3107 kWh. This means that the additional steam available for generation of electricity during peak electricity price periods is 23.9%. The total amount of steam required during the whole 24 hour period equals the amount required in base case, which means that a larger amount of steam is required in off electricity price periods.

6.2.5 Varying solvent regeneration

In the mode of varying degree of solvent regeneration, only the steam rate utilized for solvent regeneration is decreased during peak electricity price periods, while the flue gas and solvent flow rate are kept constant. The production plan is illustrated in Figure 6.13c where the steam rate to the reboiler is decreased by 24% in electricity price intensive periods and increased to 111% when the prices normalize. The results are presented in Figure 6.17.

The 24 hour average CO_2 capture rate presented in Figure 6.17a is 87.2%, slightly lower than 90% due to partly off-design and partly suboptimal operation (lower and higher lean loadings). Large variations in lean loading is seen in Figure 6.17b, which causes slower dynamic responses compared to the exhaust gas venting operating mode. As seen in the figure, the mixing effects of the buffer tank delays the response in lean loading.

The produced CO_2 response shown in Figure 6.17c is fast and follows the amount of steam provided to the reboiler. Small inverse responses are also seen in this case at the time of load chnage.

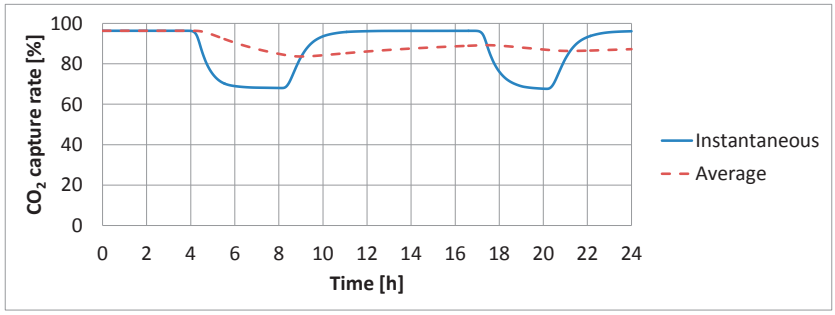

(A) CO_2 capture rate

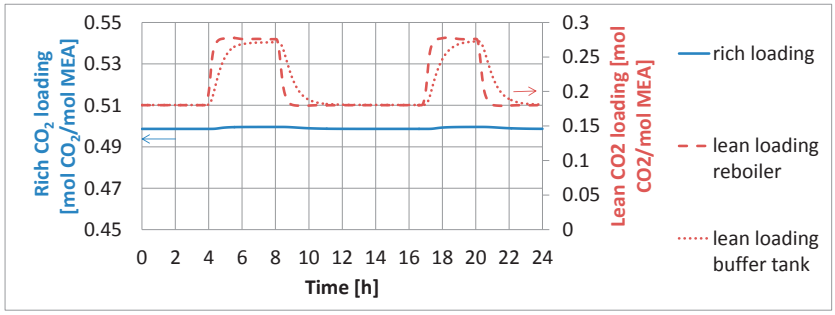

(B) CO_2 loading

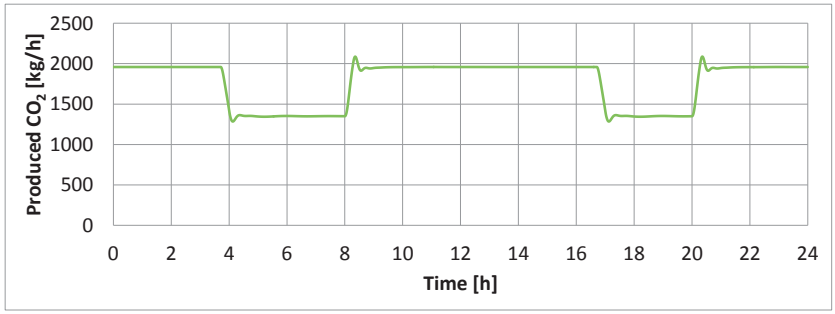

(C) Produced CO_2

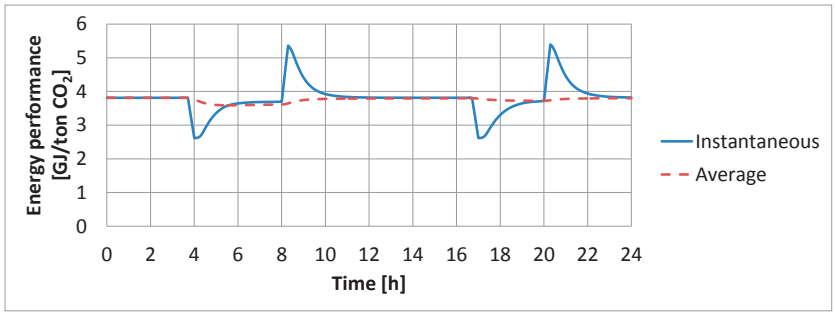

(D) Energy performance

FIGURE 6.17: Simulation results for the operating mode of varying solvent regeneration.

The 24 hour average energy consumption is 3.80 MJ/kg CO_2, which is higher than base case due to partly suboptimal operation (higher lean loadings).

The total amount of steam saved during peak electricity price periods is 4950 kg which corresponds to 3107 kWh. This means that the additional steam available for generation of electricity during peak electricity price periods is 23.9%, as for the exhaust gas venting mode.

6.2.6 Solvent storage (intermittent stripping)

In the operating mode of solvent storage, a fraction of the rich solvent is routed to a solvent storage tank during peak electricity price periods, while it is regenerated at a later stage when the electricity is less expensive. The production plan is illustrated in Figure 6.13d where 25% solvent is stored during peak electricity price periods. The desorber load (rich solvent flow rate and steam rate to reboiler) is therefore increased to 112% in off-peak electricity price periods in order to regenerate the excess rich solvent.

The 24 hour average in CO_2 capture rate presented in Figure 6.18a is 90.1%. Lean and rich CO_2 loadings are kept more or less constant during the whole simulation time as seen in Figure 6.18b. The produced CO_2 response as shown in Figure 6.18c is fast and follows the amount of steam provided to the reboiler, and the 24 hour average energy consumption is 3.67 MJ/kg CO_2.

The total amount of steam saved during peak electricity price periods is 5149 kg which corresponds to 3232 kWh. This means that the additional steam available for generation of electricity during peak electricity price periods is 25%. However, two large storage tanks are needed in order to conduct this operation plan, and for 25% storage a total storage volume of 2x50 m^3 is required. Two tanks of 60 m^3 was utilized in these simulations (to give some extra buffer), and the time varying level of the two tanks is presented in Figure 6.19.

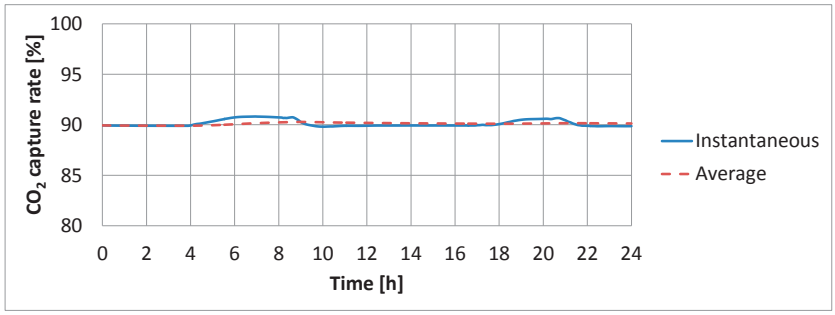

(A) CO_2 capture rate

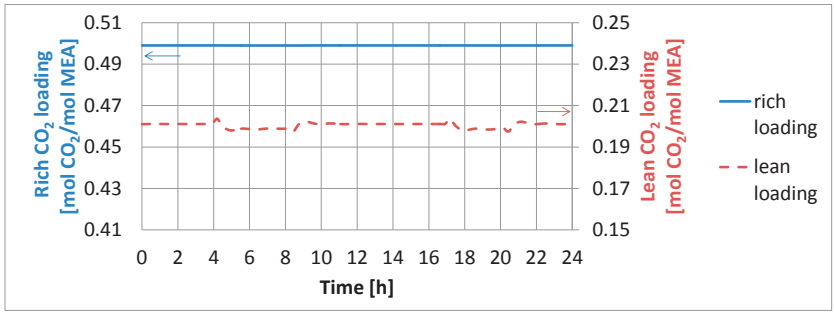

(B) CO_2 loading

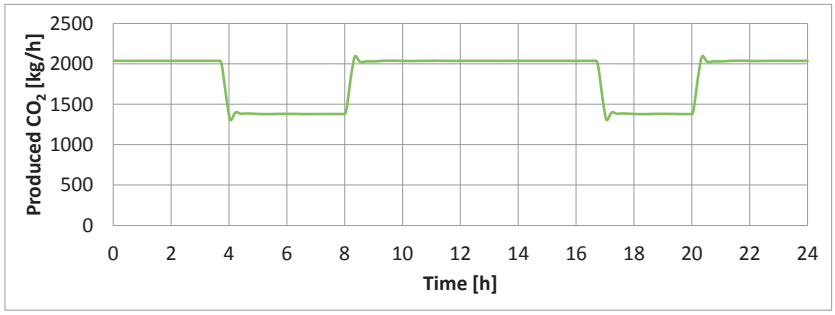

(C) Produced CO_2

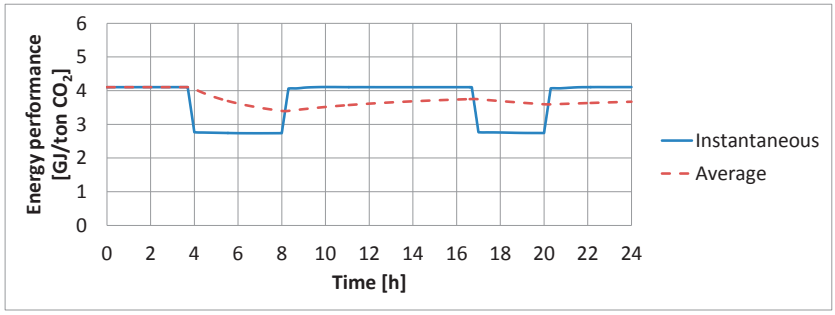

(D) Energy performance

FIGURE 6.18: Simulation results for the operating mode of solvent storage.

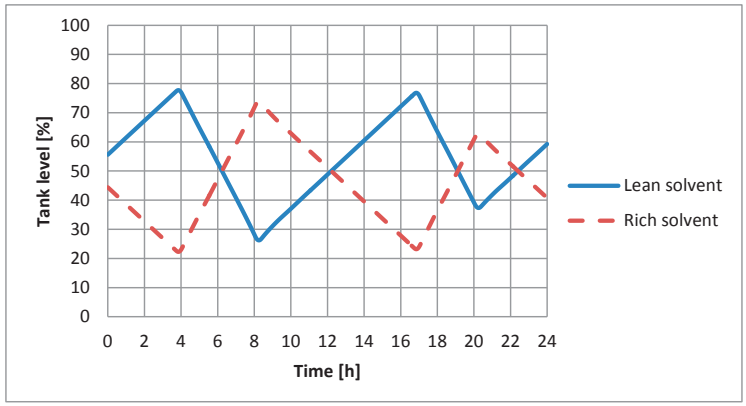

FIGURE 6.19: Solvent tank levels during flexible operation.

6.2.7 Summary

Simulations of the load following operation mode shows that the process reacts fast to power plant load changes and is able to stabilize at both part and full load operation.

Three other scenarios of flexible operation are simulated with the objective of reducing the steam consumption during electricity price intensive periods, while still aiming for 90% time average capture rate. This will allow a larger amount of steam for electricity generation during periods where it is more economical. Only basic control of solvent flow rate and reboiler duty is utilized in the simulations, and no online optimization of the dynamic behavior is performed. However, the potential of the three flexible operating modes is demonstrated and seems to be promising.

Solvent storage as a flexible operating mode, gives satisfactory results when it comes to average capture rate and energy performance in a varying electricity market. The capture and energy performances are equal or even slightly improved compared to base case. Solvent storage was the only mode in the varying electricity price scenario which is able to keep the capture rate above 90% at all times. This operating mode is only limited by the solvent storage tanks capacity and regeneration section capacity and ability to operate at part load. However, considerable investments are required for solvent storage tanks and additional operating solvent.

The modes of exhaust gas venting and varying solvent regeneration seem to work satisfactorily and are easy to conduct without process modifications. However these modes rely on the possibility of increased capture rate above 90% to obtain a close to 90% average capture rate. The maximum capture rate in the simulations of these operating modes is close to 98% where the energy requirement for regeneration starts to increase dramatically as indicated in Figure 6.20. Capturing close to 100% CO_2 is practically impossible, and the economical limit of the maximum capture rate seems to be close to 98%.

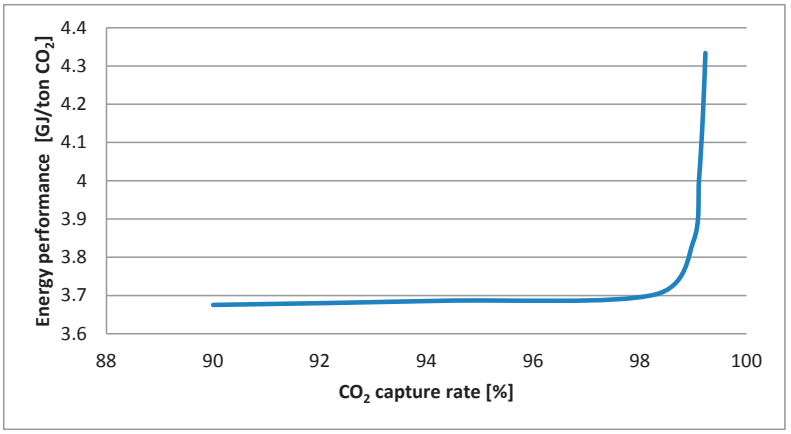

FIGURE 6.20: Simulation of the energy performance as a function of CO_2 capture rate for the Brindisi pilot plant using 30 wt% MEA.

For the scenario with exhaust gas venting the lean CO_2 loading stays more or less constant during the whole simulation time; however, the absorber packing hold-up will be disturbed. For varying degree of solvent regeneration, the absorber L/G will remain constant, but the lean loading will vary in time. The simulations indicate that the latter mode will give a larger disturbance of the overall system, and slower dynamic responses. Further, shifting hydraulic conditions did not seem to cause any significant operational problems, as was the main concern of Lin et al. (2012). This coincides with the operational experience of the Brindisi pilot plant. In fact, operating at lower lean loadings may cause other operational challenges like solvent flashing in the cross heat exchanger (Mangiaracina et al., 2014).

Only basic control of solvent and steam flow rates is applied in these simulations. However, as seen for the exhaust gas venting and varying regeneration options, this may lead to suboptimal conditions during off-design operation. The modes of flue gas venting and varying solvent regeneration consequently did not manage

to reach a 90% time average capture rates. However, by process optimization for flexible operation especially the mode of exhaust gas venting has a good potential to reach a 90% average capture rate by allowing just a small extra amount of steam to the reboiler in off-peak electricity price periods. An advanced control system like model-predictive-control (MPC) would allow off-design operation to be performed more optimally and efficiently. In practice a combination of the exhaust gas venting and varying regeneration mode could be more optimal where both the solvent flow rate and steam rate to the reboiler is controlled to set the optimal lean loading for the given conditions and electricity price. Further, a simple predictive electricity price scenario is considered in this study, where the solvent and steam flow rates are set based on an operation plan of relative proportional control. However, for a more realistic and complex scenario of electricity price variations, MPC will have clear benefits in reaching possible operational profit improvements.

Operating the regeneration section in a cyclic on/off manner as suggested by (Cohen et al., 2010) may lead to significant re-pressurization and stabilization time as described by Mangiaracina et al. (2014). A more realistic approach will be to only store part of the solvent and avoid complete shut-down of the regeneration section. The mode of solvent storage is then only limited by the solvent storage capacity and the regeneration sections maximum capacity and part load operational limits. In the present simulations 25% solvent storage was evaluated, which requires an available storage volume of 2x50 m^3. A scale-up to full size capture plant connected to a 660 MW coal-fired power plant corresponds to 2x11100 m^3 of solvent capacity. The two large storage tanks and the additional amount of solvent required entails extensive additional capital cost. The solvent storage option should therefore be evaluated economically to give a fair basis for comparison to the other suggested modes. This is outside the scope of the present study. However, when comparing to the techno-economic evaluation of Mac Dowell and Shah (2015) for a similar power plant and storage capacity, a 4% improvement in short run marginal cost profitability was probable compared to their base case scenario.

Chapter 7

Conclusions and recommendations for future work

7.1 Conclusions

A considerable effort has been devoted to research for developing and improving CO_2 capture technologies in recent years. Unfortunately, full-scale deployment of these technologies remains limited. Relatively high costs related to commercialization of large scale CCS, both in terms of CAPEX and OPEX, has been the main reason for the slow deployment despite intensive research. International emission agreements and intensives in the form of CO_2 taxes and quotas have to be imposed to make the technologies commercially attractive. Meanwhile, research must still be devoted to keep improving and optimizing the processes and make them even more attractive in the future.

The present work provides contributions to the investigation of dynamic operation of post-combustion CO_2 capture based on amines. The objectives of this thesis are fourfold: 1) development of robust dynamic process models for post-combustion CO_2 capture based on chemical absorption, 2) generation of dynamic pilot plant data through specifically designed dynamic experiments, 3) process model validation both at steady state and dynamic mode, and finally 4) utilization of the developed and validated models for investigation of transient process performance.

A literature review of dynamic modeling of post-combustion CO_2 capture based on amines was presented in Section 4.2. Different model premises were further

evaluated, and it is concluded that the rate-based approach for modeling interphase mass transfer using an enhancement factor for representing the effect of chemical reactions showed improved results compared to a simplified equilibrium-stage model. Even though the equilibrium-stage model can be adjusted with the number of stages that give overall absorption rate results in good agreement with observations in pilot scale process plants, the rate-based approach is preferred for detailed simulations of the local performance in the absorber column. For simulation of other dynamic process responses, however, the equilibrium-stage approach gives very similar transient results. Depending on the application of the model, the equilibrium-stage approach might therefore be adequate for dynamic simulations of the process, that is for instance for MPC where the model is frequently adjusted to measured online process data. For detailed dynamic simulations of the local absorber performance, however, the rate-based approach is highly recommended.

The enhancement factor can be implemented in different degrees of complexity; that is advanced expressions using the DeCoursey relation or more simpler approaches assuming $E = Ha$ for absorber conditions and $E = E_\infty$ for desorber conditions. However, both these methods require iteration of the unknown liquid film interface CO_2 concentration in order to estimate E_∞, which is rather impractical for dynamic simulations due to increased computational demands. It was also demonstrated that $E = E_\infty$ might not always be the best approximation for the desorber column, as in fact $E = Ha$ is a better assumption for certain conditions. Simplifying the enhancement factor in both columns by $E = Ha$ resulted in equally good results for the overall absorption/desoprtion rate. Further, the uncertainties using empirical correlations for prediction of mass transfer coefficients for desorber conditions are significant, as the correlations are mainly developed for absorber conditions. It was demonstrated as a general trend that the local gas and/or liquid mass transfer coefficients are overpredicted for desorber conditions, and they should therefore be adjusted to give better estimations of desorber temperature and concentration profiles.

Two different correlations for interface mass transfer and column hydraulics are also investigated, i.e. the method developed by Billet and Schultes (1999) and a second method developed by Rocha et al. (1993) and Rocha et al. (1996). It was early concluded that the effective interface area predicted by the Billet correlation was unreasonably low and the simulated process was not able to meet the absorption rates observed in experiments for the two different pilot plants used for

comparison. The effective interface area of the Billet correlation is therefore pre-multiplied by a factor to fit the model to experimental observations. The factor used is 2.25 for the Gløshaugen data and 2.5 for TCM, however, in Paper E in Appendix C.5 it was suggested that this factor might be dependent on L/G, itself based on the deviations observed in the simulation results. The Rocha correlations are however able to predict reasonable values for the effective interface area and very good results without any parameter adjustments for both pilot plants used in the validations. The model deviation for CO_2 absorption at steady state is 2.2% and 3.1% for the Billet and Rocha models, respectively, compared to the Gløshaugen experiments and 4.6% for both correlations compared to the TCM experiments.

Lack of dynamic data for model validation has remained a problem reported by several research environments. Previously, other simulation tools or steady state pilot plant data have been the best options for model validation. Some logged pilot plant data have also been available, however, these data do not necessarily reflect important process dynamics, as they may not be logged during periods of transient operation. Pilot plant campaigns are usually performed in order to determine key numbers for certain technologies or solvents at steady state, e.g. energy performance U-curves as is the case for the available TCM data (Hamborg et al., 2014). Thus, the focus on dynamic pilot plant responses and behavior is neglected. However, when operational changes are performed to shift the operating conditions from one steady state point to another, the pilot plant will go through a transient period where the logged data might represent relevant process dynamics. However, important information, e.g. solvent CO_2 loading, might not be available during these transient periods, as the main focus of the campaign is steady state performance. In the present work a considerable set of both steady state and specifically designed transient test data are obtained in the Gløshaugen pilot plant. The generated steady state data show very good pilot plant mass balances, which confirms their reliability. Transient testing is conducted by performing set-point changes in lean solvent flow rate or reboiler duty, while process responses are measured and logged every minute. Solvent samples are also withdrawn frequently and CO_2 loading is successfully correlated with online density measurements to provide a more detailed time description of the solvent dynamics. The gathered pilot plant data are available to anyone who might be interested.

The MATLAB® model is validated towards data from completely different pilot

plants, with different configurations, capacities and absorber and desorber packing materials. The Gløshaugen pilot plant is a small-scale plant, while the Tiller and TCM pilot plants are relatively large and more similar to industrial sized plants. Unfortunately, there were not any dynamic data available for the Tiller plant. The model is however able to predict reasonable steady state results for two very different cases, that is one natural gas-based case and the other is a coal-based case. This demonstrates that the model has a broad applicability. Further, the model predicts very well for all three plants used in the validation, taking measurement uncertainties reflected by the calculated experimental CO_2 mass balances into consideration. Also the dynamic behavior seems adequate based on comparison of specific process responses. It is believed that the general model equations are valid for other plants as well provided the correct equipment sizing and parameter settings. The main uncertainties are believed to be related to the empirical models used for prediction of mass transfer and effective interface area, which are developed for specific packings and specific range of operation conditions. However, once the model is validated at steady state for a given process plant, it is believed to perform adequately also in the transient mode. It is, however, emphasized that simulations of a wide range of operating conditions should be compared to experimental results in order to ensure the general validity of the model, since the operational conditions and process performance may shift frequently during transient operation.

The K-Spice® model is developed for the Brindisi pilot plant in the *Octavius* project and is therefore only validated against data from this specific plant. However the dynamic performance of the model seems to match the experimental observations, and the model is considered adequate for process simulations. Further, the rate-based correlations implemented in K-Spice rely on the same relations that are implemented in MATLAB.

It is important to have sufficient knowledge about the data sets used for model validation. If the model is fitted to incorrect or inaccurate measurements, it might not be able to generate desirable results in agreement with the real process. All experimental data sets used in the present work have certain weaknesses, which are important to keep in mind when comparing simulation results. The data sets gathered in the Gløshaugen pilot plant seem to measure slightly higher CO_2 production rates compared to the estimated absorption rates from gas phase and to liquid phase at steady state. The data from the Brindisi plant do not provide

a measurement of inlet flue gas, thus this input variable is estimated based on pressure drop in the absorber. The TCM data sets do not have continuous measurements of the CO_2 absorber inlet and outlet gas concentrations, since one single analyzer is utilized for all gas phase concentration measurements, in a cycling manner. The weaknesses of the two latter data sets are considered extra critical as both flue gas flow rate and absorber inlet CO_2 concentration are used as model input in the validation studies. If the abovementioned measures are incorrect, it will affect the performance of the whole process model and model outputs which are used for comparison to measured pilot plant data. This will give an incorrect indication of the reliability and confidence of the models, thus these are important issues to be aware of when analyzing experimental data and comparing simulation results.

Certain operational phenomena are not included in the dynamic model. For instance, possible flashing in the cross heat exchanger is neglected as this unit model assumes only liquid phase. Further the desorber model assumes solvent feed to be liquid phase only. However, cross heat exchanger flashing is often observed in pilot plant testing, especially for high rich CO_2 loadings. The consequence is therefore deviations in the simulated desorber inlet temperature and desorber temperature profiles. The simulated inlet temperature will be higher than that experimentally measured in the case of heat exchanger flashing, and the model will therefore predict instantaneous flashing and decreasing temperature in the upper part of the desorber packing. Further, TCM reported observations of foaming in the desorber in some of their experiments. This is believed to cause steam channeling and deviating desorber temperature profiles are therefore expected. The basic control systems are implemented according to process flow sheets. An evaluation of the simulated control system in the Gløshaugen pilot plant shows that the controllers are able to maintain process set-points as observed in the pilot plant, however, slightly more fluctuating control variables are observed in the pilot results while the simulated control variables behave more smoothly. This deviation is most likely caused by a delay in the real process, both in the measurement itself, the transfer of control signal and the valve action, which are all effects that are neglected in the model. The modeled controllers are therefore slightly idealized compared to the real plant. Further, some sub-models are developed for 30 wt% MEA only, e.g the VLE soft model, while most of the pilot plant experiments were conducted at slightly different MEA concentration ranging from about 27% to 34%. This may also cause deviations in the simulation results. However, two of the dynamic cases

at TCM were conducted for higher MEA concentrations; one for MEA addition where the concentration was increased from 30 wt% to 40 wt%, and the second a dynamic period performed at 40 wt% MEA. The model shows adequate agreement to the pilot plant measurements also for these cases, however, the slightly higher deviation is expected to improve if all sub-models are updated to accept varying MEA concentration.

Section 6.1 presented application of the Tiller pilot plant model developed in MATLAB to investigate various time constants at different locations of the process and determine its dominant dynamics. It is concluded that that the overall stabilization time of the process is up to 6 hours, even though the solvent residence time is only 2 - 3 hours. The fact that lean solvent is recirculated back to the absorber causes considerably higher stabilization times for operational changes that affects the solvent CO_2 loading. Thus, controlling solvent loading is important in order to reduce the stabilization time. Further, the effect of chemical reaction and heat and mass transfer rates in the absorber column on the overall process dynamics is believed to be very limited. This is also supported by the dynamic simulations of the Gløshaugen pilot plant using the equilibrium-stage model, which resulted in very similar process responses compared to the rate-based model. Finally, the reported stabilization times for set-point changes in flue gas flow rate are significantly lower compared to set-point changes in solvent flow rate and reboiler duty. The estimated 90% settling times for the response in absorbed CO_2 in the Tiller pilot plant are less than 1 hour, 3.5 - 6 hours and 3.5 - 4 hours for step changes in flue gas flow rate, solvent flow rate and reboiler duty, respectively.

Section 6.2 discussed various modes of flexible operation of an integrated CO_2 capture power plant based on variations in electricity demand and prices. The K-Spice model of the Brindisi pilot plant was used to simulate four different operating modes; load following, flue gas venting, varying solvent regeneration and solvent storage. It is concluded that the process reacts fast to power plant load changes, and it is able to stabilize at both part and full load operation. The operating mode of solvent storage gives satisfactory results when it comes to instantaneous and time average capture rate and energy performance in a varying electricity market. The CO_2 capture and energy performances are equal or even slightly improved compared to a base case where the capture plant is operated in a standard steady state manner at 90% capture rate. Solvent storage is also the only mode in the varying electricity price scenario which is able to keep the

capture rate at or above 90% at all times. However, considerable investments are required for solvent storage tanks and additional operating solvent. The modes of exhaust gas venting and varying solvent regeneration seem to work satisfactory and are easy to conduct without process modifications. However these modes rely on the possibility of relaxing the constraint of 90% capture rate for short periods and later increasing the capture rate above 90% in order to obtain a close to 90% time average capture rate. The maximum capture rate in the simulations of the two latter operating modes was close to 98%, where the energy requirement for regeneration starts to increase dramatically. Suboptimal conditions are observed in these simulations, consequently the operating modes of flue gas venting and varying solvent generation are not able to reach a 90% time average capture rate. However, only basic control of solvent and steam flow rates are applied in these simulations and a more advanced control system (such as MPC) is expected to improve the process performance during flexible operation in this manner. In practice a combination of the exhaust gas venting and varying regeneration mode is likely to be more optimal, where both the solvent flow rate and steam rate to the reboiler are controlled to set the optimal instantaneous capture rate and lean loading for the given conditions and electricity price. The time average capture rate of 90% is a constraint in such an optimization problem, while the operating cost is minimized.

7.2 Future work

For future improvements of the process model it is suggested to investigate new options for prediction of interface mass transfer coefficients for desorber conditions. This will improve the representation of the desorber column and give an improved fit of desorber temperature and concentration profiles. Some of the sub-models need to be expanded for possible variations of MEA concentrations, e.g. the VLE model. This will give a more versatile model which allows simulations using higher weight fractions of MEA. The sub-models for physical, chemical and thermodynamic properties should also be expanded for other solvent systems, as this is one of the main areas for future process improvement.

The available dynamic data for model validation is in general scarce. This thesis uses data from both the Gløshaugen and Brindisi pilot plants that are specifically designed for investigation of process dynamics. It is however highly encouraged

that dynamic data from larger plants are generated and made available for model validation and comparison.

The potential of flexible operation of the integrated power generation and CO_2 capture process should be investigated more thoroughly. Other possible operating modes and different ramp rates during load changes should be simulated in order to determine the operational limits of the capture process. The operational limits of the regeneration process in the solvent storage mode should be investigated in particular, to determine how far the regeneration section can be ramped down and operated at part load before it has to be stopped. Start-up and shut-down procedures should be developed in order to simulate possible on/off operation that is suggested in the literature to give economic savings. This mode of operation was in fact tested in the Brindisi pilot plant, where considerate re-pressurization and stabilization times were observed for start-up of the regeneration process.

The integration between CCS and power generation should also be investigated dynamically as the efficiency and flexibility of the integrated system is still not demonstrated. Further, the integrated power generation and PCC process should be coupled to economic models to study the sensitivity of electricity price variations during flexible operation.

The process model developed in MATLAB is proven adequate for dynamic simulations of PCC processes. It is regarded as a relevant basis for model predictive control and optimization purposes. For future work it is therefore suggested to apply this model for design and implementation of MPC systems. Model simplifications and reductions may be necessary in order to meet the demands of a dynamic optimization.

Bibliography

Afkhamipour, M. and Mofarahi, M. Comparison of rate-based and equilibrium-stage models of a packed column for post-combustion CO_2 capture using 2-amino-2-methyl-1-propanol (amp) solution. *International Journal of Greenhouse Gas Control*, 15:186–199, 2013.

Åkesson, J., Laird, C. D., Lavedan, G., Prölß, K., Tummescheit, H., Velut, S., and Zhu, Y. Nonlinear model predictive control of a CO_2 post-combustion absorption unit. *Chemical Engineering & Technology*, 35:445–454, 2012.

Arce, A., Mac Dowell, N., Shah, N., and Vega, L. F. Flexible operation of solvent regeneration systems for CO_2 capture processes using advanced control techniques: Towards operational cost minimisation. *International Journal of Greenhouse Gas Control*, 11:236–250, 2012.

Arora, S., Dhaliwal, S. S., and Kukreja, V. K. Solution of two point boundary value problems using orthogonal collocation on finite elements. *Applied Mathematics and Computation*, 171(1):358–370, 2005.

Biliyok, C., Lawal, A., Wang, M., and Seibert, F. Dynamic modelling, validation and analysis of post-combustion chemical absorption CO_2 capture plant. *International Journal of Greenhouse Gas Control*, 9:428–445, 2012.

Billet, R. and Schultes, M. Prediction og mass transfer columns with dumped and arranged packings: Updated summary of the calculation method of Billet and Schultes. *Chemical Engineering Research and Design*, 77(6):498–504, 1999.

Brigman, N., Shah, M. I., Falk-Pedersen, O., Cents, T., Smith, V., De Cazenove, T., Morken, A. K., Hvidsten, O. A., Chhaganlal, M., Feste, J. K., Lombardo, G., Bade, O. M., Knudsen, J., Subramoney, S. C., Fostås, B. F., de Koeijer, G., and Hamborg, E. S. Results of amine plant operations from 30 wt% and

40 wt% aqueous MEA testing at the CO_2 technology centre mongstad. *Energy Procedia*, 63:6012–6022, 2014.

Bui, M., Gunawan, I., Verheyen, V., Feron, P., Meuleman, E., and Adeloju, S. Dynamic modelling and optimisation of flexible operation in post-combustion CO_2 capture plants - A review. *Computers and Chemical Engineering*, 61:245–265, 2014.

Caplow, M. The reaction of CO_2 with ethanolamines. *Journal of the American Chemical Society*, 90(24):6795–6803, 1968.

Chalmers, H., Gibbins, J., and Leach, M. Valuing power plant flexibility with ccs: the case of post-combustion capture retrofits. *Mitigation and Adaptation Strategies for Global Change*, 17:621–649, 2012.

Cheng, S., Meisen, A., and Chakma, A. Predict amine solution properties accurately. *Hydrocarbon Processing*, 75(2):81–84, 1996.

Cohen, S. M., Rochelle, G. T., and Webber, M. E. Turning CO_2 capture on and off in response to electric grid demand: A baseline analysis of emissions and economics. *Journal of Energy Resources Technology*, 132(2):021003–1–021003–8., 2010.

Crooks, J. E. and Donnellan, J. P. Kinetics and mechanism of the reaction between carbon dioxide and amines in aqueous solution. *Journal of the Chemical Society, Perkin Transactions 2*, pages 331–333, 1989.

Cussler, E. L. *Diffusion: mass transfer in fluid systems.* Cambridge University Press, Cambridge, UK, 3rd edition, 2009.

Danckwerts, P. V. The reaction of CO_2 with ethanolamines. *Chemical Engineering Science*, 34:443–446, 1979.

Davison, J. Performance and costs of power plants with capture and storage of CO_2. *Energy*, 32(7):1163–1176, 2007.

DeCoursey, W. J. Enhancement factors for gas absorption with reversible reaction. *Chemical Engineering Science*, 37(10):1483–1489, 1982.

Dietl, K., Joos, A., and Schmitz, G. Dynamic analysis of the absorption/desorption loop of a carbon capture plant using an object-oriented approach. *Chemical Engineering and Processing: Process Intensification*, 52:132–139, 2012.

DiGuilio, R. M., Lee, R. J., Schaeffer, S. T., Brasher, L. L., and Teja, A. S. Densities and viscosities of the ethanolamines. *Journal of Chemical & Engineering Data*, 37(2):239–242, 1992.

Dugas, R. E. Pilot plant study of carbon dioxide capture by aqueous monoethanolamine. Diploma thesis, The University of Texas at Austin, USA, 2006.

Dutta, B. K. *Principles of Mass Transfer and Separation Processes*. PHI Learning Private Limited, New Delhi, India, 3rd edition, 2009.

Enaasen, N., Zangrilli, L., Mangiaracina, A., Mejdell, T., Kvamsdal, H. M., and Hillestad, M. Validation of a dynamic model of the Brindisi pilot plant. *Energy Procedia*, 63:1040–1054, 2014.

Faber, R., Köpcke, M., Biede, O., Knudsen, J. N., and Andersen, J. Open-loop step responses for the MEA post-combustion capture process: Experimental results from the Esbjerg pilot plant. *Energy Procedia*, 4:1427–1434, 2011.

Flø, N. E., Knuutila, H., Kvamsdal, H. M., and Hillestad, M. Dynamic model validation of the post-combustion CO_2 absorption process. *International Journal of Greenhouse Gas Control*, 41:127–141, 2015.

Freguia, S. Modeling of CO_2 removal from flue gases with monoethanolamine. Diploma thesis, The University of Texas at Austin, USA, 2002.

Garðarsdóttir, S. O., Normann, F., Andersson, K., Prölß, K., Emilsdóttir, S., and Johnsson, F. Post-combustion CO_2 capture applied to a state-of-the-art coal-fired power plant - The influence of dynamic process conditions. *International Journal of Greenhouse Gas Control*, 33:51–62, 2015.

Gáspár, J. and Cormoş, A.-M. Dynamic modeling and validation of absorber and desorber columns for post-combustion CO_2 capture. *Computers & Chemical Engineering*, 35(10):2044–2052, 2011.

Gáspár, J. and Cormoş, A.-M. Dynamic modeling and absorption capacity assessment of CO_2 capture process. *International Journal of Greenhouse Gas Control*, 8:45–55, 2012.

Gavhane, K. A. *Chemical Reaction Engineering II*. Nirali Prakashan, Pune, India, 5th edition, 2009.

Geankoplis, C. J. *Transport Processes and Separation Process Principles*. Prentice Hall, New Jersey, USA, 4th edition, 2003.

Greer, T., Bedelbayev, A., Igreja, J. M., Gomes, J. F., and Lie, B. A simulation study on the abatement of CO_2 emissions by de-absorption with monoethanolamine. *Environmental Technology*, 31(1):107–115, 2010.

Hamborg, E. S., Smith, V., Cents, T., Brigman, N., Falk-Pedersen, O., De Cazenove, T., Chhaganlal, M., Feste, J. K., Ullestad, Ø., Ulvatn, H., Gorset, O., Askestad, I., Gram, L. K., Fostås, B. F., Shah, M. I., Maxson, A., and Thimsen, D. Results from MEA testing at the CO_2 Technology Centre Mongstad. Part II: Verification of baseline results. *Energy Procedia*, 63:5994–6011, 2014.

Hangos, K. M. and Cameron, I. T. *Process Modelling and Model Analysis*. Academic Press, London, UK, 1st edition, 2001.

Hartono, A., Mba, E. O., and Svendsen, H. F. Prediction of N_2O solubility in alkanolamine solutions from the excess volume property. *Energy Procedia*, 37: 1744–1750, 2013.

Hartono, A., Mba, E. O., and Svendsen, H. F. Physical properties of partially CO_2 loaded aqueous monoethanolamine (MEA). *Journal of Chemical & Engineering Data*, 59:1808–1816, 2014.

Harun, N., Douglas, P. L., Ricardez-Sandoval, L., and Croiset, E. Dynamic simulation of MEA absorption processes for CO_2 capture from fossil fuel power plant. *Energy Procedia*, 4:1478–1485, 2011.

Harun, N., Nittaya, T., Douglas, P. L., Croiset, E., and Ricardez-Sandoval, L. Dynamic simulation of MEA absorption process for CO_2 capture from power plants. *International Journal of Greenhouse Gas Control*, 10:295–309, 2012.

IEA. Technology roadmap: Carbon capture and storage. Technical report, International Energy Agency, Paris, France, 2009.

IEA. Energy technology perspectives 2012. Pathways to a clean energy system. Technical report, International Energy Agency, Paris, France, 2012.

IPCC. Special report on carbon dioxide capture and storage. Technical report, Intergovernmental Panel on Climate Change, Geneva, Switzerland, 2005.

IPCC. Climate change 2014: Synthesis report. Technical report, Intergovernmental Panel on Climate Change, Geneva, Switzerland, 2014.

Jayarathna, S. A., Lie, B., and Melaaen, M. C. NEQ rate based modeling of an absorption column for post combustion CO_2 capturing. *Energy Procedia*, 4: 1797–1804, 2011.

Jayarathna, S. A., Lie, B., and Melaaen, M. C. Dynamic modelling of the absorber of a post-combustion CO_2 capture plant: Modelling and simulations. *Computers & Chemical Engineering*, 53:178–789, 2013a.

Jayarathna, S. A., Lie, B., and Melaaen, M. C. Amine based CO_2 capture plant: Dynamic modeling and simulations. *International Journal of Greenhouse Gas Control*, 14:282–290, 2013b.

Jayarathna, S. A., Lie, B., and Melaaen, M. C. Development of a dynamic model of a post combustion CO_2 capture process. *Energy Procedia*, 37:1760–1769, 2013c.

Karimi, M., Hillestad, M., and Svendsen, H. F. Investigation of the dynamic behavior of different stripper configurations for post-combustion CO_2 capture. *International Journal of Greenhouse Gas Control*, 7:230–239, 2012.

Kenig, E. Y., Schneider, R., and Górak, A. Reactive absorption: Optimal process design via optimal modelling. *Chemical Engineering Science*, 56(2):343–350, 2001.

Kim, I., Hoff, K. A., and Mejdell, T. Heat of absorption of CO_2 with aqueous solutions of MEA: New experimental data. *Energy Procedia*, 63:1446–1455, 2014.

Ko, J.-J., Tsai, T.-C., Lin, C.-Y., Wang, H.-M., and Li, M.-H. Diffusivity of nitrous oxide in aqueous alkanolamine solutions. *Journal of Chemical and Engineering Data*, 46(1):160–165, 2000.

Kohl, A. L. and Nielsen, R. B. *Gas purification*. Gulf Publishing Company, Houston, Texas, USA, 5th edition, 1997.

Kumar, P. S., Hogendoorn, J. A., Feron, P. H. M., and Versteeg, G. F. Approximate solution to predict the enhancement factor for the reactive absorption of a gas in a liquid flowing through a microporous membrane hollow fiber. *Journal of Membrane Science*, 213:231–245, 2003.

Kvamsdal, H. M. and Hillestad, M. Selection of model parameter correlations in a rate-based CO_2 absorber model amied for process simulation. *International Journal of Greenhouse Gas Control*, 11:11–20, 2012.

Kvamsdal, H. M. and Rochelle, G. T. Effects of the temperature bulge in CO_2 absorption from flue gas by aqueous monoethanolamine. *Industrial and Engineering Chemistry Research*, 47(3):867–875, 2008.

Kvamsdal, H. M., Jakobsen, J. P., and Hoff, K. A. Dynamic modeling and simulation of a CO_2 absorber column for post-combustion CO_2 capture. *Chemical Engineering and Processing: Process Intensification*, 48(1):135–144, 2009.

Lawal, A., Wang, M., Stephenson, P., and Yeung, H. Dynamic modelling of CO_2 absorption for post combustion capture in coal-fired power plants. *Fuel*, 88(12): 2455–2462, 2009a.

Lawal, A., Wang, M., Stephenson, P., and Yeung, H. Dynamic modelling and simulation of CO_2 chemical absorption process for coal-fired power plants. *Computer Aided Chemical Engineering*, 27:1725–1730, 2009b.

Lawal, A., Wang, M., Stephenson, P., Koumpouras, G., and Yeung, H. Dynamic modelling and analysis of post-combustion CO_2 chemical absorption process for coal-fired power plants. *Fuel*, 89(10):2791–2801, 2010.

Lawal, A., Wang, M., and Stephenson, P. Investigating the dynamic response of CO_2 chemical absorption process in enhanced-O_2 coal power plant with post-combustion CO_2 capture. *Energy Procedia*, 4:1035–1042, 2011.

Lawal, A., Wang, M., Stephenson, P., and Okwose, O. Demonstrating full-scale post-combustion CO_2 capture for coal-fired power plants through dynamic modelling and simulation. *Fuel*, 101:115–128, 2012.

Léonard, G., Mogador, B. C., Belletante, S., and Heyen, G. Dynamic modelling and control of a pilot plant for post-combustion CO_2 capture. *Computer Aided Chemical Engineering*, 32:451–456, 2013.

Lide, D. R. *CRC Handbook of Chemistry and Physics*. CRC Press, Boca Raton, Fl, USA, 66th edition, 1985.

Lienhard V, J. H. and Lienhard IV, J. H. *Heat transfer*. Dover Publications, USA, 4th edition, 2011.

Lin, Y.-J., Pan, T.-H., Wong, D. S.-H., Jang, S.-S., Chi, Y.-W., and Yeh, C.-H. Plantwide control of CO_2 capture by absorption and stripping using monoethanolamine solution. *Industrial & Engineering Chemistry Research*, 50(3): 1338–1345, 2011.

Lin, Y.-J., Wong, D. S.-H., Jang, S.-S., and Ou, J. J. Control strategies for flexible operation of power plant with CO_2 capture plant. *AIChE Journal*, 58 (9):2697–2704, 2012.

Luo, X., Hartono, A., Hussain, S., and Svendsen, H. Mass transfer and kinetics of carbon dioxide absorption into loaded aqueous monoethanolamine. *Chemical Engineering Science*, 123:57–69, 2015.

Mac Dowell, N. and Shah, N. The multi-period optimisation of an amine-based CO_2 capture process integrated with a super-critical coal-fired power station for flexible operation. *Computers and Chemical Engineering*, 74:169–183, 2015.

Mac Dowell, N., Samsatli, N.-J., and Shah, N. Dynamic modelling and analysis of an amine-based post-combustion CO_2 capture absorption column. *International Journal of Greenhouse Gas Control*, 12:247–258, 2013.

Ma'mun, S., Svendsen, H. F., Hoff, K. A., and Juliussen, O. Selection of new absorbents for carbon dioxide capture. *Energy Conversion and Management*, 48(1):251–258, 2007.

Mangiaracina, A., Zangrilli, L., Robinson, L., Kvamsdal, H. M., and Van Os, P. Octavius: Evaluation of flexibility and operability of amine based post combustion CO_2 capture at the Brindisi pilot plant. *Energy Procedia*, 63:1617–1636, 2014.

Mathonat, C., Majer, V., Mather, A. E., and Grolier, J. P. E. Use of flow calorimetry for determining enthalpies of absorption and the solubility of CO_2 in aqueous monoethanolamine solutions. *Industrial & Engineering Chemistry Research*, 37 (10):4136–4141, 1998.

Monteiro, J. G. M.-S. *Contributions to kinetics and equilibrium of CO_2 absorption into N,N-diethyl-ethanomelamine (DEEA), N-Methyl-1,3-propane-diamine (MAPA) and their blends*. PhD thesis, NTNU, Norway, 2014.

Monteiro, J. G. M.-S., Pinto, D. D. D., Zaidy, S. A. H., Hartono, A., and Svendsen, H. F. VLE data and modelling of aqueous N,N-diethylethanolamine (DEEA) solutions. *International Journal of Greenhouse Gas Control*, 19:432–440, 2013.

Nittaya, T., Douglas, P. L., Croiset, E., and Richardez-Sandoval, L. Dynamic modelling and control of MEA absorption processes for CO_2 capture from power plants. *Fuel*, 116:672–691, 2014a.

Nittaya, T., Douglas, P. L., Croiset, E., and Richardez-Sandoval, L. Dynamic modelling and evaluation of an industrial-scale CO_2 capture plant using monoethanolamine absorption processes. *Industrial & Engineering Chemistry Research*, 53(28):11411–11426, 2014b.

Panahi, M. and Skogestad, S. Economically efficient operation of CO_2 capturing process. Part II. Design of control layer. *Chemical Engineering and Processing*, 52:112–124, 2012.

Peng, J., Lextrait, S., Edgar, T. F., and Eldridge, R. B. A comparison of steady-state equilibrium and rate-based models for packed reactive distillation columns. *Industrial & Engineering Chemistry Research*, 41:2735–2744, 2002.

Peng, J., Edgar, T. F., and Eldridge, R. B. Dynamic rate-based and equilibrium models for a packed reactive distillation column. *Chemical Engineering Science*, 58(12):2671–2680, 2003.

Pinto, D. D. D., Knuutila, H., Fytianos, G., Haugen, G., Mejdell, T., and Svendsen, H. F. CO_2 post combustion capture with a phase change solvent. Pilot plant campaign. *International Journal of Greenhouse Gas Control*, 31:153–164, 2014.

Posch, S. and Haider, M. Dynamic modeling of CO_2 absorption from coal-fired power plants into an aqueous monoethanolamine solution. *Chemical Engineering Research and Design*, 91(6):977–987, 2013.

Prölß, K., Tummescheit, H., Velut, S., and Åkesson, J. Dynamic model of a post-combustion absorption unit for use in a non-linear model predictive control scheme. *Energy Procedia*, 4:2620–2627, 2011.

Razi, N., Bolland, O., and Svendsen, H. Review of design correlations for CO_2 absorption into MEA using structured packings. *International Journal of Greenhouse Gas Control*, 9:193–219, 2012.

Reid, R. C., Prausnitz, J. M., and Poling, B. E. *The properties of Gases and Liquids*. McGraw-Hill Book Company, New York, USA, 4th edition, 1987.

Rocha, J. A., Bravo, J. L., and Fair, J. R. Distillation columns containing structured packings: A comprehensive model for their performance. 1. Hydraulic models. *Industrial & Engineering Chemistry Research*, 32:641–651, 1993.

Rocha, J. A., Bravo, J. L., and Fair, J. R. Distillation columns containing structured packings: A comprehensive model for their performance. 2. Mass-transfer model. *Industrial & Engineering Chemistry Research*, 35:1660–1667, 1996.

Sada, E., Kumazawa, H., and Butt, M. A. Solubility and diffusivity of gases in aqueous solutions of amines. *Journal of Chemical and Engineering Data*, 23(2): 161–163, 1978.

SaskPower. Boundary Dam Carbon Capture Project, June 2015. URL `http://saskpowerccs.com/ccs-projects/boundary-dam-carbon-capture-project/`.

Singh, S. K. *Process control: Concepts, Dynamics And Applications*. PHI Learning Private Ltd, New Delhi, India, 2009.

Taylor, R. and Krishna, R. *Multicomponent Mass Transfer*. Wiley, New York, USA, 1993.

Tobiesen, F. A., Svendsen, H. F., and Juliussen, O. Experimental validation of a rigorous absorber model for CO_2 postcombustion capture. *AIChE Journal*, 53 (4):846–865, 2007.

Tobiesen, F. A., Juliussen, O., and Svendsen, H. F. Experimental validation of a rigorous desorber model for CO_2 post-combustion capture. *Chemical Engineering Science*, 63(10):2641–2656, 2008.

Ugochukwu, E. A., Ghondal, S., Hessen, E. T., Haug-Warberg, T., Hartono, A., Hoff, K. A., and Svendsen, H. F. Equilibrium in the H_2O-MEA-CO_2 system: New data and modeling. *Proceedings of the 1st Post Combustion Capture Conference, Abu Dhabi, United Arab Emirates*, 2011.

Vegeais, J. A. and Stadtherr, M. A. Parallel processing strategies for chemical process flowsheeting. *AIChE Journal*, 38(9):1399–1407, 1992.

Versteeg, G. F. and van Swaaij, W. P. M. Solubility and diffusivity of acid gases (CO_2,N_2O) in aqueous alkanolamine solutions. *Journal of Chemical & Engineering Data*, 33(1):29–34, 1988.

Wang, M., Lawal, A., Stephenson, P., Sidders, J., and Ramshaw, C. Post-combustion CO_2 capture with chemical absorption: A state-of-the-art review. *Chemical Engineering Research and Design*, 89(9):1609–1624, 2011.

Westerberg, A. W. and Piela, P. C. Equation-based process modeling. Technical report, Department of Chemical Engineering and the Engineering Design Research Center, Carnegie Mellon University, Pittsburgh, PA, USA, 1994.

Whitman, W. G. The two-film theory of gas absorption. *Chemical and Metallurgical Engineering*, 29:146–148, 1923.

Wiley, D. E., Ho, M. T., and Donde, L. Technical and economic opportunities for flexible CO_2 capture at australian black coal fired power plants. *Energy Procedia*, 4:1893–1900, 2011.

Xie, H.-B., Zhou, Y., Zhang, Y., and Johnson, J. K. Reaction mechanism of monoethanolamine with CO_2 in aqueous solution from molecular modeling. *Journal of Physical Chemistry A*, 114(43):11844–11852, 2010.

Ziaii, S., Rochelle, G. T., and Edgar, T. F. Dynamic modeling to minimize energy use for CO_2 capture in power plants by aqueous monoethanolamine. *Industrial & Engineering Chemistry Research*, 48(13):6105–6111, 2009.

Ziaii, S., Rochelle, G. T., and Edgar, T. F. Optimum design and control of amine scrubbing in response to electricity and CO_2 prices. *Energy Procedia*, 4:1683–1690, 2011.

Appendix A

Model development

A.1 The mixing tank

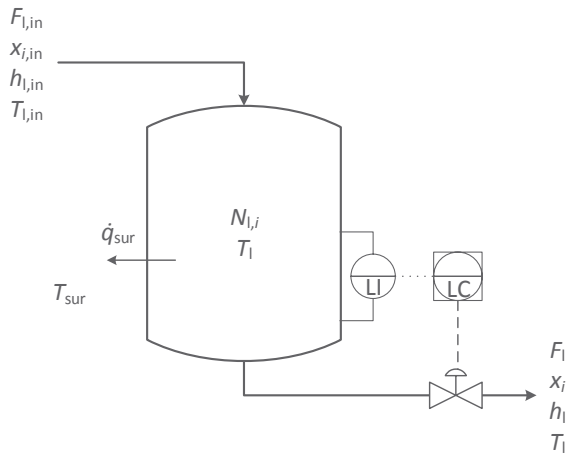

FIGURE A.1: Illustration of the mixing tank model.

A.1.1 Assumptions

- only liquid phase is considered and vaporization is disregarded
- perfectly mixed liquid phase
- no reactions occurring
- level control

A.1.2 Component material balance

The component material balance is given by:

$$\frac{dN_{\mathrm{l},i}}{dt} = F_{\mathrm{l,in}}x_{i,\mathrm{in}} - F_{\mathrm{l}}x_i \tag{A.1}$$

where $N_{\mathrm{l},i}$ is the molar hold-up of component i, $F_{\mathrm{l,in}}$ and F_{l} are the inlet and outlet molar flow rates, respectively, and $x_{i,\mathrm{in}}$ and x_i are the inlet and outlet mole fractions.

A.1.3 Energy balance

The mixing tank energy balance is given by:

$$\frac{dU_{\mathrm{l}}}{dt} = F_{\mathrm{l,in}}h_{\mathrm{l,in}} - F_{\mathrm{l}}h_{\mathrm{l}} - A_{\mathrm{sur}}\dot{q}_{\mathrm{sur}} \tag{A.2}$$

where U is internal energy, $h_{\mathrm{l,in}}$ and h_{l} are the molar enthalpies of inlet and outlet streams, A_{sur} is the vessel area exposed to the surroundings and $\dot{q}_{\mathrm{sur}}$ is the heat loss flux to surroundings.

For incompressible fluids the change in internal energy is assumed to equal change in enthalpy, thus

$$dU = dH - d(PV) \approx dH = d(N_{\mathrm{tot}}h) = N_{\mathrm{tot}}dh + hdN_{\mathrm{tot}} \tag{A.3}$$

Further, no phase change is occurring inside the control volume, thus

$$dh = C_p dT \tag{A.4}$$

which inserted into Equation A.2 yields:

$$\frac{dU_{\mathrm{l}}}{dt} = N_{\mathrm{l,tot}}C_{\mathrm{p,l}}\frac{dT_{\mathrm{l}}}{dt} + h_{\mathrm{l}}\frac{dN_{\mathrm{l,tot}}}{dt} = F_{\mathrm{l,in}}h_{\mathrm{l,in}} - F_{\mathrm{l}}h_{\mathrm{l}} - A_{\mathrm{sur}}\dot{q}_{\mathrm{sur}} \tag{A.5}$$

The overall material balance given by

$$\frac{dN_{\mathrm{l,tot}}}{dt} = F_{\mathrm{l,in}} - F_{\mathrm{l}} \tag{A.6}$$

is inserted into Equation A.5:

$$N_{\mathrm{l,tot}} C_{p,\mathrm{l}} \frac{dT_{\mathrm{l}}}{dt} = F_{\mathrm{l,in}}(h_{\mathrm{l,in}} - h_{\mathrm{l}}) - A_{\mathrm{sur}} \dot{q}_{\mathrm{sur}} \tag{A.7}$$

Enthalpy is defined by

$$h = h_0 + \int_{T_0}^{T} C_p dT \approx h_0 + C_p(T_0 - T) \tag{A.8}$$

which allows $(h_{\mathrm{l,in}} - h_{\mathrm{l}})$ to be replaced by $C_{\mathrm{p,l}}(T_{\mathrm{l,in}} - T_{\mathrm{l}})$. Further, $\dot{q}_{\mathrm{sur}}$ represents heat loss to the environment which is expressed by:

$$\dot{q}_{\mathrm{sur}} = \hat{h}_{\mathrm{sur}}(T_{\mathrm{l}} - T_{\mathrm{sur}}) \tag{A.9}$$

The final temperature equation for solvent in mixing tank is therefore given by:

$$N_{\mathrm{l,tot}} C_{p,\mathrm{l}} \frac{dT_{\mathrm{l}}}{dt} = F_{\mathrm{l,in}} C_{\mathrm{p,l}}(T_{\mathrm{l,in}} - T_{\mathrm{l}}) - A_{\mathrm{sur}} \hat{h}_{\mathrm{sur}}(T_{\mathrm{l}} - T_{\mathrm{sur}}) \tag{A.10}$$

A.2 The flash tank

A.2.1 Assumptions

- gas and liquid phases are considered
- both phases are perfectly mixed
- no reactions occurring
- ideal gas phase (due to low pressure)
- vapor-liquid equilibrium
- level control
- temperature and pressure controller is included for the condenser

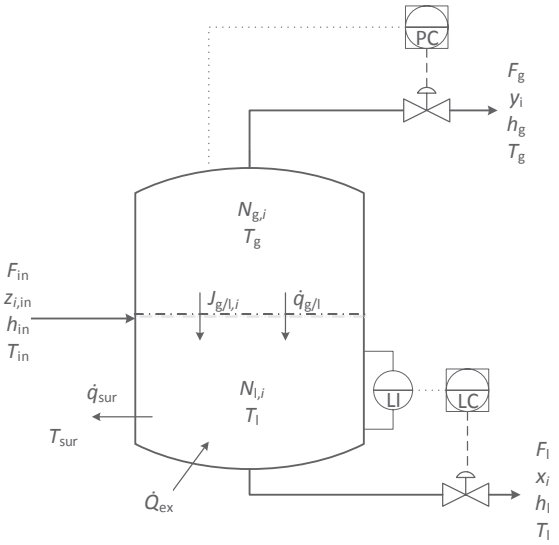

FIGURE A.2: Illustration of the flash tank model.

A.2.2 Component material balances

The liquid phase component material balance is given by:

$$\frac{dN_{l,i}}{dt} = F_{l,in}x_{i,in} - F_l x_i + A_{g/l}J_{g/l,i} \tag{A.11}$$

where $A_{g/l}$ is the interface area between gas and liquid, and $J_{g/l,i}$ is the interface molar flux of component i defined from gas to liquid phase.

Similarly, the gas phase component material balance is given by:

$$\frac{dN_{g,i}}{dt} = F_{g,in}y_{i,in} - F_g y_i - A_{g/l}J_{g/l,i} \tag{A.12}$$

A.2.3 Energy balances

The liquid phase energy balance is developed from:

$$\frac{dU_l}{dt} = F_{l,in}h_{l,in} - F_l h_l + A_{g/l}\sum_{k=1}^{nc} J_{g/l,k}h_{g,k} + A_{g/l}\dot{q}_{g/l} - A_{sur}\dot{q}_{sur} + \dot{Q}_{ex} \tag{A.13}$$

where h_g is the molar enthalpy of the outlet gas stream, $\dot{q}_{g/l}$ is the heat flux from gas to liquid and $\dot{Q}_{ex}$ is heat supplied from external source.

Equation A.3 is assumed to be valid for incompressible fluids, and no phase change is assumed to occur inside the control volume (Equation A.4), thus

$$\begin{aligned}\frac{dU_l}{dt} &= N_{l,tot}C_{p,l}\frac{dT_l}{dt} + h_l\frac{dN_{l,tot}}{dt} \\ &= F_{l,in}h_{l,in} - F_l h_l + A_{g/l}\sum_{k=1}^{nc} J_{g/l,k}h_{g,k} + A_{g/l}\dot{q}_{g/l} - A_{sur}\dot{q}_{sur} + \dot{Q}_{ex}\end{aligned} \tag{A.14}$$

The overall material balance given by

$$\frac{dN_{l,tot}}{dt} = F_{l,in} - F_l + A_{g/l}\sum_{k=1}^{nc} J_{g/l,k} \tag{A.15}$$

is inserted into Equation A.14:

$$N_{l,tot}C_{p,l}\frac{dT_l}{dt} = F_{l,in}(h_{l,in} - h_l) + A_{g/l}\sum_{k=1}^{nc} J_{g/l,k}(h_{g,k} - h_{l,k}) + A_{g/l}\dot{q}_{g/l} - A_{sur}\dot{q}_{sur} + \dot{Q}_{ex} \tag{A.16}$$

$(h_{l,in} - h_l)$ is eliminated by the definition of enthalpy in Equation A.8. $\dot{q}_{out}$ is given by Equation A.9, while $\dot{q}_{g/l}$ represents heat transfer between gas and liquid phase given by

$$\dot{q}_{g/l} = -\hat{h}_{g/l}(T_l - T_g) \tag{A.17}$$

The specific enthalpy difference between gas and liquid phase represents heat of absorption for CO_2 and heat of vaporization for H_2O and MEA:

$$(h_{g,CO_2} - h_{l,CO_2}) = \Delta h^{abs}_{CO_2} \tag{A.18}$$

$$(h_{g,H_2O} - h_{l,H_2O}) = \Delta h^{vap}_{H_2O} \tag{A.19}$$

$$(h_{g,MEA} - h_{l,MEA}) = \Delta h^{vap}_{MEA} \tag{A.20}$$

Inserted into Equation A.16 yields:

$$\begin{aligned}N_{l,tot}C_{p,l}\frac{dT_l}{dt} &= F_{l,in}C_{p,l}(T_{l,in} - T_l) + A_{g/l}\Delta h^{abs}_{CO_2}J_{g/l,CO_2} \\ &+ A_{g/l}\Delta h^{vap}_{H_2O}J_{g/l,H_2O} + A_{g/l}\Delta h^{vap}_{MEA}J_{g/l,MEA} \\ &- A_{g/l}\hat{h}_{g/l}(T_l - T_g) - A_{sur}\hat{h}_{sur}(T_l - T_{sur}) + \dot{Q}_{ex}\end{aligned} \tag{A.21}$$

The gas phase energy balance is developed from:

$$\frac{dU_{\mathrm{g}}}{dt} = F_{\mathrm{g,in}}h_{\mathrm{g,in}} - F_{\mathrm{g}}h_{\mathrm{g}} - A_{\mathrm{g/l}}\sum_{k=1}^{\mathrm{nc}} J_{\mathrm{g/l},k}h_{g,k} - A_{\mathrm{g/l}}\dot{q}_{\mathrm{g/l}} - A_{\mathrm{sur}}\dot{q}_{\mathrm{sur}} + Q_{\mathrm{ex}} \tag{A.22}$$

The change in internal energy for gases is given by $du = C_v dT$, thus

$$dU = d(N_{\mathrm{tot}}u) = N_{\mathrm{tot}}C_v dT + u dN_{\mathrm{tot}} \tag{A.23}$$

which inserted into Equation A.22 yields:

$$\begin{aligned}\frac{dU_{\mathrm{g}}}{dt} &= N_{\mathrm{g,tot}}C_{\mathrm{v,g}}\frac{dT_{\mathrm{g}}}{dt} + u_{\mathrm{g}}\frac{dN_{\mathrm{g,tot}}}{dt} \\ &= F_{\mathrm{g,in}}h_{\mathrm{g,in}} - F_{\mathrm{g}}h_{\mathrm{g}} - A_{\mathrm{g/l}}\sum_{k=1}^{\mathrm{nc}} J_{\mathrm{g/l},k}h_{\mathrm{g,k}} - A_{\mathrm{g/l}}\dot{q}_{\mathrm{g/l}} - A_{\mathrm{sur}}\dot{q}_{\mathrm{sur}} + \dot{Q}_{\mathrm{ex}}\end{aligned} \tag{A.24}$$

The overall material balance given by

$$\frac{dN_{\mathrm{g,tot}}}{dt} = F_{\mathrm{g,in}} - F_{\mathrm{g}} - A_{\mathrm{g/l}}\sum_{k=1}^{\mathrm{nc}} J_{\mathrm{g/l},k} \tag{A.25}$$

is inserted into Equation A.24. Further, the internal energy is defined by $U = H - PV$, where $PV = NRT$. Thus $u = h - RT$ and:

$$N_{\mathrm{g,tot}}C_{\mathrm{v,g}}\frac{dT_{\mathrm{g}}}{dt} = F_{\mathrm{g,in}}(h_{\mathrm{g,in}} - h_{\mathrm{g}}) + RT_{\mathrm{g}}(F_{\mathrm{g,in}} - F_{\mathrm{g}} - A_{\mathrm{g/l}}\sum_{k=1}^{\mathrm{nc}} J_{\mathrm{g/l},k}) - A_{\mathrm{g/l}}\dot{q}_{\mathrm{g/l}} - A_{\mathrm{sur}}\dot{q}_{\mathrm{sur}} + \dot{Q}_{\mathrm{ex}} \tag{A.26}$$

By using the definition of enthalpy from Equation A.8 and the expressions for $\dot{q}_{\mathrm{out}}$ and $\dot{q}_{\mathrm{g/l}}$ in Equation A.9 and A.17 the following general gas phase flash tank temperature equation is derived:

$$\begin{aligned}N_{\mathrm{g,tot}}C_{\mathrm{v,g}}\frac{dT_{\mathrm{g}}}{dt} &= F_{\mathrm{g,in}}C_{\mathrm{p,g}}(T_{\mathrm{g,in}} - T_{\mathrm{g}}) + RT_{\mathrm{g}}(F_{\mathrm{g,in}} - F_{\mathrm{g}} - A_{\mathrm{g/l}}\sum_{k=1}^{\mathrm{nc}} J_{\mathrm{g/l},k}) \\ &\quad + A_{\mathrm{g/l}}\hat{h}_{\mathrm{g/l}}(T_{\mathrm{l}} - T_{\mathrm{g}}) - A_{\mathrm{sur}}\hat{h}_{\mathrm{sur}}(T_{\mathrm{g}} - T_{\mathrm{sur}}) + \dot{Q}_{\mathrm{ex}}\end{aligned} \tag{A.27}$$

The reboiler liquid phase temperature equation is given by Equation A.21 directly. The reboiler has however no inlet gas flow, and no external heat heat supply to the gas or heat loss to the surroundings is assumed, thus the reboiler gas phase temperature equation is simplified to:

$$N_{\mathrm{g,tot}} C_{\mathrm{v,g}} \frac{dT_{\mathrm{g}}}{dt} = RT_{\mathrm{g}}\left(-F_{\mathrm{g}} - A_{\mathrm{g/l}} \sum_{k=1}^{\mathrm{nc}} J_k^{\mathrm{g}\to\mathrm{l}}\right) + A_{\mathrm{g/l}} \hat{h}_{\mathrm{g/l}} (T_{\mathrm{l}} - T_{\mathrm{g}}) \tag{A.28}$$

The condenser has ho inlet liquid flow and no external heat supply to the liquid phase is assumed, thus Equation A.21 reduces to:

$$\begin{aligned} N_{\mathrm{l,tot}} C_{\mathrm{p,l}} \frac{dT_{\mathrm{l}}}{dt} = {} & A_{\mathrm{g/l}} \Delta h^{\mathrm{abs}}_{\mathrm{CO_2}} J_{\mathrm{g/l,CO_2}} + A_{\mathrm{g/l}} \Delta h^{\mathrm{vap}}_{\mathrm{H_2O}} J_{\mathrm{g/l,H_2O}} + A_{\mathrm{g/l}} \Delta h^{\mathrm{vap}}_{\mathrm{MEA}} J_{\mathrm{g/l,MEA}} \\ & - A_{\mathrm{g/l}} \hat{h}_{\mathrm{g/l}} (T_{\mathrm{l}} - T_{\mathrm{g}}) - A_{\mathrm{sur}} \hat{h}_{\mathrm{sur}} (T_{\mathrm{l}} - T_{\mathrm{sur}}) \end{aligned} \tag{A.29}$$

The condenser gas phase is assumed to have negligible heat loss to the surroundings, thus Equation A.27 reduces to:

$$N_{\mathrm{g,tot}} C_{\mathrm{v,g}} \frac{dT_{\mathrm{g}}}{dt} = F_{\mathrm{g,in}} C_{\mathrm{p,g}} (T_{\mathrm{g,in}} - T_{\mathrm{g}}) + RT_{\mathrm{g}} \left(F_{\mathrm{g,in}} - F_{\mathrm{g}} - A_{\mathrm{g/l}} \sum_{k=1}^{\mathrm{nc}} J_{\mathrm{g/l},k}\right) + A_{\mathrm{g/l}} \hat{h}_{\mathrm{g/l}} (T_{\mathrm{l}} - T_{\mathrm{g}}) + \dot{Q}_{\mathrm{ex}} \tag{A.30}$$

A.3 The general column

A.3.1 Assumptions

- two-phase counter-current flow
- one-dimensional plug flow regime for both phases (back mixing is disregarded)
- radial gradients in temperature and concentration are neglected
- ideal gas phase (due to low pressure)
- linear pressure drop with fixed outlet pressure

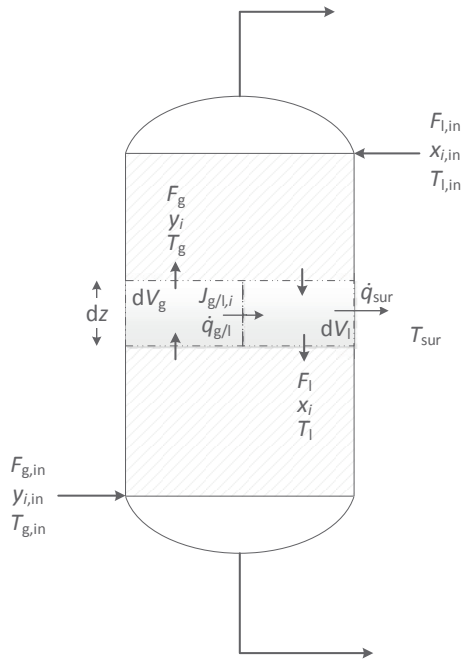

FIGURE A.3: Illustration of the general column model.

- instantaneous momentum balance ($\frac{\partial P}{\partial t} = 0$)
- mass and heat transfer are described by the two-film theory
- no accumulation in gas and liquid films
- equilibrium occurs at the gas/liquid interface
- chemical reactions are restricted to the liquid-film only
- liquid film CO_2 reactions are accounted for by an enhancement factor in the overall CO_2 mass transfer coefficient
- interface fluxes of CO_2, H_2O and MEA are allowed in both directions

A.3.2 Overall material balances

The overall material balance for liquid phase for control volume dV of the packed column is given by:

$$\frac{dN_{tot,\mathrm{l}}}{dt} = (F + dF)_{\mathrm{l}} - F_{\mathrm{l}} + A_{\mathrm{g/l}} \sum_{k=1}^{\mathrm{nc}} J_{\mathrm{g/l},k} \tag{A.31}$$

Equation A.31 divided by control volume dV yields:

$$\varepsilon_{\mathrm{l}} \frac{d}{dt}\left(\frac{N_{tot,\mathrm{l}}}{dV_{\mathrm{l}}}\right) = \frac{(F + dF)_{\mathrm{l}} - F_{\mathrm{l}}}{dV} + \frac{A_{\mathrm{g/l}}}{dV} \sum_{k=1}^{\mathrm{nc}} J_{\mathrm{g/l},k} \tag{A.32}$$

where $dV_{\mathrm{l}} = \varepsilon_{\mathrm{l}} dV$ is the liquid part of the control volume and ε_{l} is the liquid hold-up fraction of the total volume. $dV = Adz$ where A is the column cross sectional area. The limit $dz \to 0$ $\frac{(F+dF)_{\mathrm{l}} - F_{\mathrm{l}}}{Adz} = \frac{\partial F_{\mathrm{l}}}{A\partial z}$ yields:

$$\varepsilon_{\mathrm{l}} \frac{\partial C_{\mathrm{l,tot}}}{\partial t} = \frac{\partial F_{\mathrm{l}}}{A\partial z} + a_{\mathrm{g/l}} \sum_{k=1}^{\mathrm{nc}} J_{\mathrm{g/l},k} \tag{A.33}$$

$a_{\mathrm{g/l}}$ is the specific area of the packing material in $[\mathrm{m}^2/\mathrm{m}^3]$.

It is assumed that $\frac{\partial C_{\mathrm{tot,l}}}{\partial t} = 0$ and $\frac{F_{\mathrm{l}}}{A}$ is the molar flux of liquid through the column (G_{l}). The final material balance for the liquid phase in a packed column is therefore given by:

$$0 = \frac{\partial G_{\mathrm{l}}}{\partial z} + a_{\mathrm{g/l}} \sum_{k=1}^{\mathrm{nc}} J_{\mathrm{g/l},k} \tag{A.34}$$

Similarly, the overall material balance for gas phase for control volume dV of a packed column is given by:

$$\frac{dN_{tot,\mathrm{g}}}{dt} = (F + dF)_{\mathrm{g}} - F_{\mathrm{g}} - A_{\mathrm{g/l}} \sum_{k=1}^{\mathrm{nc}} J_{\mathrm{g/l},k} \tag{A.35}$$

Equation A.35 divided by control volume dV, where $dV_{\mathrm{g}} = \varepsilon_{\mathrm{g}} dV$, $dV = Adz$ and $\lim dz \to 0$ yields:

$$\varepsilon_{\mathrm{g}} \frac{\partial C_{\mathrm{g,tot}}}{\partial t} = -\frac{\partial F_{\mathrm{g}}}{A\partial z} - a_{\mathrm{g/l}} \sum_{k=1}^{\mathrm{nc}} J_{\mathrm{g/l},k} \tag{A.36}$$

$\frac{F_g}{A}$ is the molar flux of gas through the column (G_g). The ideal gas law is assumed such that $C_{\mathrm{g,tot}} = \frac{P}{RT_{\mathrm{g}}}$ and:

$$\varepsilon_{\mathrm{g}}\left(\frac{1}{RT_{\mathrm{g}}}\frac{\partial P}{\partial t}+\frac{P}{R}\frac{\partial\left(\frac{1}{T_{\mathrm{g}}}\right)}{\partial t}\right)=-\frac{\partial G_{\mathrm{g}}}{\partial z}-a_{\mathrm{g/l}}\sum_{k=1}^{\mathrm{nc}}J_{\mathrm{g/l},k} \tag{A.37}$$

The pressure is assumed to change instantaneously, thus $\frac{\partial P}{\partial t}=0$, and the final material balance for gas flowing through a packed column is:

$$0=-\frac{\partial G_{\mathrm{g}}}{\partial z}+\varepsilon_{\mathrm{g}}\frac{C_{\mathrm{g,tot}}}{T_{\mathrm{g}}}\frac{\partial T_{\mathrm{g}}}{\partial t}-a_{\mathrm{g/l}}\sum_{k=1}^{\mathrm{nc}}J_{\mathrm{g/l},k} \tag{A.38}$$

A.3.3 Component mass balances

The material balance for component i in liquid phase for control volume dV is given by:

$$\frac{dN_{\mathrm{l},i}}{dt}=(F+dF)_{\mathrm{l},i}-F_{\mathrm{l},i}+A_{\mathrm{g/l}}J_{\mathrm{g/l},i} \tag{A.39}$$

Divided by control volume dV, where $dV_{\mathrm{l}}=\varepsilon_{\mathrm{l}}dV$ yields:

$$\varepsilon_{\mathrm{l}}\frac{d}{dt}\left(\frac{N_{\mathrm{l},i}}{dV_{\mathrm{l}}}\right)=\frac{(F+dF)_{\mathrm{l},i}-F_{\mathrm{l},i}}{dV}+\frac{A_{\mathrm{g/l}}}{dV}J_{\mathrm{g/l},i} \tag{A.40}$$

$dV=Adz$ and $\lim dz\to 0$ gives:

$$\varepsilon_{\mathrm{l}}\frac{\partial C_{\mathrm{l},i}}{\partial t}=\frac{\partial(F_{\mathrm{l}}x_i)}{A\partial z}+a_{\mathrm{g/l}}J_{\mathrm{g/l},i} \tag{A.41}$$

$\frac{F_{\mathrm{l}}}{A}$ is the molar flux of gas through the column (G_{l}). Using the chain rule of derivatives, the concentration balance is transferred into a mole balance:

$$\varepsilon_{\mathrm{l}}\left(C_{\mathrm{l,tot}}\frac{\partial x_i}{\partial t}+x_i\frac{\partial C_{\mathrm{l,tot}}}{\partial t}\right)=G_{\mathrm{l}}\frac{\partial x_i}{\partial z}+x_i\frac{\partial G_{\mathrm{l}}}{\partial z}+a_{\mathrm{g/l}}J_{\mathrm{g/l},i} \tag{A.42}$$

$$\varepsilon_{\mathrm{l}}C_{\mathrm{l,tot}}\frac{\partial x_i}{\partial t}=G_{\mathrm{l}}\frac{\partial x_i}{\partial z}-x_i\left(\varepsilon_{\mathrm{l}}\frac{\partial C_{\mathrm{l,tot}}}{\partial t}-\frac{\partial G_{\mathrm{l}}}{\partial z}\right)+a_{\mathrm{g/l}}J_{\mathrm{g/l},i} \tag{A.43}$$

The total liquid material balance where $\varepsilon_{\mathrm{l}}\frac{\partial C_{\mathrm{l,tot}}}{\partial t} - \frac{\partial G_{\mathrm{l}}}{\partial z} = a_{\mathrm{g/l}}\sum_{k=1}^{\mathrm{nc}} J_{\mathrm{g/l},k}$ (Equation A.34) is inserted into Equation A.43 to yield the final component material balance of liquid phase:

$$\varepsilon_{\mathrm{l}} C_{\mathrm{l,tot}}\frac{\partial x_i}{\partial t} = G_{\mathrm{l}}\frac{\partial x_i}{\partial z} - x_i a_{\mathrm{g/l}}\sum_{k=1}^{\mathrm{nc}} J_{\mathrm{g/l},k} + a_{\mathrm{g/l}} J_{\mathrm{g/l},i} \tag{A.44}$$

The material balance for component i in gas phase for control volume dV is given by:

$$\frac{dN_{\mathrm{g},i}}{dt} = (F + dF)_{\mathrm{g},i} - F_{\mathrm{g},i} - A_{\mathrm{g/l}} J_{\mathrm{g/l},i} \tag{A.45}$$

Divided by control volume dV, where $dV_{\mathrm{g}} = \varepsilon_{\mathrm{g}} dV$, $dV = Adz$ and $\lim dV \to 0$ yields:

$$\varepsilon_{\mathrm{g}} C_{\mathrm{g,tot}}\frac{\partial y_i}{\partial t} = -G_{\mathrm{g}}\frac{\partial y_i}{\partial z} - y_i\left(\varepsilon_{\mathrm{g}}\frac{\partial C_{\mathrm{g,tot}}}{\partial t} + \frac{\partial G_{\mathrm{g}}}{\partial z}\right) - a_{\mathrm{g/l}} J_{\mathrm{g/l},i} \tag{A.46}$$

Inserting the expression for total gas material balance (Equation A.38) where $\varepsilon_{\mathrm{g}}\frac{\partial C_{\mathrm{g,tot}}}{\partial t} = -\frac{\partial F_{\mathrm{g}}}{A\partial z} - a_{\mathrm{g/l}}\sum_{k=1}^{\mathrm{nc}} J_{\mathrm{g/l},k}$ gives the final component material balance for gas phase:

$$\varepsilon_{\mathrm{g}} C_{\mathrm{g,tot}}\frac{\partial y_i}{\partial t} = -G_{\mathrm{g}}\frac{\partial y_i}{\partial z} + y_i a_{\mathrm{g/l}}\sum_{k=1}^{\mathrm{nc}} J_{\mathrm{g/l},k} - a_{\mathrm{g/l}} J_{\mathrm{g/l},i} \tag{A.47}$$

A.3.4 Energy balances

The energy balance for liquid phase in control volume dV is given by:

$$\frac{dU_{\mathrm{l}}}{dt} = (F + dF)_{\mathrm{l}}(h + dh)_{\mathrm{l}} - F_{\mathrm{l}} h_{\mathrm{l}} + A_{\mathrm{g/l}}\sum_{k=1}^{\mathrm{nc}} J_{\mathrm{g/l},k} h_{\mathrm{g,k}} + A_{\mathrm{g/l}}\dot{q}_{\mathrm{g/l}} - A_{\mathrm{out}}\dot{q}_{\mathrm{out}} \tag{A.48}$$

Equation A.3 and A.4 is used for incompressible fluids, thus

$$N_{\text{tot,l}} C_{p,l} \frac{dT_l}{dt} + h_l \frac{N_{\text{tot,l}}}{dt} = (F + dF)_{\text{l}}(h + dh)_{\text{l}} - F_{\text{l}} h_{\text{l}} + A_{\text{g/l}} \sum_{k=1}^{\text{nc}} J_{\text{g/l},k} h_{\text{g,k}} + A_{\text{g/l}} \dot{q}_{\text{g/l}} - A_{\text{sur}} \dot{q}_{\text{sur}} \tag{A.49}$$

The overall material balance given by Equation A.31 is inserted into the Equation A.49:

$$N_{\text{tot,l}} C_{p,l} \frac{dT_l}{dt} = (F + dF)_{\text{l}}((h + dh)_{\text{l}} - h_l) + A_{\text{g/l}} \sum_{k=1}^{\text{nc}} J_{\text{g/l},k}(h_{\text{g}} - h_{\text{l}}) + A_{\text{g/l}} \dot{q}_{\text{g/l}} - A_{\text{sur}} \dot{q}_{\text{sur}} \tag{A.50}$$

Divided by control volume dV, where $dV_{\text{l}} = \varepsilon_{\text{l}} dV$, $dV = A dz$ and $\lim dz_{\text{l}} \to 0$ yields:

$$\varepsilon_{\text{l}} C_{\text{tot,l}} C_{p,l} \frac{dT_l}{dt} = G_{\text{l}} \frac{dh_l}{dz} + a_{\text{g/l}} \sum_{k=1}^{\text{nc}} J_{\text{g/l},k}(h_{\text{g}} - h_{\text{l}}) + a_{\text{g/l}} \dot{q}_{\text{g/l}} - a_{\text{sur}} \dot{q}_{\text{sur}} \tag{A.51}$$

The definition of enthalpy from Equation A.4 is used to find $\frac{dh_l}{dz} = C_{p,l} \frac{dT_l}{dz}$. Further, the heat fluxes in Equation A.9 and A.17 and the heat of absorption for CO_2 and heat of vaporization for H_2O and MEA from Equation A.18 - A.20 is inserted to yield the final column temperature equation for liquid phase:

$$\varepsilon_{\text{l}} C_{\text{tot,l}} C_{p,l} \frac{dT_l}{dt} = G_{\text{l}} C_{p,l} \frac{dT_l}{dz} + a_{\text{g/l}} J_{\text{g/l,H}_2\text{O}} \Delta h^{\text{vap}}_{\text{H}_2\text{O}} + a_{\text{g/l}} J_{\text{g/l,MEA}} \Delta h^{\text{vap}}_{\text{MEA}} + a_{\text{g/l}} J_{\text{g/l,MEA}} \Delta h^{\text{abs}}_{\text{CO}_2} + a_{\text{g/l}} \hat{h}_{\text{g/l}}(T_{\text{l}} - T_{\text{g}}) - a_{\text{sur}} \hat{h}_{\text{sur}}(T_{\text{l}} - T_{\text{sur}}) \tag{A.52}$$

The energy balance for gas phase in control volume dV is given by:

$$\frac{dU_{\text{g}}}{dt} = (F + dF)_{\text{g}}(h + dh)_{\text{g}} - F_{\text{g}} h_{\text{g}} - A_{\text{g/l}} \sum_{k=1}^{\text{nc}} J_{\text{g/l},k} h_{\text{g,k}} - A_{\text{g/l}} \dot{q}_{\text{g/l}} - A_{\text{sur}} \dot{q}_{\text{sur}} \tag{A.53}$$

Relation A.23 for internal energy for gases is utilized to yield:

$$N_{\text{tot}}C_{\text{v,g}}\frac{dT_{\text{g}}}{dt} + h_g\frac{dN_{\text{tot}}}{dt} - \frac{d(PV)}{dt} = (F+dF)_{\text{g}}(h+dh)_{\text{g}} - F_{\text{g}}h_{\text{g}} - A_{\text{g/l}}\sum_{k=1}^{\text{nc}} J_{\text{g/l},k}h_{\text{g,k}} - A_{\text{g/l}}\dot{q}_{\text{g/l}} - A_{\text{sur}}\dot{q}_{\text{sur}} \tag{A.54}$$

The total material balance from Equation A.35 is inserted:

$$N_{\text{tot}}C_{\text{v,g}}\frac{dT_{\text{g}}}{dt} = (F+dF)_{\text{g}}((h+dh)_{\text{g}} - h_g) + \frac{d(PV)}{dt} - A_{\text{g/l}}\dot{q}_{\text{g/l}} - A_{\text{sur}}\dot{q}_{\text{sur}} \tag{A.55}$$

Divided by control volume dV, where $dV_{\text{g}} = \varepsilon_{\text{g}}dV$, $dV = Adz$ and $\lim dz \to 0$ yields:

$$C_{\text{tot,g}}C_{\text{v,g}}\frac{dT_{\text{g}}}{dt} = -G_{\text{g}}\frac{dh_g}{dz} + \frac{dP}{dt} - a_{\text{g/l}}\dot{q}_{\text{g/l}} - a_{\text{sur}}\dot{q}_{\text{sur}} \tag{A.56}$$

$\frac{dP}{dt}$ is assumed to be zero since pressure change is instantaneous. Finally, the enthalpy relation in Equation A.4 is used together with expressions for heat transfer between phases (Equation A.17) and heat loss to the surroundings (Equation A.9) to yield the final temperature equation of gas phase in packed columns:

$$C_{\text{tot,g}}C_{\text{v,g}}\frac{dT_{\text{g}}}{dt} = -G_{\text{g}}C_{\text{p,g}}\frac{T_g}{dz} + a_{\text{sur}}\hat{h}_{\text{sur}}(T_{\text{l}} - T_{\text{sur}}) + a_{\text{g/l}}\hat{h}_{\text{g/l}}(T_{\text{l}} - T_{\text{g}}) \tag{A.57}$$

A.4 Heat exchanger

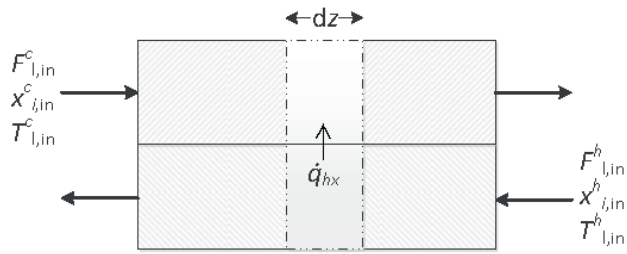

FIGURE A.4: Illustration of the heat exchanger model.

A.4.1 Assumptions

- only liquid phase is considered and any vaporization is disregarded (no flashing)
- one-dimensional plug flow regime for both sides
- no reaction occurring

A.4.2 Overall material balances

The overall material balance for the hot side of the heat exchanger for control volume dV_h is given by:

$$\frac{dN_{l,tot}^{\mathrm{h}}}{dt} = (F + dF)_l^{\mathrm{h}} - F_l^{\mathrm{h}} \tag{A.58}$$

Divided by control volume dV_h yields:

$$\frac{d}{dt}\left(\frac{N_{l,tot}^{\mathrm{h}}}{dV_h}\right) = \frac{(F + dF)_l^{\mathrm{h}} - F_l^{\mathrm{h}}}{dV_h} \tag{A.59}$$

$dV_h = A_h dz$ and $\lim dz \to 0$ yields:

$$\frac{\partial C_{l,tot}^{\mathrm{h}}}{\partial t} = \frac{\partial F_l^{\mathrm{h}}}{A \partial z} = \frac{\partial G_l^{\mathrm{h}}}{\partial z} \tag{A.60}$$

Assume $\frac{\partial C_{l,tot}^{\mathrm{h}}}{\partial t} = 0$, thus

$$0 = \frac{\partial G_l^{\mathrm{h}}}{\partial z} \tag{A.61}$$

Similarly, the overall material balance for cold side of the heat exchanger for control volume dV_c is given by:

$$\frac{dN_{tot}^{\mathrm{c}}}{dt} = (F + dF)_l^{\mathrm{c}} - F_l^{\mathrm{c}} \tag{A.62}$$

which yields:

$$0 = -\frac{\partial G_l^{\mathrm{c}}}{\partial z} \tag{A.63}$$

A.4.3 Component mass balances

The material balance for component i for hot side of the heat exchanger for control volume dV_h is given by:

$$\frac{dN_{l,i}^{\mathrm{h}}}{dt} = (F + dF)_{l,i}^{\mathrm{h}} - F_{l,i}^{\mathrm{h}} \tag{A.64}$$

Divided by control volume dV_h yields:

$$\frac{d}{dt}\left(\frac{N_{l,i}^{\mathrm{h}}}{dV_h}\right) = \frac{(F + dF)_{l,i}^{\mathrm{h}} - F_{l,i}^{\mathrm{h}}}{dV_h} \tag{A.65}$$

$dV_h = A_h dz$, $\frac{F_l}{A} = G_l$ and $\lim dV_h \to 0$ yields:

$$\frac{\partial C_{l,tot}^{\mathrm{h}} x_i^{\mathrm{h}}}{\partial t} = \frac{\partial G_l^{\mathrm{h}} x_i^{\mathrm{h}}}{\partial z} \tag{A.66}$$

Using the chain rule for derivatives and the total mass balance ($\frac{\partial C_{l,tot}^{\mathrm{h}}}{\partial t} - \frac{\partial G_l^{\mathrm{h}}}{\partial z} = 0$) yields:

$$C_{l,tot}^{\mathrm{h}} \frac{\partial x_i^{\mathrm{h}}}{\partial t} = G_l^{\mathrm{h}} \frac{\partial x_i^{\mathrm{h}}}{\partial z} - x_i^{\mathrm{h}} \frac{\partial G_l^{\mathrm{h}}}{\partial z} = G_l^{\mathrm{h}} \frac{\partial x_i^{\mathrm{h}}}{\partial z} \tag{A.67}$$

The material balance for component i for cold side of the heat exchanger for control volume dV_c is similarly given by:

$$C_{l,tot}^{\mathrm{c}} \frac{\partial x_i^{\mathrm{c}}}{\partial t} = -G_l^{\mathrm{c}} \frac{\partial x_i^{\mathrm{c}}}{\partial z} \tag{A.68}$$

A.4.4 Energy balances

The energy balance for hot side of the heat exchanger for control volume dV_h is given by:

$$\frac{dU_l^{\mathrm{h}}}{dt} = (F + dF)_l^{\mathrm{h}}(h + dh)_l^{\mathrm{h}} - F_l^{\mathrm{h}} h_l^{\mathrm{h}} - A_{\mathrm{hx}}\dot{q}_{\mathrm{hx}} \tag{A.69}$$

where A_{hx} is the heat exchanger area and $\dot{q}_{hx}$ is the heat flux from hot to cold side. Using the relation of internal energy and change in enthalpy for incompressible fluids of Equation A.3 and A.4 gives:

$$N_{l,tot}^{\mathrm{h}} C_{\mathrm{p,l}}^{\mathrm{h}} \frac{dT_l^{\mathrm{h}}}{dt} + h_l^{\mathrm{h}} \frac{dN_{l,tot}^{\mathrm{h}}}{dt} = (F + dF)_l^{\mathrm{h}}(h + dh)_l^{\mathrm{h}} - F_l^{\mathrm{h}} h_l^{\mathrm{h}} - A_{hx}\dot{q}_{\mathrm{hx}} \tag{A.70}$$

The total mass balance from Equation A.58 is inserted:

$$N_{l,tot}^{\mathrm{h}} C_{\mathrm{p,l}}^{\mathrm{h}} \frac{dT_l^{\mathrm{h}}}{dt} + h_l^{\mathrm{h}}((F + dF)_l^{\mathrm{h}} - F_l^{\mathrm{h}}) = (F + dF)_l^{\mathrm{h}}(h + dh)_l^{\mathrm{h}} - F_l^{\mathrm{h}} h_l^{\mathrm{h}} - A_{hx}\dot{q}_{\mathrm{hx}} \tag{A.71}$$

$$N_{l,tot}^{\mathrm{h}} C_{\mathrm{p,l}}^{\mathrm{h}} \frac{dT_l^{\mathrm{h}}}{dt} = (F + dF)_l^{\mathrm{h}}((h + dh)_l^{\mathrm{h}} - h_l^{\mathrm{h}}) - A_{hx}\dot{q}_{\mathrm{hx}} \tag{A.72}$$

Divided by control volume dV_h, where $dV_h = A_h dz$ yields:

$$C_{l,tot}^{\mathrm{h}} C_{\mathrm{p,l}}^{\mathrm{h}} \frac{dT_l^{\mathrm{h}}}{dt} = (F + dF)_l^{\mathrm{h}} \frac{((h + dh)_l^{\mathrm{h}} - h_l^{\mathrm{h}})}{A_h dz} - \frac{A_{hx}}{dV_h}\dot{q}_{\mathrm{hx}} \tag{A.73}$$

$\frac{F_l}{A} = G_l$ and $\lim dV_h \to 0$ gives:

$$C_{l,tot}^{\mathrm{h}} C_{\mathrm{p,l}}^{\mathrm{h}} \frac{dT_l^{\mathrm{h}}}{dt} = G_l^{\mathrm{h}} \frac{dh_l^{\mathrm{h}}}{dz} - a_{\mathrm{hx}}^{h}\dot{q}_{\mathrm{hx}} \tag{A.74}$$

where a_{hx}^{h} is the ratio heat exchanger surface area to fluid volume of the hot side of the heat exchanger. Using the change of enthalpy relation of Equation A.4 and heat transfer given by $a_{\mathrm{hx}} = \hat{h}_{\mathrm{hx}}(T_l^h - T_l^c)$ gives:

$$C_{l,tot}^{\mathrm{h}} C_{\mathrm{p,l}}^{\mathrm{h}} \frac{dT_l^{\mathrm{h}}}{dt} = G_l^{\mathrm{h}} C_{\mathrm{p,l}}^{\mathrm{h}} \frac{dT_l^{\mathrm{h}}}{dz} - a_{hx}^{h}\hat{h}_{hx}(T_l^h - T_l^c) \tag{A.75}$$

The equivalent temperature equation for cold side of the heat exchanger is given by:

$$C_{l,tot}^{\mathrm{c}} C_{\mathrm{p,l}}^{\mathrm{c}} \frac{dT_l^{\mathrm{c}}}{dt} = -G_l^{\mathrm{c}} C_{\mathrm{p,l}}^{\mathrm{c}} \frac{dT_l^{\mathrm{c}}}{dz} + a_{hx}^{c}\hat{h}_{hx}(T_l^h - T_l^c) \tag{A.76}$$

A.5 Process controllers

The various controllers are modeled as either P or PI type controllers. The manipulated variable (MV) for a general PID-controller is given by the following equation:

$$u(t) = K_p\left(e(t) + \frac{1}{T_i}\int_0^t e(\tau)d\tau + T_d\frac{d}{dt}e(t)\right) \tag{A.77}$$

where the control parameters K_p, T_i and T_d are the proportional gain, the time integral and the derivative time, respectively. The proportional gain is given in units percent per unit, such that $u(t)$ range the span from 0 (closed valve) to 100 % (fully open valve). Further, $e(t)$ is the error or process value (PV) deviation from set-point (SP):

$$e(t) = SP - PV \tag{A.78}$$

For PI- and P-controllers which are used in the model, Equation A.77 simplifies to:

$$\begin{aligned} u(t) &= K_p\left(e(t) + \frac{1}{T_i}\int_0^t e(\tau)d\tau\right) \\ &= K_p\max(0, e(t) + \frac{1}{T_i}\kappa(t))) \end{aligned} \tag{A.79}$$

and

$$u(t) = K_p\max(0, e(t)) \tag{A.80}$$

respectively. $\kappa(t)$ in Equation A.79 is given by:

$$\kappa(t) = \int_0^t e(\tau)d\tau \tag{A.81}$$

Appendix B

Additional simulation results

B.1 Dynamic simulation results using the equilibrium-stage model

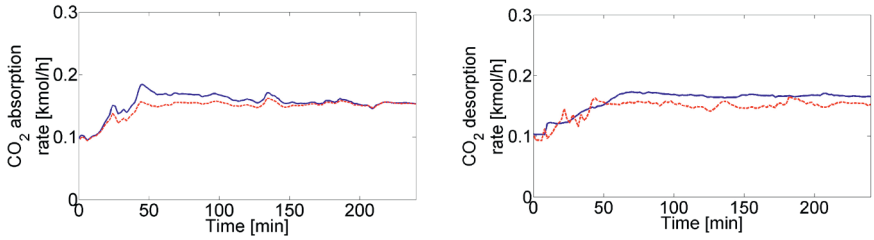

(A) Case 1: absorbed CO_2 to the left, desorbed CO_2 to the right

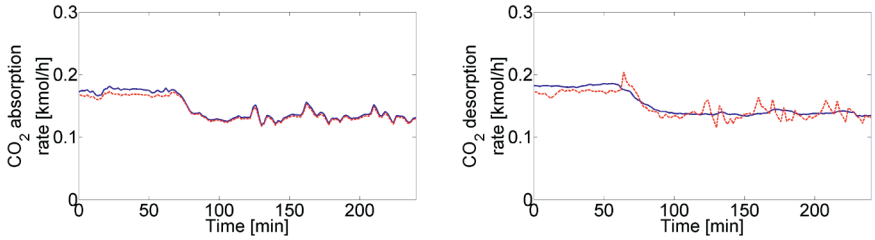

(B) Case 2: absorbed CO_2 to the left, desorbed CO_2 to the right

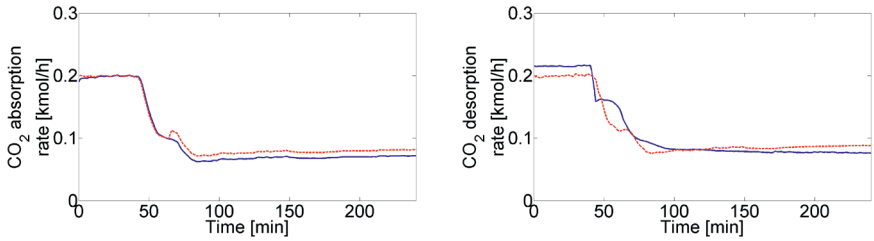

(C) Case 3: absorbed CO_2 to the left, desorbed CO_2 to the right

FIGURE B.1: Dynamic simulation results for CO_2 absorption and desorption in the Gløshaugen pilot plant using the equilibrium-stage model. (—) Model, (---) Pilot results. (Continues next page).

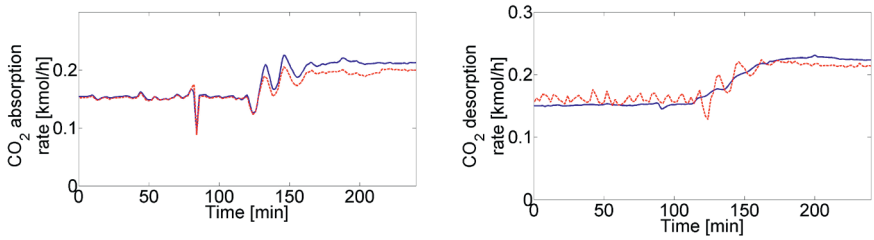

(D) Case 5: absorbed CO_2 to the left, desorbed CO_2 to the right

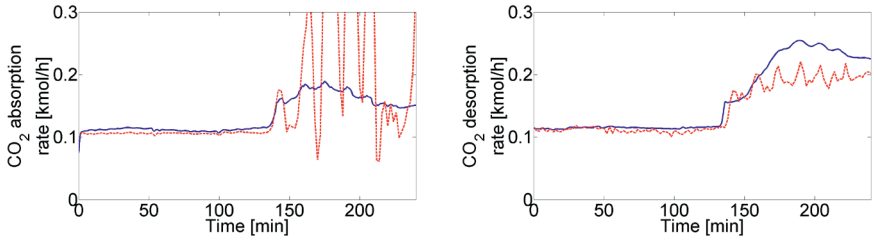

(E) Case 6: absorbed CO_2 to the left, desorbed CO_2 to the right

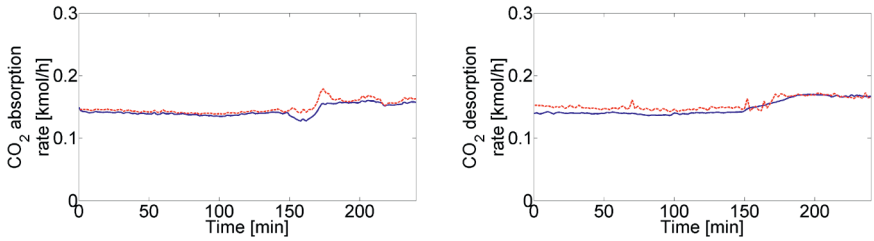

(F) Case 7: absorbed CO_2 to the left, desorbed CO_2 to the right

FIGURE B.1: Dynamic simulation results for CO_2 absorption and desorption in the Gløshaugen pilot plant using the equilibrium-stage model. (—) Model, (---) Pilot results. (Continued from previous page).

Appendix C

Published and submitted papers

C.1 Paper A: Dynamic Modeling of Post-combustion CO_2 Capture Using Amines – A Review.

Available online at www.sciencedirect.com

SciVerse ScienceDirect

Energy Procedia 23 (2012) 82 – 91

Energy Procedia

6th Trondheim Conference: CO_2 Capture, Transport and Storage

Dynamic Modeling of Post-combustion CO_2 Capture Using Amines – A Review.

Actor Chikukwa[a]*, Nina Enaasen[b], Hanne M. Kvamsdal[a], Magne Hillestad[b]

[a]*SINTEF Materials and Chemistry, Department of Process Technology, N-7465 Trondheim, Norway*
[b]*Department of Chemical Engineering, Norwegian University of Science and Technology, N-7491 Trondheim, Norway*

Abstract

The recent years have seen growing attention towards the study of dynamic behavior in post-combustion CO_2 capture plants using amines, albeit, apparently contesting yet without comparison or critique. This paper reviews what has been reported in literature concerning issues pertinent to transient behavior of CO_2 capture including interaction with power plants. Details of models used, their validation and modeling tools as well as an attempt to piece-out convergent points from the various conclusions are given. Knowledge gaps and areas that still need more attention are emphasized.

© 2012 The Authors. Published by Elsevier Ltd. Selection and/or peer-review under responsibility of SINTEF Energi AS

Keywords: Dynamic modeling; post-combustion; flexibility; integration; review.

1. Introduction

Humanity is facing an inherently paradoxical challenge: meeting the increasing global energy demand while simultaneously mitigating climate change. Consequently, there is growing concern across the world over rising concentrations of anthropogenic greenhouse gases in the atmosphere, mainly CO_2 which is considered to be the chief culprit propelling climate change. Fossil fueled power generation, apparently indispensable at the moment [5, 6], is the largest source of CO_2 emission.

Carbon capture and storage (CCS) is suggested as one of the main options for reducing global CO_2 emissions. However, the design of the existing fossil-fueled power plants was not meant to accommodate CCS. For this reason, post-combustion CO_2 capture has a significant edge over other alternatives because the technology can simply be implemented as an 'end-of-the-pipe' retrofit without the need for radical changes to existing power plants [7]. As such, the most mature, sufficiently studied and documented technology for post-combustion CO_2 separation is chemical absorption using amines. However, most of these amine-based CO_2 capture studies available in literature, be they experimental or validated theoretical simulations or modeling, are premised on steady state [8].

* Corresponding author. Tel.: +47-93238290; fax: +47-73596995.
E-mail address: Actor.Chikukwa@sintef.no

1876-6102 © 2012 The Authors. Published by Elsevier Ltd. Selection and/or peer-review under responsibility of SINTEF Energi AS
doi:10.1016/j.egypro.2012.06.063

Relative to steady state there is a modicum, nevertheless, growing attention towards the study of dynamic behavior in CO_2 capture over the recent years (being evidenced by an increasing amount of literature on the topic), apparently contesting yet without aggregational collation or critique. The aim of this paper is, therefore, to give a review of what has been reported in the literature concerning dynamic post-combustion CO_2 capture as well as pertinent studies on interactions between power plants and CO_2 capture plants. The main focus is on modeling of the capture plant and the interactions with the power plant are handled as external disturbances.

2. Motivation: Dynamic modeling is a practical necessity

It is becoming increasingly cogent (technically) that post-combustion CO_2 capture is heading towards full scale. Most probably, this will naturally be followed by subsequent commercialization. However, there is no real-world experience with large scale integration with power plants thus far. The extent to which the capture plant will affect the flexibility of the power plant is of great interest, especially during transient operation.

The absorber/stripper process is fairly complex, characterized by interactive interference between the columns. Moreover, incorporation of optimal design and operational improvements of the absorption process (e.g. intercooling, lean vapor recompression, multistage stripping) will contribute further to inherent complexity. In case of biofuels and coal-based power plants, the condition of the fuel might vary during operation implying varying flue gas composition. In addition, the path towards carbon neutral energy systems (with the expected growth of renewables and other ´green´ energy sources) will require an even higher degree of flexibility in fossil-fueled power generation. As an illustration, Figure 1 shows the expected dynamic interaction between conventional power generation (coal or gas) and the renewable alternatives. Of importance to note is that this prediction is based on realistic simulation of wind and tidal output data (from 2007) scaled-up to meet the anticipated goal of 38% from renewables in the UK by 2025 [1]. Obviously, the need for an in-depth grasp of the power/capture plant's operational flexibility is a palpable necessity before full-scale CO_2 capture can be realized.

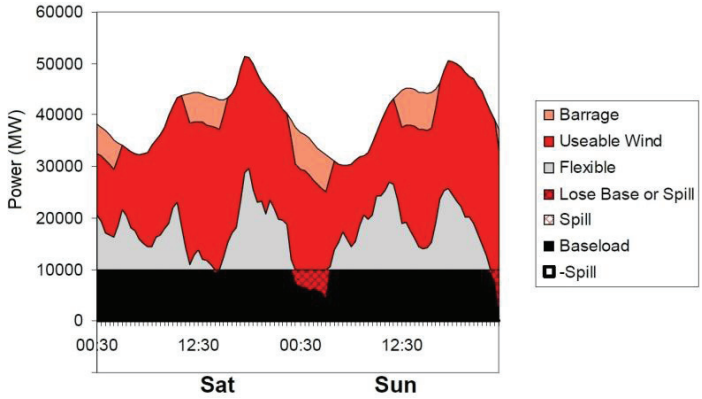

Figure 1: A schematic showing the expected dynamic interaction (speculative) between the green energy sources vs coal/gas power generation in 2025. Adapted from [1].

In order to get a full understanding of the transient characteristics of a power plant with CCS, both the power plant and capture process should be investigated in a combined dynamic model. The power plant steam cycle and CO_2 capture unit are integrated [9, 10] and therefore, highly dependent on each other's performance [11, 12]. The transient behavior of the power plants occurring during start-up, shut-down, and load variation, are well-known through operational experience. However, there is little knowledge of how the absorption process operates during these sequences. Due to chemical reactions occurring in the capture process, the dynamic behavior is more complicated compared to that of the power plant (mainly related to variations in mass and energy rates). Dynamic simulation will play a pivotal role in identifying any operational bottlenecks at transient conditions for the integrated power and CO_2 capture plants.

3. Modeling of post-combustion CO_2 capture using amines

The conventional CO_2 capture loop basically consists of two columns: an absorber and a stripper coupled via a heat exchanger, see Figure 4. In principle, the two columns require different conditions (tailored to favor either CO_2 absorption in the absorber or desorption in the stripper) for optimal operation. The chemical solvent is loaded with CO_2 in the absorber and then pumped to the desorber where the CO_2 will be stripped off. A condenser removes water from the gas exiting the stripper, leaving a CO_2 product of almost 99% purity which is then compressed for transportation. The lean solvent is circulated back to the absorber.

The importance and necessity to develop mathematical models that describe the absorption and desorption process as accurate as possible can not be overstated. For modeling fluid flow, simple plug flow models are widely used for both gas and liquid phase. However, describing mass and heat transfer is seen as a more challenging part of model development. Particularly two philosophies are popularly used in literature for modeling mass and heat transfer across the interphase, namely the two-film theory and the penetration theory. It seems the two-film theory is more popularly used compared to its counterpart. The concept is illustrated in Figure 2 and shows how CO_2 diffuses from the gas bulk phase through a gas film, before being absorbed at the interface and then diffuses through a liquid film to the liquid bulk phase. It is assumed that the resistance to mass transfer is concentrated entirely in the films adjacent to the interphase. In the fluid bulk phases outside the films, the level of mixing is assumed to be sufficiently high so that there is no composition gradient.

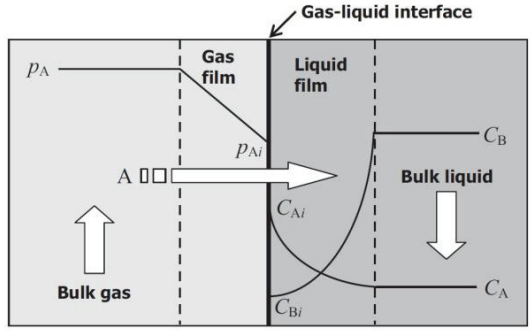

Figure 2: A schematic showing the concept of mass transfer model based on the two-film theory. Adapted from [3].

Absorption of CO_2 by amines involves chemical reactions, and in most cases the chemical reactions are fast enough to influence the rate of mass transfer in the films. Thus, mass transport and chemical reaction occurs simultaneously giving changes in the concentration gradients. This leads to enhancement of the mass transfer which must be described in the model.

Different modeling approaches are used to describe and model mass and heat transfer in the columns. Generally, two concepts are commonly used: the equilibrium and non-equilibrium stage models. The essence of the equilibrium approach is ideal for non-reactive systems and is based on theoretical segments (linked through mass and energy balance equations) in which the liquid and gas are assumed to attain equilibrium characterized by infinitely fast mass transport. The performance of the individual stages is then

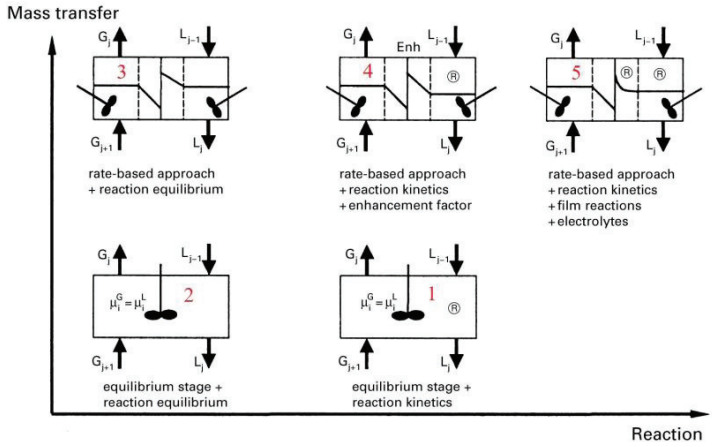

Figure 3: Theoretical representation of the different levels of model complexity for one segment. Adapted from [2]. The models are labeled 1-5 for convenience in reference, especially in Table 1.

adjusted by means of a tray efficiency factor. All the same, chemical reactions between CO_2 and amines imply that vapor-liquid equilibrium is rarely attainable in practice. This makes the non-equilibrium (i.e. rate-based) approach more appropriate. The gist of this concept takes into account the actual rates of mass and heat transfer including chemical reactions. Mass and heat transfer across the interphase can be described by the two-film model as explained above. The reaction depends on the kinetics regime, and can either be considered instantaneous (equilibrium can be assumed) or kinetically controlled.

Both approaches have varying degrees of complexity largely differentiated by intricacies as illustrated in Figure 3, in which the horizontal and vertical axes show increasing complexity for both reaction and mass transfer respectively. According to Baur et al [13], it is advisable to employ the rate-based approach when dealing with reactive columns. Nevertheless, rigorous dynamic descriptions of industrial gas-liquid contactors lead to extended systems of equations difficult to solve reliably and quickly enough. All the same, this seems to be less of a hindrance nowadays, thanks to the advances made to the processing speed of the modern computers.

4. Characterizing literature on dynamic modeling

4.1. General trends

Until only a few years ago, there has been some appreciable degree of inadvertence regarding dynamic modeling in the research of post-combustion CO_2 capture by chemical absorption. Generally, the main thrust has been directed towards steady state analysis of power plants operating at design conditions (full-load), and consequently, numerous publications on the topic exist. Nevertheless, steady state analysis does not correctly represent neither issues related to daily operations nor the transient behavior of these plants. All the same, there seems to be some kind of awakening towards dynamic modeling in recent years as depicted in Table 1. This tabulation attempts to categorize the issues addressed in literature regarding dynamic modeling. In this case, the main emphasis was directed towards technical aspects of the conventional post-combustion CO_2 capture by chemical solvents. It seems that there has not been so much effort towards dynamic modeling before 2008, albeit a dramatic increase on studies attempting to deal with the subject is noticeable.

Of importance to note is that quite a significant number of authors model either the absorber or the stripper only, although a greater majority attempts to include both columns in their models. Most of the models assume plug flow for both gas and liquid phase, and the modeling approach for describing mass and heat transfer as well as the effect of chemical reactions is indicated in the table according to Figure 3. Further more, it appears that almost all model validation is based on steady state, save a single attempt by Kvamsdal et al [14]. Even so, this effort does not give a complete picture because it deals with the absorber section only. Although there is a sizeable, growing and diversified list of tested and tried solvents, apparently all modelers have thus far chosen to use MEA for dynamic modeling on post-combustion CO_2 capture. Notwithstanding, the overall basis for evaluating dynamic behavior is quite broad, ranging from variations in power plant load to perturbations in reboiler duty including other important aspects like disturbances in flue gas composition, flow rates, rich/lean loadings, water balance, etc. It is also interesting to note that a variety of modeling tools (MATLAB, gPROMS, Modelica, Aspen Plus, etc) have been used for implementation of the developed models.

4.2. Summary of main results based on literature in Table 1

In this section we seek to discuss the major findings of the articles in Table 1. To start with, it is important to note that the basis on which dynamic behavior has been studied by the various researchers is quite diverse. In general, the majority of the articles show that there is a time lag between perturbations and system response, which needs to be taken care of as the system moves from one steady state to another [15, 16]. A cross-examination of the results, obtained by different researchers, concerning the capture system's time response suggests that it is strongly influenced by local size and setup.

Table 1: **An epitomic overview of literature survey on dynamic modeling of post combustion CO_2 capture. All researchers in this table used MEA as the chemical solvent.**

Reference & (Year of publication)	Modeled Section (Absorber or Desorber)	Data used for Validation		Level of Complexity & Modeling Tool		Basis for Evaluating Dynamic Behavior
		Steady State	Dynamic State	Level (Figure 3)	Model Implementation Tool	
Noorlisa et al [8] (2010)	Both	x	-	4	gPROMS	– flue gas flow rate
Ziaii et al [20] (2009)	Both	-	-	5	MATLAB	– reboiler duty – rich solvent load
Ziaii et al [21] (2009)	desorber	-	-	5	Aspen Custom Modeller	– reboiler duty – rich stream flow rate
Ziaii et al [22] (2011)	Both	-	-	not specified	Aspen Custom Modeller	– partial boiler load – partial steam load
Sanoja et al [16] (2010)	absorber	x	-	4	MATLAB	– power plant load
Prölß et al [23] (2011)	Both	-	-	4	Modelica	– flue gas flow rate
Gáspár and Cormos [19] (2011)	Both	x	-	4	MATLAB & Simulink	– changing power plant load – decreasing rich stream temperature
Lawal et al [15] (2010)	Both	x	-	5	gPROMS	– water balance – flue gas flow rate – reboiler duty – flue gas composition
Lawal et al [24] (2011)	Both	x	-	not specified	gPROMS	– flue gas composition
Lawal et al [17] (2009)	Both	x	-	5	gPROMS	– power plant load – reboiler duty
Lawal et al [25] (2010)	Both	x	-	3	gPROMS	– power plant load – CO_2 capture level
Lawal et al [18] (2009)	absorber	x	-	2 & 5	Aspen Plus	– power plant load – lean loading
Greer et al [26] (2010)	desorber	x	-	not specified	MATLAB	– flue gas composition
Kvamsdal et al [27] (2009)	absorber	x	-	4	gPROMS	– L/G ratio
Kvamsdal et al [14] (2011)	absorber	x	X	4	MATLAB	– L/G ratio – flue gas composition
Greer, T [28] (2008)	Both	x	-	4	MATLAB	– perturbations in model parameters & inputs

Noorlisa et al [8] generally concluded that the partial reduction of the flue gas load significantly affects absorber/stripper performance. This is further supported by Lawal et al [17, 18], in which it is shown that absorber operation is more sensitive to perturbations in L/G ratio compared to individual liquid or gas flow rates while the regenerator performance is quite sensitive to disturbances in the reboiler duty.

However, findings by Gáspár and Cormos [19] suggest that the capture unit has even higher sensitivity to changes in the desorber feed stream temperature compared to the L/G ratio. Along the same line of thought, the studies by Ziaii et al [20, 21] suggest that the liquid residence time in the reboiler at the final steady state condition could be the dominant factor in the response time of the stripping section. In another study, Ziaii et al [22] found that for reboiler steam partial load, a linear relationship exists between optimum solvent rate and reboiler steam rate.

In a separate study, Lawal et al [25] extended their effort to include two dynamic case studies in which they surmise that the CO_2 capture section has a slower response compared to the power plant. It is further discussed how CO_2 capture level affects the power plant output together with the associated difficulties in achieving a steady power output quickly.

It can generally be said that the work done thus far regarding characterization of amine-based post-combustion of CO_2 capture in the dynamic mode is still largely an incongruous mixture of indeterminate conclusions. As such, it is still inherently difficult to affirmatively piece-out the puzzle regarding dynamic behavior of a CO_2 capture unit. Resultantly, clear strategy on how to handle the CO_2 capture unit in transient mode is still lacking although the technology seems to be moving towards full-scale. This is further compounded by the fact that the existing motley of conclusions is all essentially based on steady state validation. In other words, the present knowledge regarding dynamic behavior of CO_2 capture is incomplete both theoretically and in practice. The obvious implication is that this might slow down implementation of CCS if left unaddressed until full-scale.

4.3. Other issues discussed within dynamic behavior

Some of the works (in Table 1) extended their studies to include a variety of other issues. For example, Ziaii et al [21] attempted to address how flexibility in both power and CO_2 capture plants can improve operating profits by facilitating the operators to examine the balance between power output and pricing as determined by market conditions. In this regard, the authors essentially emphasize the fact that sound knowledge on the dynamic behavior is crucial in order to determine optimal loads as well as when and how to operate CO_2 capture lucratively on hourly basis. The success of such an approach is closely linked to a clear understanding of how dynamic optimal operation of the capture plant works.

At a technical level, Lawal et al [17] compare the equilibrium and rate-based approaches in modeling the absorber dynamically. As one would expect, it was concluded that the rate-based approach yields better predications compare to its equilibrium-based counter part. Besides discussing the technical dynamic behavior of the absorber section Kvamsdal et al [14] went further to investigate the effect on the overall performance of the model, by substituting different parameter-correlations available from various sources in literature. Important observations and indications are noted in their analysis; notwithstanding, the fact that this work was confined to the absorber section only makes the associated conclusions difficult to generalize.

5. Interaction between the power plants and CO_2-capture plants

CCS in general gives rise to an energy penalty which decreases the net efficiency of the power plant [29]. The sources leading to energy penalty are largely constituted by heat supply to the desorber reboiler (steam taken directly from the power cycle), shaft power to compression of CO_2 and other electric power consumers like pumps, blowers etc [10]. However, CO_2 separation (reboiler duty) is energy intensive, responsible for the largest (relative) energy penalty [7, 30]. A simplified diagram showing how the two plants interact with each other is given in Figure 4.

In comparative terms, efficiency has become the dominant issue when designing and selecting power plants with CO_2 capture. Other aspects, like reliability and operability, have been given less importance, if any at all, in literature. This section focuses on studies pertinent to the transient interaction between the power plant and the post-combustion CO_2 capture plant. As such, direct relevance to the integrated flexibility of both the power and capture plants has been of prime interest in this case. Due to the integration of power plant steam cycle with desorber reboiler in the capture plant, these units are highly dependent on each others performance and should be investigated in a fully combined dynamic model to identify any operational bottlenecks at transient condition. However, most of these studies assume steady state and full-load design, albeit, covering a diversity of investigations ranging from power plant types,

usage of different grades and quality of fuels [5] to a variety of solvents. Resultantly, generalization and application of results is thus largely subject to considerable limitations.

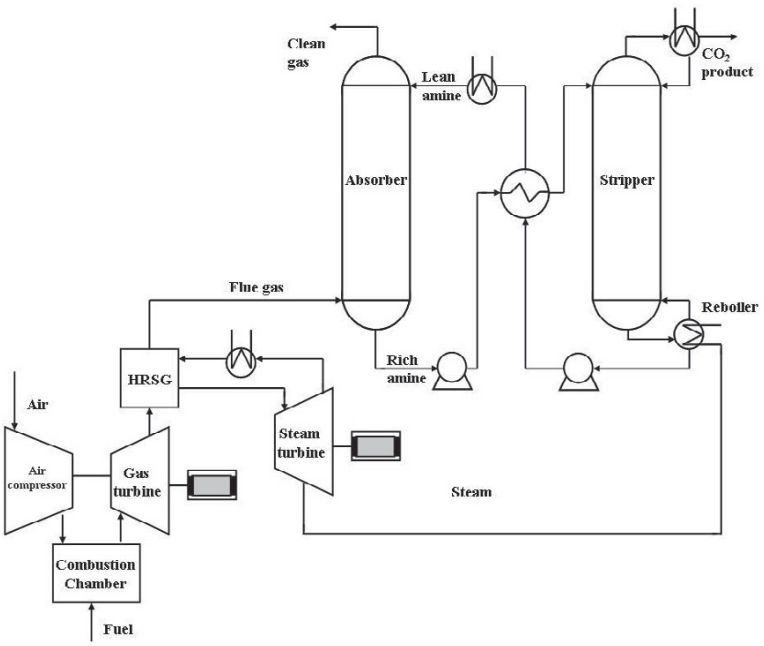

Figure 4: Simplified diagram to illustrate the integration of a natural gas power plant and a CO_2-capture plant. Adapted from [4] with modifications.

A study by Alie et al [31] focuses on the operability of power plants with CCS and highlights how flexibility is critical to integral operability. The article takes note of the inroad studies addressing issues related to flexibility, controllability, start-up, shut down and other aspects characteristic to the transient mode exist, albeit, techniques used are basically theoretical methodologies and experience-based approaches.

Sanpasertparnich et al [10] studied how various important parameters in the power plant, CO_2 capture plant and compression unit affects the coal-fired power plant performance. Focus is not only on full load, but also on the impact of part load. Their conclusions suggest that CO_2 capture efficiency yielding to optimal energy penalty is independent of type of coal studied and steam extraction location.

Generally, the closest various researchers have come to address the issue of integrated flexibility of power and capture plants is based on part load studies. Even so, steady state is assumed at partial load. Efforts to study what goes on as the system moves from one steady state to another seem to be lacking still. In this regard, Chalmers and Gibbins [11] highlights the need for some comprehensive understanding of the potential impacts of post-combustion capture on dynamic performance of the power plant to be able to optimize the process during varying operation. Identifying potential improvements to plant dynamic performance is important, since this may improve the power plant's economics [32].

6. Conclusions

There is in general a notable awakening and multifaceted activity towards dynamic modeling of post-combustion CO_2 capture using amines. However, one problem is visibly salient: lack of dynamic data to validate the developed models. As such, the majority of the models is validated against steady state data and based on one solvent, MEA. Attempts to assess flexible integration of power plants and CO_2 capture plants are basically based on part load, however, still assuming steady state.

Another outstanding feature that traverses literature analyzed in this work is that dynamically validated models are critical towards comprehension of the potential impacts of post-combustion capture on net flexible performance of integrated power/capture plants. Moreover, it is now technically cogent that post-combustion CO_2 capture is heading towards full scale and subsequent commercialization. However, the path towards synergistic and interactive hybridization of fossil-fueled power generation with intermittent 'green' energy sources will undoubtedly exert an even higher demand for dynamic flexibility on integrated power/CCS plants.

To the contrary, dynamic flexibility of integrated plants is still not sufficiently studied, since efforts on this topic (so far) are still largely theoretical and just based on experience to some extent. Moreover, the ability to predict accurately potential improvements and optimization of integrated dynamic performance can provide real economic benefits. Dynamic modeling naturally gives detailed foresight that is fundamental to the establishment of proper regulation as well as control and procedural strategies even as early as plant design stage.

Acknowledgements

"This publication has been produced with support from the BIGCCS Centre, performed under the Norwegian research program Centres for Environment-friendly Energy Research (FME). The authors acknowledge the following partners for their contributions: Aker Solutions, ConocoPhilips, Det Norske Veritas, Gassco, Hydro, Shell, Statkraft, Statoil, TOTAL, GDF SUEZ and the Research Council of Norway (193816/S60)."

References

1. Boston, A., *Effect of renewables on electricity system.* https://ktn.innovateuk.org/c/document_library/get_file?p_l_id=56852&folderId=1030999&name=DLFE-10006.pdf, 2010.
2. Kenig, E.Y., R. Schneider, and A. Górak, *Reactive absorption: Optimal process design via optimal modelling.* Chemical Engineering Science, 2001. **56**(2): p. 343-350.
3. Khan, F.M., V. Krishnamoorthi, and T. Mahmud, *Modelling reactive absorption of CO2 in packed columns for post-combustion carbon capture applications.* Chemical Engineering Research and Design, 2010. **In Press, Corrected Proof**.
4. Mores, P., N. Scenna, and S. Mussati, *Post-combustion CO2 capture process: Equilibrium stage mathematical model of the chemical absorption of CO2 into monoethanolamine (MEA) aqueous solution.* Chemical Engineering Research and Design, 2011. **89**(9): p. 1587-1599.
5. Lucquiaud, M., H. Chalmers, and J. Gibbins, *Capture-ready supercritical coal-fired power plants and flexible post-combustion CO2 capture.* Energy Procedia, 2009. **1**(1): p. 1411-1418.
6. Kotowicz, J., T. Chmielniak, and K. Janusz-Szymanska, *The influence of membrane CO2 separation on the efficiency of a coal-fired power plant.* Energy, 2010. **35**(2): p. 841-850.
7. Lucquiaud, M. and J. Gibbins, *Effective retrofitting of post-combustion CO2 capture to coal-fired power plants and insensitivity of CO2 abatement costs to base plant efficiency.* International Journal of Greenhouse Gas Control, 2010. **5**(3): p. 427-438.

8. Harun, N., P.L. Douglas, L. Richardes-Sandoval, and E. Croiset, *Dynamic Simulation of MEA Absorption Processes for CO2 Capture from Fossil Fuel Power Plant.* Energy Procedia, 2011. **4**: p. 1478-1485.
9. Pfaff, I., J. Oexmann, and A. Kather, *Optimised integration of post-combustion CO2 capture process in greenfield power plants.* Energy, 2010. **35**(10): p. 4030-4041.
10. Sanpasertparnich, T., R. Idem, I. Bolea, D. deMontigny, and P. Tontiwachwuthikul, *Integration of post-combustion capture and storage into a pulverized coal-fired power plant.* International Journal of Greenhouse Gas Control, 2010. **4**(3): p. 499-510.
11. Chalmers, H. and J. Gibbins, *Initial evaluation of the impact of post-combustion capture of carbon dioxide on supercritical pulverised coal power plant part load performance.* Fuel, 2007. **86**(14): p. 2109-2123.
12. Adams, R.G., J. Alin, O. Biede, N.J. Booth, D. deMontigny, R. Drew, R. Idem, M. Laursen, D. Peralta-Solorio, T. Sanpasertparnich, and A. Trunkfield, *CAPRICE project--Engineering study on the integration of post combustion capture technology into the power plant gas path and heat cycle.* Energy Procedia, 2009. **1**(1): p. 3801-3808.
13. Baur, R., A.P. Higler, R. Taylor, and R. Krishna, *Comparison of equilibrium stage and nonequilibrium stage models for reactive distillation.* Chemical Engineering Journal, 2000. **76**(1): p. 33-47.
14. Kvamsdal, H.M., A. Chikukwa, M. Hillestad, A. Zakeri, and A. Einbu, *A comparison of different parameter correlation models and the validation of an MEA-based absorber model.* Energy Procedia, 2011. **4**: p. 1526-1533.
15. Lawal, A., M. Wang, P. Stephenson, G. Koumpouras, and H. Yeung, *Dynamic modelling and analysis of post-combustion CO2 chemical absorption process for coal-fired power plants.* Fuel, 2010a. **89**(10): p. 2791-2801.
16. Jayarathna, S.A., B. Lie, and M.C. Melaaena, *NEQ Rate Based Modeling of an Absorption Column for Post Combustion CO2 Capturing.* Energy Procedia, 2010.
17. Lawal, A., M. Wang, P. Stephenson, and H. Yeung, *Dynamic Modeling and Simulation of CO2 Chemical Absorption Process for Coal-Fired Power Plants*. Computer Aided Chemical Engineering, 2009. **27**: p. 1725-1730.
18. Lawal, A., M. Wang, P. Stephenson, and H. Yeung, *Dynamic modelling of CO2 absorption for post combustion capture in coal-fired power plants.* Fuel, 2009a. **88**(12): p. 2455-2462.
19. Gáspár, J. and A.-M. Cormos, *Dynamic modeling and validation of absorber and desorber columns for post-combustion CO2 capture.* Computers & Chemical Engineering, 2011. **35**(10): p. 2044-2052.
20. Ziaii, S., S. Cohen, G.T. Rochelle, T.F. Edgar, and M.E. Webber, *Dynamic operation of amine scrubbing in response to electricity demand and pricing.* Energy Procedia, 2009. **1**(1): p. 4047-4053.
21. Ziaii, S., G.T. Rochelle, and T.F. Edgar, *Dynamic Modeling to Minimize Energy Use for CO2 Capture in Power Plants by Aqueous Monoethanolamine.* Ind. Eng. Chem. Res, 2009. **48**: p. 6105–6111.
22. Ziaii, S., G.T. Rochelle, and T.F. Edgar, *Optimum design and control of amine scrubbing in response to electricity and CO2 prices.* Energy Procedia, 2011. **4**: p. 1683-1690.
23. Prölß, K., H. Tummescheit, S. Velut, and J. Åkesson, *Dynamic model of a post-combustion absorption unit for use in a non-linear model predictive control scheme.* Energy Procedia, 2011. **4**: p. 2620-2627.
24. Lawal, A., M. Wang, and P. Stephenson, *Investigating the dynamic response of CO2 chemical absorption process in enhanced- O2 coal power plant with post-combustion CO2 capture.* Energy Procedia, 2011. **4**: p. 1035-1042.
25. Lawal, A., M. Wang, P. Stephenson, and O. Obi, *Demonstrating full-scale post-combustion CO2 capture for coal-fired power plants through dynamic modelling and simulation.* Fuel, 2010. **In Press, Corrected Proof**.

26. Greer, T., A. Bedelbayev, J.M. Igreja, J.F.P. Gomes, and B. Lie, *A dynamic model for the de-absorption of carbon dioxide from monoethanolamine solution.* Environmental Technology, 2010. **31**(1): p. 107-115.
27. Kvamsdal H.M, J.P. Jakobsen, and K.A. Hoff, *Dynamic modeling and simulation of a CO_2 absorber column for post-combustion CO_2 capture.* Chemical Engineering and Processing: Process Intensification, 2009. **48**: p. 135-144.
28. Greer, T., *Modeling and Simulation of Post Combustion CO_2 Capturing*, in *Faculty of Technology*. 2008, Telemark University College. p. 166.
29. Liebenthal, U., S. Linnenberg, J. Oexmann, and A. Kather, *Derivation of correlations to evaluate the impact of retrofitted post-combustion CO2 capture processes on steam power plant performance.* International Journal of Greenhouse Gas Control, 2011. **5**(5): p. 1232-1239.
30. Davison, J., *Performance and costs of power plants with capture and storage of CO2.* Energy, 2007. **32**(7): p. 1163-1176.
31. Alie, C., P.L. Douglas, and J. Davison, *On the operability of power plants with CO2 capture and storage.* Energy Procedia, 2009. **1**(1): p. 1521-1526.
32. Chalmers, H., M. Leach, M. Lucquiaud, and J. Gibbins, *Valuing flexible operation of power plants with CO2 capture.* Energy Procedia, 2009. **1**(1): p. 4289-4296.

C.2 Paper B: Dynamic Modeling of the Solvent Regeneration Part of a CO_2 Capture Plant.

Available online at www.sciencedirect.com

SciVerse ScienceDirect

Energy Procedia 37 (2013) 2058 – 2065

Energy Procedia

GHGT-11

Dynamic Modeling of the Solvent Regeneration Part of a CO_2 Capture Plant

Nina Enaasen[a]*, Andrew Tobiesen[b], Hanne M. Kvamsdal[b], Magne Hillestad[a]

[a]*Norwegian University of Science and Technology, Sem Sælandsvei 4, 7491 Trondheim, Norway*
[b]*SINTEF Materials and Chemistry, Sem Sælands vei 2a, 7491 Trondheim, Norway*

Abstract

In this work, a system of unit operations is modeled and implemented in MATLAB for dynamic simulation of the regeneration part of the CO_2 capture process. The system consists of a stripper, a reboiler and a condenser, and it is solved by a simultaneous equation based method. The method proves to be suitable for solving the regeneration part of the CO_2 capture process and it shows numerically stable behavior in general. Further, two dynamic simulation cases are carried out and compared to steady state simulation results from CO2SIM. The dynamic simulation results show reasonably good agreement with steady state simulations, even though a very simplified flash tank model is used for simulation of reboiler and condenser and a simplified thermodynamic model is applied compared to the more robust CO2SIM model. Due to lack of dynamic pilot data, validation of the dynamic regeneration model has been difficult at this point. However, this is necessary for a thorough validation of the model for transient conditions.

© 2013 The Authors. Published by Elsevier Ltd.
Selection and/or peer-review under responsibility of GHGT

Keywords: Post combustion CO_2 capture; solvent regeneration; dynamic modelling

1. Introduction

It is difficult to foresee dynamic behavior of complex chemical processes, especially integrated processes such as that of a CO_2 capture process located downstream a power plant process. Steady state modeling and simulation has been widely applied for various studies of capture processes for several

* Corresponding author. Tel.: +47 994 78 919.
E-mail address: nina.enaasen@chemeng.ntnu.no.

1876-6102 © 2013 The Authors. Published by Elsevier Ltd.
Selection and/or peer-review under responsibility of GHGT
doi:10.1016/j.egypro.2013.06.084

years, but recently there has also been a growing interest for dynamic modeling and simulation. Dynamic modeling and simulation will help us to understand the transient behavior and the interactions of complex chemical processes in a much more efficiently manner.

However, dynamic modeling is more challenging compared to steady state modeling, both with respect to numerics and determining the model parameters. While steady-state models are described by a set of algebraic equations (considered that any spatial domain is discretized), the dynamic models will consist of a set of differential and algebraic equations. Furthermore, compared to steady state simulations, additional properties and parameters are necessary to describe the transient behavior of a system. These additional properties describe the gas and liquid hold-up, in addition to the capacitance of the process equipment. The mass transfer rate equations are described as empirical correlations of the process states. Some of the model parameters used in steady state simulators can often be regarded as constant and independent of any state. This is a reasonable assumption when the states do not change much throughout the process or process unit. However, these states can vary considerably during a course of dynamic simulation. Another difference from steady state modeling and a possible benefit is that the dynamic effects we are studying may not require the same level of model complexity. However, yet this remains to be explored in detail for post-combustion type of CO_2 capture using amine solvents.

A dynamic column model has previously been developed at NTNU and SINTEF. The column model was validated for absorber mode using the corresponding steady state column unit in CO2SIM (an in-house simulator developed at SINTEF and NTNU), and it was verified that the dynamic model at steady state gives similar results to the rigorous steady state model. This ensures that the model is implemented correctly, based on the given assumptions. The dynamic column model was further compared transient performance data obtained in the absorber of the VOCC pilot rig at NTNU and SINTEF. Some results are shown in Tobiesen et al. (2011) [1].

For the present paper a simulation study has been performed to test the dynamic performance of the CO_2 regeneration process. The same column model validated for the absorber is extended with simplified models for the condenser and the reboiler to simulate the regeneration process. Two test cases with variations in the inlet stream to the stripper are simulated, and steady state simulations in CO2SIM have been carried out to validate the dynamic model in steady state mode. However, dynamic pilot data from the regeneration part of the process is very limited and not available in the literature. Thus dynamic model validation is very difficult at the moment.

Nomenclature

a	Hydraulic interfacial area of wetted packing [m^2/m^3]
C	Molar concentration [$kmol/m^3$]
C_p	Specific heat capacity [kJ/kmol K]
F	Molar flow rate [kmol/s]
h	Heat transfer coefficient [W/m^2 K]
ΔH	Heat of reaction [kJ/kmol]
k'	Interfacial mass transfer coefficient [$kmol/m^2$ kPa s]
K	Phase equilibrium constant

L	Height of packing [m]
N	Interfacial molar flux [kmol/m^2 s]
nc	Number of components
n	Total molar hold-up [kmol/h]
P	Pressure [kPa]
R	Universal gas constant [kJ/kmol K]
T	Temperature [K]
t	Time [s]
u	Velocity [m/s]
x	Mole fraction in liquid phase [-]
y	Mole fraction in gas phase [-]
z	Axial distance for packing [m]
ε	Gas or liquid hold-up [-]
Φ	Molar flux [kmol/m^2 s]
Subscripts	
eq	Equilibrium
i	Component number
in	Inlet
L,G	Liquid or gas phase
n	Normalized
ref	Reference

2. Implementation

2.1. Dynamic model equations

The regeneration section modeled here consists of a packed column, a reboiler and a condenser as illustrated in Figure 1.

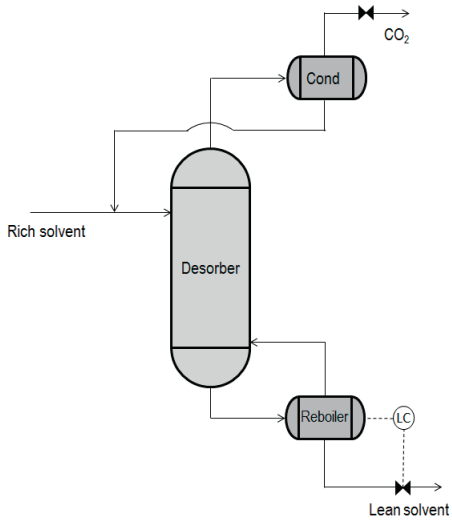

Fig. 1. Flow sheet of the simulated regeneration part of the CO_2 capture plant.

The model for the dynamic packed column is based on the following model equations:

Gas phase equations — *Boundary conditions at z_n=0*

$$\varepsilon_G C_G \frac{\partial y_i}{\partial t} = -\Phi_G \frac{1}{L}\frac{\partial y_i}{\partial z_n} - \left(N_i a - y_i \sum_j N_j a\right) \quad (1)$$

$$y_i(z_n = 0) = y_{i,\text{feed}}$$

$$\frac{d\Phi_G}{dz} = -\sum_j N_j a + \frac{d(\varepsilon_G C_G)}{dt} \quad (2)$$

$$\Phi_G(z_n = 0) = \Phi_{G,\text{feed}}$$

$$\varepsilon_G \frac{dT_G}{dt} = -u_G \frac{1}{L}\frac{\partial T_G}{\partial z_n} - \frac{a}{\sum_i (C_i C_{p,i})_G} \cdot h_{G/L}(T_L - T_G) \quad (3)$$

$$T_G(z_n = 0) = T_{G,\text{feed}}$$

Liquid phase equations — *Boundary conditions at z_n=1*

$$\varepsilon_L C_L \frac{\partial x_i}{\partial t} = \Phi_L \frac{1}{L}\frac{\partial x_i}{\partial z_n} + \left(N_i a - x_i \sum_j N_j a\right) \quad (4)$$

$$x_i(z_n = 1) = x_{i,\text{feed}}$$

$$\frac{d\Phi_L}{dz} = -\sum_j N_j a \quad (5)$$

$$\Phi_L(z_n = 1) = \Phi_{L,\text{feed}}$$

$$\varepsilon_L \frac{dT_L}{dt} = -u_L \frac{1}{L}\frac{\partial T_L}{\partial z_n} - \frac{a}{\sum_i (C_i C_{p,i})_L} \cdot \left(h_{L/G}(T_L - T_G) - \sum_j \Delta H_j N_j\right) \quad (6)$$

$$T_L(z_n = 1) = T_{L,\text{feed}}$$

$$C_G = P/(RT_G) \quad (7)$$

$$N_i = k_g^{'}\left(P_i - P_i^{eq}\right) \quad (8)$$

$$z_n = z/L \quad (9)$$

The details on the development of the dynamic packed column model are described by Tobiesen et al. (2011) [1] and Kvamsdal et al (2009) [2].

Both the reboiler and the condenser are simulated as dynamic flash tanks and the flash tank model is based on the differential algebraic equations presented below.

$$\frac{dn_i}{dt} = F_{in}x_{in,i} - F_G y_i - F_L x_i \quad (10)$$

$$0 = n_i - n_G y_i - n_L x_i \quad (11)$$

$$y_i = K_i x_i \quad (12)$$

$$0 = 1 - \sum_{j=1} y_j \quad (13)$$

Phase equilibrium is assumed in this model, and the equilibrium constants are constant for simplification. The first equation (10) gives *nc* number of equations from which the total component hold-up in both liquid and gas (n_i) is calculated. Equation 11 and 12 gives the molar fractions in the liquid (x_i) and vapor phase (y_i), respectively. The last equation (13) gives the thermodynamic pressure in the flash tank. Included in the flash tank model is also a valve on the vapor side as well as a level controller at the liquid side. The level controller is modeled as a P-controller. The temperature in the flash tank is assumed to be constant.

All independent variables are normalized to increase robustness, both in the packed column model and the flash tank model.

2.2. Numerical solution

The column model contains partial differential equations (PDEs). This requires discretization with regard to the axial direction (column height), and the method of orthogonal collocation is used for this purpose. The discretized PDEs are in this way transformed into a system of ordinary differential equations and algebraic equation (DAE) with time as the independent variable. The flash tank model does not contain any spatial variables, thus this model is already described by a system of DAEs and does not need any similar pre-treatment.

The numerical method for solving the model equations is a simultaneous equation based method. Here, this means that the model equations for all three process units (stripper, condenser, and reboiler) are solved simultaneously by the same integration routine in MATLAB (ode15s).

3. Simulation results and steady state model verification

Two test cases are simulated by the dynamic regeneration model in order to study the dynamic behavior of the regeneration process when two different types of disturbances are introduced. In case 1, the effect of changes in inlet liquid flow rate is studied, while as in case 2, the CO_2 loading in the rich solvent entering the stripper was varied. In both cases the dynamic simulations were performed until a

new steady state conditions was reached and the results are compared to steady state simulation results from CO2SIM.

3.1. Case 1

In the first case the flow rate of rich solvent entering the stripper column is increased by 10 % during 60s. Results from the dynamic MATLAB model together with steady state CO2SIM results are presented in the following figures. The superficial liquid velocity profile through the column for some points in time is shown in Figure 2 (a), while the corresponding steady state CO2SIM results (for the base case liquid flow rate and for 10% increase in liquid flow rate) are shown in Figure 2 (b). The effect of increasing liquid flow rate on the liquid temperature and CO_2 loading profiles for some points in time are shown in Figures 3 (a) and (b), respectively. There is only a slight effect observed on temperatures and CO_2 loading profiles when liquid flow rate is increased by 10 %. Similar results were observed with the steady state CO2SIM model and this is in accordance with the equilibrium profile, which is likely very flat for the specific flow rates.

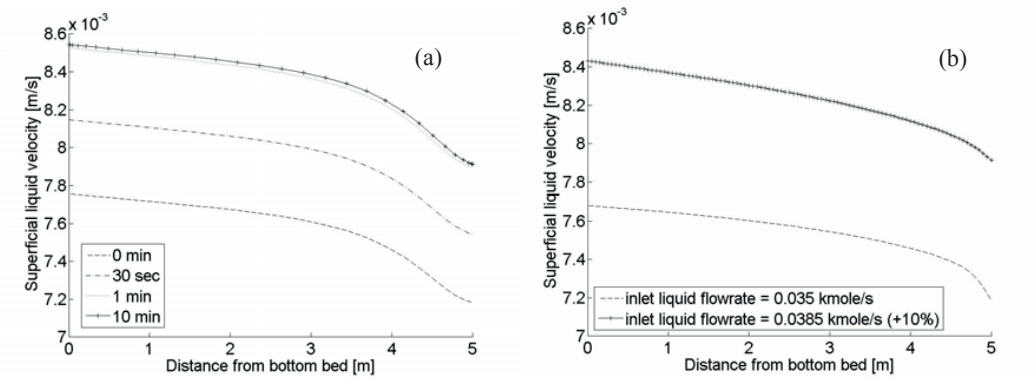

Fig. 2. (a) Superficial liquid velocity in dynamic MATLAB model and (b) superficial liquid velocity in steady state CO2SIM model

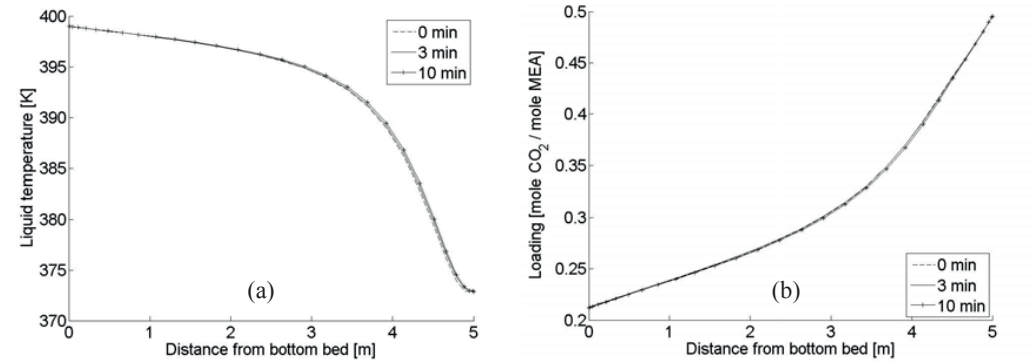

Fig. 3. (a) Liquid temperature profile and (b) CO_2 loading profile in dynamic MATLAB model.

3.2. Case 2

In the second case, the loading of the rich solvent entering the stripper is decreased by 10% during 60s. Results from the dynamic MATLAB model together with steady state CO2SIM results are presented in the following figures. The effects of the loading decrease of the entering solvent on the superficial liquid velocity and the liquid temperature profiles are shown for some points in time in Figures 4 (a) and (b), respectively. The new steady state condition is reached after about 10 minutes. Figure 5 (a) shows the CO_2 loading profile through the stripper column for some points in time as the loading of entering solvent is decreased, while Figure 5 (a) shows the corresponding steady state CO2SIM results (for the base case solvent loading and for 10% decrease in loading of entering solvent). The profile predicted by the dynamic MATLAB model seems slightly more non-linear than the profile predicted by the CO2SIM model, and the observed difference is caused by a slight difference in the packed column model and thermodynamic model. However, the dynamic and steady state results show good agreement.

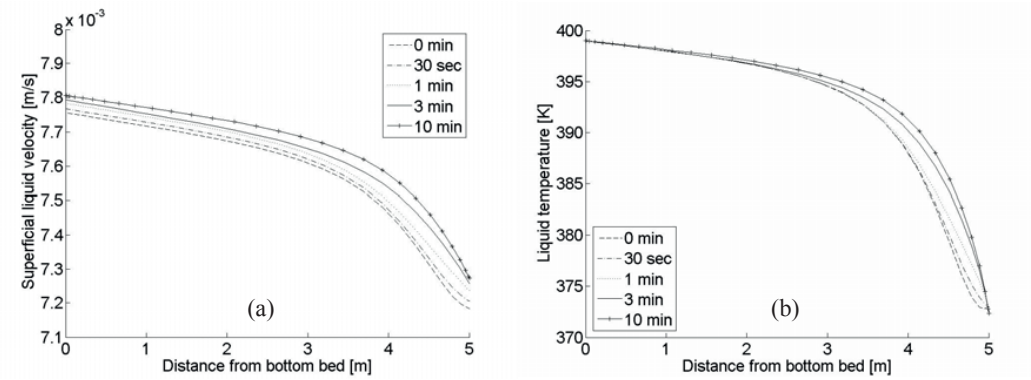

Fig. 4. (a) Superficial liquid velocity profile and (b) liquid temperature profile in dynamic MATLAB model

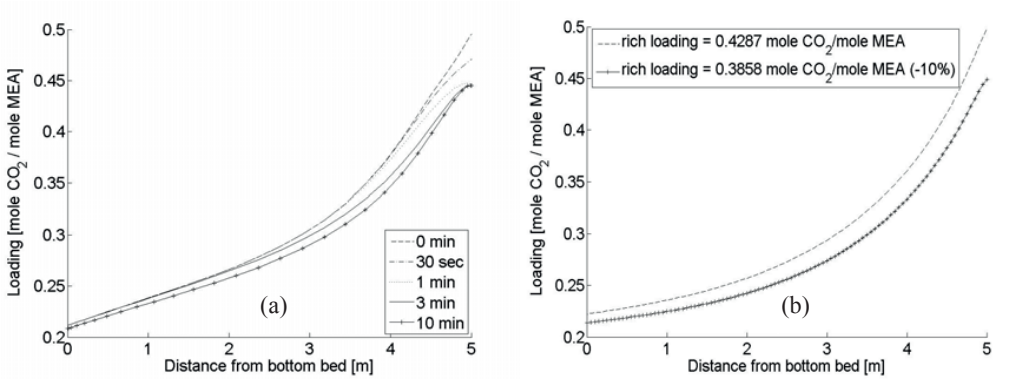

Fig. 5. (a) CO_2 loading profile in dynamic MATLAB model and (b) CO_2 loading profile in steady state CO2SIM model

4. Conclusion

In this work, a dynamic model of the regeneration part of the CO_2 capture process is developed in MATLAB for transient modeling of CO_2 desorption. The model consists of a packed column, a reboiler and a condenser, and the complete system of equations is solved by a simultaneous equation based method. Steady state model verification towards CO2SIM steady state simulations has been presented with two examples of usage. The simultaneous equation based method shows numerically stable behavior for the regeneration section of the CO_2 capture process, and the dynamic simulations at steady state gives similar results to the steady state simulations in CO2SIM. In future work a more accurate dynamic flash tank model will be developed for the reboiler and condenser in the regeneration process. The improved flash tank model will include an equilibrium model predicting phase equilibrium constants as well as differential model equations representing the energy balances to allow calculation of actual flash temperature. A thorough validation towards dynamic pilot data will also be presented.

Acknowledgements

"This publication has been produced with support from the BIGCCS Centre, performed under the Norwegian research program Centres for Environment-friendly Energy Research (FME). The authors acknowledge the following partners for their contributions: Aker Solutions, ConocoPhilips, Det Norske Veritas, Gassco, Hydro, Shell, Statkraft, Statoil, TOTAL, GDF SUEZ and the Research Council of Norway (193816/S60)."

References

[1] Tobiesen FA, Hillestad M, Kvamsdal H, Chikuwa A. A general column model in CO2SIM for transient modeling of CO_2 absorption processes. *Energy Procedia* 2012; **23**:129-139.

[2] Kvamsdal HM, Jakobsen JP, Hoff KA. Dynamic modeling and simulation of CO_2 absorber column for post-combustion CO_2 capture. *Chemical Engineering and Processing* 2009; **48(1):**135–144.

C.3 Paper C: A Numerical Solution Strategy for Dynamic Simulation of Post-combustion CO_2 Capture.

Available online at www.sciencedirect.com

SciVerse ScienceDirect

Energy Procedia 37 (2013) 1670 – 1677

Energy Procedia

GHGT-11

A Numerical Solution Strategy for Dynamic Simulation of Post-combustion CO_2 Capture

Nina Enaasen[a]*, Andrew Tobiesen[b], Hanne M. Kvamsdal[b], Magne Hillestad[a]

[a]*Norwegian University of Science and Technology, Sem Sælandsvei 4, 7491 Trondheim, Norway*
[b]*SINTEF Materials and Chemistry, Sem Sælands vei 2a, 7491 Trondheim, Norway*

Abstract

This paper describes in detail the numerical solution of a dynamic process developed for post-combustion absorption based CO_2 capture. The method used in this work is sequential modular integration. This means that each process unit is modeled and integrated individually while co-ordination algorithms are developed to synchronize process units in time and provide input between connecting units. A pressure-flow interaction algorithm (p-f network solver) is also developed to provide estimates of downstream pressures for each unit. This is required in order to calculate the outlet flow from the units. The complete process plant model is developed to enable simulation of the post-combustion CO_2 capture process at power plant load variations. Two examples of load variations are presented in this paper.

© 2013 The Authors. Published by Elsevier Ltd.
Selection and/or peer-review under responsibility of GHGT

Keywords: post-combustion CO_2 capture; dynamic modelling; sequential modular integration; pressure flow network solver

1. Introduction

We are now moving towards realization of full-scale CO_2 removal plants for power generation. However, varying electricity demand caused by seasonal variations in ambient conditions during a year will force a more flexible operation of the fossil fueled power stations. In fact power plants may also change load quite frequently to cope with changing demand on a daily basis. Together with the increasing

* Corresponding author. Tel.: +47 994 78 919.
E-mail address: nina.enaasen@chemeng.ntnu.no.

1876-6102 © 2013 The Authors. Published by Elsevier Ltd.
Selection and/or peer-review under responsibility of GHGT
doi:10.1016/j.egypro.2013.06.042

use of renewable sources, this will require an even higher degree of flexibility in fossil-fueled power generation.

It is difficult to predict dynamic behavior of chemical processes, especially for complex processes such as an integrated CO_2 capture process downstream a power plant process. Dynamic simulation is a valuable tool to study and identify possible challenges related to daily operation, and identify any negative effects and potential operational bottlenecks for the integrated power- and CO_2 capture process at transient conditions.

The purpose of the present work has been to develop and demonstrate a dynamic process model for simulation of a simplified post-combustion absorption based CO_2 capture process at varying process conditions.

Nomenclature

C_v	Valve constant [kg/s √(Pa)]
$f(u)$	Manipulating variable
W	Mass flow rate [kg/s]
P	Pressure [Pa]
t	Time [s]
T_h	Global time step [s]
δ	Directionality (+1/-1)
τ	Volume multiplied with density pressure differential [kg/Pa]

Subscripts

i,j	Node index
k	Time index

2. Sequential modular integration

The sequential modular based method (modular integration) implies that the process is divided into sub-systems which typically represent process units and all sub-systems are integrated individually. An overall process plant model is used to handle communication between connecting units and synchronizing them in time. The process plant model will treat each process unit as a "black box" that produces output given input.

The total simulation window is divided into time intervals and ccouplings between units occur only at the end of each time interval. The unit's external variables of entering mass flows and downstream pressures need to be described as functions of time, such as polynomials.

The sequential modular based method offer the possibility of computational speed through parallel processing of the individual process units. An additional advantage is the possibility of tailoring the integration algorithm to each process unit and its dynamic behaviour, which offers desirable convergence and stability properties. Specifying initial conditions that satisfy the system of equations for each process

unit is also easier compared to specifying consistent initial conditions for the simultaneously solved complete process model [1].

2.1. Process unit modeling

In order to demonstrate modular integration and the pressure-flow network solver, a simplified model of the CO_2 absorption process (indicated by the grey-shaded units shown in Figure 1) is considered here. This means that the cross heat-exchanger and pumps are treated as black boxes in the simulations implying that the solvent temperatures and pressures at the inlet of both the absorber and the stripper are fixed. The absorber model is based on the column model described by Kvamsdal et al [2]. The regeneration part of the CO_2 capture process is here treated as one unit which consists of a packed column, a reboiler and a condenser, and the complete model is described in detail by Enaasen et al (2012) [3]. A simplified flash tank model with fixed temperature and equilibrium constants is used for simulation of reboiler and condenser in the regeneration part.

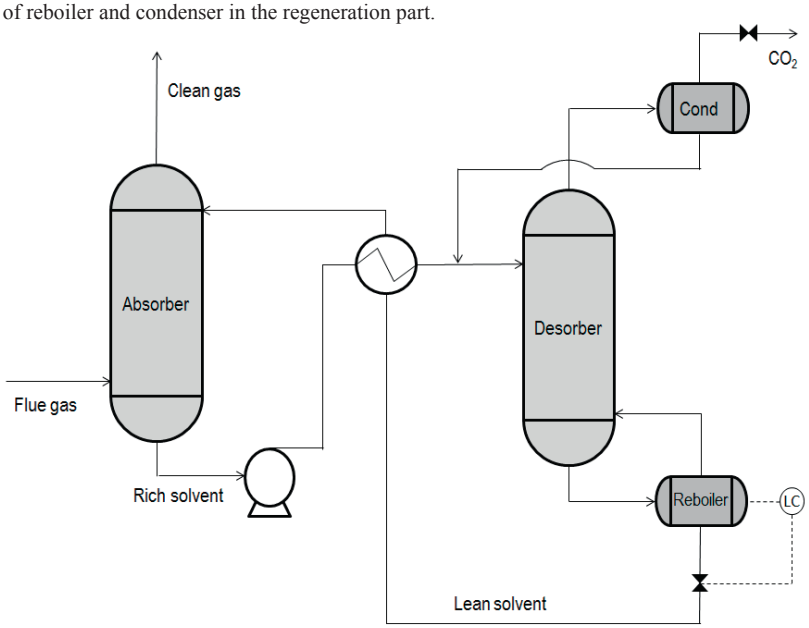

Fig. 1. Flowsheet of the simulated process

2.2. Coordination algorithms

The sequential modular based method requires additional coordination algorithms to handle information flow between units and a pressure-flow network solver, which predicts downstream pressures.

The co-ordination algorithm should also keep the various process units synchronized in time and it should be able to handle recirculation loops. The simulation window is divided into time intervals (with

time step T_h), and couplings between units is allowed at the end of each time interval. Thus, input variables to each unit such as flow rate, pressure, temperature and composition are updated at the end of each time step as a function of time based on their respective gradients during the current time interval. Recirculation loops must be iterated, and a direct substitution method is used for this purpose.

2.3. Pressure-flow network solver

Since outlet flow from a process unit is pressure driven, the downstream pressures must also be provided to each unit. Hence, pressure-flow interaction loops exist between the connected process units. These loops may be solved by an iterative procedure on the modular integration level. Alternatively, by decoupling the problem in two levels (one for fast pressure dynamics and one for slow dynamics) the loops can be solved by a pressure-flow interaction algorithm (p-f network solver) on flowsheet level without or with minimum iteration. Pressure predictions will subsequently be used as input to the modular integration level.

The overall process can be described by unidirectional graphs where the vertices are nodes representing the units and the connections represent streams between units in which the pressure can propagate from one unit to another. The W_{ij} represent the mass flow rate from unit *i* to unit *j* (see Figure 2). As the graph is undirected it implies that $W_{ij} = W_{ji}$.

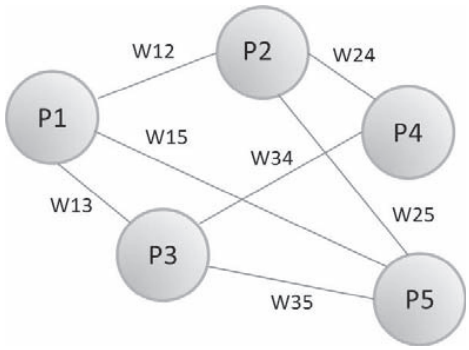

Fig. 2. Illustration of units and connections in the pressure-flow network solver

The flow between nodes *i* and *j* may be given by a model similar to the valve equation:

$$W_{ij} = C_v f(u)\sqrt{P_i - P_j} \tag{1}$$

Also compressors and pumps may be represented by similar equations, where the flow rate is calculated from the work input and the pressures.

The model of pressure change in node *i* is given by

$$\frac{dP_i}{dt} = \frac{1}{\tau_i}\sum_j^n \delta_{ij} W_{ij} \tag{2}$$

where δ takes care of directionality by being +1 when directed to node *i* from node *j*, and -1 when

directed from node *i* to node *j*, or otherwise 0. The parameter τ is given by

$$\tau_i = V_i\left(\frac{\partial \rho_i}{\partial P_i}\right) \tag{3}$$

and can be considered a constant in this context.

Based on the present situation of mass flow rates, it is desired to predict how the pressure will evolve in each unit. A linearization of the pressure model is made by linearizing the valve equation (1) around time t_k:

$$\frac{dP_i}{dt} = \frac{1}{\tau_i}\sum_j^n \delta_{ij} W_{ij}^k + \frac{1}{\tau_i}\sum_j^n \delta_{ij}\left(\frac{\partial W_{ij}}{\partial P_i}\right)_{P_j} \frac{dP_i}{dt}(t-t_k) + \frac{1}{\tau_i}\sum_j^n \delta_{ij}\left(\frac{\partial W_{ij}}{\partial P_j}\right)_{P_i} \frac{dP_j}{dt}(t-t_k) \tag{4}$$

Applying the time horizon concept and introducing T_h being the global time step $T_h = t_{k+1}$-t_k and converting to matrix form:

$$\left[\mathbf{I} - T_h \mathbf{J}_k\right]\frac{d\mathbf{P}}{dt} = \begin{bmatrix} \frac{1}{\tau_1}\sum_j^n \delta_{1j} W_{1j}^k \\ \vdots \\ \frac{1}{\tau_n}\sum_j^n \delta_{nj} W_{nj}^k \end{bmatrix} \tag{5}$$

which by implicit Euler integration yields:

$$\mathbf{P}_{k+1} - \mathbf{P}_k = T_h\left[\mathbf{I} - T_h \mathbf{J}_k\right]^{-1} \begin{bmatrix} \frac{1}{\tau_1}\sum_j^n \delta_{1j} W_{1j}^k \\ \vdots \\ \frac{1}{\tau_n}\sum_j^n \delta_{nj} W_{nj}^k \end{bmatrix} \tag{6}$$

This is solved as a linear system $Ax = b$ without iterations.

For typical process plant simulations the assumption of a fast propagating pressure change is reasonable. As the changes in composition due to chemical reaction, separation and phase separation happen on a large time scale in comparison with the pressure change, the pressure propagation in the process units can be described as a pseudo steady-state process [4]. By removing this fast mode of the model, the stiffness of solving the collection of sub-problems in the network solver is simplified.

3. Results

Two examples of load variations are simulated. In the first case, the feed gas flow rate to the absorber column is increased by 10%, while as in the second case, the CO_2 composition in the feed gas to the absorber is decreased by 10%. The time interval (T_h) used in these simulations is 10 seconds.

3.1. Increase in feed gas flow rate

The feed gas flow rate is increased by 10% in one single step change. Figure 2 and 3, shows the loading in the rich solvent exiting the absorber and the lean solvent exiting the regeneration unit, respectively, both as functions of time. The rich loading is increasing as the gas load to the absorber is increased, and the lean loading is increasing as well when rich loading is increased. The effect on lean

loading is however very small and this is partly caused by the simplified flash tank model used in the model of the reboiler in the regeneration section. However, a time delay in mass transportation from the absorber column to the stripper column is observed, since the loading in the solvent exiting the stripper remains constant for about 200 seconds after the disturbance is introduced. This is an effect of the process unit's capacitance, and it demonstrates the importance of including correct equipment sizing in dynamic modeling.

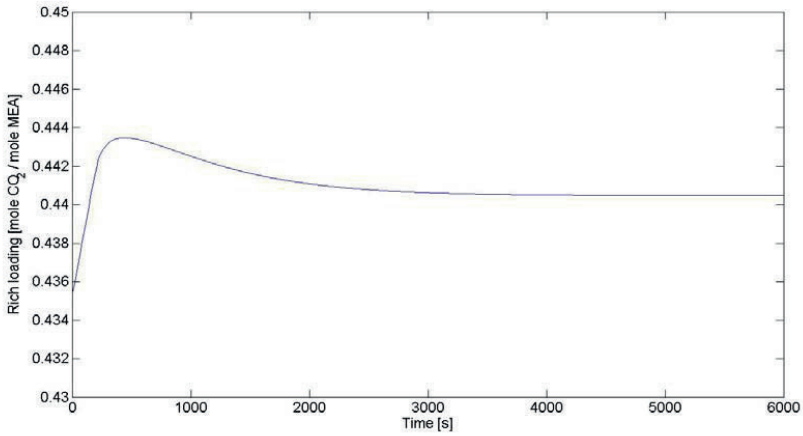

Fig. 3. Loading in rich solvent exiting the absorber as a function of time

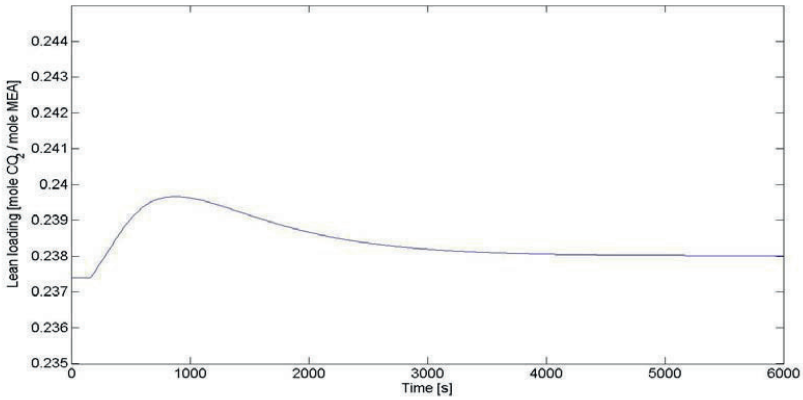

Fig. 4. Loading in lean solvent exiting the stripper as a function of time

3.2. Decrease in CO_2 load in the feed gas

In the second case, the CO_2 concentration in the feed gas to the absorber is decreased by 10 %. The rich and lean loading in this case is presented as functions of time in Figure 4 and 5. In this case the rich loading is decreasing as CO_2 concentration in the feed gas is decreased, and the same effect is observed in the loading of the lean solvent exiting the stripper. The effect on lean loading is however very small also in this case.

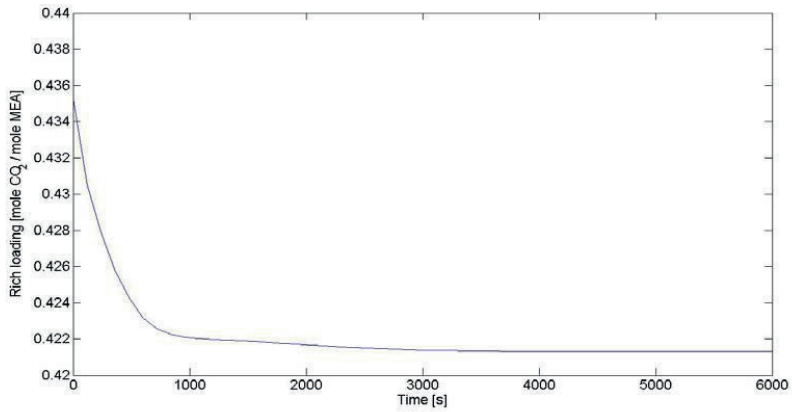

Fig. 5. Loading in rich solvent exiting the absorber as function of time

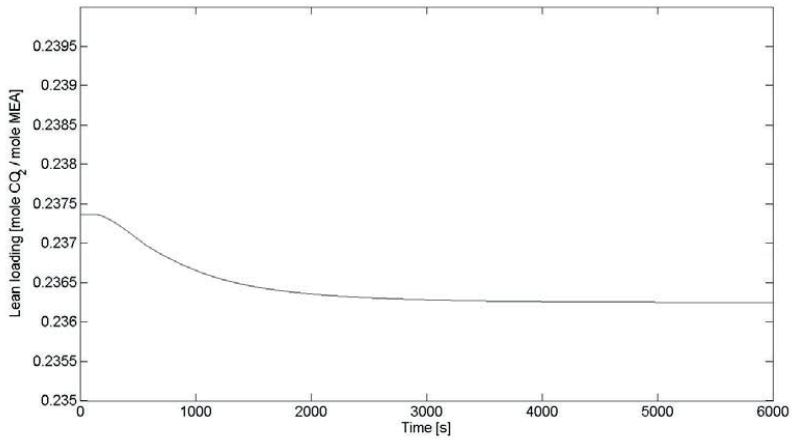

Fig. 6. Loading in lean solvent exiting the stripper as function of time

4. Conclusions

Modular integration is investigated as a numerical solution strategy for simulation of post-combustion CO_2 capture processes. The method proves to offer desirable convergence and stability properties for a simplified plant model consisting of an absorber model and a regeneration model. In future work, a more accurate dynamic flash tank model will be developed and implemented in the unit model of the regeneration section. This model will include differential equations representing the energy balances which will allow variations in the flash temperature, in addition to an equilibrium model predicting actual equilibrium constants. A cross heat-exchanger will also be included in the overall process model in order to enable studies of transient behaviour in a more realistic manner where also liquid temperatures in the inlet streams to the columns are allowed to vary.

Acknowledgements

"This publication has been produced with support from the BIGCCS Centre, performed under the Norwegian research program Centres for Environment-friendly Energy Research (FME). The authors acknowledge the following partners for their contributions: Aker Solutions, ConocoPhilips, Det Norske Veritas, Gassco, Hydro, Shell, Statkraft, Statoil, TOTAL, GDF SUEZ and the Research Council of Norway (193816/S60)."

References

[1] Brosilow CB, Liu Y-C, Cook J, Klatt J. Modular integration methods for simulation of large dynamic systems. *Modeling, Identification and control* 1985; **6(3):**153-179.

[2] Kvamsdal HM, Jakobsen JP, Hoff KA. Dynamic modeling and simulation of CO_2 absorber column for post-combustion CO_2 capture. *Chemical Engineering and Processing* 2009; **48(1):**135–144.

[3] Enaasen N, Tobiesen A, Kvamsdal HM, Hillestad M. Dynamic modeling of the solvent regeneration part of a CO_2 capture plant. To be presented at GHGT-11, November 18^{th}-22^{nd} 2012 and published in Energy Procedia.

[4] Hillestad M, Hertzberg T. Dynamic simulation of chemical engineering systems by the sequential modular approach. *Computers & Chemical Engineering* 1986; **10(4)**:377-388.

C.4 Paper D: Validation of a Dynamic Model of the Brindisi Pilot Plant.

Available online at www.sciencedirect.com

ScienceDirect

Energy Procedia 63 (2014) 1040 – 1054

Energy Procedia

GHGT-12

Validation of a Dynamic Model of the Brindisi Pilot Plant

Nina Enaasen[a]*, Luigi Zangrilli[b], Angela Mangiaracina[c], Thor Mejdell[d], Hanne M. Kvamsdal[d], Magne Hillestad[a]

[a]*Department of Chemical Engineering, NTNU, Sem Sælandsvei 4, N-7491 Trondheim, Norway*

[b]*ENEL Engineering and Research Division, Loc. Cerano – Litoranea Salentina Brindisi, 72020 Tuturano, Italy*

[c]*ENEL Engineering and Research Division, Via Andrea Pisano 120, 56122 Pisa, Italy*

[d]*Department of CO_2 Capture Process Technology, SINTEF Materials and Chemistry, Post Office Box 4760, Sluppen, N-7465 Trondheim, Norway*

Abstract

In this work, a dynamic model of the Brindisi CO_2 capture pilot plant is implemented in K-spice general simulation tool. The model is used to simulate relevant step changes performed during a pilot plant campaign conducted in the EU project *Octavius* in May and June 2013. Model results are compared to dynamic pilot plant data and it shows good transient agreement to the experimental results. The model is therefore able to capture the main process dynamics. An offset is, however, observed in some cases, especially during the initial simulation time. This is most likely caused by the fact that the model was given a steady state starting point, while the pilot plant was not necessarily completely at steady state when the step change was introduced. It is challenging to ensure steady state conditions prior to dynamic tests in a pilot plant, especially for one that is connected to a real power production unit as this one. Power production variations will act as disturbances to the capture unit, and due to slow transients in the solvent inventory of the capture unit, it will take several hours to ensure steady state conditions with stable inlet flue gas conditions.

© 2014 The Authors. Published by Elsevier Ltd. This is an open access article under the CC BY-NC-ND license (http://creativecommons.org/licenses/by-nc-nd/3.0/).
Peer-review under responsibility of the Organizing Committee of GHGT-12

Keywords: post-combustion CO_2 capture, dynamic modelling, dynamic validation

* Corresponding author. Tel.: +47-994-78-919.
E-mail address: enaasen@ntnu.no

1876-6102 © 2014 The Authors. Published by Elsevier Ltd. This is an open access article under the CC BY-NC-ND license (http://creativecommons.org/licenses/by-nc-nd/3.0/).
Peer-review under responsibility of the Organizing Committee of GHGT-12
doi:10.1016/j.egypro.2014.11.111

1. Introduction

CO_2 capture and storage (CCS) applied to fossil fuel fired power plants is a promising technical solution to reduce anthropogenic carbon emissions and mitigate global warming. Post combustion CO_2 capture using amine absorption is considered one of the most mature techniques to achieve the targets of carbon emission reduction [1]. Integration of a CO_2 absorption unit with a power station results in a complex overall process that may lead to operational challenges, thus research on CO_2 absorption dynamics has gained increasing interest the recent years [2]. The capture process has to be able to follow frequent and fast load changes without sacrificing the performance of the power station.

Dynamic modelling and simulation has also been recognized as a useful tool to study the transient performance of the CO_2 capture unit during power plant load variations [3]. Simulation studies will improve the general understanding of process dynamics of the CO_2 absorption process, ease challenges concerning process scale-up and possibly identify operational bottlenecks at an early stage before full-scale capture plants are realized.

In this work, a system of unit operations representing the Brindisi pilot plant has been implemented in K-Spice general simulation tool provided by Kongsberg Oil & Gas Technologies. In order to ensure the validity of the dynamic model, a thorough validation using proper dynamic pilot plant data is performed. Several simulation cases with varying flue gas flow rate, solvent flow rate and steam flow rate has been performed and the resulting transient responses has been compared to pilot plant data from experiments conducted in the Brindisi pilot plant.

Nomenclature

α	CO_2 loading
a_i,b_i,c_i	Constants
E	Enhancement factor
$F_{fluegas}$	Flue gas flow rate [Nm^3/h]
G_g	Gas mass flux [kg/s m^2]
G_l	Liquid mass flux [kg/s m^2]
$k_l a$	Gas mass transfer coefficient [kmol/m^3 kPa s]
$k_g a$	Liquid mass transfer coefficient [kmol/m^3 kPa s]
tab1	Table value
tab2	Table value
T	Temperature [K]
ΔP_{abs}	Absorber pressure drop [mbar]

2. The Brindisi pilot plant

A fully instrumented post-combustion CO_2 absorption pilot plant based on amines has been realized by ENEL in Brindisi, Italy. The goal was to gain experience in CO_2 capture unit design and operation. The capture plant is attached to a full scale coal fired power plant and both units are operated by ENEL. The capture plant is designed for 10 000 Nm^3/h flue gas, capturing about 2.0 ton/h of CO_2. The absorber and stripper columns contain Mellapak M250X structured packing of 22 meter and random packing of 11 meter, respectively.

In the EU project *Octavius* a pilot plant campaign was conducted in May and June 2013 using 30 wt% monoethanolamine (MEA) as solvent. As part of the campaign various transient tests with step-wise changes in different operational parameters such as flue gas flow rate, reboiler duty and solvent flow rate has been performed, while the responses and performance of the capture plant has been monitored and logged every minute. The flue gas flow rate was not measured directly, but is estimated based on measured pressure drop in the absorber column using the following equation:

$$F_{\text{fluegas}} = 3140.3\ \Delta P_{\text{abs}}^{0.4914} \tag{1}$$

Solvent samples were also withdrawn frequently and analyzed to determine amine concentration and CO_2 loading. The pilot plant was operated with the minimum solvent hold-up of about 61 m^3 in order to get a faster response after step-changes were imposed.

3. Dynamic process model

A system of unit operations representing the Brindisi pilot plant has been implemented in the K-Spice general dynamic simulation tool. A control scheme corresponding to the control structure found in the Brindisi pilot plant is also applied. The process flow sheet is shown in Figure 1.

Thermodynamic data for the specific system in study are provided from interpolation of data tables generated by MultiFlash provided by InfoChem ltd. A total of 3 thermodynamic tables were generated; separate tables for the solvent system tuned for both absorber and desorber conditions, along with a water/steam table for the reboiler.

The thermodynamic tables are only valid for physical equilibrium between two or more phases which means that the chemical reaction between CO_2 and MEA is not accounted for. An add-on reaction set module (ChemAbsorption module) is used to compensate for the MEA-CO_2 reaction. This module acts as a secondary look-up table for the MEA-CO_2 equilibrium and the chemistry of the absorption process is configured separately within this module. A single gas component is configured with a single liquid absorbent, thus CO_2 exists as two components in the model; gas phase CO_2 and absorbed CO_2. The module contains correlations that calculate mass transfer for gas component to liquid absorbent and interfacial mass fluxes with an enhancement factor that compensates for the chemical reaction. This corresponds to a rate based approach for calculation of mass transfer.

The mass and heat transfer is characterized by the following properties:

- Chemical equilibrium
- Heat of reaction
- Mass transfer coefficients and enhancement factor

Information about these properties is provided as tables and correlations in the ChemAbsorption module for various temperatures and absorbent loadings. The tables and correlation constants were generated from SINTEF's CO2SIM software. A figure that illustrates the table information for equilibrium pressure of CO_2 at various temperatures and loadings is included in Figure 2. Isotherms are provided for 20 °C to 140 °C with 20 °C interval.

The liquid mass transfer coefficient ($k_l a$) and the enhancement factor (E) are in addition correlated to gas and liquid mass flux through the column. The gas mass transfer coefficient ($k_g a$) is given as a correlation of gas and liquid mass flux only.

$$k_l a = \text{tab1}(\alpha, \text{T}) \cdot \left(a_1 + a_2 \cdot \text{G}_g^{a_3} \cdot G_l^{a_4} \right) \tag{2}$$

$$k_g a = \left(b_1 + b_2 \cdot T \right) \cdot \text{G}_g^{b_3} \cdot \text{G}_l^{b_4} \tag{3}$$

$$\text{E} = 1 + \text{tab2}(\alpha, \text{T}) \cdot \frac{c_1}{c_2 + c_3 \cdot G_g + c_4 \cdot G_l} \tag{4}$$

A set of packing sections interfaced with the ChemAbsorption module with 30 wt% MEA as solvent is used to model the absorber and stripper columns. Drums are used to model absorber and desorber sump, reboiler, condenser and buffer tank. All vessels are given the correct dimensions according to the Brindisi pilot plant and provided with level controllers to ensure correct solvent hold-up.

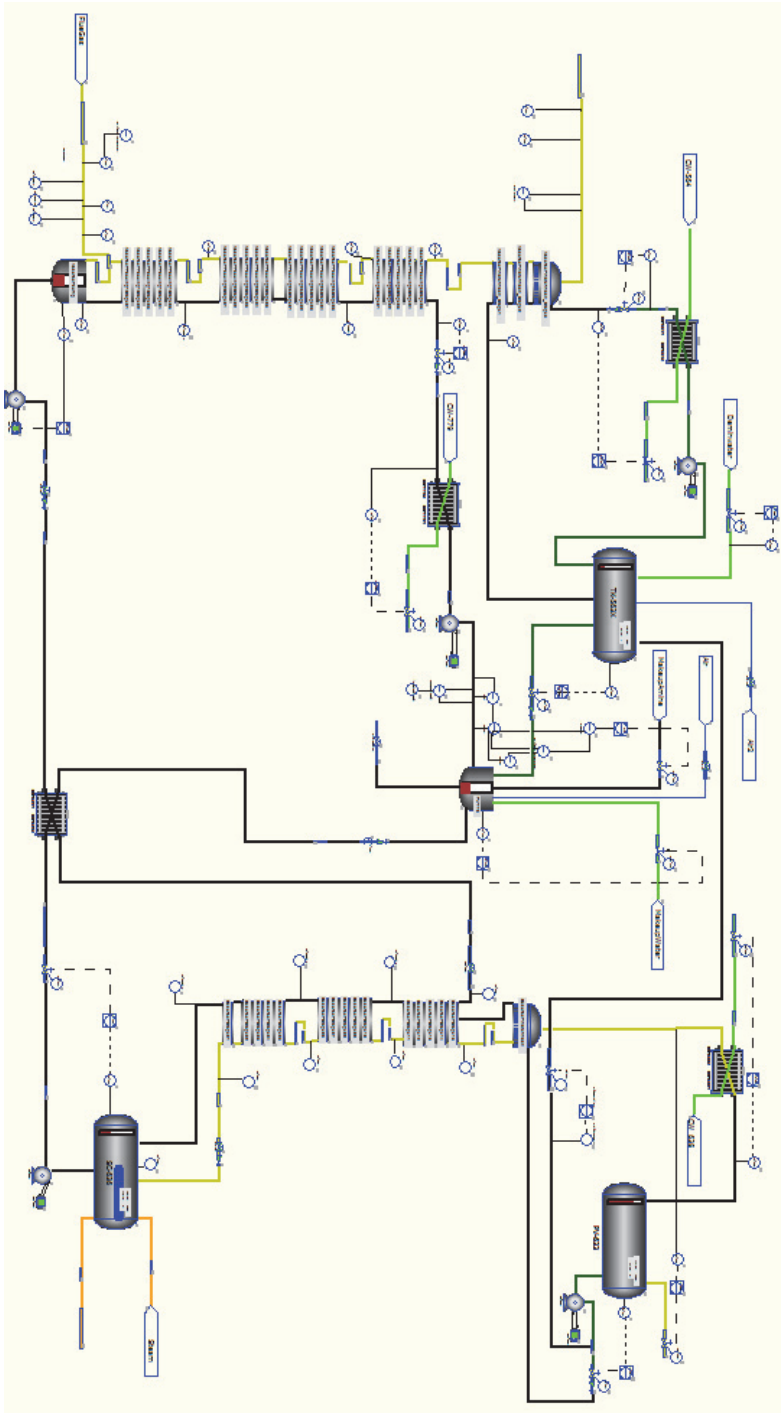

Fig. 1. Process flow sheet of the dynamic model in K-spice

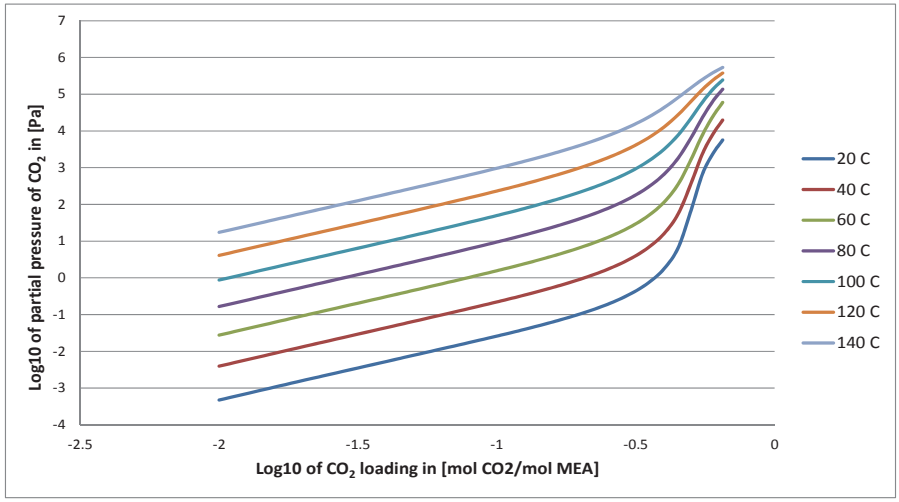

Fig. 2. Partial pressures of CO_2 at equilibrium for various CO_2-loadings and temperatures in 30 wt% MEA solution

4. Results

4.1. Step changes in steam flow rate to reboiler

An experiment with varying steam flow rate and constant flue gas flow rate of 10 000 Nm^3/h was conducted in the pilot plant. The steam flow rate was ramped down from 3150 kg/h to 2400 kg/h in 3 steps and then increased again in 3 steps to 3330 kg/h over a total period of 27 hours. A single step change in solvent flow rate was also performed after 15.5 hours as illustrated in Figure 3.

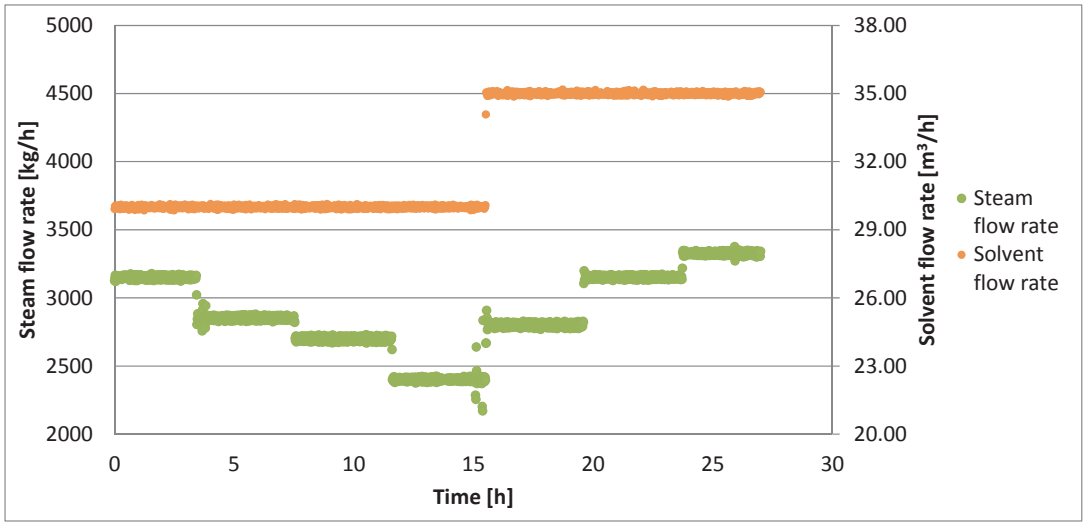

Fig. 3. Step changes in steam flow rate and solvent flow rate

The effect on released CO_2 from the stripper is presented in Figure 4. The model follows the transient behavior observed in the pilot plant quite accurately, even though there is some deviation in the amount of desorbed CO_2, especially for the lowest steam flow rates. The model predicts a lower CO_2 flow rate than what is observed in the pilot experiment.

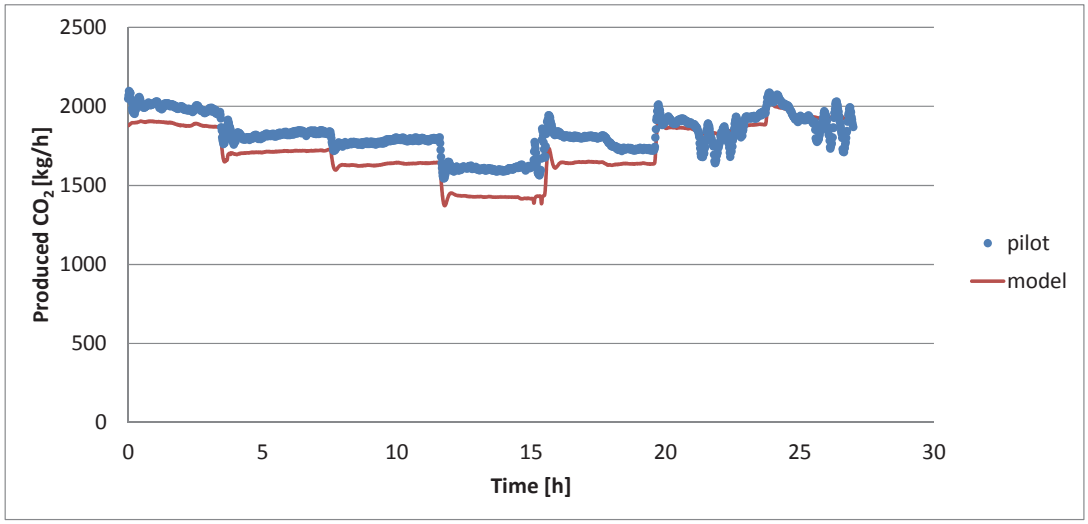

Fig. 4. Response in CO_2 flow rate from the stripper

The lean and rich CO_2 loadings are presented in Figure 5. The model seems to overpredict both the lean and rich loading slightly. However, it can be seen that the model predicts a similar transient behavior to what is observed in the pilot plant.

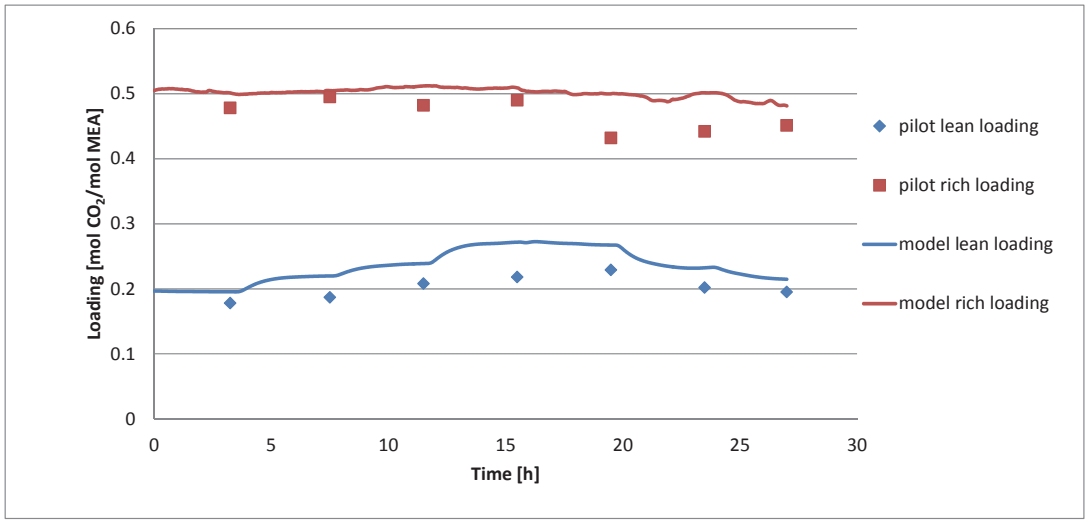

Fig. 5. Response in CO_2 loadings

Since the flue gas originates from a real power station, the absorber inlet CO_2 concentration will naturally have some variations during the course of time. During this specific experimental period it varied in the range of 9 to 12.5 vol% as shown in Figure 6 (a). The vol% of CO_2 of the gas exiting the absorber is also presented in the same figure. The response in outlet CO_2 concentration predicted by the model is compared to the pilot plant data in figure 6 (b).

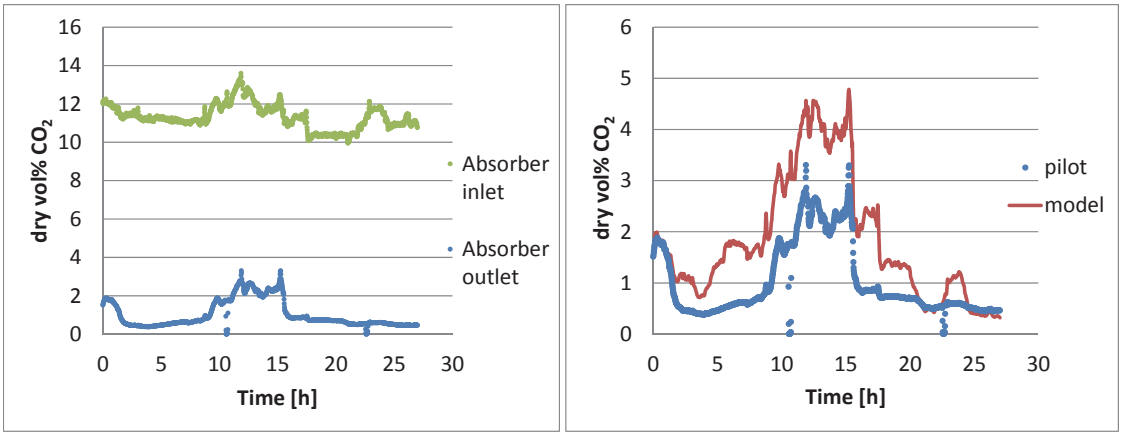

Fig. 6. (a) Absorber inlet and outlet vol% CO_2; (b) Response in absorber outlet vol% CO_2.

The predicted absorber outlet CO_2 concentration is in general higher than observed in the pilot plant data. The main dynamics are still captured by the model, but the observed behavior seems smoother that what is predicted by the model. The model predicts faster transients for the outlet absorber gas, thus there might exist some mixing effects in the real system that is not captured by the model.

The absorber temperature profiles for various points in time are presented in Figure 7 and shows good agreement between model and pilot plant data. The transient trend is also captured.

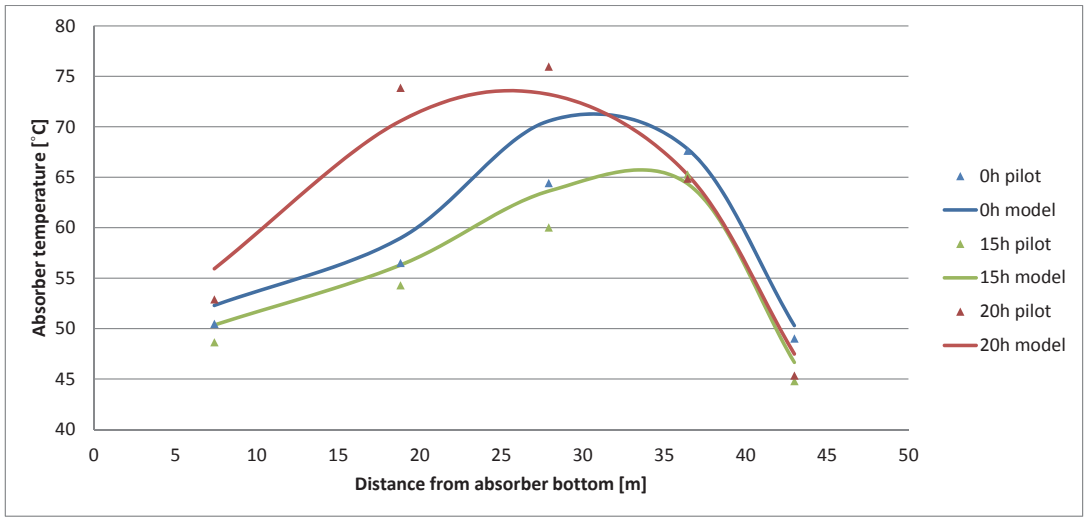

Fig. 7. Absorber column temperature profiles

The calculated CO_2 capture rate for both pilot and model data is presented in Figures 8 (a) and (b).

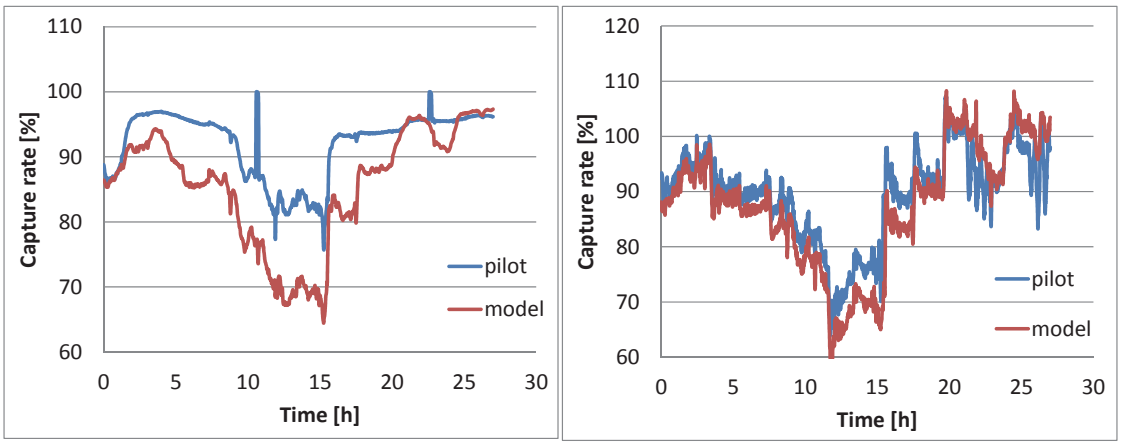

Fig. 8. (a) CO_2 capture rate based on absorber inlet and outlet data (b) CO_2 capture rate based on desorber outlet and absorber inlet data

The model predicted capture rate based on absorber outlet CO_2 flow (red line in Figure 8 (a)) is in general lower than observed in the pilot plant data due to the predicted higher amount of CO_2 slipping through the absorber compared to the pilot plant results as showed in Figure 6 (b). The pilot plant capture rate shows again a bit smoother behavior compared to model predictions. This corresponds to the similar trend in figure 6 (b) and the deviation is most likely caused by un-modelled mixing effects.

However, if the capture rate is calculated based on CO_2 flow outlet the desorber instead of absorption in the absorber, the agreement between pilot and model data is much better, both in terms of level and transient behavior. This indicates a mass balance weakness or measurement errors for absorber inlet or outlet gas data. It might have to do with the CO_2 analyzer measuring outlet CO_2 concentration, but it can also results from the flue gas flow rate correlation (Equation 1). A plot of the calculated amount of CO_2 captured in the pilot plant absorber compared to the amount of CO_2 released by the desorber is shown in Figure 9.

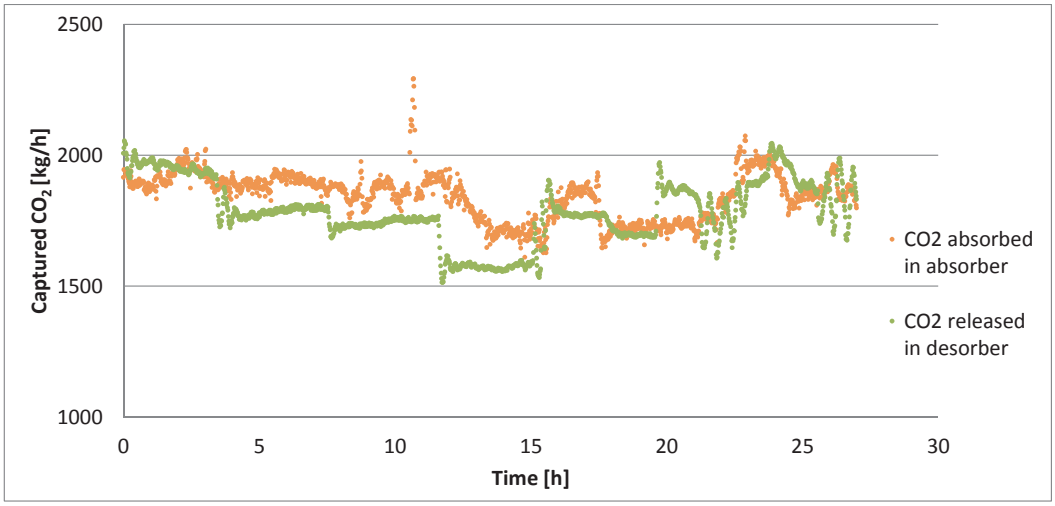

Fig. 9. Comparison of the pilot plant CO_2 absorbed in absorber and CO_2 released in desorber

A general trend of a higher amount of CO_2 captured in the absorber compared to what is released in the desorber is observed. In fact the deviation is about 4.2 % during this period. Since these are dynamic data, they cannot be expected to be equal at each point in time, but they should average equal over a longer period. The measured loading data suggest a lower amount of CO_2 absorbed in the solvent towards the end of the experiment compared to the beginning (a slightly smaller difference between lean and rich loading's towards the end). This means that an even higher total amount of CO_2 released by the desorber should have been observed compared to what is absorbed in the absorber, which supports the indicated error in some of the measured gas data.

4.2. Step changes in solvent flow rate

The solvent flow rate was stepped down from 35.6 m^3/h to 25.6 m^3/h as shown in Figure 10. The flue gas flow rate and steam flow rate was kept constant at 10 000 Nm^3/h and 2900 kg/h, respectively, during this period. The total time for this experiment was 5 hours.

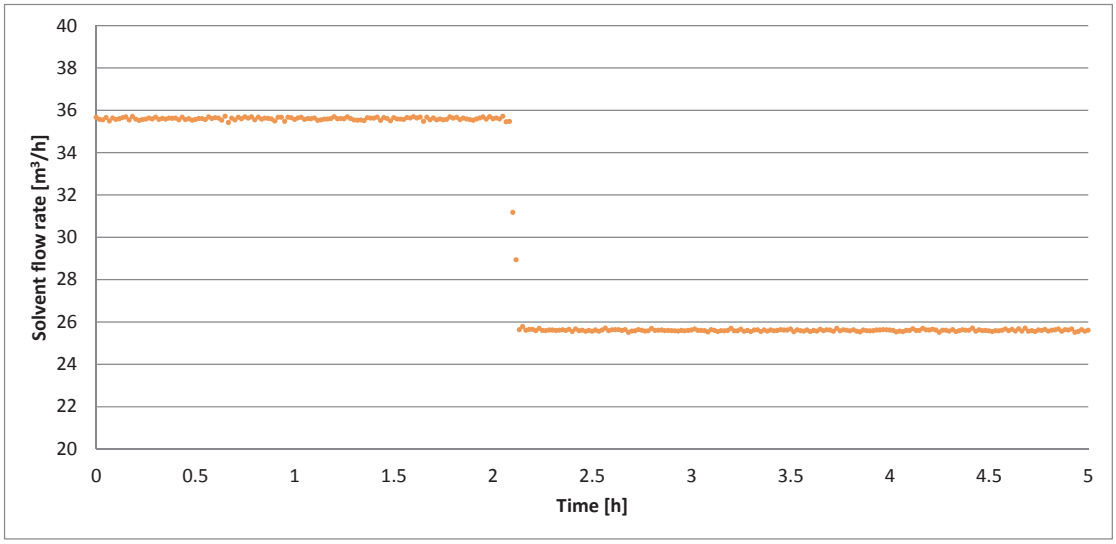

Fig. 10. Step changes in solvent flow rate

The step change in solvent flow rate did hardly affect the released CO_2 in desorber as illustrated in Figure 11. A small step down in the response is, however, observed both in pilot plant and model results after 2.2 hours. The lean and rich CO_2 loadings are presented in Figure 12. As for the previous case the model seems to overpredict both the lean and rich loading slightly. The deviation is larger in the beginning of the simulation time and decreases towards the end. A loading decrease is observed for lean solvent both in model and pilot plant results. The initial deviation might have to do with the fact that the pilot was not completely at steady state when the step change in solvent flow rate was introduced due to previous dynamic testing or other external disturbances. The same offset in initial CO_2 flow rate from stripper (Figure 11) supports this theory.

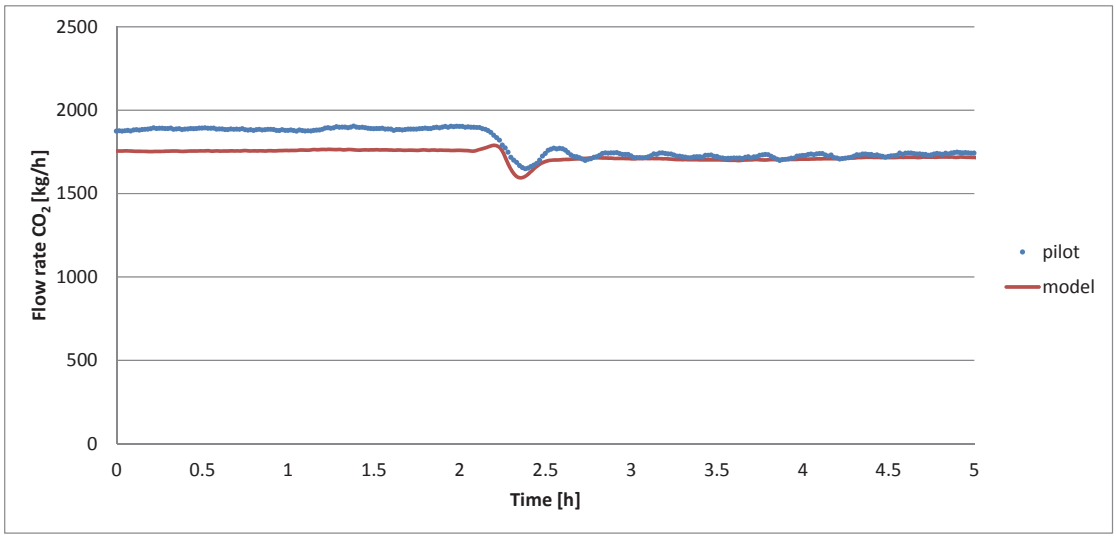

Fig. 11. Response in CO_2 flow rate from the stripper

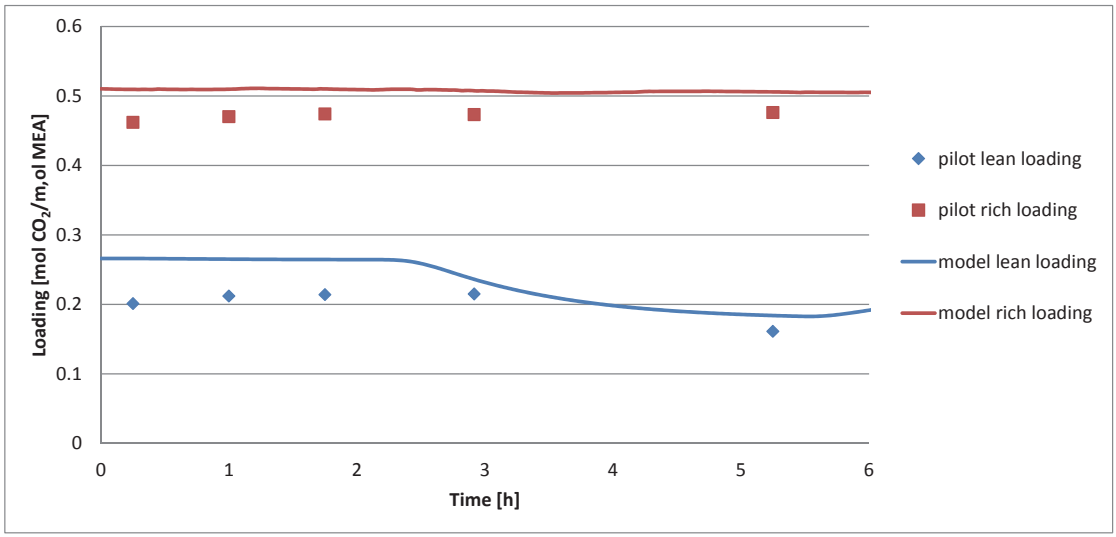

Fig. 12. Response in CO_2 loadings

The inlet vol% of CO_2 to the absorber varied a bit during this period, but a clear response in the absorber outlet vol% of CO_2 is observed when the solvent flow rate was reduced. The inlet and outlet CO_2 concentration is plotted in Figure 13 (a). The response in outlet CO_2 concentration predicted by the model is compared to the pilot plant data in Figure 13 (b).

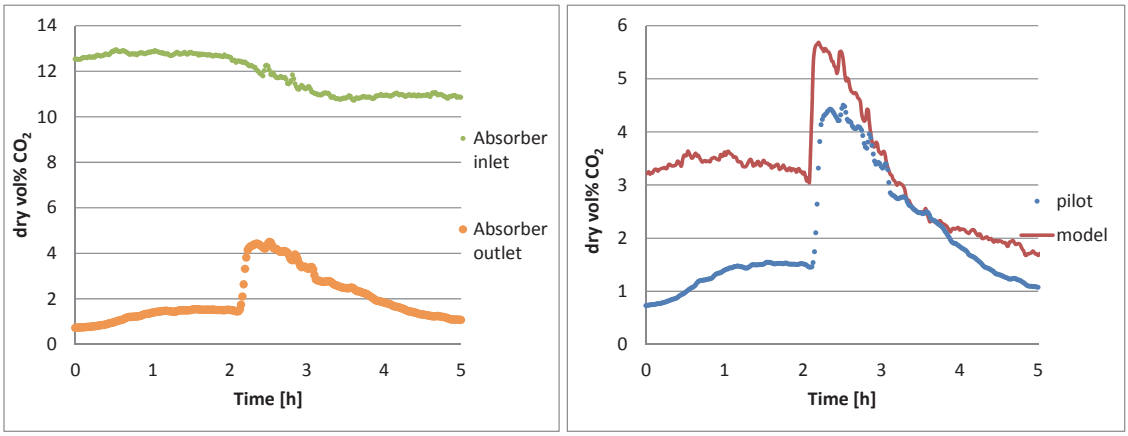

Fig. 13. (a) Absorber inlet and outlet vol% CO_2; (b) Response in absorber outlet vol% CO_2.

The predicted absorber outlet CO_2 concentration is in general higher than observed in the pilot plant data and the response predicted by the model shows slightly faster transients than what is observed in the pilot data. Again as for the previous case there might exist some mixing effects in the real system that is not captured by the model.

The calculated CO_2 capture rate for both pilot and model data is presented in Figures 14 (a) and (b).

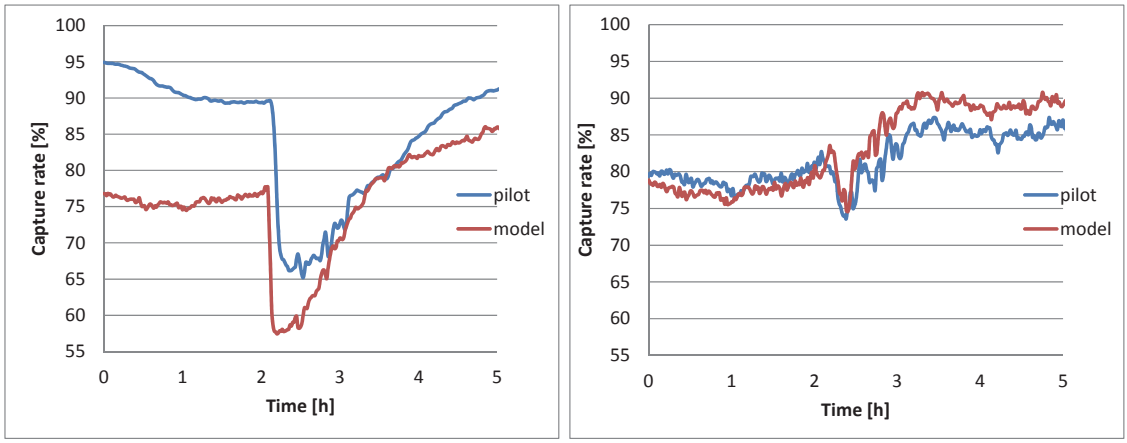

Fig. 14. (a) CO_2 capture rate based on absorber inlet and outlet data (b) CO_2 capture rate based on desorber outlet and absorber inlet data

Again the capture rate calculated based on desorber outlet CO_2 flow shows a much better agreement between model and pilot plant data. The initial offset between pilot plant CO_2 capture rate calculated by absorber data only (95%) and desorber outlet CO_2 flow (80 %) supports the theory of pilot plant not being at steady state initially.

A plot of the calculated amount of CO_2 captured in the absorber compared to the amount of CO_2 released by the desorber is shown in Figure 15. Again a general trend of a higher amount of CO_2 captured in the absorber compared to what is released in the desorber is observed. The overall deviation for this period is about 2 %. However, it should be noted that the experimental period is much shorter in this case (only 5 hours compared to 27 hours in the first case) and that the pilot plant was not at steady state initially. The basis for comparison of absorbed and desorbed CO_2 is therefore not as relevant as for the former case.

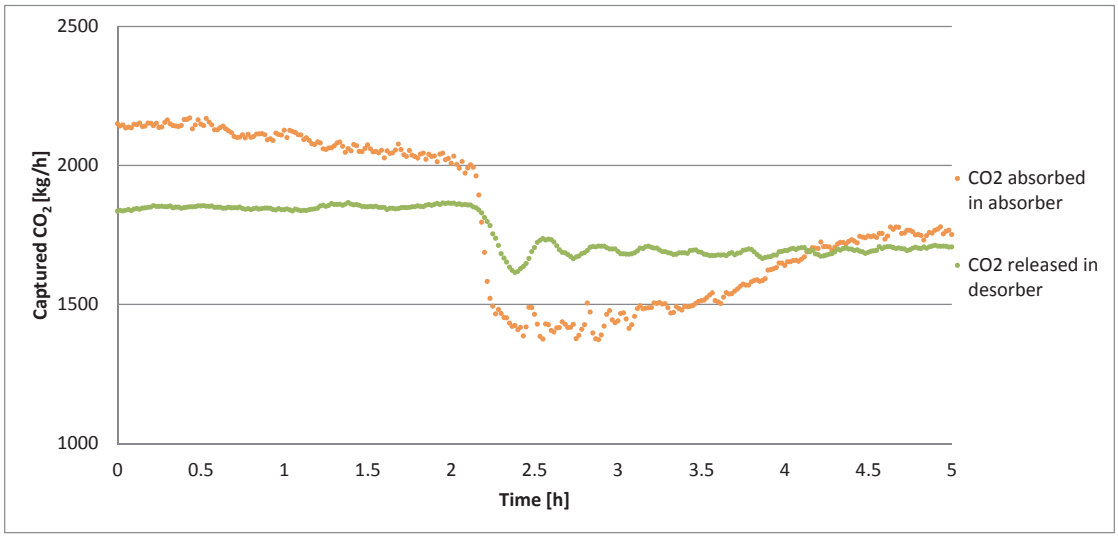

Fig. 15. Comparison of CO_2 absorbed in absorber and released in desorber

4.3. Step changes in flue gas flow rate

A third case that was tested in the pilot plant and afterwards simulated was step changes in flue gas flow rate. The flue gas flow rate was decreased from 11 000 Nm^3/h in two steps to 10 000 and 8 900 Nm^3/h as shown in Figure 16. The total time for this experiment was 10 hours and the solvent flow rate and steam flow rate to reboiler was kept at a constant level during this period.

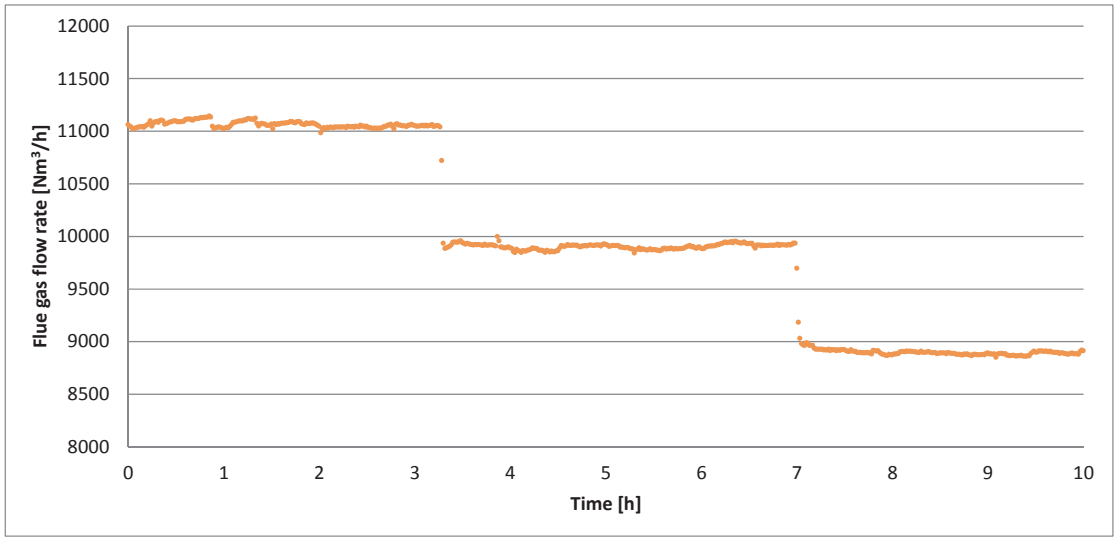

Fig. 16. Step changes in flue gas flow rate

The step change in flue gas flow rate did not affect the amount of released CO_2 in the desorber or CO_2 loadings significantly as illustrated in Figures 17 (a) and (b).

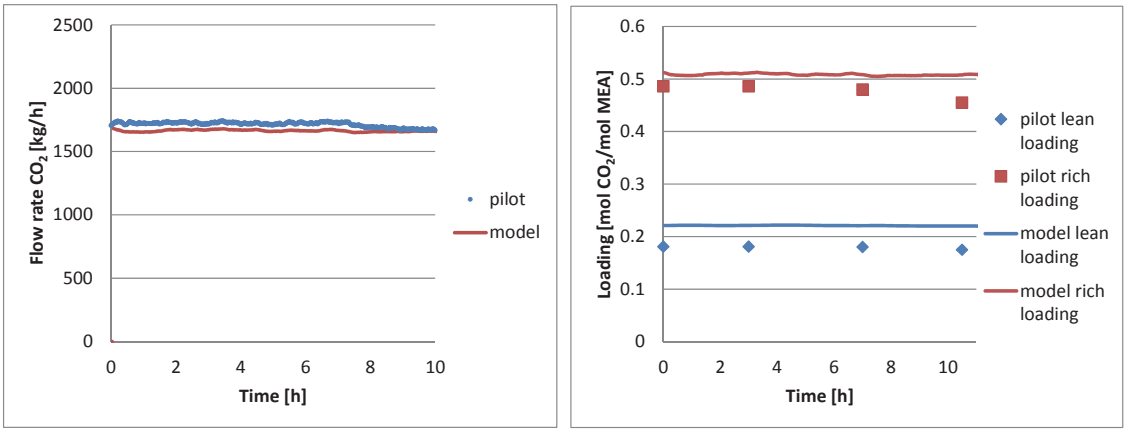

Fig. 17. (a) Response in CO_2 flow rate from the stripper (b) Response in CO_2 loadings

As for the previous cases the model tends to overpredict both the lean and rich loadings slightly.

The flue gas CO_2 concentration was quite stable at 10-11 vol% during this period. The response in outlet CO_2 concentration predicted by the model is compared to the pilot plant data in Figure 18.

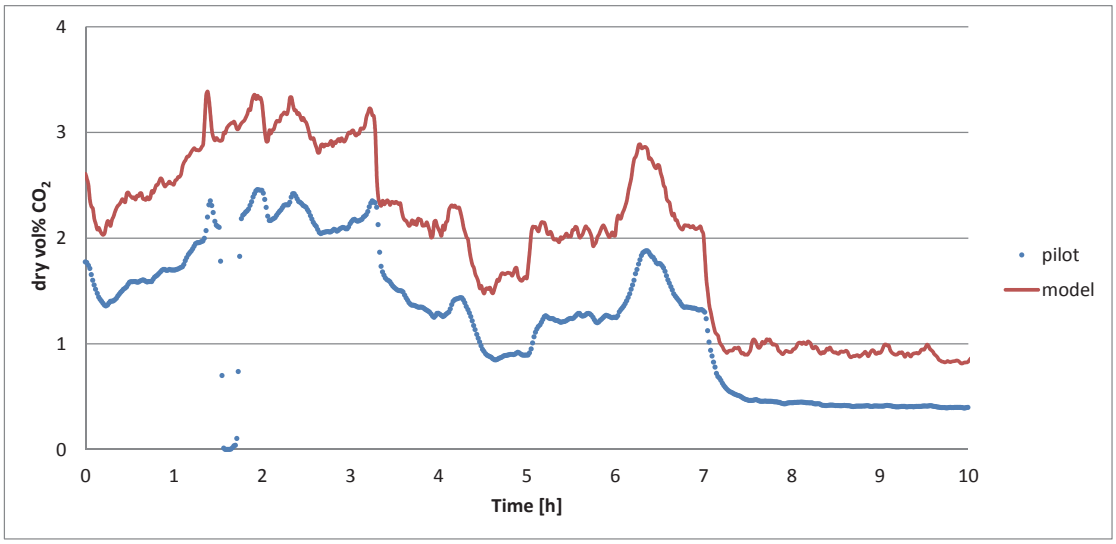

Fig. 18. Response in absorber outlet vol% CO_2.

The predicted absorber outlet CO_2 concentration is in general higher than observed in the pilot plant data but the transient behavior is represented very well. The lag that was observed for varying solvent flow rates is not detected in this case, which suggests the possible mixing effects are related to solvent flow rate variations.

The calculated CO_2 capture rate for both pilot plant and model data is presented in Figure 19.

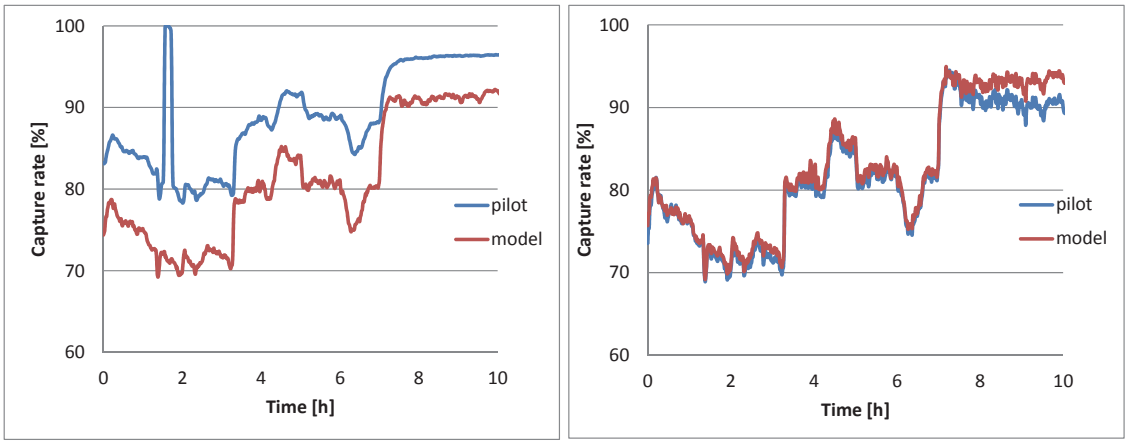

Fig. 19. (a) CO_2 capture rate based on absorber inlet and outlet data (b) CO_2 capture rate based on desorber outlet and absorber inlet data

Again the capture rate calculated based on desorber data shows a much better agreement between the model and the pilot plant. A plot of the calculated amount of CO_2 captured in the absorber compared to the amount of CO_2 released by the desorber is shown in Figure 20. Again a general trend of a higher amount of CO_2 captured in the absorber compared to what is released in the desorber is observed. The overall deviation for this period is about 7 %.

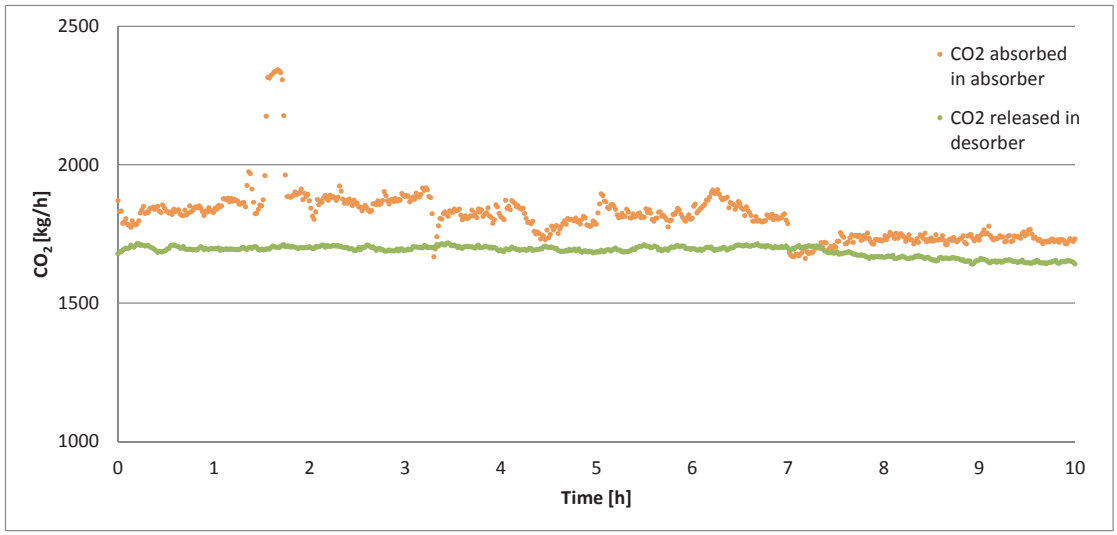

Fig. 20. Comparison of CO_2 absorbed in absorber and released in desorber

5. Discussion and conclusion

In general the model predicts a lower CO_2 capture rate compared to pilot plant results. However, the fit is better for capture rates calculated based on desorber outlet CO_2 flow than for absorber outlet CO_2 flow as seen in Figures 8, 14 and 19. The calculated amount of CO_2 captured in the absorber is in general higher than what is released from the desorber for the pilot plant data as shown in Figure 9, 15 and 20. This suggests a mass balance weakness for the pilot plant or possible measurement errors for absorber inlet or outlet gas data. One possible source of error might be the flue gas flow rate correlation (Equation 1), which does not take into account gas density variations due to fluctuations in inlet gas temperature, pressure or composition. It is therefore likely that the inlet flue gas flow rate is overpredicted by this correlation. This result in a higher predicted absorber CO_2 input to the model which causes a larger CO_2 slip through the absorber column and consequently lower CO_2 capture rate compared to the experimental results. The desorber outlet CO_2 flow rate is therefore more reliable for capture rate calculations. By performing the simulations with a more realistic flue gas flow rate, the absorber outlet CO_2 concentration would probably have been shifted downwards and a better fit between the model and pilot plant results would have been obtained in Figures 6 b), 13 b) and 18.

There is also a tendency of overprediction of rich and lean CO_2 loadings in the model. These parameters are naturally highly related and will affect each other. A possible explanation of the observed deviation might be that K-spice only allows the add-on reaction set module to be interfaced with the packing sections, and not with the drum that represents the reboiler. Thus the modelled reboiler does not include chemical equilibrium in the flash calculations and the resulting phase distribution is therefore given by the physical equilibrium only. This result in slightly higher lean loadings compared to pilot plant data, which again affects the rich loadings. It should also be noted that a 5 % error in loading analysis is probable.

One challenge for validation studies is providing a reasonable starting point for the model before a step change is simulated. K-spice does not allow actual initial state conditions (given by pilot data) to be loaded, thus the best way is to run the model until steady state and start the simulation with the calculated states at stable conditions. However, the pilot plant which in this case is attached to a real power station might not be at steady state initially due to flue gas disturbances in composition, flow rate and temperature, steam quality and flow rate disturbances or other external disturbances that are not measured. Even when the pilot plant seems to be stable it might still not be at steady state due to slow transients which takes hours to adjust. These effects are more significant for larger relative solvent hold-ups, where the overall retention time is higher. The total solvent hold-up in the Brindisi pilot plant was during this particular campaign about 61 m^3, which with a solvent flow rate of 30 m^3/h gives an overall solvent retention time of about 2 hours. CO_2 loadings and other solvent parameters will therefor adjust very slowly compared to for instance absorber outlet gas parameters such as temperature and composition, and the pilot plant might therefore not be at steady state even when parameters seems stable.

Even though an offset is observed between model and pilot plant data, especially initially as discussed above, it seems like the model is able to capture the main dynamics of the pilot plant and similar transient responses are observed. The model predicts slightly faster and more sensitive dynamics for the absorber column compared to the pilot results, which indicates a tendency of back-mixing effects in the real system that is not captured by the model.

Acknowledgements

This work has been performed within the European FP7 OCTAVIUS project (Grant Agreement n° 295645).

References

[1] Puxty G, Rowland R, Allport A, Yang Q, Brown M, Burns R, Meader M, Attalla M. Carbon Dioxide Postcombustion Capture: A Novel Screening Study of the Carbon Dioxide Absorption Performance of 76 Amines. *Envirnomnental Science & Technology* 2008;43(16):6427-6433.

[2] Kvamsdal HM, Jakobsen JP, Hoff KA. Dynamic modeling and simulation of a CO_2 absorber column for post-combustion CO_2 capture. *Chemical Engineering and Processing* 2009:48:135-144.

[3] Lawal A, Wang M, Stephenson P, Yeung H. Dynamic modelling of CO_2 absorption process for post-combustion capture in coal-fired power plants. *Fuel* 2009:88(12):2455-2462.

C.5 Paper E: Dynamic model validation of the post-combustion CO_2 absorption process

International Journal of Greenhouse Gas Control 41 (2015) 127–141

Contents lists available at ScienceDirect

International Journal of Greenhouse Gas Control

journal homepage: www.elsevier.com/locate/ijggc

Dynamic model validation of the post-combustion CO_2 absorption process

Nina Enaasen Flø [a,*], Hanna Knuutila [a], Hanne Marie Kvamsdal [b], Magne Hillestad [a]

[a] Department of Chemical Engineering, NTNU, Sem Sælandsvei 4, N-7491 Trondheim, Norway
[b] Department of CO_2 Capture Process Technology, SINTEF Materials and Chemistry, Post Office Box 4760, Sluppen, N-7465 Trondheim, Norway

ARTICLE INFO

Article history:
Received 13 January 2015
Received in revised form 7 May 2015
Accepted 1 July 2015

Keywords:
Post combustion CO_2 capture
Chemical absorption
MEA
Dynamic modelling
Pilot plant
Dynamic validation

ABSTRACT

A general dynamic process model of the post-combustion carbon dioxide (CO_2) absorption process based on aqueous monoethanolamine (MEA) is developed and implemented in MATLAB. The overall process model contains several unit models developed from first principle conservation laws for mass and energy, each representing individual process equipment. An equation based numerical integration method is used to solve the overall equation system simultaneously in MATLAB. Pilot plant data from specifically designed dynamic experiments with 30 wt% MEA is collected from a pilot plant at NTNU and SINTEF laboratories. This includes steady state data for eight different conditions along with six dynamic data sets with relevant step changes in lean solvent flow rate and reboiler duty. The pilot plant data show a very good steady state mass balance which indicates that the generated data sets are reliable. Two of the dynamic data sets are used for model validation and the results shows adequate agreement between model and pilot plant data. An average of 0.3% and −2.8% deviation in absorbed CO_2 is seen for the two simulated cases compared to pilot plant results and it is concluded that the model is able to capture the main dynamics of the experiments. The main cause of deviation is believed to concern uncertainties in mass transfer and effective mass transfer area correlations.

© 2015 Elsevier Ltd. All rights reserved.

1. Introduction

Anthropogenic carbon emissions are altering the natural carbon cycle and have in fact been recognized as a major contributing factor to global warming and climate change. Carbon capture and sequestration (CCS) is considered a key solution to mitigate global climate change with the increasing demand for energy world wide (Metz et al., 2005). Post-combustion CO_2 absorption using aqueous amine solutions has received particular attention among CO_2 capture technologies and is presented as a viable option for reducing carbon emissions from fossil fuel fired power plants. Chemical absorption of CO_2 has been thoroughly studied both experimentally and theoretically and it is in fact considered the most mature technology for carbon capture from power stations (Puxty et al., 2009).

Several research groups have developed models of the CO_2 absorption process in order to study process performance and limitations in an easy, efficient and relatively inexpensive way. Even though the main focus has been on steady state modeling, it has been recognized that stationary models provide limited knowledge on the complex coupling between the absorption process and power stations (Kvamsdal et al., 2009). Increasing requirement of flexible power generation make dynamic analysis a necessity in order to predict the transient effect of conditions that are superimposed on the CO_2 absorption process. It has been concluded that dynamic simulators are required in order to fully understand the transient behavior of the capture process, identify possible process bottlenecks and observe the effect of interactions between integrated parts of the process (Lawal et al., 2009). A dynamic process model can also be used to develop and configure basic control structures (Panahi and Skogestad, 2011; Karimi et al., 2012; Nittaya et al., 2014) and study process controllability (Lawal et al., 2010, 2012; Panahi and Skogestad, 2012; Lin et al., 2012; Nittaya et al., 2014). It can even be used as a tool in optimal operation using nonlinear model predictive control (NMPC) (Panahi and Skogestad, 2012; Åkesson et al., 2012; Sahraei and Ricardez-Sandoval, 2014).

Some dynamic process models of CO_2 absorption in aqueous amine solutions have been developed recently. Bui et al. (2014) gives an overview of recent contributions to dynamic modeling, model validations and relevant process simulation studies reported in the literature. Several authors have performed validation of their

* Corresponding author.
E-mail addresses: enaasen@ntnu.no (N. Enaasen Flø), hanna.knuutila@ntnu.no (H. Knuutila), hanne.kvamsdal@sintef.no (H.M. Kvamsdal), magne.hillestad@ntnu.no (M. Hillestad).

http://dx.doi.org/10.1016/j.ijggc.2015.07.003
1750-5836/© 2015 Elsevier Ltd. All rights reserved.

a	specific area ($m^2\ m^{-3}$)
C	molar concentration ($kmol\ m^{-3}$)
C	constant
C_f	valve constant ($kmol\ s^{-1}\ kPa^{-3/2}$)
C_p	specific heat capacity ($kJ\ kmol^{-1} K^{-1}$)
C_q	valve constant ($kW\ ^\circ C^{-1}$)
d	diameter (m)
D	mass diffusion coefficient ($m^2\ s^{-1}$)
e	error
E	enhancement factor (–)
F	molar flow ($kmol\ s^{-1}$)
g	gravitational acceleration ($m\ s^{-2}$)
H	molar enthalpy ($kJ\ kmol^{-1}$)
He	Henry's law constant ($m^3\ kPa\ kmol^{-1}$)
h	heat transfer coefficient ($W\ m^{-2}\ K$)
k	film mass transfer coefficient ($m\ s^{-1}$)
k_{rx}	reaction rate coefficient ($m^3\ kmol^{-1}\ s$)
K_p	proportional gain (–)
K_{tot}	overall mass transfer coefficient ($kmol\ m^{-2}\ kPa^{-1}\ s^{-1}$)
n	molar hold-up (kmol)
nc	number of components
$N^{g\rightarrow l}$	interface molar flux ($kmol\ m^{-2}\ s^{-1}$)
P	pressure (kPa)
PV	process value
q	heat flux ($W\ m^{-2}$)
Q	heat (kW)
R	universal gas consonant ($kJ\ m^{-2}\ kPa^{-1}\ s^{-1}$)
SP	set-point
t	time (s)
T	temperature (K)
T_i	integral gain (s)
u	superficial velocity ($m\ s^{-1}$)
$u(t)$	controller output
x	liquid mole fraction (–)
y	gas mole fraction (–)
z	axial coordinate (m)

Greek symbols

α	CO_2 loading (mol CO_2/ mol MEA)
ΔH^{rx}	heat of reaction ($kJ\ kmol^{-1}$)
ΔH^{vap}	heat of vaporization ($kJ\ kmol^{-1}$)
ε	void fraction or hold-up ($m^3\ m^{-3}$)
Φ	material flux ($kmol\ m^{-2}\ s^{-1}$)
η	dynamic viscosity (pa s)
ρ	density ($kg\ m^{-3}$)
ν	kinematic viscosity ($m^2\ s^{-1}$)
σ	surface tension ($kg\ s^{-2}$)

Subscripts

abs	absorber
bt	buffer tank
c	cold side
cond	condenser
cool	lean cooler
des	desorber
fl	flooding point
g	gas
h	hot side
hx	cross heat exchanger
i	component i
in	inlet
l	liquid
out	outlet
ph	interface
reb	reboiler
s	loading point
tot	total
g/l	gas–liquid interface

Superscripts

eq*	equilibrium
$g\rightarrow l$	gas to liquid
*	free

dynamic models using steady state pilot plant data or comparisons to steady state simulation results (Kvamsdal et al., 2009; Lawal et al., 2010; Harun et al., 2011; Gáspár and Cormos, 2011; Jayarathnaa et al., 2011). It is however emphasized that applicable dynamic pilot plant data are needed in order to validate the model's behavior during transient conditions. Lack of appropriate data for model validation has, however, remained problematic (Bui et al., 2014).

Biliyok et al. (2012) conducted a dynamic validation of their process model based on logged data from a campaign in the Separation Research Program (SRP) pilot plant at the University of Texas at Austin (Biliyok et al., 2012; Lawal et al., 2012). However, specific dynamic step tests were not performed during the campaign where the data were collected, and it is therefore not certain that the collected data reflect all important dynamics. Enaasen et al. (2014) validated a process model in K-spice general simulation tool using pilot plant data generated in a dynamic campaign in the Brindisi pilot plant in Italy. It was concluded that appropriate dynamic pilot plant data from specifically designed dynamic experiments is an important necessity in order to ensure that the model will predict dynamic responses adequately.

The paper by Bui et al. (2014) presented pilot plant data from a dynamic campaign in the CSIRO PCC pilot plant using MEA as solvent. Absorber and desorber column temperature profiles during step changes in flue gas and solvent flow rate were presented. Further, the use of density meters to correlate CO_2 loading was also evaluated, and the authors reported a strong potential for instantaneous monitoring of solvent CO_2 loading.

A CO_2 absorber model, developed by Kvamsdal et al. (2009), was validated against a dynamic data-set with 30 wt% MEA from a campaign carried out in the Validation Of Carbon Capture (VOCC) pilot plant at NTNU and SINTEF laboratories (Kvamsdal et al., 2011). The absorber model of Kvamsdal et al. (2009) is the basis for an improved general column model used to represent both absorber and stripper columns in the present work. Other major process units such as reboiler, condenser, cross heat exchanger, buffer tank and absorber sump is included to complete the capture plant process model. Furthermore, a dynamic test campaign has been conducted in a pilot plant at NTNU and SINTEF to generate dynamic data which are used for model validation. The pilot plant results and validation are presented in the present paper.

2. The Gløshaugen pilot plant

The experimental part of this work was carried out in the Gløshaugen (NTNU/SINTEF) pilot plant. A flow sheet of the pilot plant is presented in Fig. 1. A detail description of the pilot is given in Pinto et al. (2014) and only a short overview is given here.

The absorber is a 150 mm diameter column, while the desorber is 100 mm in diameter. Both columns contain Sulzer BX structured

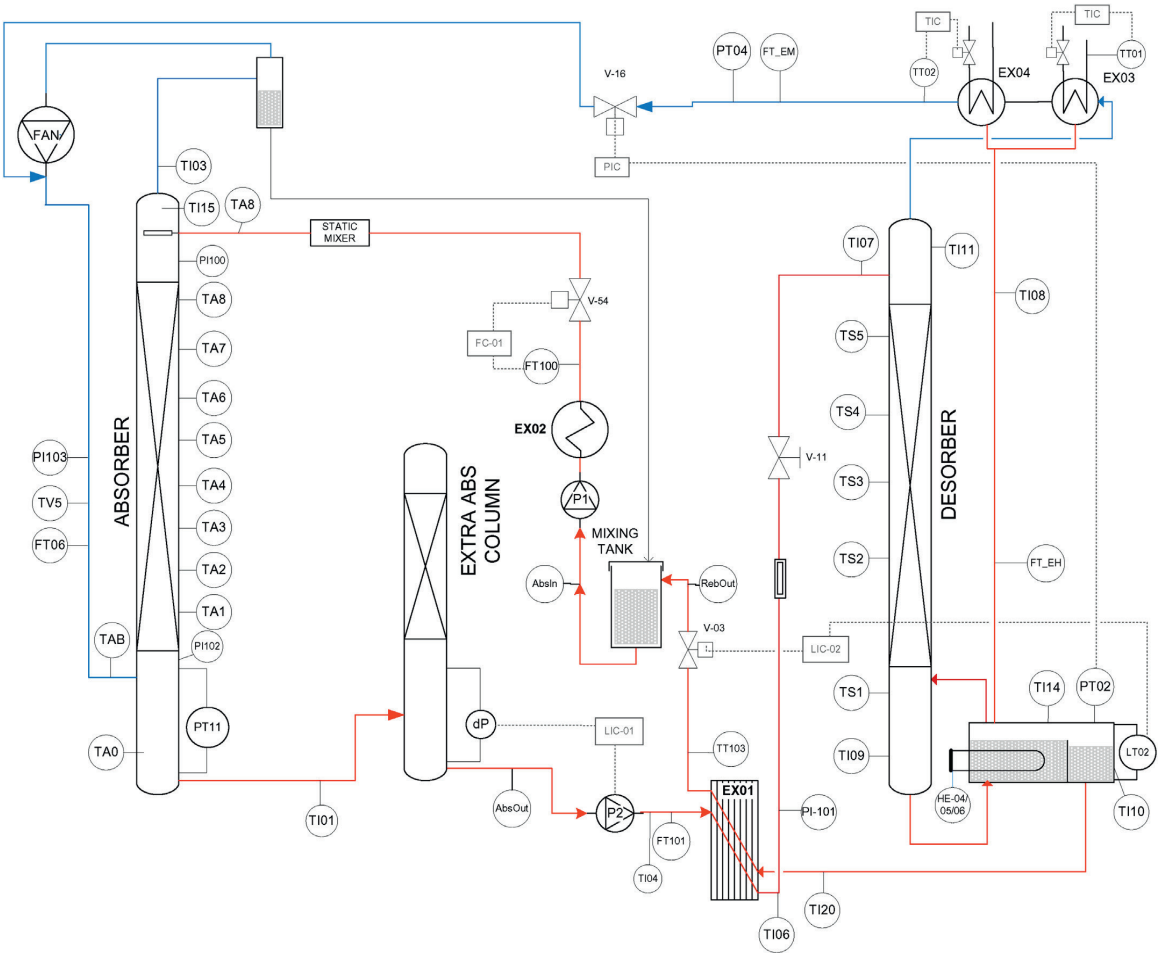

Fig. 1. A schematic overview of the Gløshaugen pilot plant.

packing, 4.23 m and 3.57 m for absorber and desorber, respectively. In the pilot plant, the solvent enters the top of the absorption column, trickles downwards and meets the gas containing CO_2 flowing counter-currently. From the bottom of the absorber the rich solvent is pumped to the stripper column via the cross heat exchanger EX01. The solvent flows from top to bottom in the stripper column and meets the upcoming vapor from an electrically heated reboiler. This vapor contains the energy required to regenerate the solvent and release CO_2. The regenerated amine solution from the reboiler outlet flows through the cross heat exchanger EX01, into a mixing tank and through the lean cooler EX02 that controls the solvent temperature, before it enters the top of the absorber. As seen from Fig. 1, the complete plant was operated as a closed system, thus all stripped CO_2 was transferred back to the gas prior to entering the absorber. The extra column shown in Fig. 1 was not in operation. However the rich solvent passed through the extra column sump where the liquid level was controlled by the rich solvent pump P2.

Typical solvent hold-ups and residence times with a solvent flow rate of 2.5–4.5 L/min are given in Table 1.

Table 1
Solvent hold-ups and residence times in the Gløshaugen pilot plant.

	Solvent hold-up [L]	Residence time [min]
Absorber packing	7	1.6–2.8
Absorber sump and extra column	20	4.4–8
Desorber packing	3	0.7–1.2
Desorber sump and reboiler	65	14.4–26
Buffer tank	25	5.6–10
Heat exchanger and piping	40	8.9–16
Total	160	35.6–64

3. Model description

A complete dynamic process model of the conventional amine based CO_2 capture process is developed and implemented in MATLAB. The process model consists of various process unit models which are developed from the first principle balance equations for mass and energy each representing individual process equipment. A dynamic model of the NTNU/SINTEF pilot plant is developed based on these process unit models as illustrated in Fig. 2.

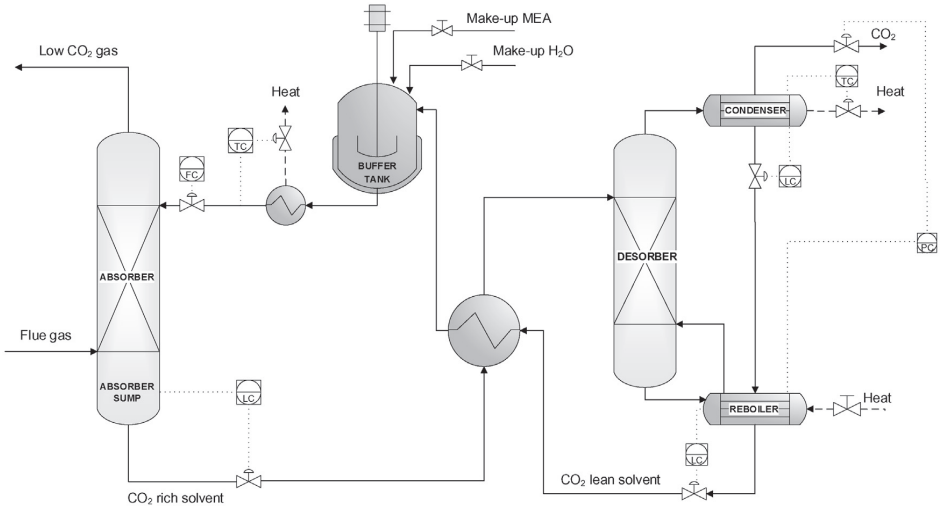

Fig. 2. A flowsheet of the conventional amine-based CO_2 absorption process model.

The overall process model can be summarized as follows:

- General column model: absorber and stripper columns.
- Flash tank model: reboiler and condenser.
- Continuous stirred-tank model: absorber sump and buffer tank.
- Heat exchanger model: cross heat exchanger and lean cooler.

The desorber sump is lumped into the reboiler and modeled as a single flash tank. The pilot plant extra column is lumped into the absorber sump and simulated as one single stirred-tank. Solvent piping is lumped with the cross heat exchanger.

3.1. The general column model

A general dynamic column model is used for simulation of both absorber and stripper columns. This is a distributed parameter model and the relevant model equations and dependent variables are listed in Table 2.

The following assumptions applies to the model:

- 2 phase counter-current flow
- 1 dimensional plug flow regime for both phases (back mixing is disregarded)
- radial gradients in temperature and concentration are neglected
- ideal gas phase (due to low pressure)
- linear pressure drop with fixed outlet pressure
- instantaneous momentum balance $\left(\frac{\partial P}{\partial t} = 0\right)$
- mass and heat transfer are described by the two-film theory
- no accumulation in gas and liquid films
- equilibrium occurs at the interphase
- chemical reactions are restricted to the liquid-film only
- liquid film CO_2 reactions are accounted for by an enhancement factor in the overall CO_2 mass transfer coefficient
- interphase fluxes of CO_2, H_2O and MEA are allowed in both directions

3.1.1. Interphase heat and mass transfer

A rate-based (non-equilibrium) approach is applied to model mass and heat transfer between gas and liquid phases. The molar component fluxes are given by Eq. (7) and heat flux is given by Eq. (8).

$$N_i^{g\to l} = K_{tot,i}\left(P_i - P_i^{eq*}\right) \tag{7}$$

$$q^{g\to l} = h_{g/l}\left(T_g - T_l\right) \tag{8}$$

$K_{tot,i}$ is the overall mass transfer coefficient, P_i is the partial pressure and P_i^{eq*} is the equilibrium pressure of component i, respectively. $h_{g/l}$ is the interface heat transfer coefficient, while T_g and T_l are temperatures in gas and liquid phases, respectively. It is assumed that the resistance to mass transfer of H_2O and MEA in the liquid film is negligible so that the overall mass transfer coefficient of H_2O and MEA is given by Eq. (9).

$$K_{tot,i} = \frac{k_{g,i}}{RT_g} \tag{9}$$

The overall mass transfer coefficient of CO_2 is enhanced by chemical reactions between CO_2 and the solvent component MEA. This is accounted for by an enhancement factor in the overall mass transfer coefficient as described by Eq. (10).

$$K_{tot,CO_2} = \frac{1}{\frac{RT_g}{k_{g,CO_2}} + \frac{He_{CO_2}}{k_{l,CO_2}E_{CO_2}}} \tag{10}$$

$k_{g,i}$ and $k_{l,i}$ are gas and liquid film mass transfer coefficients, respectively, which are calculated based on correlations by Billet and Schultes (1999) given in Eqs. (11) and (12).

$$k_{g,CO_2}\cdot a_{ph} = C_g\frac{1}{(\varepsilon-\varepsilon_l)^{1/2}}\frac{a^{3/2}}{d_h^{1/2}}D_{g,i}\left(\frac{u_g}{a\nu_g}\right)^{3/4}\left(\frac{\nu_g}{D_{g,i}}\right)^{1/3}\left(\frac{a_{ph}}{a}\right) \tag{11}$$

$$k_{l,CO_2}\cdot a_{ph} = C_l 12^{1/6}\left(\frac{u_l}{\varepsilon_l}\right)^{1/2}\left(\frac{D_{l,i}}{d_h}\right)^{1/2} a\left(\frac{a_{ph}}{a}\right) \tag{12}$$

He_{CO_2} in Eq. (10) is the Henry's law constant for CO_2 and E_{CO_2} is the enhancement factor representing increased flux due to reactions

Table 2
Unit model equation for the general column

Gas phase equations		
Total material balance	$0 = -\frac{\partial \Phi_g}{\partial z} + \varepsilon_g \frac{C_{g,tot}}{T_g}\frac{\partial T_g}{\partial t} - a_{ph}\sum_{k=1}^{nc} N_k^{g\to l}$	(1)
Component material balance	$\varepsilon_g C_{g,tot}\frac{\partial y_i}{\partial t} = -\Phi_g \frac{\partial y_i}{\partial z} + y_i a_{ph}\sum_{k=1}^{nc} N_k^{g\to l} - a_{ph} N_i^{g\to l}$	(2)
Energy balance	$\varepsilon_g C_{g,tot} C_{p,g}\frac{\partial T_g}{\partial t} = -\Phi_g C_{p,g}\frac{\partial T_g}{\partial z} + a_{ph} h_{g/l}(T_l - T_g)$	(3)
Dependent variables	Φ_g, y_i, T_g	
Liquid phase equations		
Total material balance	$0 = \frac{\partial \Phi_l}{\partial z} + a_{ph}\sum_{k=1}^{nc} N_k^{g\to l}$	(4)
Component material balance	$\varepsilon_l C_{l,tot}\frac{\partial x_i}{\partial t} = \Phi_l \frac{\partial x_i}{\partial z} - x_i a_{ph}\sum_{k=1}^{nc} N_k^{g\to l} + a_{ph} N_i^{g\to l}$	(5)
Energy balance	$\varepsilon_l C_{l,tot} C_{p,l}\frac{\partial T_l}{\partial t} = \Phi_l C_{p,l}\frac{\partial T_l}{\partial z} - a_{ph} h_{g/l}(T_l - T_g) - \frac{4h_{out}}{d}(T_l - T_{out}) + a_{ph}\Delta H_{H_2O}^{vap} N_{H_2O}^{g\to l} + a_{ph}\Delta H_{CO_2}^{rx} N_{CO_2}^{g\to l}$	(6)
Dependent variables	Φ_l, x_i, T_l	

taking place in the liquid phase. The enhancement factor is given by:

$$E_{CO_2} = \frac{\sqrt{k_{rx,CO_2} C_{l,MEA}^{*} D_{l,CO_2}}}{k_{l,CO_2}} \tag{13}$$

where k_{rx,CO_2} is the reaction rate coefficient for reaction between CO_2 and MEA, $C_{l,MEA}^{*}$ is the liquid concentration of free MEA in the solution and D_{l,CO_2} is the diffusivity of CO_2 in aqueous MEA.

3.1.2. Hydrodynamics

Calculation of effective interface area (a_{ph}) and liquid hold-up (ε_l) are calculated from correlations given by Billet and Schultes (1999) which for conditions at and below the loading point are given in Eqs. (14) and (15).

$$\frac{a_{ph}}{a} = 1.5(a d_h)^{-0.5}\left(\frac{u_l d_h}{\nu_l}\right)^{-0.2}\left(\frac{u_l^2 \rho_l d_h}{\sigma_l}\right)^{0.75}\left(\frac{u_l^2}{g d_h}\right)^{-0.45} \tag{14}$$

$$\varepsilon_l = \left(12\frac{1}{g}\frac{\eta_l}{\rho_l}u_l a^2\right)^{1/3} \tag{15}$$

For conditions above the loading point (s), increased shear stress will dam up the falling film causing increased solvent hold-up and effective interface area. In this case, the relations given in Eqs. (16) and (17) is used where $a_{ph,s}$ is given by Eq. (14), $\varepsilon_{l,s}$ is given by Eq. (15) and $a_{ph,fl}$, $\varepsilon_{l,fl}$ and $u_{g,fl}$ given by Billet and Schultes (1999).

$$\frac{a_{ph}}{a} = \frac{a_{ph,s}}{a} + \left(\frac{a_{ph,fl}}{a} - \frac{a_{ph,s}}{a}\right)\left(\frac{u_g}{u_{g,fl}}\right)^{13} \tag{16}$$

$$\varepsilon_l = \varepsilon_{l,s} + \left(\varepsilon_{l,fl} - \varepsilon_{l,s}\right)\frac{u_g}{u_{g,fl}} \tag{17}$$

3.2. The flash tank model

A general dynamic two-phase flash tank model is developed and used for simulation of the stripper reboiler and condenser. The flash tank model is developed from the first principle conservation laws for mass and energy and the model equations and dependent variables are given in Table 3. The dynamic flash tank model is based on the following assumptions:

- 2 phases are considered
- both phases are perfectly mixed
- ideal gas phase (due to low pressure)
- vapor–liquid equilibrium
- PI level controller
- PI temperature and pressure controller is included for the condenser

3.3. The continuous stirred-tank model

A general dynamic continuous stirred-tank model is used for simulation of the absorber sump and buffer-tank. The model equations and dependent variables are listed in Table 4. The following assumptions applies:

- only liquid phase is considered and any vaporization is disregarded
- perfectly mixed liquid phase
- no reaction occurs in the tank
- PI level controller

3.4. The heat exchanger model

The cross heat exchanger and lean cooler are represented by a general dynamic counter-current heat exchanger model. The model is a distributed parameter model and the equation set and dependent variables listed in Table 5 are based on the following assumptions:

- only liquid phase is considered and any vaporization is disregarded (no flashing)
- 1 dimensional plug flow regime for both sides
- no reaction occurs

3.5. PI controllers

Continuous PI-controllers are implemented as part of the equation set for the flash tank and the continuous stirred-tank models. The general gas and liquid flow equation is given by:

$$F = C_f u(t)\sqrt{\Delta P} \tag{30}$$

Table 3
Unit model equation for the flash tank.

Gas phase equations		
Component material balance	$\frac{\partial n_{g,i}}{\partial t} = F_{g,in}y_{i,in} - F_g y_i - a_{g/l}N_i^{g\to l}$	(18)
Energy balance	$n_{g,tot}C_{p,g}\frac{\partial T_g}{\partial t} = F_{g,in}H_{g,in} - F_g H_g - C_{p,g}T_g\frac{\partial n_{g,tot}}{\partial t} + a_{g/l}h_{g/l}(T_l - T_g)$	(19)
Dependent variables	$n_{g,i}$, T_g	
Liquid phase equations		
Component material balance	$\frac{\partial n_{l,i}}{\partial t} = F_{l,in}x_{i,in} - F_l x_i + a_{g/l}N_i^{g\to l}$	(20)
Energy balance	$n_{l,tot}C_{p,l}\frac{\partial T_l}{\partial t} = F_{l,in}H_{l,in} - F_l H_l - C_{p,l}T_l\frac{\partial n_{l,tot}}{\partial t} - a_{g/l}h_{g/l}(T_l - T_g) - a_{out}h_{out}(T_l - T_{out}) + a_{g/l}\Delta H^{vap}_{H_2O}N^{g\to l}_{H_2O} + a_{g/l}\Delta H^{rx}_{CO_2}N^{g\to l}_{CO_2}$	(21)
Dependent variables	$n_{l,i}$, T_l	

Table 4
Unit model equation for the continuous stirred-tank.

Continuous stirred-tank model equations		
Component material balance	$\frac{\partial n_i^l}{\partial t} = F_{in}^l x_{i,in} - F^l x_i$	(22)
Energy balance	$n_{tot}^l C_p^l \frac{\partial T^l}{\partial t} = F_{in}^l H_{in}^l - F^l H^l - H^l\frac{\partial n_{tot}^l}{\partial t} - a^{out}h^{out}(T^l - T^{out})$	(23)
Dependent variables	n_i^l, T	

Table 5
Unit model equations for the heat exchanger.

	Hot side model equations		Cold side model equations	
Total material balance	$0 = -\frac{\partial \Phi_l^h}{\partial z}$	(24)	$0 = \frac{\partial \Phi_l^c}{\partial z}$	(25)
Component material balance	$C_{l,tot}^h\frac{\partial x_i^h}{\partial t} = -\Phi_l^h\frac{\partial x_i^h}{\partial z}$	(26)	$C_{l,tot}^c\frac{\partial x_i^c}{\partial t} = \Phi_l^c\frac{\partial x_i^c}{\partial z}$	(27)
Energy balance	$C_{l,tot}^h C_{p,l}^h\frac{\partial T_l^h}{\partial t} = -\Phi_l^h C_{p,l}^h\frac{\partial T_l^h}{\partial z} - ah(T_l^h - T_l^c)$	(28)	$C_{l,tot}^c C_{p,l}^c\frac{\partial T_l^c}{\partial t} = \Phi_l^c C_{p,l}^c\frac{\partial T_l^c}{\partial z} + ah(T_l^h - T_l^c)$	(29)
Dependent variables	Φ_l^h, x_l^h, T_l^h		Φ_l^c, x_l^c, T_l^c	

where C_f is a valve constant, $u(t)$ is the controller output (in this case valve position) and ΔP is the pressure difference over the valve.

For temperature control, the following equation is applied:

$$Q = C_q u(t) \tag{31}$$

The controller output, $u(t)$, is for PI-controllers given by:

$$u(t) = K_p\left(e(t) + \frac{1}{T_i}\int_0^t e(\tau)d\tau\right) \tag{32}$$

where K_p is the proportional gain, T_i is the integral gain and e is the difference between the process value (PV) and the set point (SP) given by:

$$e = SP - PV \tag{33}$$

The control parameters implemented in the model is taken from the pilot plant. The parameter values are listed in Table 6.

Table 6
Control parameters.

	K_p	T_i [s]
Absorber sump level	−1	25
Reboiler level	−1	4
Reboiler pressure	−3	5
Condenser temperature	−0.4	10
Condenser level[a]	−1	4
Lean solvent temperature	−1	10

[a] Condenser level controller parameters is set equal to reboiler level controller parameters.

3.6. Physical and thermodynamic properties

Table 7 gives an overview of the literature references for some physical properties used in the model.

3.7. Numerical solution

The general column and the heat exchanger models are distributed and require discretization with regard to the axial direction. As the model formulations constitute two point boundary value problems, orthogonal collocation is applied as a suitable method for discretization. The discretized PDEs become a system of ordinary differential and algebraic equations (DAE), with time as the independent variable. All state variables are normalized to improve numerical robustness.

The entire set of model equations is integrated simultaneously by the same integration algorithm (equation based numerical

Table 7
Physical and thermodynamic properties.

Property	Symbol	Reference
Liquid density	ρ_l	Cheng and Meisen (1996)
Mass diffusion coefficient of CO_2 in aqueous MEA solution	D_{l,CO_2}	Luo et al. (2015)
Mass diffusion coefficient of CO_2 in gas phase	D_{g,CO_2}	Reid et al. (1996)
Heat of reaction of CO_2	$\Delta H^{rx}_{CO_2}$	Kim (2009)
Vapor pressure of CO_2	P_{CO_2}	Brúder et al. (2010)
Equilibrium pressure of H_2O	$P^{eq*}_{H_2O}$	Xu (2011)
Equilibrium pressure of MEA	P^{eq*}_{MEA}	Xu (2011)

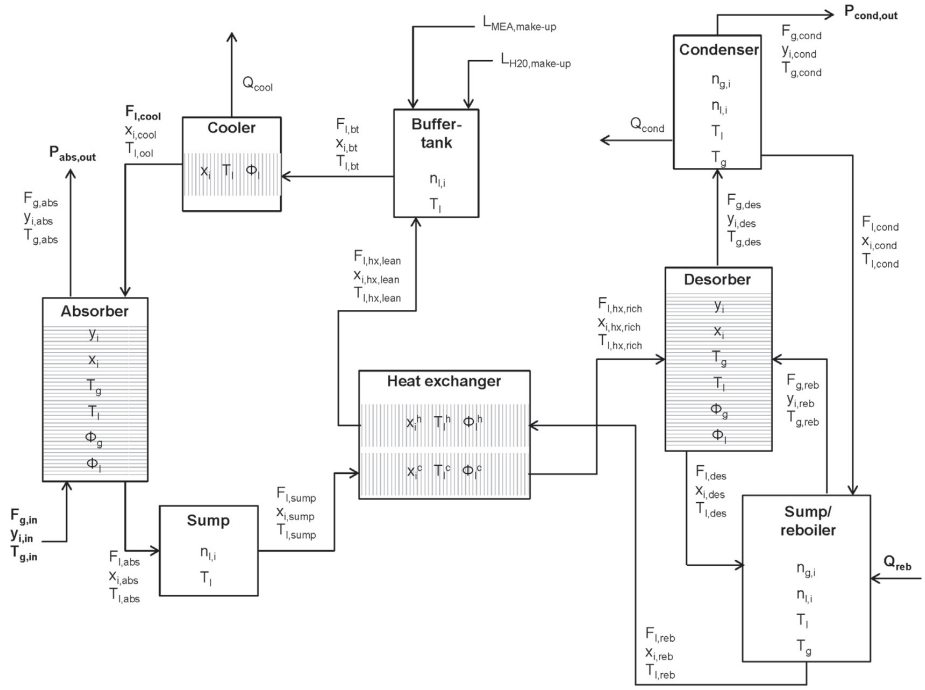

Fig. 3. A schematic overview of the dynamic model including unit connections. Distributed unit models and perfectly mixed models are indicated with shaded and white boxes, respectively. Bold letters indicate system boundary.

solution method); ode15s in MATLAB is used for this purpose. This method provides an easy way to define connections between units, and no iteration is needed on tear streams since all equations are solved simultaneously for each time step. However, providing a realistic set of initial conditions becomes very important in order to obtain convergence. Steady state initial conditions are therefore simulated based on steady state input data and used to initialize the model prior to dynamic simulations. Routines that provide information between connecting units (unit boundary conditions) are also developed. A lay-out of the overall equation system is illustrated in Fig. 3. Shaded units indicate distributed parameter models, while the white boxes represent mixing models. Unit state variables and boundary conditions (connection between units) are also listed in Fig. 3. Bold letters indicate system boundary conditions which are treated as input to the overall process model. These are:

- Absorber gas flow rate ($F_{g,in}$), composition ($y_{i,in}$) and temperature ($T_{g,in}$)
- Absorber outlet pressure ($P_{abs,out}$)
- Condenser outlet pressure ($P_{cond,out}$)
- Lean solvent flow rate into absorber column ($F_{l,cool}$)
- Reboiler duty (Q_{reb})

The special pilot plant configuration with recirculation of CO_2 gas is therefore not included as part of the model.

3.8. Model validation

A piecewise steady state verification using all eight cases was first performed to determine certain correlation parameters and process unit heat loss. The absorber and absorber sump section was validated using measured inlet gas and lean solvent conditions as model input, comparing responses in absorption rate, rich loading and absorber temperature profile. The heat loss coefficient was determined and the wetting factor defined by Eq. (14) that determines the effective interface area (a_{ph}) was corrected by a factor of 2.25 to meet the desired CO_2 absorption. The regeneration section (desorber, reboiler and condenser) was validated using rich solvent conditions and reboiler duty and pressure as model input, comparing responses in desorption rate, lean loading and desorber temperature profile. The heat loss coefficient was determined and the effective interface area (a_{ph}) was corrected by a factor of 0.5. The cross heat exchanger was validated using lean and rich solvent conditions as model input to determine the heat-exchanger heat transfer coefficient that gives the desired output temperatures. The three separate sections were afterward connected and combined to one complete process model with system boundary conditions as listed above as model inputs. The steady state deviation of absorbed CO_2 was within ±8% for all cases. The steady state verified process model was afterward used for dynamic simulations and the results were compared to pilot plant responses for verification.

4. Experimental description

All dynamic tests were carried out from a steady state starting point. Three liquid samples were withdrawn from chosen locations shown in Fig. 1 before any step change was performed. These liquid samples were lean solvent in to the absorber (*AbsIn*), rich solvent out of the absorber (*AbsOut*) and lean solvent out of the reboiler (*RebOut*). The lean solvent samples should be equal because the pilot is a closed system and sampling was done at steady state. The liquid samples were analyzed for CO_2 content of the liquid and for amine concentration.

After steady state sampling, a step change was performed and solvent samples of the rich solvent out of the absorber (*AbsOut*) and lean solvent from reboiler outlet (*RebOut*) were withdrawn every 15 min during the first hour. Additionally, samples of the lean solvent in to the absorber (*AbsIn*) were withdrawn after 30, 45 and 60 min. After 60 min the pilot plant started to approach steady state condition and only slow changes in the density and temperatures were observed. The manual solvent sampling was therefore stopped. Flow rates, temperatures, pressures, gas compositions and liquid density of the rich and lean solvent were logged every minute throughout the experiments and was continued even though liquid sampling was stopped. Based on previous experience, the pilot plant was operated without any further external impact for at least 6 h after every dynamic step change to ensure a steady state starting point for the next dynamic experiment (Pinto et al., 2014). The logged measurements were also checked prior to each experiment to ensure stable values.

The online density measurements of lean and rich solvent were used to correlate CO_2 loadings according to Eq. (34).

$$\rho = \left(1 + 222.25267\frac{\alpha}{T} + \frac{2.49573 \cdot 10^5}{T^2}\right) \times \exp\left(-\frac{394.9888}{T} + 0.04254\sqrt{\frac{\alpha}{T}}\right) \quad (34)$$

A two-channel CO_2 analyzer (Rosemount Binos 100) connected to the absorber inlet and outlet measured the CO_2 content in gas phase on a dry basis. The CO_2 analyzers were calibrated once a day using gas mixtures produced from calibrated mass flow controllers (Bronkhorst Hi-Tec) for CO_2 and N_2. At least 4–5 different concentrations were used covering the whole range of relevance. The lean solvent into the absorber was controlled at a temperature of 40 °C and the reboiler was operated at a pressure in the range of 170–190 kPa.

Step changes in reboiler duty and solvent flow rate were made according to the experimental overview presented in Table 8. The goal was to obtain data for a wide range of operating conditions which is important in order to validate the model for different conditions and step changes. Steady state data for all eight cases are available in Appendix A, and the total dynamic data sets for case 1, 2, 3, 5, 6 and 7 are available on request.

5. Results

5.1. Mass balance and comparison with previous data for reboiler duty under steady state operation

As mentioned earlier, the pilot plant was operated at steady state conditions prior to each dynamic experiment. The steady state data was used to check the reliability of the pilot plant data. During the campaign two different methods for calculating the absorbed CO_2 was utilized:

1 Based on the inlet and outlet gas phase CO_2 concentrations measured with the IR-analyzers and the gas flow measurement located prior the gas inlet of the absorber:

$$N^{g}_{CO_2,abs} = F_{g,abs,in}y_{CO_2,abs,in} - F_{g,abs,out}y_{CO_2,abs,out} \quad (35)$$

where $F_{g,abs,out}$ is estimated based on the calculated inert gas flow through the column.

2 Based on the liquid flow rate and analysis of liquid samples in and out from the absorber:

$$N^{l}_{CO_2,abs} = F_{l,abs,out}C_{CO_2,rich} - F_{l,abs,in}C_{CO_2,lean} \quad (36)$$

Table 8
Experimental overview.

Case	Gas flow rate	Solvent flow rate	Reboiler duty	Absorber inlet CO_2	CO_2 loading [molCO_2/mol MEA]		Steady state mass balance	Step change
					Lean	Rich	$\frac{N^{g}_{CO_2,abs} - N^{l}_{CO_2,abs}}{avg(N^{g}_{CO_2,abs}, N^{l}_{CO_2,abs})}$ [%]	
	[Nm^3h^{-1}]	[kg/h]	[kW]	[dry vol%]				
1	78.6	166.9	6.8	3.5	0.30	0.42	1.34	Reboiler duty +17%
2	75.8	172.3	9.2	6.8	0.26	0.45	3.41	Solvent flow rate +22%
3	112.2	152.1	10.0	3.0	0.22	0.49	0.69	Reboiler duty −30%
5	109.1	240.9	10.4	3.9	0.27	0.41	2.95	Solvent flow rate −24%
6	107.6	178.7	6.1	5.4	0.34	0.49	0.63	Reboiler duty +33%
7	107.4	238.8	8.3	4.6	0.31	0.44	1.58	Solvent flow rate −18%

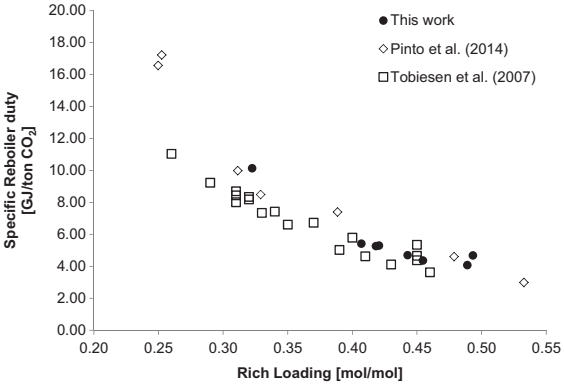

Fig. 4. Specific reboiler duty as a function of rich loading.

The average deviation between these two methods, shown in Table 8, was 1.76% with maximum deviation of 3.41%. The small deviations indicate that the logged data are reliable, that the pilot plant had no leakages and that steady state conditions were attained in the start of each experiment.

Two other campaigns with 30 wt% MEA have been performed over the years in the same pilot plant. Fig. 4 shows a comparison of the specific reboiler duty as a function of rich loading in all the three campaigns when the pilot is operated at steady state.

The specific reboiler duty (GJ/ton CO_2) is calculated by:

$$SRD = \frac{Q_{reb}}{(F_{l,abs,in}C_{CO_2,rich} - F_{l,abs,out}C_{CO_2,lean})M_{CO_2}} \quad (37)$$

where Q_{reb} is the reboiler duty (kW), $F_{l,abs,in}$ and $F_{l,abs,out}$ are the solvent flow rates in and out from the absorber, respectively (kg s^{-1}) and $C_{CO_2,rich}$ and $C_{CO_2,lean}$ are the analyzed CO_2 concentrations in the rich and lean solution, respectively (mol kg^{-1}). The amount of CO_2 absorbed from the gas phase could also have been used to calculate the specific reboiler duty. This would, however, not have made any significant difference due to the strong steady state mass balance presented in Table 8.

It can be seen from Fig. 4 that slightly higher energy performance values were measured in the campaign by Pinto et al. (2014) and in this study compared to Tobiesen et al. (2007). The difference is not very large and can most likely be explained by the change of packing material and packing height in the stripper. In Tobiesen et al. (2007), Mellapak 250Y was used in the stripper and the packing height was 4.1 m, whereas Sulzer BX of packing height 3.57 m was used during the campaigns presented in Pinto et al. (2014) and the present work. Additionally it should be noted that the small differences seen in the figure might also come from the fact that the solutions were stripped to different lean loadings during the different campaigns and experimental runs. Overall it is clear that the data gathered here is in good agreement with data from Pinto et al. (2014) and Tobiesen et al. (2007).

5.2. Dynamic model validation

The simulation results from two different transient scenarios and associated comparison to the pilot results are presented in this section. The selected cases are representative for the transient scenarios that are desirable to validate. The first case is case 1 (from Table 8) with 17% step change in reboiler duty, whereas the other is case 2 with 22% step change in solvent flow rate.

The fact that the released CO_2 is recirculated and mixed with the absorber outlet gas before it is fed back to the absorber inlet causes variations in the CO_2 content of the absorber inlet gas. Any step change in solvent flow rate or reboiler duty will consequently affect the CO_2 content of the absorber inlet gas, which is used as an input to the model. These variations serve as an additional disturbance to the system and are therefore presented graphically for both cases. For further details about the cases, see Table 8.

5.2.1. Case 1: step change in reboiler duty

The reboiler duty was increased by 17% from 6.8 kW to 8.0 kW after 10 min in case 1. The absorber inlet CO_2 gas concentration (used as input to the model) varied according to Fig. 5.

Fig. 6 shows the response in absorber gas outlet CO_2 concentration. The agreement between model and pilot data is very good and the model is able to capture the dynamic behavior.

Fig. 7a and b shows the response in lean and rich CO_2 loading, respectively. The model predicts a similar dynamic trajectory as is observed in the pilot plant.

The absorbed and desorbed amounts of CO_2 are presented in Fig. 8a and b. The dynamic behavior is well described by the model, and the average deviations between model and pilot results are 0.3% and −2.1%, respectively.

The absorber temperature profile at the beginning of the test period is presented in Fig. 9a, whereas the profile at the end of the test period is presented in Fig. 9b. The desorber temperature profile at the beginning and end of the test period is presented in Fig. 10a and b, respectively. The model shows very good agreement with the measured absorber temperatures, as well as for the measured desorber temperature at the beginning of the test period. The deviation is slightly larger for desorber temperature at the end of the test period.

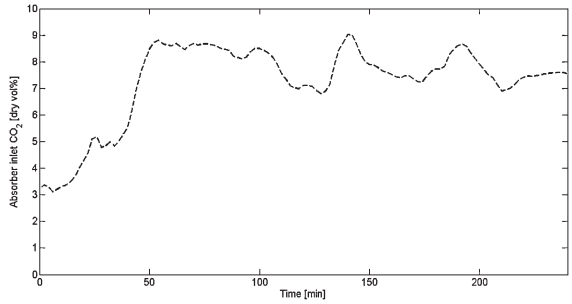

Fig. 5. Absorber inlet CO_2 concentration.

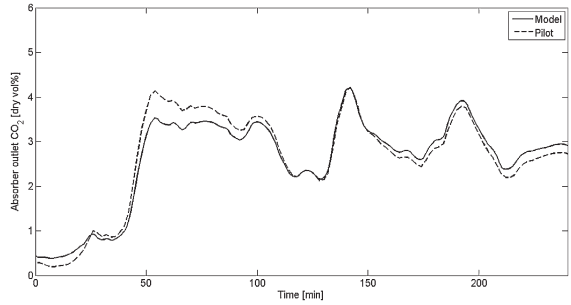

Fig. 6. Absorber inlet CO_2 concentration.

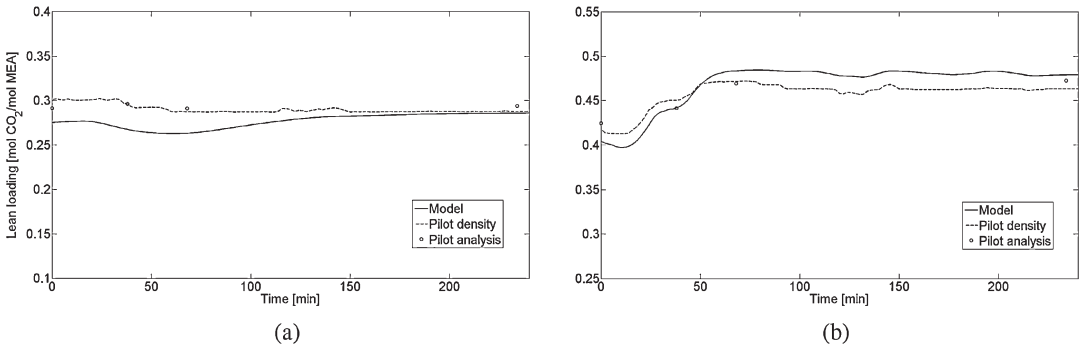

Fig. 7. (a) Lean and (b) rich CO_2 loadings.

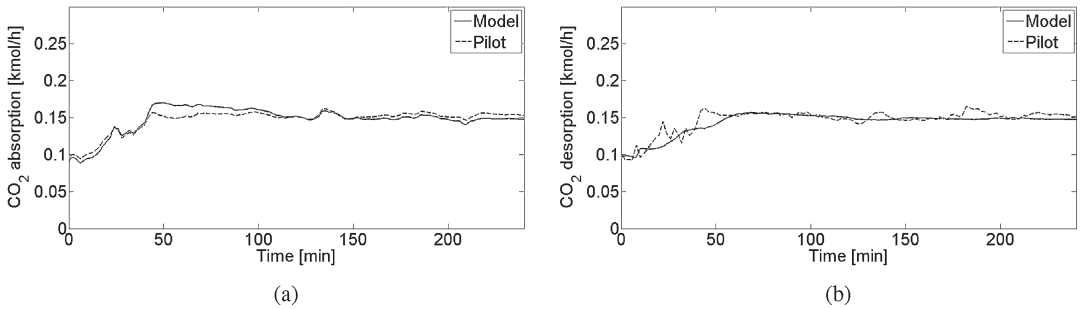

Fig. 8. (a) Absorbed and (b) desorbed CO_2.

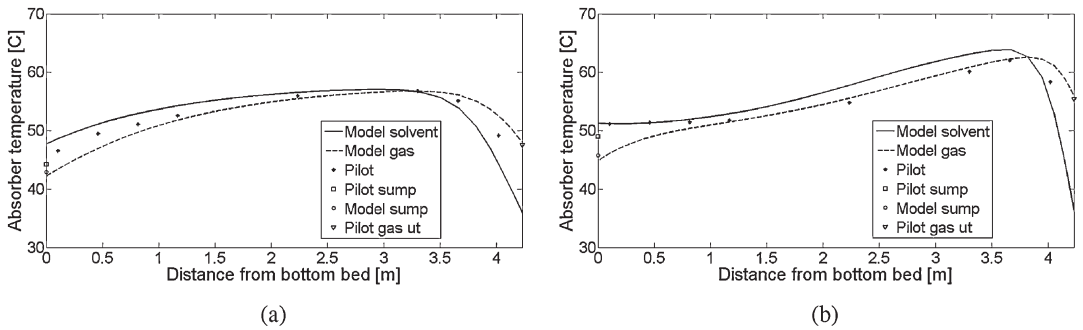

Fig. 9. Absorber temperature profile at the (a) beginning and (b) end of the test period.

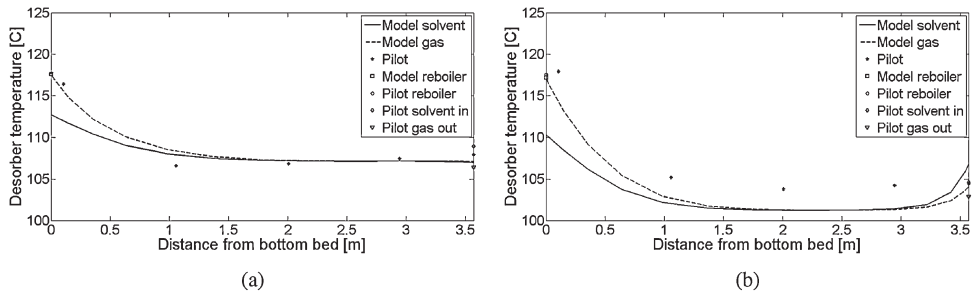

Fig. 10. Desorber temperature profile at the (a) beginning and (b) end of the test period.

5.2.2. Case 2: step change in solvent flow rate

The lean solvent circulation rate was increased by 21.8% from 172.3 kg/h to 209.9 kg/h after 60 min in case 2. The absorber inlet CO_2 concentration, used as model input, varied according to Fig. 11.

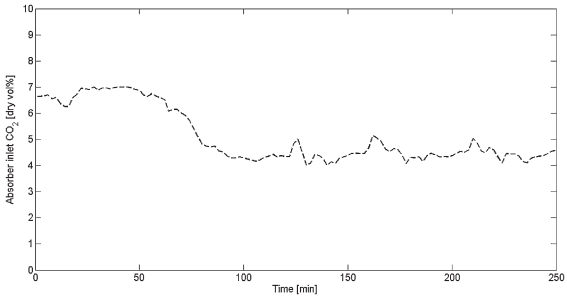

Fig. 11. Absorber inlet CO_2 concentration.

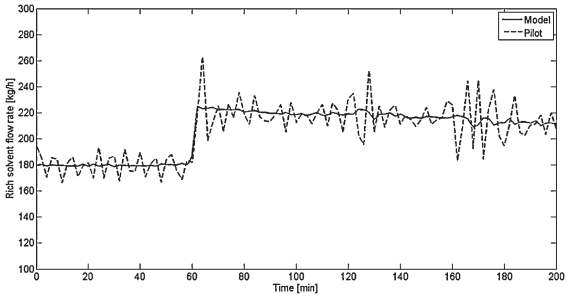

Fig. 12. Rich solvent flow rate.

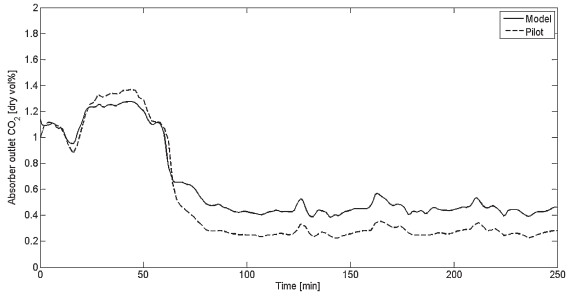

Fig. 13. Absorber outlet CO_2 concentration.

Fig. 12 shows the response in rich solvent flow rate (both simulated and measured in the pilot) as the lean solvent flow rate is increased. The measured rich solvent flow rate shows some fluctuations due to flashing in the cross heat exchanger which is not captured by the model. However, the average response is adequate.

Fig. 13 shows the response in absorber gas outlet CO_2 concentration. The model follows the same dynamic behavior that is observed in the pilot plant, however a small stationary offset is observed after the step change, as the predicted absorber outlet mole fraction of CO_2 is higher than observed in the pilot experiment.

Fig. 14a and b shows the response in lean and rich CO_2 loading, respectively, which also shows a small off-set.

The absorbed and desorbed amounts of CO_2 are presented in Fig. 15a and b. A small off-set is observed corresponding to Fig. 13. However, the dynamic behavior is well described by the model, and the average deviations between model and pilot results are −2.8% and −5.3%, respectively.

The absorber temperature profiles at the beginning and end of the test period is presented in Fig. 16a and b, respectively. The desorber temperature profile at the beginning and end of the test

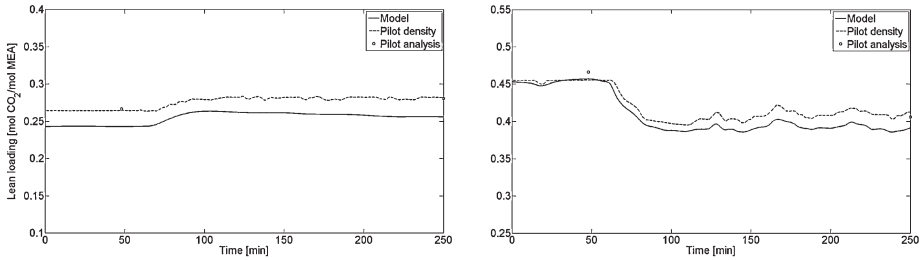

Fig. 14. (a) Lean and (b) rich CO_2 loadings.

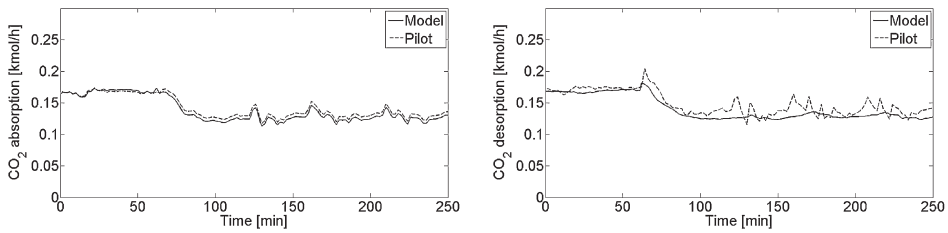

Fig. 15. (a) Absorbed and (b) desorbed CO_2.

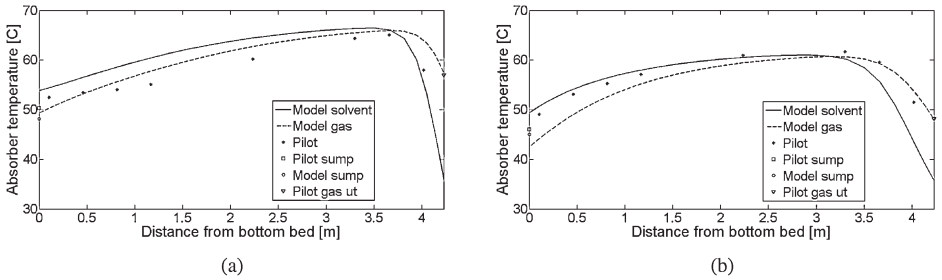

Fig. 16. Absorber temperature profile at the (a) beginning and (b) end of the test period.

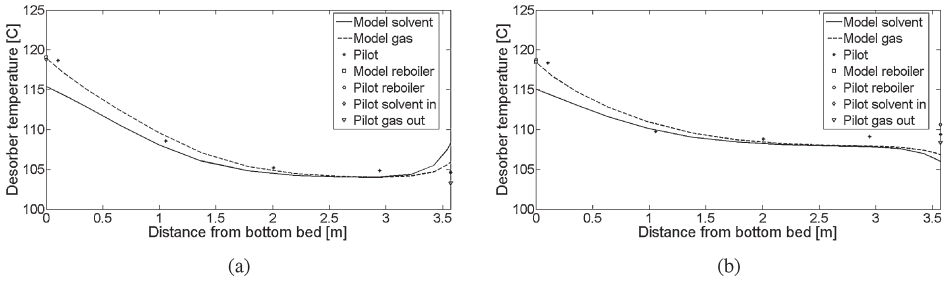

Fig. 17. Desorber temperature profile at the (a) beginning and (b) end of the test period.

period is presented in Fig. 17a and b, respectively. The model is able to give a very good prediction of column temperatures.

6. Discussion

The nature of the process design with solvent recirculated on a closed loop makes modeling and validation of the CO_2 absorption process challenging. Any error or inaccuracy in the desorption section of the model may affect the performance of the modeled absorption section, and vice versa. Errors might therefore easily evolve and propagate through the system. One should therefore take care ensuring that each section of the model is able estimate reasonable results and act as a realistic boundary condition to the connecting units. Each section (the absorber, the regeneration and the cross heat exchanger section) is therefore verified separately with relevant pilot plant data as model inputs, comparing model outputs to relevant measured responses in the pilot plant at steady state. Some parameters are adjusted to meet desired absorption and desorption rates along with column temperature profiles and CO_2 loadings. However, once the sections are connected, they will affect and depend on each other and possible errors might propagate.

When analyzing an experimental data set it is important to consider measurement accuracy and to know which measurements to trust and which are less reliable. The small deviations in the calculated mass balance at steady state for the current experiments indicate that the generated pilot plant data are reliable. The flow rate of CO_2 from the desorber (FT_EH) was compared to the calculated amount of CO_2 captured in the absorber ($N^{g}_{CO_2,abs}$) at steady state, and it was on average about 3.2% larger, however in some cases also smaller. The good agreement between calculated amount of absorbed CO_2 based on both gas measurements ($N^{g}_{CO_2,abs}$) and solvent phase measurements ($N^{l}_{CO_2,abs}$) suggest that the CO_2 flow measurement (FT_EH) is slightly overpredicting in most cases.

During the dynamic experiments frequent solvent samples were withdrawn to enable liquid analyses of CO_2 and MEA content in order to monitor the dynamic changes in the solvent. Online density measurements were also successfully correlated with CO_2 loading, which provides a continuous and instantaneous method of monitoring the solvent changes. These results are also supported by the study of Bui et al. (2014).

Case 1 shows a very good agreement between the model results and the pilot plant data. For case 2, where the solvent flow rate is disrupted the deviations are slightly larger, especially after the step change was performed. Changes in solvent flow rate do therefore seem to cause greater process disturbances than changes in reboiler duty. Probably, this relates to disruptions of column L/G that causes a shift in the operating zone described by Billet and Schultes (1999). Fast changes in operating conditions during variations in L/G was also reported by Kvamsdal and Rochelle (2008), where the magnitude and location of the temperature bulge was used to evaluate effects of various model parameters. In experimental case 2, the pilot plant is initially operated at a low solvent flow rate before it is increased. Thus, the model predicts initial operation of the absorber below the loading point. Predicting solvent hold-up and effective interface area is quite simple in this zone reflected by the good fit between model and pilot plant data. However, after the solvent flow rate is increased, the operation is shifted towards the loading point where the uncertainties of the correlations predicting solvent hold-up and effective interface area are larger. The model might therefore not be able to predict the correct loading point in this case, and the operating zone together with hydraulic conditions is therefore incorrectly estimated. This might cause the stationary deviations observed after the step change is introduced in case 2. Most empirical packing correlations available in the literature are developed and tested for specific chemical systems, specific packing types, and specific process designs and conditions. Such correlations are also designed for steady state systems. One should therefore take care choosing empirical correlations for mass transfer and effective area, and be sure to validate the correlations

performance with pilot, or full scale plant data from CO_2 capture with the same chemical solvent. The wetting factor that determines the effective interface area (a_{ph}) for the absorber in this model was corrected by a factor of 2.25 in these simulations. However, the fact that the model accuracy seem to depend on solvent flow rates suggest that this correction factor might be dependent of L/G.

Accurate prediction of column temperature profiles is important due to the temperature dependence of various parameters such as CO_2 solubility, CO_2 kinetic reaction rates and other physical properties such as heat capacity, density, etc. Vaporization of water is also an important phenomenon that depends on the temperature profile. Heat required for vaporization of water will also affects the temperature profile itself. In the pilot plant, column temperatures are measured by temperature sensors located at five different positions along the packing. The temperature measurements are in general very good and clear experimental column temperature profiles are generated. Previous experience from the pilot plant does also support realistic temperature measurements (Tobiesen et al., 2007, 2008). It is however not clear whether it is gas or liquid contacting these sensors and whether the reported temperatures are for gas phase or liquid phase (most probably it is a mixture) (Tobiesen et al., 2007). Due to all these simultaneous factors, it is clear that the column temperature profile is very challenging to model and fit to experimental measurements. However, the accordance of measured and simulated temperatures in this work is shown to be adequate. The model results resembles the measured temperature profiles for all cases and the deviation is acceptable given the challenges mentioned above. Overall, the model is able to describe the dynamic behavior for the two cases that are simulated. Small deviations are observed, but the model is considered adequate for dynamic simulations of such processes. It is an aim to develop models for MPC and it is believed that this model is a relevant basis for such purpose. It is, however, important to note that the model is validated against this specific pilot plant only, and it must be compared to several plants and various conditions in order to ensure general validity. It is believed that the developed set of unit model equations may be applied in a general manner to other systems. However, the parameter correlations are limited to their specific range of development, thus care must be taken when applying such correlations for other processes, systems or for new operating conditions without verification to experimental data. This conclusion is also supported by Kvamsdal and Hillestad (2012), where a parameter sensitivity analysis was conducted for simulations of two different pilot plants.

7. Conclusion

Performing dynamic model validation has been challenging due to lack of appropriate dynamic pilot plant data. Several validations have been performed using steady state pilot plant data, and a few attempts using dynamic data have been reported the recent years. However, in most cases there were not performed specific dynamic step tests, and it is therefore not certain that the collected data reflect all important dynamics. Specifically designed dynamic experiments are an important necessity in order to obtain appropriate data for dynamic model validation and to ensure that the model will predict dynamic responses accurately.

In this work, six complete dynamic data sets of the CO_2 absorption process with 30 wt% MEA has been generated in the Gløshaugen pilot plant. Relevant step changes in solvent flow rate and reboiler duty are performed. The pilot plant shows a very good steady state mass balance which indicates that the generated data are reliable. Two of the experimental cases has been simulated by a dynamic process model of the amine based CO_2 capture process developed in MATLAB. The results are compared to the dynamic pilot plant data and indicate that changes in solvent flow rate, or essentially column L/G, causes greater process disturbances compared to changes in reboiler duty. It is concluded that the model is able to describe the dynamic behavior of the pilot plant and is therefore considered adequate for dynamic simulations of such processes. However, verification towards several plants at a wide range of operating conditions is required in order to ensure general dynamic validity of the model. The developed set of unit model equations is considered to be sufficient for modeling similar CO_2 capture plants and systems. However, the parameter correlations are limited to their specific range of development. Thus, care must be taken when applying such correlations for other processes or for new operating conditions without verification to experimental data.

Acknowledgments

This publication is produced with support from the BIGCCS Centre, performed under the Norwegian research program Centres for Environment-friendly Energy Research (FME). The authors acknowledge the following partners for their contributions: Aker Solutions, ConocoPhillips, Gassco AS, GDF SUEZ, Shell Technology AS, Statoil Petroleum AS, TOTAL E&P Norge AS, and the Research Council of Norway (193816/S60).

Appendix A. Steady state data

TAG	Unit	Case							
		1	2	3	4	5	6	7	8
CO2_IN	[dry %]	3.52	6.77	7.41	3.57	3.90	5.41	4.57	1.55
CO2_OUT	[dry %]	0.29	1.19	3.05	0.00	0.44	3.09	1.38	0.00
FT-100	[kg/h]	166.93	172.33	152.07	142.13	240.87	178.72	238.82	239.09
FT-101	[kg/h]	171.04	179.79	156.95	146.43	246.13	180.31	241.74	240.34
FT06	[m^3/h]	89.77	90.09	127.02	100.10	125.94	118.96	118.87	118.57
FT_EH	[kg/h]	2.91	4.16	4.60	3.93	5.56	2.11	3.49	5.42
FT_EM	[kg/h]	4.41	7.71	8.99	6.53	7.21	4.95	6.63	3.25
FT_VASK	[kg/h]	23.51	23.21	294.18	271.00	264.18	196.66	228.23	251.49
HE-04/05/06	[kW]	6.82	9.23	10.02	8.29	10.35	6.13	8.33	8.26
LT-01	[L]	11.32	11.32	11.32	11.32	11.63	11.95	11.95	11.95
LT-02	[L]	54.03	53.31	53.84	53.67	53.67	54.75	54.39	54.40
PI-100	[mbar]	1014.07	1002.74	1040.05	1027.44	1012.10	1030.53	1031.27	1001.61
PI-102	[mbar]	1019.19	1005.78	1048.13	1032.30	1020.73	1038.75	1041.48	1010.21
PI-103	[mbar]	1016.60	1010.37	1056.40	1035.01	1029.00	1042.66	1045.31	1014.50
PT-02	[barg]	0.90	0.90	0.90	0.90	0.90	0.70	0.70	0.70
PT-04	[barg]	0.89	0.88	0.88	0.89	0.88	0.69	0.68	0.70
PT11	[L]	6.48	6.89	6.97	5.86	6.60	6.49	6.78	5.67
QT-100	[kg/l]	1.069	1.065	1.053	1.057	1.069	1.075	1.071	1.059

TAG	Unit	Case							
		1	2	3	4	5	6	7	8
QT-101	[kg/l]	1.091	1.097	1.102	1.097	1.092	1.102	1.096	1.073
TAOO	[°C]	45.14	51.61	47.91	44.15	45.55	35.78	39.16	35.96
TA01	[°C]	46.62	52.68	48.73	45.30	47.05	36.56	40.79	38.52
TA02	[°C]	49.38	53.57	48.67	47.59	50.02	37.27	43.82	42.51
TA03	[°C]	50.97	54.13	48.61	49.28	51.80	37.96	45.76	44.62
TA04	[°C]	52.49	55.10	48.67	51.04	53.27	38.75	47.36	45.99
TA05	[°C]	56.29	60.10	50.85	56.19	57.25	42.86	52.69	48.32
TA06	[°C]	57.47	64.31	56.46	58.26	58.64	48.13	55.60	46.78
TA07	[°C]	56.03	65.03	58.90	58.25	58.36	49.21	54.88	44.16
TA08	[°C]	49.10	58.31	57.95	53.51	52.17	46.94	50.02	40.90
TAB	[°C]	42.18	49.24	46.68	41.78	44.38	38.93	39.58	36.57
TI-01	[°C]	44.96	51.39	47.67	43.92	45.45	35.76	39.16	36.01
TI-03	[°C]	43.37	51.32	51.62	47.70	45.92	41.79	43.21	36.39
TI-04	[°C]	44.15	50.31	46.72	43.07	44.87	35.14	38.56	35.58
TI-05	[°C]	36.06	35.92	35.95	36.12	38.44	36.30	36.46	36.24
TI-06	[°C]	109.87	109.15	109.62	110.49	112.31	103.18	105.44	110.81
TI-07	[°C]	107.81	105.50	105.29	107.40	110.10	100.05	102.80	109.65
TI-08	[°C]	15.70	20.81	24.87	18.50	22.00	15.20	19.07	15.51
TI-09	[°C]	112.66	115.45	118.52	117.59	114.97	106.07	108.57	113.87
TI-11	[°C]	105.46	103.77	103.72	105.68	108.39	97.97	101.07	110.38
TI-15	[°C]	48.35	57.02	57.20	52.59	50.35	45.73	47.26	39.43
TI10	[°C]	117.57	118.79	121.07	120.61	118.85	113.05	113.85	116.16
TS01	[°C]	116.73	118.69	120.65	120.23	118.29	111.46	113.24	115.82
TS02	[°C]	109.20	108.20	114.29	112.43	111.21	98.98	101.82	111.92
TS03	[°C]	106.76	104.84	109.70	108.18	109.76	99.03	101.69	111.39
TS04	[°C]	106.59	104.87	106.01	106.98	109.46	99.37	101.99	111.62
TS05	[°C]	107.02	105.07	104.84	106.98	109.20	99.56	102.18	111.24
TT-01	[°C]	30.65	30.64	30.74	30.62	30.62	30.63	30.60	30.63
TT-02	[°C]	18.08	25.01	29.40	22.57	25.99	16.98	22.26	18.94
TT-03	[°C]	36.80	36.63	36.68	37.28	39.07	37.10	37.09	36.84
TT103	[°C]	48.25	52.63	49.43	46.17	47.98	38.06	41.48	39.77
TV5	[°C]	43.26	50.54	49.37	43.55	47.16	40.71	41.86	37.87

References

Åkesson, J., Laird, C.D., Lavedan, G., Prölß, K., Tummescheit, H., Velut, S., Zhu, Y., 2012. Nonlinear model predictive control of a CO_2 post-combustion absorption unit? Chem. Eng. Technol. 35 (3), 445–454.

Biliyok, C., Lawal, A., Wang, M., Seibert, F., 2012. Dynamic modelling, validation and analysis of post-combustion chemical absorption CO_2 capture plant. Int. J. Greenhouse Gas Control 9, 428–445.

Billet, R., Schultes, M., 1999. Prediction of mass transfer columns with dumped and arranged packings. Updated summary of the calculation method of Billet and Schultes. Trans. IChemE 77 (A), 498–504.

Brúder, P., Grimstvedt, A., Mejdell, T., da Silva, E.F., Svendsen, H.F., 2010. CO_2 capture into aqueous solutions of the mixed solvent Cesar 1. Adv. Gas Process., 31–40.

Bui, M., Gunawan, I., Verheyen, V., Feron, P., Meuleman, E., Adeloju, S., 2014. Dynamic modelling and optimisation of flexible operation in post-combustion CO_2 capture plants – a review. Comput. Chem. Eng. 61, 245–265.

Bui, M., Gunawan, I., Verheyen, V., Meuleman, E., Feron, P., 2014. Dynamic operation of post-combustion CO_2 capture in Australian coal-fired power plants. Energy Procedia 63, 1368–1375.

Cheng, S., Meisen, A., 1996. Predict amine solution properties accurately. Hydrocarbon Process. 75 (2).

Enaasen, N., Zangrilli, L., Mangiaracina, A., Mejdell, T., Kvamsdal, H., Hillestad, M., 2014. Validation of a dynamic model of the Brindisi pilot plant. Energy Procedia 63, 1040–1054.

Gáspár, J., Cormos, A.M., 2011. Dynamic modeling and validation of absorber and desorber columns for post-combustion CO_2 capture. Comput. Chem. Eng. 35, 2044–2052.

Harun, N., Douglas, P.L., Sandoval, L.R., Croiset, E., 2011. Dynamic simulation of MEA absorption processes for CO_2 capture from fossil fuel power plant. Energy Procedia 4, 1478–1485.

Jayarathnaa, S.A., Lie, B., Melaaen, M.C., 2011. NEQ rate based modeling of an absorption column for post combustion CO_2 capturing. Energy Procedia 4, 1797–1804.

Kim, I., 2009. Heat of Reaction and VLE of Post Combustion CO_2 Absorbents (PhD dissertation). Norwegian University of Science and Technology.

Kvamsdal, H.M., Chikukwa, A., Hillestad, M., Zakeri, A., Einbu, A., 2011. A comparison of different parameter correlation models and the validation of an MEA-based absorber model. Energy Procedia 4, 1526–1533.

Kvamsdal, H.M., Hillestad, M., 2012. Selection of model parameter correlations in a rate-based CO_2 absorber model aimed for process simulation. Int. J. Greenhouse Gas Control 11, 11–20.

Kvamsdal, H.M., Jakobsen, J.P., Hoff, K.A., 2009. Dynamic modeling and simulation of a CO_2 absorber column for post-combustion CO_2 capture. Chem. Eng. Process. 48, 135–144.

Kvamsdal, H.M., Rochelle, G.T., 2008. Effects of the temperature bulge in CO_2 absorption from flue gas by aqueous monoethanolamine. Ind. Eng. Chem. Res. 47, 867–875.

Karimi, M., Hillestad, M., Svendsen, H.F., 2012. Investigation of the dynamic behavior of different stripper configurations for post-combustion CO_2 capture. Int. J. Greenhouse Gas Control 7, 230–239.

Lawal, A., Wang, M., Stephenson, P., Koumpouras, G., Yeung, H., 2010. Dynamic modelling and analysis of post-combustion CO_2 chemical absorption process for coal-fired power plants? Fuel 89 (10), 2791–2801.

Lawal, A., Wang, M., Stephenson, P., Obi, O., 2012. Demonstrating full-scale post-combustion CO_2 capture for coal-red power plants through dynamic modelling and simulation. Fuel 101, 115–128.

Lawal, A., Wang, M., Stephenson, P., Yeung, H., 2009. Dynamic modelling of CO_2 absorption process for post-combustion capture in coal-fired power plants? Fuel 88 (12), 2455–2462.

Lin, Y.-J., Wong, D.S.-H., Jang, S.-S., 2012. Control strategies for flexible operation of power plant with CO_2 capture plant. AIChE J. 58 (9), 2697–2704.

Luo, X., Hartono, A., Hussain, S., Svendsen, H.F., 2015. Mass transfer and kinetics of carbon dioxide absorption into loaded aqueous monoethanolamine solutions. Chem. Eng. Sci. 123, 57–69.

Metz, B., Davidson, O., de Coninck, H., Loos, M., Meyer, L., 2005. IPCC Special Report on Carbon Dioxide Capture and Storage. Cambridge University Press, Cambridge, UK, Available from: http://www.ipcc.ch/pdf/special-reports/srccs/srccs_wholereport.pdf

Nittaya, T., Douglas, P.L., Croiset, E., Ricardez-Sandoval, L.A., 2014. Dynamic modeling and evaluation of an industrial-scale CO_2 capture plant using monoethanolamine absorption processes. Ind. Eng. Chem. Res. 53, 11411–11426.

Nittaya, T., Douglas, P.L., Croiset, E., Ricardez-Sandoval, L.A., 2014. Dynamic modeling and control of MEA absorption processes for CO_2 capture from power plants. Fuel 116, 672–691.

Panahi, M., Skogestad, S., 2011. Economically efficient operation of CO_2 capturing process. Part I: Self-optimizing procedure for selecting the best controlled variables. Chem. Eng. Process. 50, 247–253.

Panahi, M., Skogestad, S., 2012. Economically efficient operation of CO_2 capturing process. Part II: Design of control layer. Chem. Eng. Process. 52, 112–124.

Pinto, D.D.D., Knuutila, H., Fytianos, G., Haugen, G., Mejdell, T., Svendsen, H.F., 2014. CO_2 post combustion capture with a phase change solvent. Pilot plant campaign. Int. J. Greenhouse Gas Control 31, 153–164.

Puxty, G., Rowland, R., Allport, A., Yang, Q., Bown, M., Burns, R., Maeder, M., Attalla, M., 2009. Carbon dioxide postcombustion capture: a novel screening study of the carbon dioxide absorption performance of 76 amines? Environ. Sci. Technol. 43 (16), 6427–6433.

Reid, R.C., Prausnitz, J.M., Poling, B.E., 1996. The Properties of Gases and Liquids, 4th ed. McGraw-Hill Book Company, New York, USA.

Sahraei, M.H., Ricardez-Sandoval, L.A., 2014. Controllability and optimal scheduling of a CO_2 capture plant using model predictive control. Int. J. Greenhouse Gas Control 30, 58–71.
Tobiesen, F.A., Juliussen, O., Svendsen, H.F., 2008. Experimental validation of a rigorous desorber model for CO_2 post-combustion capture. Chem. Eng. Sci. 63, 2641–2656.
Tobiesen, F.A., Svendsen, H.F., Juliussen, O., 2007. Experimental validation of a rigorous absorber model for CO_2 post-combustion capture? AIChE J. 53 (4), 846–865.
Xu, Q., 2011. Thermodynamics of CO_2 Loaded Aqueous Amines (PhD dissertation). The University of Texas at Austin.

C.6 Paper F: Dominating Dynamics of the Post-combustion CO_2 Absorption Process

Dominating Dynamics of the Post-combustion CO_2 Absorption Process

Nina Enaasen Flø[a,*], Hanne Marie Kvamsdal[b], Magne Hillestad[a], Thor Mejdell[b]

[a]*Department of Chemical Engineering, NTNU, Sem Sælandsvei 4, N-7491 Trondheim, Norway*
[b]*Department of CO_2 Capture Process Technology, SINTEF Materials and Chemistry, Post Office Box 4760, Sluppen, N-7465 Trondheim, Norway*

Abstract

A dynamic model of the post-combustion CO_2 capture process based on absorption is used to investigate the transient behavior and dynamic responses of the process and to detect stabilization time when various disturbances are introduced. Plant dimensions and parameter settings are based on the SINTEF CO_2 capture pilot plant at Tiller, and the overall process model is validated using two sets of steady state pilot plant data. A deviation between model and pilot results of -0.8 and -4.5 % in absorbed CO_2 and 2.6 and 1.2 % in desorbed CO_2 is seen for the two cases used in validation, respectively. The model deviation is within the observed pilot plant CO_2 mass balance error of +/-3 to 6 % for these cases. The simulated absorber and desorber temperature profiles shows adequate agreement to the pilot plant measurements. The model is further used to simulate set-point changes in flue gas flow rate, reboiler duty and solvent flow rate in order to investigate typical stabilization times at various locations in the process. As expected, mixing models like the absorber sump and reboiler will introduce time constants that affect the dynamic response profiles, while plug flow models like the cross heat exchanger causes pure transport delays and no additional settling time. Mass transfer and chemical reaction rates causes some process inertia, but it is relatively small compared to the inertia of larger mixing vessels like the absorber sump, reboiler and buffer tank and transport delay caused by plug flow. Changes in solvent flow rate are also seen as a larger disturbance to the process compared to changes in flue gas flow rate and reboiler duty, reflected by longer process stabilization time to reach new steady state conditions. The estimated 90 % settling times for the response in absorbed CO_2 in the Tiller pilot plant are less than 1 hour, 3.5-6 hours and 3.5-4 hours for step changes in flue gas flow rate, solvent flow rate and reboiler duty, respectively.

Keywords: Post combustion CO_2 capture, absorption, process dynamics, time constants, stabilization time

1. Introduction

The attention around dynamic modeling of post-combustion CO_2 absorption is increasing as the combined CO_2 capture and power generation process is getting closer to full-scale realization. Power plant load changes have been identified as a possible operational challenge for the downstream CO_2 capture unit (Chalmers and Gibbins, 2007).

*Corresponding author. Tel.:+47 99478919.
Email addresses: enaasen@ntnu.no (Nina Enaasen Flø), hanne.kvamsdal@sintef.no (Hanne Marie Kvamsdal), magne.hillestad@ntnu.no (Magne Hillestad), thor.mejdell@sintef.no (Thor Mejdell)

These load changes may be quite large and frequent due to flexible power generation according to daily fluctuations in energy demand and prices. The dynamic performance of the integrated power generation and CO_2 capture process is therefore critical for optimal operation of the overall process.

A power plant reacts quite fast during load transitions and the dynamics are well documented through years of operational experience. The experience of the capture units abilities to adapt to power plant load changes is however limited. It is believed that load changes will influence both the dynamic operation and optimal design of the capture plant (Chalmers et al., 2009). A dynamic process model can be used to study the transient behavior of a process, determine its dynamic responses and detect how long time it takes to stabilize the system after a disturbance is introduced. It can also be utilized to study interactions between the power generation unit and the capture plant and to identify possible operational bottlenecks at an early stage of the process development and realization. The overall residence time of the system will affect these aspects, but column mass transfer and reaction rates may also contribute important inertia that influence the overall stabilization time. Typical process time constants and dead times should therefore be identified and their effects on the optimal process design should be studied.

A number of dynamic models of the post-combustion CO_2 capture process have been developed the recent years. Previously, most of these models have concerned individual process units only such as standalone absorber (Kvamsdal et al., 2009; Lawal et al., 2009), desorber (Ziaii et al., 2009), or reboiler (Arce et al., 2012). Dynamic models of the complete absorption process have also been developed more recently. Some of these models have been used to investigate the transient behavior of the process when an operational related disturbance is superimposed on the process. Lawal et al. (2010) investigated dynamic responses of a post-combustion CO_2 capture plant by introducing possible disturbances to the flue gas flow rate, flue gas CO_2 concentration, reboiler duty and water balance control. For the case of reducing reboiler duty a time constant of 57 min was estimated. The column sump and solvent buffer tank volumes contribute to this time constant; however, transport delay was not accounted for in their model. Harun et al. (2012) studied the transient response of the MEA absorption process performing step changes in the reboiler duty, and ramp changes and a sinusoidal change in the flue gas flow rate. The results were similar to those reported by Lawal et al. (2010).

Faber et al. (2011) reported experimental step response results from a transient pilot plant campaign at the Esbjerg pilot plant as part of the EU project CESAR. The flue gas flow rate, lean solvent flow rate and reboiler duty were individually changed in a stepwise manner to introduce disturbances to a process at initially steady state condition and to evaluate the transient performance of the process. The average time for the entire system to reach the new steady state operating condition after perturbation was between 1h15min and 1h45min.

The present study uses a comprehensive dynamic model developed in MATLAB to investigate the dynamic behavior of the post combustion CO_2 capture process when various disturbances are introduced to the system at steady state condition. The process model has previously been validated dynamically towards experimental pilot plant data collected at the Gløshaugen pilot plant (Enaasen Flø et al., 2015). Even though a different pilot plant was used for dynamic model validation, it is expected that the general unit model equations will be valid for other plants provided

the correct unit dimensions. The effect of set-point changes in flue gas flow rate, solvent flow rate and reboiler duty are investigated in the present work. The resulting dynamic responses at various locations of the process are compared and utilized to quantitatively estimate dead times and 90 % settling times. These measures are further used to determine the main inertia of the process and various process units are categorized according to their effect on and contribution to the overall dynamic progress.

2. Stabilization time

In order to identify and compare the main inertia of the process, time constants and transport delay or dead-time of dynamic responses for various process units should be determined. The dead time (θ) describes how long time it takes before a process begins to respond when a disturbance is introduced to the system. A time constant describes how fast the process responds once it has started to react to the change. For a simple 1st order system, the time constant equals the time it takes before the step response reaches $1 - e^{-1} = 63.2\%$ of its final asymptotic value. An illustration of the principle is shown in Figure 1a, where $u(t)$ is the process input and $y(t)$ represents a response in process output. When a step change (Δu) is introduced, the process response will change from initial value y_0 to some final asymptotic value y_∞. The dead time (θ) and 1st order time constant (t_{1st}) are also indicated in Figure 1a. However, for a higher order system with complex eigenvalues of the linearized problem (see Figure 1b), the response may show a more complex behavior and an analytic expression for the overall time response of an output can be even impossible to find. One widely used measure for more complex systems is the settling time (t_s) which is defined as the time it takes to reach and stay within a certain relative level of the final value (Singh, 2009). Typical levels are 90%, 95% or 99%. The 90% settling time (or the 90% response time) is therefore defined as the time it takes for the process output to settle within +/-10% of the final value compared to the starting point, that is $y_\infty - 0.1\Delta y < y < y_\infty + 0.1\Delta y$.

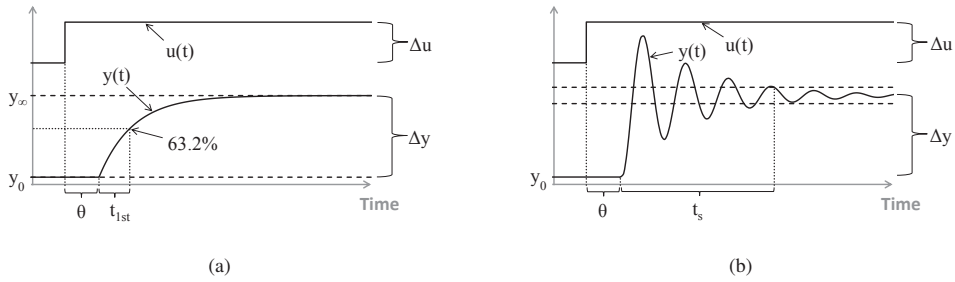

Figure 1: (a) Dead time (θ) and time constant (t_s) for a 1st order process step response (b) Dead time (θ) and settling time (t_s) for a higher order process step response.

3. Dynamic process model

A dynamic process model of the conventional CO_2 absorption process based on amines is developed in MATLAB from first principle conservation laws. The process model consists of dynamic unit models representing each piece of process equipment: absorber, stripper, absorber sump, reboiler, condenser, cross heat exchanger, lean cooler and buffer tank, as illustrated in Figure 2. The models of the absorber, stripper, cross heat exchanger and lean cooler units are distributed parameter models, while the other units are assumed to be perfectly mixed.

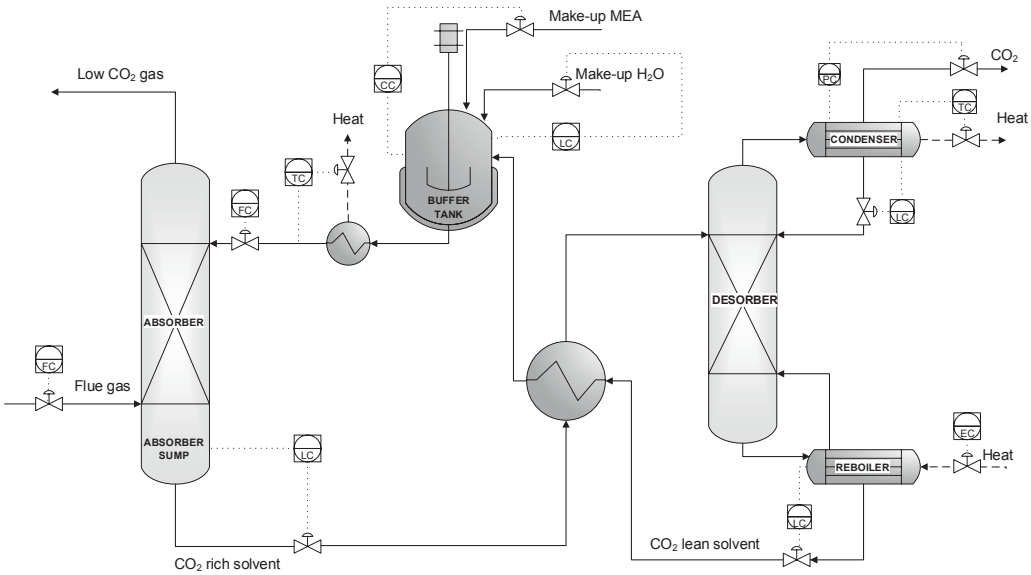

Figure 2: Process flow diagram of the model including basic control scheme.

Details about the model assumptions behind the general column model that is used to represent both the absorber and stripper columns are described by Kvamsdal et al. (2009) and Tobiesen et al. (2012), and the model equations are listed in Enaasen et al. (2013). A rate based approach is used to describe mass- and heat transfer in the packed sections of the columns. The current study uses correlations described by Rocha et al. (1996) to estimate mass transfer coefficients ($k_{g,i}$ and $k_{l,i}$) and the effective interface area (a_e):

$$k_{g,i} = \frac{0.054 D_{g,i}}{S}\left(\frac{(u_{g,e}+u_{l,e})\rho_g S}{\mu_g}\right)^{0.8}\left(\frac{\mu_g}{D_{g,i}\rho_g}\right)^{0.33} \tag{1}$$

$$k_{l,i} = 2\left(\frac{D_{l,i} C_E u_{l,e}}{\pi S}\right) \tag{2}$$

where $u_{g,e} = \frac{u_g}{\varepsilon(1-h_l)\sin\beta}$ and $u_{l,e} = \frac{u_l}{\varepsilon h_l \sin\beta}$

$$a_e = F_{SE} F_t a \tag{3}$$

where F_{SE} is a factor for surface enhancement given for the packing material and F_t is a dimensionless correction factor for total hold up due to effective wetted area defined by:

$$F_t = \frac{29.12(We_L Fr_L)^{0.15} S^{0.359}}{Re_L^{0.2} \varepsilon^{0.6} (1 - 0.93\cos\gamma)(sin\beta)^{0.3}} \tag{4}$$

Estimation of the solvent hold-up (h_l) is done by correlations given by Rocha et al. (1993) as presented in Equation 5-9.

$$h_l = \left(4\frac{F_t}{S}\right)^{2/3} \left(\frac{3\mu_l u_l}{\rho_l (sin\beta)\varepsilon g_e}\right)^{1/3} \tag{5}$$

$$g_e = g\left(\frac{\rho_l - \rho_g}{\rho_l}\right)\left(1 - \frac{\frac{\Delta P}{\Delta z}}{(\frac{\Delta P}{\Delta z})_{flood}}\right) \tag{6}$$

$$\frac{\Delta P}{\Delta z} = \left(\frac{\Delta P}{\Delta z}\right)_{dry} \left(1 - \frac{1}{1 - K_2 h_l}\right)^5 \tag{7}$$

where $K_2 = 0.614 + 71.35S$.

$$\left(\frac{\Delta P}{\Delta z}\right)_{dry} = \frac{0.177\rho_g}{S\varepsilon^2(\sin\beta)^2} u_g^2 + \frac{88.774\mu_g}{S^2\varepsilon\sin\beta} u_g \tag{8}$$

$$\left(\frac{\Delta P}{\Delta z}\right)_{flood} = 1025 \tag{9}$$

The heat exchanger and lean cooler models are single phase distributed parameter models, the reboiler and condenser are modeled as flash tanks and the absorber sump and buffer tank are modeled as single phase continuously stirred tanks. All unit models are developed in dynamic mode and the model equations are given in (Enaasen Flø et al., 2015).

A basic control system is also implemented with level controllers for absorber sump, reboiler, condenser and buffer tank, temperature controllers for the condenser and lean cooler, a pressure controller for the condenser and MEA concentration controller for the buffer tank. The control scheme is also illustrated in Figure 2, and the control

model equations are given in (Enaasen Fløet al., 2015). The flue gas flow rate, lean solvent flow rate and reboiler duty are controlled manually.

The overall dynamic process model results in a set of partial differential equations (PDEs) which are solved numerically and simultaneously in MATLAB using ode15s and orthogonal collocation. All dependent variables are normalized to increase numerical robustness.

4. Steady state model validation

The Tiller pilot plant is used as basis for equipment sizes and parameter settings in the process model. The design of this pilot plant with full height columns is similar to full-scale design. The gas rate ($m\,s^{-1}$) and liquid load ($m^3\,s^{-1}\,m^2$) are therefore comparable, such that the conditions for mass and heat transfer from gas to liquid and reaction rates will be very much like in industrial sized plants. Scale-up of column diameters and vessel sizes allowing larger gas and solvent flow rates will therefore represent full-scale size. It is therefore expected that the time constants for an industrial plant will resemble those of the Tiller pilot plant.

The absorber column diameter is 200 mm and the absorber tower contains 19.418 m of packing. The desorber column has a diameter of 150 mm and contains 13.78 m of packing. Both columns contains Mellapak 250Y structured packing. In the Tiller pilot plant the lean solvent enters the top of the absorption column, trickles downwards and meets the flue gas containing CO_2 flowing counter-currently. CO_2 is absorbed from the gas, and the rich solvent is pumped from the absorber sump through the cross heat exchanger and further into the desorber column. The solvent enters the top of the desorber and meets the upcoming vapor from an electrically heated reboiler. This vapor contains the energy required to heat up the solvent to stripping temperature and desorb CO_2 and regenerate the solvent. The regenerated solvent exits the reboiler and flows through the cross heat exchanger, into a mixing tank and through the lean cooler to the absorber inlet.

The solvent hold-up and residence times of various units are presented in Table 1 for a solvent flow rate of 3.5-7 liter/min.

Two sets of steady state data from a Tiller pilot plant campaign with 30 wt% MEA solvent are used for validation of the model. The first case (100612) represent a natural gas based flue gas with 3.9 % CO_2, while the second (100718) represent a coal based flue gas with 10.9 % CO_2. The amount of absorbed CO_2 in $kg\,h^{-1}$ is calculated in three different ways using the measured and logged pilot plant data:

1. Based on measured absorber inlet and outlet gas flow rates and gas phase CO_2 concentrations:

$$m^{\mathrm{g}}_{\mathrm{CO_2,abs}} = (F_{\mathrm{g,abs,in}} y_{\mathrm{CO_2,abs,in}} - F_{\mathrm{g,abs,out}} y_{\mathrm{CO_2,abs,out}}) M_{\mathrm{CO_2}} \tag{10}$$

2. Based on measured absorber inlet and outlet solvent flow rates and CO_2 analysis of the liquid samples:

$$m^{\mathrm{l}}_{\mathrm{CO_2,abs}} = (F_{\mathrm{l,abs,out}} x_{\mathrm{CO_2,rich}} - F_{\mathrm{l,abs,in}} x_{\mathrm{CO_2,lean}}) M_{\mathrm{CO_2}} \tag{11}$$

Table 1: Solvent hold-ups and residence times in the Tiller pilot plant.

	Solvent hold-up [liter]	Residence time [min]
Absorber packing	50	7 - 14
Absorber sump	16	2 5
Desorber packing	20	3 6
Desorber sump and reboiler	280	40 - 80
Buffer tank	57	8 - 16
Heat exchanger and piping	92	13 - 26
Total	515	73 - 147

3. Based on gas flow measurement of the condenser outlet gas stream:

$$m^{\mathrm{g}}_{\mathrm{CO_2,des}} = F_{\mathrm{g,des,out}} y_{\mathrm{CO_2,des,out}} M_{\mathrm{CO_2}} \tag{12}$$

Based on these calculations a steady state pilot plant CO_2 mass balance error of - 5.8 % to + 3.6 % is found for the two cases, according to Table 2.

The two steady state cases are simulated using the dynamic process model and the resulting CO_2 solvent loadings and amount of absorbed CO_2 are presented in Table 3. The deviations in absorbed CO_2 compared to the pilot plant results are -0.8 and -4.5 %, for the two cases respectively. For desorbed CO_2 the deviations are 2.6 and 1.2 %. This is within the percentage error of calculated steady state CO_2 mass balance for each case.

The absorber and desorber column temperature profiles for the two steady state cases are given in Figures 3a-3d. The simulated temperature profiles are in good agreement with the column temperature measurements, which supports the models reliability. There are no dynamic data for the Tiller pilot plant available for validation of the dynamic performance of the model. However, the process model has previously been validated dynamically, to a different pilot plant. The results are presented in (Enaasen Flø et al., 2015) and it is believed that the general unit model equations also are valid for other plants provided the correct equipment sizing and parameter settings. The main uncertainty is believed to lie in the empirical parameter correlations, which are limited to their specific range measured.

Table 2: Tiller pilot plant results for case 100612 and 100718

Input		Case 100612	Case 100718
Flue gas flow rate	$[Nm^3\,h^{-1}]$	216.4	138.4
Flue gas CO_2 content	[vol%]	3.9	10.6
Solvent flow rate	$[kg\,h^{-1}]$	222	408
Reboiler duty	[kW]	18.5	26.7
Reboiler pressure	[kPa]	180	190
Absorbed amount of CO_2			
$m^{g}_{CO_2,abs}$	$[kg\,h^{-1}]$	15.3	25.8
$m^{l}_{CO_2,abs}$	$[kg\,h^{-1}]$	14.8	25.1
$m^{g}_{CO_2,des}$	$[kg\,h^{-1}]$	14.8	24.4
CO_2 loading			
$\alpha_{CO_2,lean}$	$[molCO_2/molMEA]$	0.14	0.17
$\alpha_{CO_2,rich}$	$[molCO_2/molMEA]$	0.48	0.49
Error in calculated steady state CO_2 mass balances			
Absorber $\left(\frac{m^{g}_{CO_2,abs}-m^{l}_{CO_2,abs}}{avg\left(m^{g}_{CO_2,abs}+m^{l}_{CO_2,abs}\right)}\right)$	[%]	3.6	2.8
Desorber $\left(\frac{m^{g}_{CO_2,des}-m^{l}_{CO_2,des}}{avg\left(m^{g}_{CO_2,des}+m^{l}_{CO_2,des}\right)}\right)$	[%]	0.2	-3.1
Overall $\left(\frac{m^{g}_{CO_2,des}-m^{g}_{CO_2,abs}}{avg\left(m^{g}_{CO_2,des}+m^{g}_{CO_2,abs}\right)}\right)$	[%]	-3.4	-5.8

Table 3: Simulated results for case 100612 and 100718.

		Case 100612	Case 100718
Absorbed amount of CO_2 ($m^{g}_{CO_2,abs}$,$m^{l}_{CO_2,abs}$,$m^{g}_{CO_2,des}$)	$[kg\,h^{-1}]$	15.2	24.7
Lean CO_2 loading ($\alpha_{CO_2,lean}$)	$[molCO_2/molMEA]$	0.12	0.17
Rich CO_2 loading ($\alpha_{CO_2,rich}$)	$[molCO_2/molMEA]$	0.48	0.50

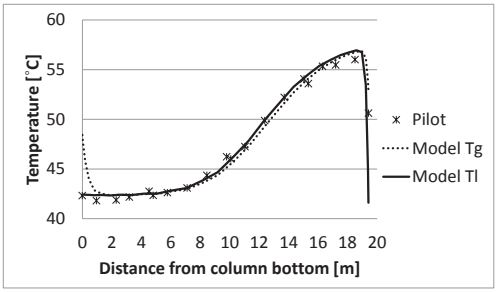

(a) Absorber temperature profile for case 100612

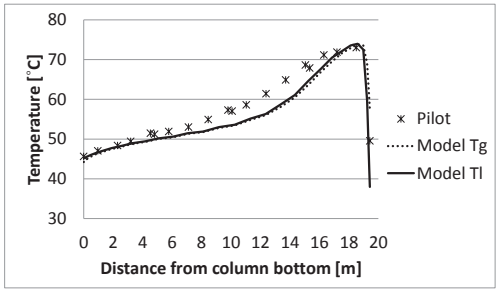

(b) Absorber temperature profile for case 100718

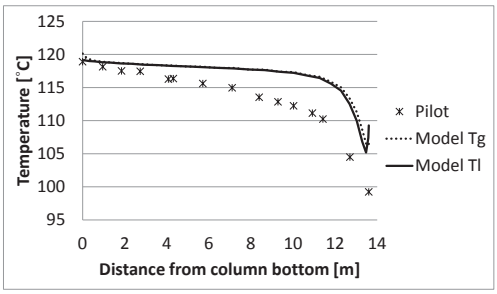

(c) Desorber temperature profile for case 100612

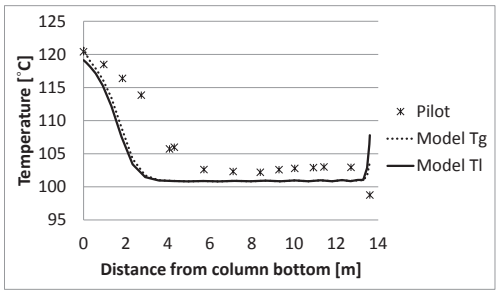

(d) Desorber temperature profile for case 100718

Figure 3: Absorber and desorber column temperature profiles for case 100612 and 100718.

5. Simulation results

A case with 216.4 $Nm^3\,h^{-1}$ of flue gas containing 3.9 vol% of CO_2 with the optimal solvent flow rate of 213.1 $kg\,h^{-1}$ and reboiler duty of 15.5 kW to reach 90 % capture rate is used as basis for the dynamic simulations. Disturbances are introduced to the process at initially steady state condition in order to create dynamic responses and compare typical settling times and dead times of the process. This will gain a better understanding of which parts of the plant causes the main inertia.

5.1. Changes in solvent flow rate

The absorber inlet solvent flow rate is increased by 20 % from 213.1 to 255.8 $kg\,h^{-1}$ as indicated by the triangle marked (blue) line in Figure 4. The disturbance is introduced as a ramp change with a total ramp rate of 1 minute. The simulations are continued for 18 hours to ensure that a new steady state condition is observed. The flue gas conditions and reboiler duty are kept constant during the whole simulation time.

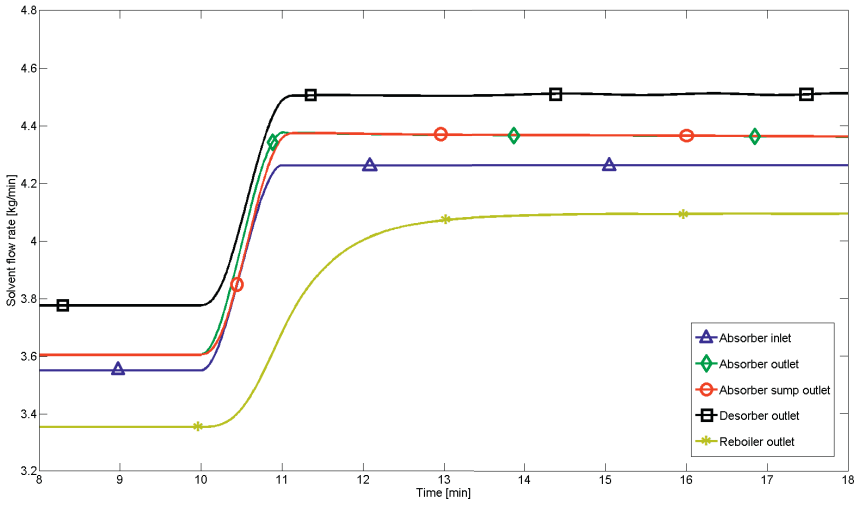

Figure 4: Response in solvent flow rate for +20% set-point change in absorber inlet solvent flow rate.

Figure 4 shows how the change in solvent flow rate propagates through the process. A minimal or no dead time between the absorber inlet and outlet solvent flow rates is observed. The same yields for the heat exchanger and desorber. This is the effect of plug flow models for incompressible fluids. The dynamic effects on dead time for the absorber sump and reboiler is also small, but noticeable, which is typical for mixing models. This is seen by comparing the circle marked (red) line to the diamond marked (green) line, and the square marked (black) line to the asterisk marked (yellow) line, respectively. The response profile of mixing model units will however change due to mixing effects. The response is smoothing out as it propagates through the mixing units. These units will therefore introduce inertia as settling time, especially the reboiler which has the largest solvent hold-up. The level controllers react however quite fast and are able to adjust very quickly to the new conditions. The flow rates reaches a new stable level after about 2-3 minutes. It can also be noted that plug flow models will not result in any additional settling time as the inlet and outlet flow rates shows exactly the same profile. Thus changes in solvent flow rate are instantaneous for such units.

The effects of plug flow transport, mass- and heat transfer and chemical reaction in the absorber and desorber packing are observed as shown in Figures 5 and 6. The response in rich CO_2 loading at the absorber outlet as presented by the diamond marked (green) line in Figure 5a is slower compared to the response in solvent flow rate presented in Figure 4. This is due to the effects of plug flow transport, possible changes in solvent hold-up in the packing material and mass transfer and chemical reaction rates which adds inertia to the process. The absorber sump and cross heat exchanger adds more transport delay, in terms of dead time. However, while the mixing effects of the absorber sump

results in a smoother loading profile at the absorber sump outlet (circle marked (red) line), the heat exchanger causes a simple transport delay as the profiles in and out are identical. The same effects are observed for the lean CO_2 loading in Figure 5b, where plug flow models represent transport delay and mixing models smoothens out the profile with additional settling times. Faster dynamics are observed for the solvent temperature profiles in Figure 6, because heat transfer between the two streams in the cross heat exchanger evens out the temperature changes more rapidly. It takes about 4-5 hours and 2-3 hours for the new conditions to adjust for CO_2 loadings and temperatures, respectively.

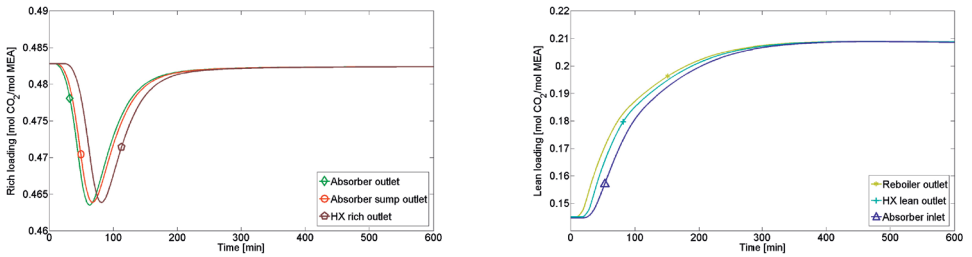

(a) (b)

Figure 5: Response in (a) rich CO_2 loadings and (b) lean CO_2 loadings for +20% set-point change in absorber inlet solvent flow rate.

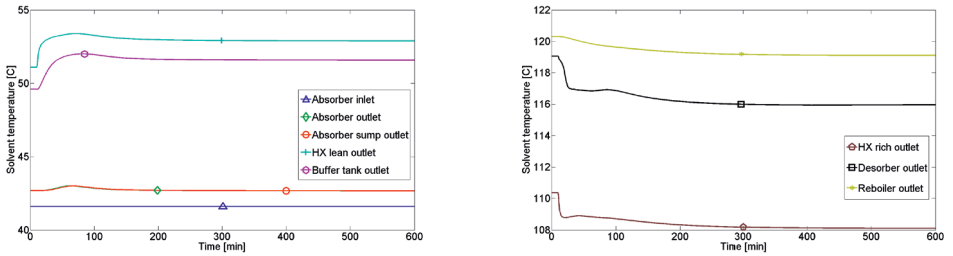

(a) (b)

Figure 6: Response in solvent temperatures for +20% set-point change in absorber inlet solvent flow rate.

An inverse response in rich CO_2 loading is observed in Figure 5a. This is caused by an initial decrease in rich CO_2 loading as the lean solvent flow rate is increased. However, once the change in solvent flow rate reaches the regeneration section, the lean solvent loading will start to increase as presented in Figure 5b. This will again cause the rich solvent loading to increase and therefore change in the opposite direction of the initial change. The dynamic profile will therefore switch from decreasing to increasing rich CO_2 loading, before it stabilizes at a level close to the initial.

Various ramp changes in solvent flow rate (-20% to +20%) are simulated and the results are presented in Figures 7-9. The changes are as previously introduced after 10 minutes and 1 minute is allowed to reach the final value. The

dead times (θ) and settling times (t_s) for different responses in the process are calculated and compared in Table 4.

For the response in solvent flow rate there are no observed dead time or change in settling time for the heat exchanger, according to Table 4, which corresponds to the effect of plug flow for incompressible fluids. A very small increase in dead time is however seen for the absorber and desorber (according to Table 4) which is related to changes in solvent hold-up when the disturbance in lean solvent flow rate is introduced. This effect is maximum 4 seconds for the simulated cases.

When comparing dead times and settling times for lean and rich CO_2 loadings, it is clear that the heat exchanger acts as a pure transport delay by adding significant dead time to the responses, while no change in settling time is observed. 13-20 minutes dead time for the cold side and 9-14 minutes for the hot side of the cross heat exchanger is observed depending on solvent flow rate. The observed dead time equals the residence time for heat exchanger and piping.

The settling time for absorbed CO_2 is 216-359 minutes for the simulated cases. An inverse response is also seen for the absorbed CO_2 in Figure 7, as it first increases/decreases for increased/decreased solvent flow rate, before it start to decrease/increase when the changes in lean loading (seen in Figure 9b) reaches the absorber. The response in desorbed CO_2 in Figure 8 adjust faster to a new steady state condition, compared to the absorbed CO_2. The settling time in this case are 11-20 minutes for decreased solvent flow rate and 98-136 minutes for increased flow rate.

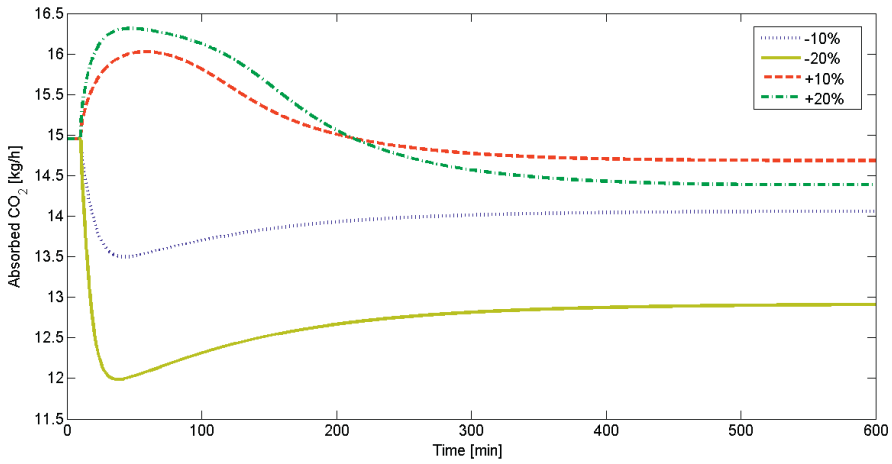

Figure 7: Response in absorbed CO_2 for set-point changes in solvent flow rate.

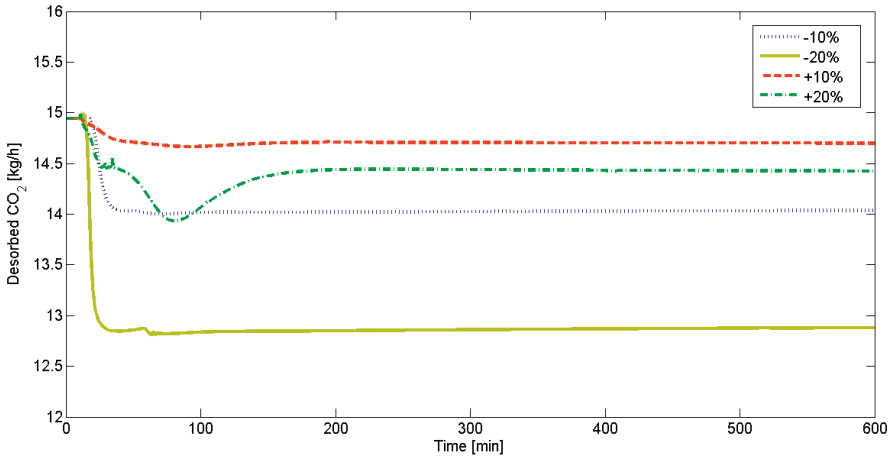

Figure 8: Response in desorbed CO_2 for set-point changes in solvent flow rate.

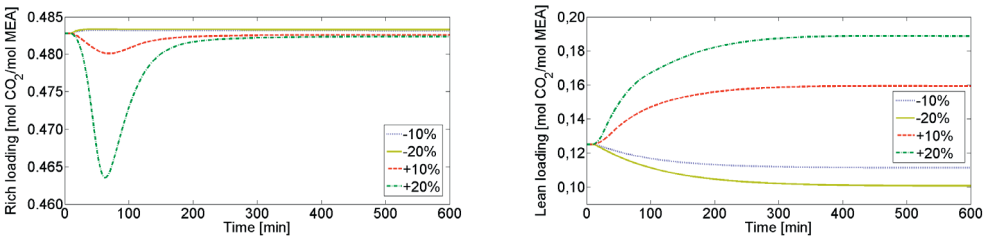

(a) (b)

Figure 9: Response in (a) rich CO_2 loadings and (b) lean CO_2 loadings for set-point changes in solvent flow rate.

Table 4: Calculated dead times (θ) and settling times (t_s) for set-point changes in solvent flow rate.

	Dead time (θ) [min]				Settling time (t_s) [min]			
Solvent flow rate	+20 %	+10 %	-10 %	-20 %	+20 %	+10 %	-10 %	-20 %
Performance								
CO_2 absorbed	0.07	0.07	0.07	0.07	355.36	359.35	237.16	216.35
CO_2 desorbed	0.07	0.10	0.10	0.07	136.37	97.90	20.40	11.26
Rich CO_2 loading								
absorber outlet	0.60	0.38	0.25	0.35	498.68	492.45	160.78	69.20
asorber sump outlet	2.43	1.40	0.55	0.65	500.92	495.90	166.05	76.17
desorber inlet	15.48	16.30	18.50	20.60	500.59	495.18	166.03	76.17
Lean CO_2 loading								
reboiler outlet	0.95	0.75	0.30	0.20	184.92	183.67	214.53	238.45
buffer tank inlet	10.10	10.75	12.68	14.07	185.02	183.73	214.54	238.45
buffer tank outlet	19.80	12.67	13.83	15.00	185.73	192.36	224.87	251.00
Flow rate								
absorber inlet	0.00	0.00	0.00	0.00	0.80	0.80	0.80	0.80
absorber outlet	0.06	0.06	0.06	0.06	0.67	0.67	0.69	0.69
asorber sump outlet	0.07	0.07	0.07	0.07	0.75	0.75	0.75	0.75
desorber inlet	0.07	0.07	0.07	0.07	0.75	0.75	0.75	0.75
desorber outlet	0.09	0.10	0.09	0.10	0.76	0.75	0.74	0.72
reboiler outlet	0.15	0.17	0.09	0.10	1.83	1.83	1.74	1.72
buffer tank inlet	0.15	0.17	0.09	0.10	1.83	1.83	1.74	1.72

5.2. Changes in reboiler duty

Four simulations with set-point changes in reboiler duty (-20% to +20%) are also performed, while the flue gas conditions and solvent flow rate are kept constant. The ramp changes are introduced after 10 minutes, and 1 minute is allowed to reach the final input value. The simulations are then continued for 18 hours to ensure that a new steady state condition is observed. The results are presented in Figures 10-12 and the calculated dead times (θ) and settling times (t_s) are presented in Table 5.

The settling time for absorbed CO_2 is 219-242 minutes for the simulated cases. For desorbed CO_2 it is only 1 minute for decreased reboiler duty and 18-27 minutes for increased reboiler duty. For the case of increased reboiler duty, the response in desorbed CO_2 has an overshoot as seen in Figure 11. The rich CO_2 loadings needs longer time to stabilize, as the settling time for the absorber outlet is 248-368 minutes, according to Table 5. However, it should be noted that the changes in rich CO_2 loading are very small for all cases, as seen in Figure 12a. Again, the effect of plug flow transportation is observed as the settling time for the response in outlet absorber sump and inlet desorber are identical, which corresponds to the cold side of the heat exchanger including piping. The same yield for the response in reboiler outlet and buffer tank inlet, which corresponds to the hot side of the heat exchanger including piping. The dead time is however, 17 and 11 minutes for cold side and hot side, respectively, which corresponds to the residence time of these parts of the process given the current flow rate. A quite considerate increase in settling time is however observed for the absorber when comparing the response in absorber outlet CO_2 loading to the inlet lean CO_2 loading. The flue gas flow rate and condition, solvent flow rate and inlet solvent temperature are in this case constant, and an increase of the settling time in CO_2 loading up to 161 minutes is observed, which can be linked to the inertia due to mass transfer and chemical reaction rates in the absorber column. However, as previously mentioned, the change in rich CO_2 loading is very small, thus the basis for comparison is limited.

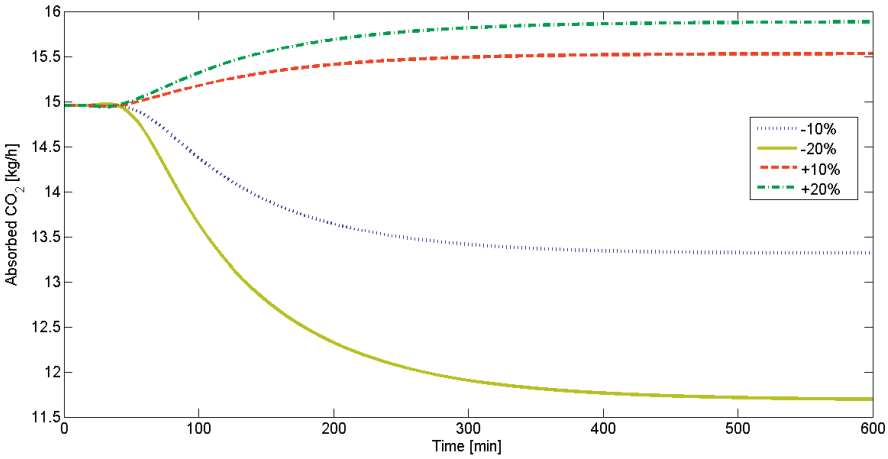

Figure 10: Response in absorbed CO_2 for set-point changes in reboiler duty.

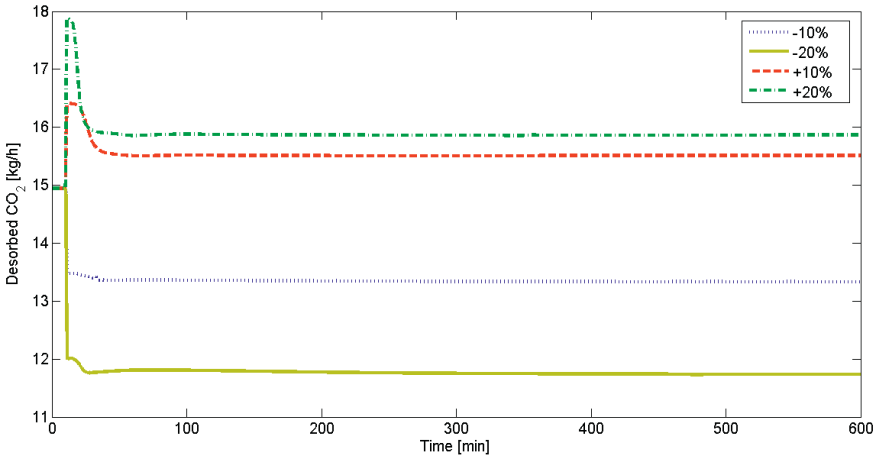

Figure 11: Response in desorbed CO_2 for set-point changes in reboiler duty.

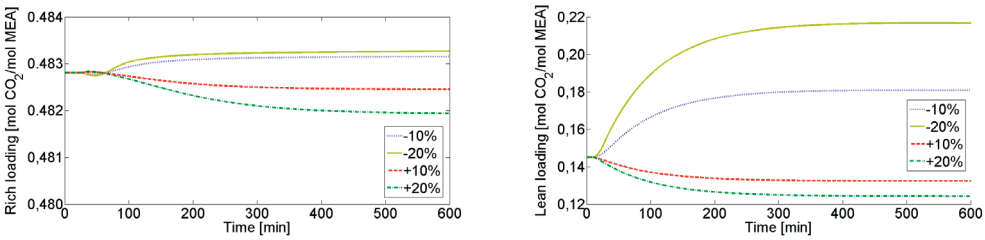

(a) (b)

Figure 12: Response in (a) rich CO_2 loadings and (b) lean CO_2 loadings for set-point changes in reboiler duty.

Table 5: Calculated dead times (θ) and settling times (t_s) for set-point changes in reboiler duty.

	Dead time (θ) [min]				Settling time (t_s) [min]			
Reboiler duty	+20 %	+10 %	-10 %	-20 %	+20 %	+10 %	-10 %	-20 %
Performance								
CO_2 absorbed	22.57	27.20	25.85	23.47	242.41	233.97	218.78	224.43
CO_2 desorbed	0.05	0.05	0.05	0.05	18.47	27.40	1.08	1.08
Rich CO_2 loading								
absorber outlet	31.03	32.73	40.53	39.12	353.59	313.84	248.30	368.05
asorber sump outlet	34.83	38.90	44.95	43.60	355.35	313.75	249.13	368.72
desorber inlet	51.75	56.45	61.77	60.37	355.37	313.80	249.13	368.75
Lean CO_2 loading								
reboiler outlet	0.55	0.55	0.60	0.65	194.48	195.22	195.68	194.28
buffer tank inlet	11.55	11.57	11.65	11.65	194.52	195.20	195.72	194.38
buffer tank outlet	13.80	14.10	15.05	14.23	205.88	205.73	204.62	206.94

5.3. *Changes in flue gas flow rate*

Four simulations with set-point changes in flue gas flow rate from -20% to +20% are also performed, while the lean solvent flow rate and reboiler duty are kept constant. The changes are as previously introduced as ramp changes after 10 minutes, where 1 minute is allowed to reach the final value. The simulations are continued for 18 hours to ensure a new steady state condition. The results are presented in Figures 13-16 and calculated dead times and settling times are presented in Table 6.

The absorbed CO_2 shown in Figure 13 stabilize very fast at a new steady state level. For increased flue gas flow rate, the final value is very close to the initial since the solvent loading capacity already is close to the limit. Thus almost no more CO_2 is absorbed after the set-point increase. The same results are is also seen for desorbed CO_2 in Figure 14 and for CO_2 loadings in Figure 16, where the response profiles for +10% and +20% set-point change keeps more or less constant. The CO_2 capture rate will naturally decrease for increased flue gas flow rate as seen in Figure 15. The settling times are 17 and 13 minutes for +20% and +10% set-point change, respectively. The residence time of the gas in the absorber column is less than 1 minute, while it for solvent is about 14 minutes. The additional time needed for stabilization of the response in absorbed CO_2 is probably linked to mass transfer and chemical reaction rates. This effect is up to 3 minutes in this case.

For decreased flue gas flow rate a decline in absorbed and desorbed CO_2 is observed, according to Figure 13 and 14. The CO_2 capture rate will however increase as seen in Figure 15, and the estimated settling times are 53 and 13 minutes for -10% and -20% set-point change, respectively.

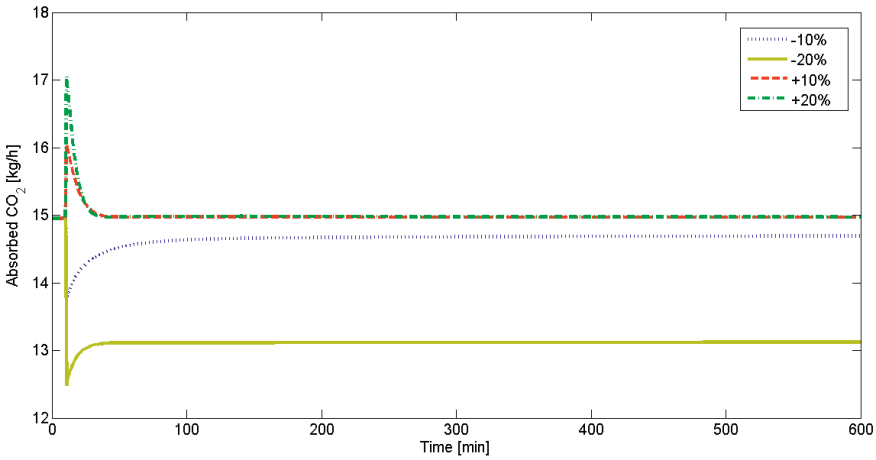

Figure 13: Response in absorbed CO_2 for set-point changes in flue gas flow rate.

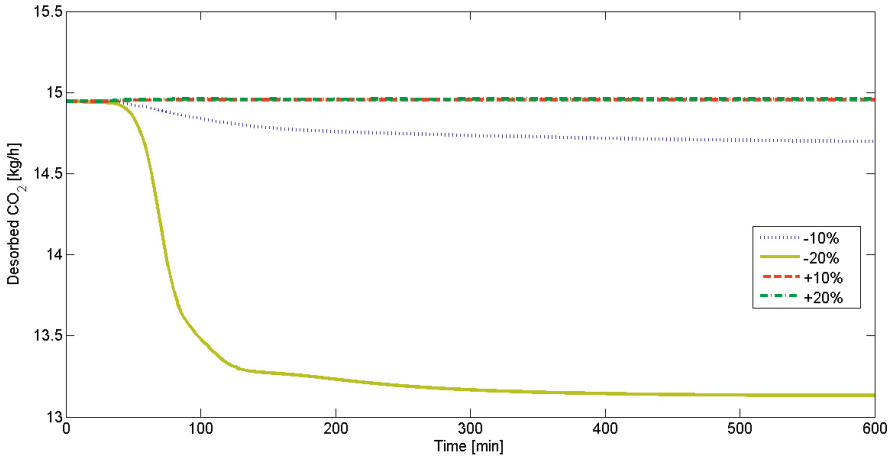

Figure 14: Response in desorbed CO_2 for set-point changes in flue gas flow rate.

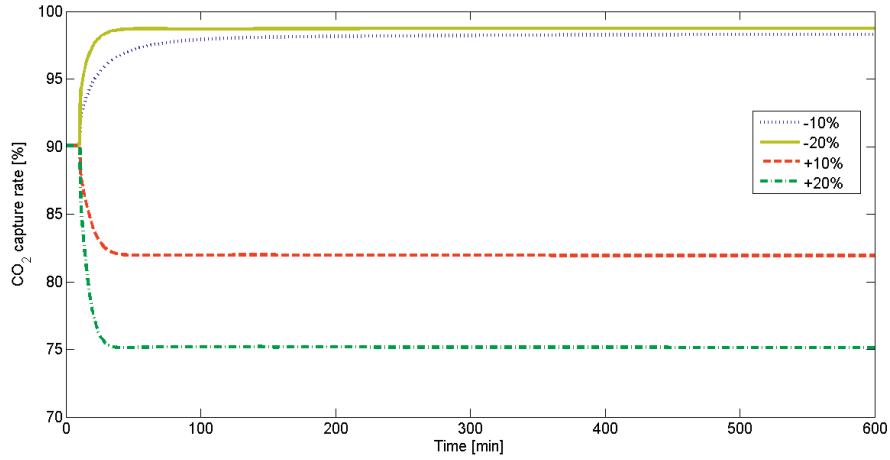

Figure 15: Response in CO_2 capture rate for set-point changes in flue gas flow rate.

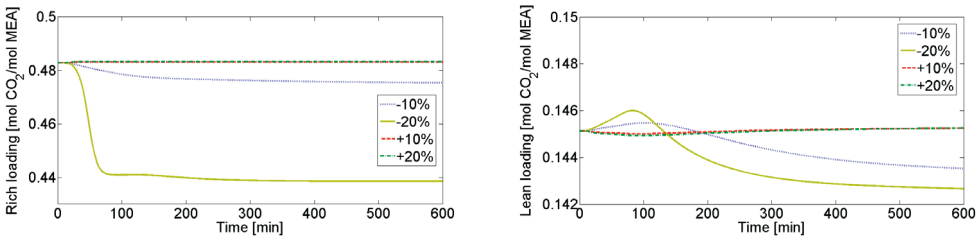

(a) (b)

Figure 16: Response in (a) rich CO_2 loadings and (b) lean CO_2 loadings for set-point changes in flue gas flow rate.

Table 6: Calculated dead times (θ) and settling times (t_s) for set-point changes in flue gas flow rate.

	Dead time (θ) [min]				Settling time (t_s) [min]			
Reboiler duty	+20 %	+10 %	-10 %	-20 %	+20 %	+10 %	-10 %	-20 %
Performance								
CO_2 capture rate	0.02	0.02	0.02	0.02	12.75	16.73	52.65	13.25
CO_2 absorbed			0.02	0.02			183.03	9.70
CO_2 desorbed			1.22	1.32			414.30	115.20
Rich CO_2 loading								
absorber outlet			0.78	2.03			335.24	54.35
asorber sump outlet			3.22	5.18			337.93	58.44
desorber inlet			19.63	21.82			338.15	58.61
Lean CO_2 loading								
reboiler outlet			1.27	0.95			606.26	438.35
buffer tank inlet			11.87	11.80			605.05	436.75
buffer tank outlet			13.00	13.63			639.93	544.44

6. Discussion

The Tiller pilot plant is used as basis for model parameter setting and equipment sizing in this work. The design of this plant resembles full-scale design with full column height, such that scale up of column diameters, vessel sizes and gas and liquid flow rates will give comparable residence times. It is therefore believed that the reported dead times and time constants also will reflect the dynamics of an industrial plant. The flow sheet in Figure 2 is identical to the lay out of the Tiller pilot plant, except the buffer tank level controller and MEA make-up controller that ensures constant MEA concentration. This was included in the model and simulations in order to give as good estimates of the time constants as possible and to enable isolation of the effects of the set-point changes only. It will not affect the results significantly as the make-up is very small and also performed in a pilot plant, manually.

Comparing set-point change responses and calculated time constants is a useful method in order to evaluate process dynamics. However, the data input to the different units does not act as step changes in this case because propagation through the process changes the response and thereby affects the input profiles. The dead time will naturally increase and the profile is smoothing out as the disturbance propagates through the process. However, by comparing a units input and output response profile, an image of how the unit contributes to changed dead time and/or time constant of the overall system can be drawn.

Solvent flow rates adjust very fast due to plug flow of incompressible fluids along with level control for all vessels. The stabilization time for flow rates are therefore within a couple of minutes. Temperatures and concentrations are more dependent on plug flow transport (which represent dead time), along with mass transfer and chemical reactions in column packing sections and will therefore need more time to stabilize. The stabilization time for CO_2 loadings is up to 8 hours depending on the disturbance introduced. This is mostly caused by mixing effects of large vessels, and larger solvent hold-ups will consequently demand longer stabilization time. However, the changes in rich CO_2 loading is in general very small. For temperatures, however, the cross heat exchanger contributes to an active connection between lean and rich side of the cross heat exchanger, and consequently the solvent does not have to be transported all the way through the system to stabilize. The connection between cold and hot side will give more rapid responses and shorter stabilization time.

The overall residence time of the system affects the stabilization time, but the fact that the process has recirculation of solvent will increase the time needed for stabilization even more. The overall residence is only 2-3 hours, but it is here proven that stabilization in CO_2 capture rate will require up to 6 hours, that is 2-3 times longer than the solvent residence time. Column mass transfer and chemical reaction rates may also hold inertia that affects the stabilization time. The simulation case with set-point changes in reboiler duty allows simulations that reflect the effect of mass and heat transfer rates and chemical reaction rates in the absorber, since the inlet and outlet loading profile can be compared more easily with more or less constant gas and solvent flow rates. The simulations indicate an absorber CO_2 loading settling time of 248-368 minutes which corresponds to an increase of 41-161 minutes compared to the inlet lean CO_2 loading. However, all changes in rich CO_2 loading are relatively small for changes in reboiler duty. The simulations

with set-point changes in flue gas flow rate shows a settling time of 13-53 minutes for the CO_2 capture rate. Increasing flue gas flow rate does not cause significant disturbances of the solvent as the lean and rich solvent loadings keeps stable, and the estimated settling time is in this case 13-17 minutes. The additional stabilization time is therefore up to 3 minutes longer than the absorber residence time, which is probably linked to mass and heat transfer and chemical reaction rates. It is not possible to predict similar estimates for the desorber, as desorber conditions depends both on dynamic effects of reboiler vapor and inlet solvent conditions. Additional effects will therefore contribute to the change in profile for the desorber column. A standalone desorber simulation with constant vapor inlet conditions will however allow such an estimate, but it is not really relevant as it has no physical meaning. Further, the desorber is usually operated close to equilibrium conditions, thus effects of mass transfer and chemical reaction rates are limited.

Overall, it seems like set-point changes in flue gas flow rate stabilize very fast as it does not disrupt the solvent dynamics significantly. Changes in reboiler duty does also allow faster stabilization than changes in flow rate. Even though the flow rates are able to adjust to the new condition very fast, this acts as a larger disturbance to the system.

7. Conclusion

This paper presents an examination of time constants related to set-point changes in flue gas flow rate, solvent flow rate and reboiler duty, which again are used to identify and describe the dominant dynamics of the process.

As expected, the mixing models (absorber sump, reboiler and buffer tank) introduce time constants that affect the dynamics of the overall system. The plug flow models (heat exchanger) contribute with some dead time, but no additional time constant is observed for these units. Plug flow units are therefore regarded as pure transport delays. For the absorber column, however, which is described by a plug flow model with chemical reaction and mass and heat transfer, some dynamic effect of chemical reaction and mass and heat transfer rates is observed. The magnitude of the effect depends on the disturbance introduced, but it is clearly not the most significant source of inertia. The simulation results and calculated dead times and time constants suggest that the main inertia of the process lies in the larger vessels like reboiler and buffer tank, along with piping and cross heat exchanger. The largest unit residence time in the process is clearly the reboiler according to Table 1, however this unit seem to adjust quite fast to changes due to tight control. The regeneration part of the process is also a quite complex system with two recirculation loops to the desorber column (condenser condensate to the top of the column and reboiler vapor to the bottom). This causes complex responses and dependencies which makes it fairly difficult to estimate time constants. However, the dynamics are still relatively fast. The simulations indicate that the absorber part of the process is somewhat slower.

Acknowledgments

This publication is produced with support from the BIGCCS Centre, performed under the Norwegian research program Centres for Environment-friendly Energy Research (FME). The authors acknowledge the following partners for their contributions: ConocoPhillips, Gassco AS, Shell Technology AS, Statoil Petroleum AS, TOTAL E&P Norge AS, GDF SUEZ, and the Research Council of Norway (193816/S60).

Contributions from the SOLVit project, financed by Gassnova and Aker Solutions, are also gratefully acknowledged.

Nomenclature

Symbol	Units	Description
a	$m^2\,m^{-3}$	Specific area
C_E	[-]	Constant
D	$m^2\,s^{-1}$	Mass diffusion coefficient
F	[-]	Factor
F	$kmol\,s^{-1}$	Molar flow
g	$m\,s^{-2}$	Gravitational acceleration
h	$m^3\,m^{-3}$	Hold-up
k	$m\,s^{-1}$	Film mass transfer coefficient
K_2		Correlation constant
m	$kg\,h^{-1}$	Absorbed amount
M	$kg\,kmol^{-1}$	Molar mass
P	kPa	Pressure
S	m	Side dimension of corrugation
t	s	Time
u	[-]	Non dimensional process input
u	$m\,s^{-1}$	Superficial velocity
x	[-]	Liquid mole fraction
y	[-]	Gas mole fraction
y	[-]	Non dimensional process output
z	m	Axial coordinate
Greek symbols		
α	$molCO_2/molMEA$	CO_2 loading
β	$^\circ$	angle with horizontal for falling film or corrugation channel
Δ		Change/difference

ε	$m^3\,m^{-3}$	Void fraction
γ	$^\circ$	contact angle between solid and liquid film
ρ	$kg\,m^{-3}$	Density
μ	$kg\,m^{-1}\,s^{-1}$	Dynamic viscosity
σ	$kg\,s^{-2}$	Surface tension
θ	min	Dead time

Subscripts

abs	absorber
des	desorber
g	gas
i	component
in	inlet
l	liquid
out	outlet
e	effective
s	settling
SE	surface enhancement
t	total hold-up due to effective wetted area
0	initial
∞	final
1_{st}	first order

Dimensionless groups

$Fr_L = \frac{u_l^2}{S_g}$	Froude number for liquid
$Re_L = \frac{u_l S \rho_l}{\mu_l}$	Reynold number for liquid
$We_L = \frac{u_l^2 \rho_l S}{\sigma}$	Weber number for liquid

Abbreviations

EC	Electrical effect controller
FC	Flow controller
LC	Level controller
PC	Pressure controller
TC	Temperature controller

References

Arce A, Mac Dowell N, Shah N, Vega LF. (2012). Flexible operation of solvent regeneration systems for CO2 capture processes using advanced control techniques: Towards operational cost minimisation. *International Journal of Greenhouse Gas Control*, 11:236–250.

Enaasen N, Tobiesen A, Kvamsdal HM, Hillestad M. (2013). Dynamic Modeling of the Solvent Regeneration Part of a CO_2 capture Plant. *Energy Procedia*, 37:2058–2065.

Faber R, Köpcke M, Beide O, Knudsen JK, Andersen J. (2011). Open-loop step responses for the MEA post-combustion capture process: Experimental results from the Esbjerg pilot plant *Energy Procedia*, 4:1427–1434.

Enaasen Flø N, Kvamsdal HM, Hillestad M. (2015). Dynamic model validation of the post-combustion CO_2 absorption process. *submitted to International Journal of Greenhouse Gas Control*

Chalmers H and Gibbins J. (2007). Initial evaluation of the impact of post-combustion capture of carbon dioxide on supercritical pulverised coal power plant part load performance. *Fuel*, 86:2109–2123.

Chalmers H, Lucquiaud M, Gibbins J, Leach M. (2009). Flexible Operation of Coal Fired Power Plants with Postcombustion Capture of Carbon Dioxide. *Journal of Environmental Engineering*, 135:449–458.

Harun N, Nittaya T, Douglas PL, Croiset E, Richardez-Sandoval LA. (2012). Dynamic simulation of MEA absorption process for CO_2 capture from power plants. *International Journal of Greenhouse Gas Control*, 10:295–309.

Kvamsdal HM, Jakobsen JP, Hoff KA. (2009). Dynamic Modeling and Simulation of CO_2 absorber column for post-combustion CO_2 capture. *Chemical Engineering and Processing*, 48(1):135–144.

Lawal A, Wang M, Stephenson P, Koumpouras G, Yeung H. (2010). Dynamic modelling and analysis of post-combustion CO_2 chemical absorption for coal-fired power plants. *Fuel*, 89(10):2791–2801.

Lawal A, Wang M, Stephenson P, Yeung, H. (2010). Dynamic modelling of CO_2 absorption for post combustion capture in coal-fired power plants. *Fuel*, 88(12):2455–2462.

Rocha JA, Bravo JL, Fair JR. (1993). Distillation Columns Containing Structured Packings: A Comprehensive Model for Their Performance. 1. Hydraulic Models. *Industrial & Engineering Chemistry Research*, 32:641–651.

Rocha JA, Bravo JL, Fair JR. (1996). Distillation Columns Containing Structured Packings: A Comprehensive Model for Their Performance. 2. Mass-Transfer Model. *Industrial & Engineering Chemistry Research*, 35:1660–1667.

Singh, SK (2009). Process control: Concepts, Dynamics And Applications. PHI Learning Private Ltd, New Delhi, India.

Tobiesen AF, Hillestad M, Kvamsdal HM, Chikuwa A. (2012). A general column model in CO2SIM for transient modelling of CO_2 absorption processes. *Energy Procedia*, 23:129–139.

Ziaii S, Rochelle GT, Edgar TF. (2009). Dynamic modeling to minimize energy use for CO_2 capture in power plants by aqueous monoethanolamine. *Industrial & Engineering Chemistry Research*, 48(13):98–101.

C.7 Paper G: Dynamic Simulation of Post-combustion CO_2 Capture for Flexible Operation of the Brindisi Pilot Plant

Dynamic Simulation of Post-combustion CO_2 Capture for Flexible Operation of the Brindisi Pilot Plant

Nina Enaasen Flø[a,*], Hanne Marie Kvamsdal[b], Magne Hillestad[a]

[a] *Department of Chemical Engineering, NTNU, Sem Sælandsvei 4, N-7491 Trondheim, Norway*
[b] *Department of CO_2 Capture Process Technology, SINTEF Materials and Chemistry, Post Office Box 4760, Sluppen, N-7465 Trondheim, Norway*

Abstract

Dynamic modeling of post combustion CO_2 capture has gained increasing attention the recent years. One of the main motivations behind this drive is the limited knowledge on CCS' operational flexibility according to variations in electricity demand and prices. This work presents an evaluation of various flexible operating modes through dynamic simulations using the K-Spice® general simulation tool. The modes evaluated are; load following, exhaust gas venting, varying solvent regeneration and solvent storage. Solvent storage as operating mode gives a large potential for flexible operation with the possibility of maintaining 90 % capture rate over the whole 24 hour simulated period. Two large solvent storage tanks are however required as part of the process configuration in order to realize this kind of flexible operation. Exhaust gas venting and varying solvent regeneration does not require any additional process equipment, but their potential is limited to the plants maximum capture capacity during off-peak electricity price periods in order to reach an average capture rate of 90 %. Exhaust gas venting seems to be the favorable option of the latter two.

Keywords: Post combustion CO_2 capture, process dynamics, operational flexibility

1. Introduction

Carbon capture and storage (CCS) has the potential to significantly reduce the amount of CO_2 emitted from fossil fuel fired power plants. However, its operation requires steam extraction for solvent regeneration and electricity for operation of flue gas blowers, solvent pumps and CO_2 compressors, which reduces the power plants net electrical output and thereby decreases its profit. The total efficiency reduction related to CO_2 capture is estimated to 8.6-9.2 percentage points for coal fired power plants (Davison , 2006), where steam for solvent regeneration accounts for up to 2/3 of the overall energy penalty (Chalmers et al., 2009). Optimal operation of the carbon capture unit is therefore an absolute necessity in order to minimize the power plant energy penalty related to carbon capture.

*Corresponding author. Tel.:+47 99478919.
Email addresses: enaasen@ntnu.no (Nina Enaasen Flø), hanne.kvamsdal@sintef.no (Hanne Marie Kvamsdal), magne.hillestad@ntnu.no (Magne Hillestad)

The power station might undergo frequent load changes according to a shifting energy demand. The electricity market may also vary quite significantly during a day, week, season or year, which motivates flexible operating modes in an attempt to reduce the time average energy penalty. By applying flexible CO_2 capture, the CO_2 capture rate can be manipulated to maximize operating profits based on the trade-off between CO_2 emission cost and the current electricity price.

The knowledge on CCS' ability for flexible operation is quite limited due to lack of large scale operational experimental experience. Thus this has been one of the main motivations behind the increasing degree of dynamic process model development the recent years. A recent review by Bui et al. (2015) gives an overview of the work on dynamic modeling and simulation of the post-combustion CO_2 absorption process. The authors points out that dynamic model validation is needed to ensure model reliability both at steady state conditions and in transient mode, which has also been emphasized by other authors (Chikukwa et al., 2012) (Biliyok et al., 2012). However, lack of dynamic data for proper model validation has remained problematic. Further, utilization of the dynamic models for simulations of relevant flexible operating modes is barely demonstrated in the literature, and this is one of the main suggestions for future work by Bui et al. (2015).

Besides techno-economic studies like Chalmers et al. (2012) and Cohen et al. (2010) the published material on flexibility is in general scarce. Techno-economic evaluations are useful in understanding the overall costs and benefits of realizing CCS and highlights the overall plant performance indicators. Recent studies also considers possible improvements with flexible operation by exploiting the variations in electricity demand and prices (Wiley et al., 2011) (Chalmers et al., 2012) (Cohen et al., 2010). However, such analyses typically ignore operating dynamics and transient performance of the CCS plant. For instance it is suggested that the capture unit can be completely switch off during peak electricity price periods, and later switch on when prices are normalized in a cyclic manner (Wiley et al., 2011) (Cohen et al., 2010). However, simulations of frequent process start-ups and shut downs and analysis of the related system response times are barely reported in the literature. On/off operation of the regeneration section may be challenging in practice, especially in a frequent manner. In the paper by Mangiaracina et al. (2014) on/off operation is demonstrated as part of a pilot plant campaign considering flexibility in the Brindisi pilot plant. The results shows in fact that significant amount of time is required for the regeneration part of the process to re-pressurize and stabilize after start-up.

Garðarsdóttir et al. (2015) applied a dynamic amine-based CO_2 capture model to investigate the transient behavior of the absorption process during power plant load changes. Part load and peak load operation was simulated in their study, and various control strategies were evaluated. Controlling the solvent flow rate and steam flow rate to the reboiler to maintain constant L/G and lean loading was concluded to improve the capture efficiency at part load operation. The authors also concluded that the response time of the system was generally lower in the cases where the solvent flow rate was controlled.

Lin et al. (2012) introduced a new strategy for flexible operation during peak electricity price periods allowing constant hydraulic conditions in the absorber and desorber columns at all times. Instead of varying both the lean

solvent flow rate and reboiler duty, they proposed a strategy with constant lean solvent flow rate and varying lean solvent loading. The gas flow through the stripper will naturally change as the reboiler duty is increased during off-peak periods. However, by recirculating part of the produced CO_2 to the bottom of the desorber, the authors claimed to stabilize the desorber hydraulics and keep constant L/G at all times. This strategy was compared to the conventional strategy of varying lean solvent flow, and satisfying results with respect to capture performance was presented. However, the authors did not demonstrate any operational challenges for the conventional strategy of varying lean solvent flow for the simulated case, nor was energy performance calculations included in this study, as one would expect a higher energy consumption to maintain the desired capture rate at suboptimal conditions (higher lean loadings).

Mac Dowell and Shah (2015) responded to the request of Bui et al. (2015) for flexibility simulations and performed a thorough technical simulation and economical optimization study of four various flexible operating modes for a super-critical coal-fired power plant integrated with an amine-based CO_2 capture process. The capture model includes dynamic unit models for packed column, absorber sump, reboiler and condenser. A steady state power plant model with varying efficiency based on load factor and a steam cycle model that estimates the available steam at each operating point is also developed. This allows optimization of the integrated power generation process with CCS. However, the capture plant model used in their study is not validated against dynamic data. Based on their simulations, the authors were able to suggest the optimal operating mode for a specific multi-period case based on a short run marginal cost profitability perspective.

In this work a dynamic process model developed in K-Spice® general simulation tool is used to evaluate various flexible operating modes from an operational and dynamic performance perspective. The model is previously validated against dynamic pilot plant data from the Brindisi pilot plant. The validation study is presented in Enaasen et al. (2014) and proves that the model is able to predict satisfying transient behavior when step changes in flue gas flow rate, solvent flow rate and reboiler duty is superimposed to the system at steady state.

The operating mode of on/off regeneration and solvent storage was tested experimentally in the Brinsidi pilot plant as part of a campaign on flexibility within the OCTAVIUS project (Mangiaracina et al., 2014). However, by performing dynamic simulations using the K-Spice model, additional flexible operating modes are investigated. Based on simple basic control of solvent flow rate and reboiler duty, possible daily operation plans are suggested with the objective of reducing the time average energy penalty for solvent regeneration, while maintaining close to 90 % average capture rate. This paper presents 24 hour dynamic simulation results and performance data during four various modes of flexible operation according to hypothetical variations in electricity demand and prices. The main focus of these simulations is on operational performance. Economic analysis are not conducted, however, the possible steam savings during electricity price intensive periods is evaluated, which gives an indication of the potential of the various flexible operating modes.

2. Flexible operating modes

The key motivation of flexible operation of power plants is related to variations in the electricity demand and price market. In the case of varying electricity generation, the power station will operate at varying loads, which the capture plant will need to follow. This type of operation is referred to as load following. A hypothetical scenario where the power station is ramped down to 70 % load during 3 hours at night time according to Figure 1a is studied in this work. The load change is done gradually, where the ramping down is started at 10 pm, 60 % load is reached at 2 am and continued until 5 am. Ramping up is started at 5 am, reaching full load again at 7 am in the morning.

In the case of varying electricity prices, flexible operation can be beneficial in order to manipulate the economic penalty of carbon capture. During peak electricity price periods it could be economical to utilize more steam for power generation, while spending more on CCS during off-peak electricity price periods. In this case a power plant operating at full load is considered, while the capture plant is ramped up and down according to a hypothetical daily electricity price profile as illustrated in Figure 1b. The simulated ramping rate is in this case 2% per min, and the electricity price intensive periods lasts for 3 hours in the evening and 2 hours in the morning.

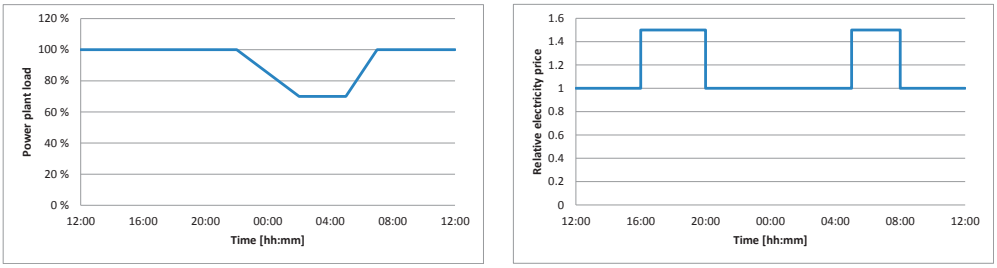

(a) Power plant load factor during part load operation

(b) Daily variations in electricity price

Figure 1: Motivation for flexible operating modes.

Three different operating modes are considered in a varying electricity market in order to assess the possibilities of increasing the process' overall profit. In the following simulations, a constant total amount of steam for regeneration is provided in the three cases, but the distribution in time may vary to reduce the steam consumption in electricity price intensive periods. The following modes are considered:

- Exhaust gas venting, where a fraction of the power station exhaust gas is vented during peak electricity price periods, allowing a momentary CO_2 capture rate below 90 %. The CO_2 capture must catch up during off-peak periods by operating the plant at conditions which increases the capture rates above 90 %.
- Varying degree of solvent regeneration, where the steam rate utilized for solvent regeneration is decreased during peak electricity price periods. CO_2 is allowed to accumulate in the solvent during these hours, while the solvent will be regenerated more deeply when the electricity prices normalizes. The momentary CO_2 capture rate will decrease

below 90 % during peak price periods, which means that the steam rate must be increased during off-peak periods to maintain an average capture rate of 90 %.

- Solvent storage or intermittent stripping, where a rich solvent tank is utilized to store fractions of the solvent during peak electricity price periods, while regenerating at a later stage when electricity is less expensive. This operating mode will also require a lean solvent tank to store the regenerated solvent which will be utilized in peak electricity price periods.

Details about the load following mode and the three other flexible modes of operation related to variations in the electricity price market are presented in Table 1 and Figure 2.

Table 1: Flexible operating modes

	Load following	Exhaust gas venting	Varying solvent regeneration	Solvent storage
Flue gas rate	variable	variable	100%	100%
Lean solvent rate	variable	variable	100%	100%
Rich solvent rate	-	-	-	variable
Steam rate	variable	variable	variable	variable
Lean CO_2 loading	constant	constant	variable	constant
CO_2 capture rate	constant	variable	variable	constant
Produced CO_2	variable	variable	variable	variable

3. Dynamic process model

The Brindisi pilot plant is used as basis for a dynamic model developed in K-spice® general simulation tool. The details of the Brindisi pilot plant is described in Mangiaracina et al. (2014) and the K-spice model is presented in Enaasen et al. (2014). Only a short summary is included in this paper.

The Brindisi pilot plant is a fully instrumented relatively large post-combustion CO_2 absorption pilot plant based on amines that has been realized by ENEL in Brindisi, Italy. It is attached to a full scale coal-fired power plant operated by ENEL. The capture plant is designed for 10 000 Nm^3/h exhaust gas (which corresponds to about 0.45 % of the total 660 MW power plant exhaust gas), capturing about 2.0 ton/h of CO_2. The pilot plant can handle flue gas flow rates up to 12 000 Nm^3/h and the maximum CO_2 production capacity is 2500 kg/h. The solvent flow rate can be varied between 20 - 80 m^3/h. Table 2 shows the nominal performance indicators of the Brindisi pilot plant, and a flow sheet is illustrated in Figure 3.

K-spice® is an advanced dynamic process simulator developed by Kongsberg Oil & Gas Technologies which is designed for simulations of oil and gas processes including natural gas treatment. It has embedded a powerful library of process units such as mixing tanks, heat exchangers, absorption column sections as well as piping, pumps, valves

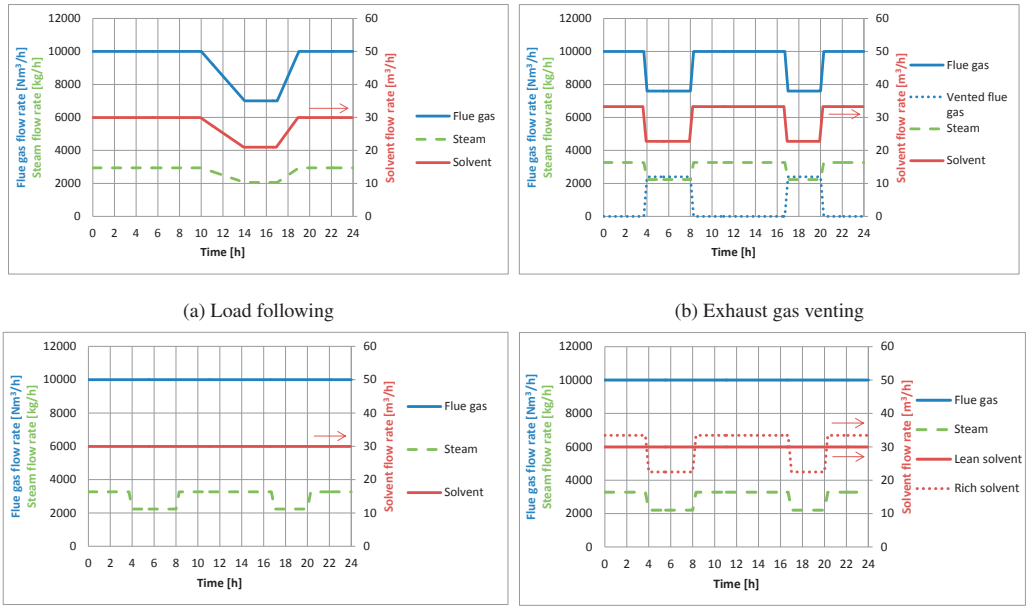

(a) Load following

(b) Exhaust gas venting

(c) Varying solvent regeneration

(d) Solvent storage

Figure 2: Flexible operating modes

etc. The library also contains basic instrumentation and control units. This library is utilized to define a process model based on the process flow sheet given in Figure 3. The absorber and desorber columns are modeled as packed sections.

Thermodynamic calculations are based on table look-ups that provides required information about the phase equilibrium. An add-on reaction set module connected to each packing section takes into account the effect of chemical reaction and mass transfer rates. This module acts as a secondary look-up table for the CO_2-MEA equilibrium and provides all necessary information (solubility data, mass transfer rates and enhancement factor) in order to predict the mass interface flux given the current process conditions, according to the rate based approach for mass transfer calculation. A table look-up for heat of reaction is also provided.

The Brindisi pilot plant has two large solvent storage tanks (PV-776/777), both situated at the lean solvent side of the process. Due to the location of these tanks, the pilot plant is not suited for a continuous solvent storage operating mode. Rich solvent meant for storage has to be passed through the desorber to reach the storage tank, while it later for regeneration has to be passed through the absorber to reach the stripper. Thus, the desorber has to be switch off for storing rich solvent, and likewise the absorber has to be switched off during regeneration of stored rich solvent as described in (Mangiaracina et al., 2014). For the purpose of simulation of solvent storage in continuous mode, the model is therefore extended with another storage tank for rich solvent, equivalent to the lean solvent storage tanks (PV-776/777) illustrated in Figure 3. The rich solvent storage tank is located between the rich solvent pump (PC-561)

and the cross heat-exchanger (SC-629X).

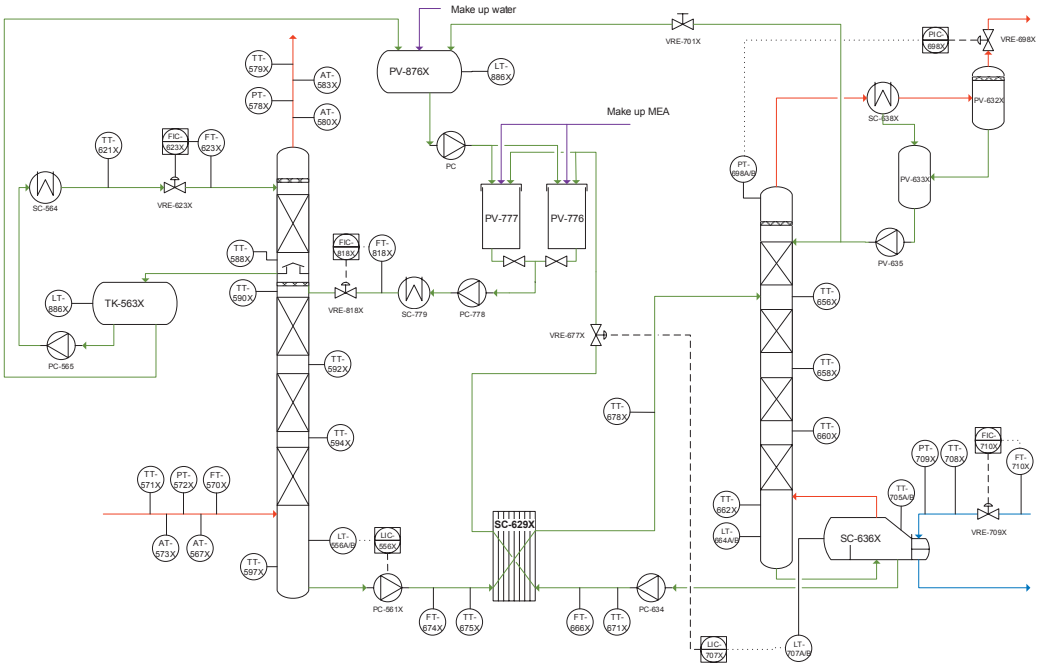

Figure 3: A schematic overview of the Brindisi pilot plant

Table 2: Brindisi pilot plant - key performance indicators (Mangiaracina et al., 2014)

Flue gas flow rate	10 000	Nm^3/h
CO_2 inlet concentration	11-12	vol%
Solvent flow rate	30	m^3/h
Amine	MEA	
Solvent concentration	30	wt%
Steam flow	2900	kg/h
CO_2 production	2000	kg/h

4. Simulation results

4.1. Base case

A steady state base case of 90 % capture rate at design-point conditions is established for reference. The conditions given in Table 3 corresponds to the optimal (square) point in Figure 4 which gives the minimum energy requirement of 3.68 MJ/kg CO_2.

Table 3: Brindisi pilot plant - base case simulations

Flue gas flow rate	10 000	Nm^3/h
CO_2 inlet concentration	11.4	dry vol%
Solvent flow rate	30	m^3/h
MEA concentration	30	wt%
Steam flow rate	2941.6	kg/h

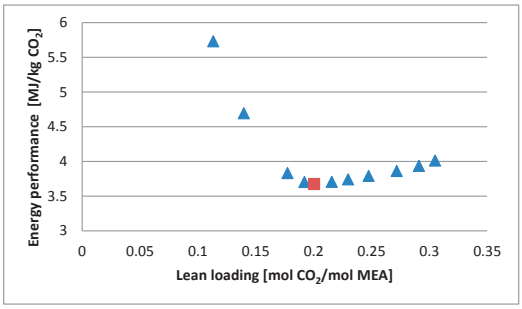

Figure 4: Energy performance as function of operating point with 90 % capture rate.

4.2. Load following

A scenario of load following capture plant operation according to Figure 1a is simulated by the K-Spice model. The solvent flow rate is in this case controlled proportionally according to the flue gas flow rate and the steam flow rate is controlled proportionally according to the solvent flow rate as illustrated in Figure 2a. The results are presented in the following.

The instantaneous and time average capture rate is presented in Figure 5a. The instantaneous capture rate maintains more or less constant during the whole period, with a small increase during part load operation. The 24 hour average CO_2 capture rate is therefore 90.2 %. The slightly higher capture rate at part load operation is caused by increased residence time and heat transfer in the cross heat exchanger.

A slightly lower lean loading and higher rich loading is seen at part load operation in Figure 5b. This is caused by increased heat transfer in the cross heat exchanger and longer solvent residence time in the absorber column. The

produced CO_2 illustrated in Figure 5c shows a response according to the amount of steam provided to the reboiler. The response is fast and the process is able to stabilize at both part and full load operation.

The overall energy performance is illustrated in Figure 5d and the 24 hour average energy consumption is 3.67 MJ/kg CO_2. This is slightly lower than base case caused by the slightly increased capture rate at part load operation.

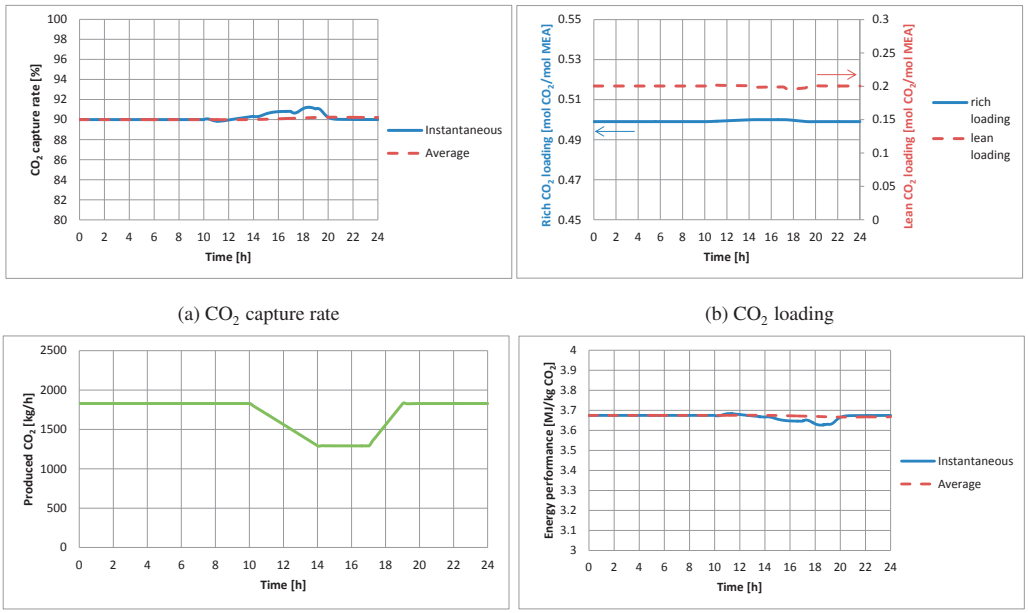

(a) CO_2 capture rate

(b) CO_2 loading

(c) Produced CO_2

(d) Energy performance

Figure 5: Load following

4.3. Exhaust gas venting

Exhaust gas venting, where a fraction of the power station exhaust gas is vented during peak electricity price periods, according to Figure 1b has the proposed production plan presented in Figure 2b. In this case the vent fraction is 24%, which means that the solvent flow rate and reboiler duty also is reduced by 24 % in this period. The solvent flow rate and reboiler duty is increased to 111% when the electricity price normalizes and all the flue gas is directed through the absorber. This scenario is simulated and the results are presented in Figure 6.

The CO_2 capture rate presented in Figure 6a shows a 24 hour average of 89.5 %, which is slightly lower than 90 % due to partly off-design operation. Only small changes in lean and rich CO_2 loadings is seen in Figure 6b. The rich loading is slightly higher in peak hours due to part load absorber operation which causes increased solvent residence time in the packing.

The produced CO_2 illustrated in Figure 6c follows the amount of steam provided to the reboiler. Small inverse responses are observed just at the time of change in reboiler duty. The desorber gas flow changes instantaneously when the reboiler duty is changed, and it takes some time before the desorber L/G will adjust. This does however not seem to cause operational problems.

The 24 hour average energy consumption is 3.69 MJ/kg CO_2 as indicated in Figure 6d, which is only slightly higher than base case. The total amount of steam saved during peak electricity price periods is, however, 4950 kg which corresponds to 3107 kWh. This means that the additional steam available for generation of electricity during peak electricity price periods is 23.9 %. The total amount of steam required during the whole 24 hour period equals the amount required in base case, which means that a larger amount of steam is required in off electricity price periods.

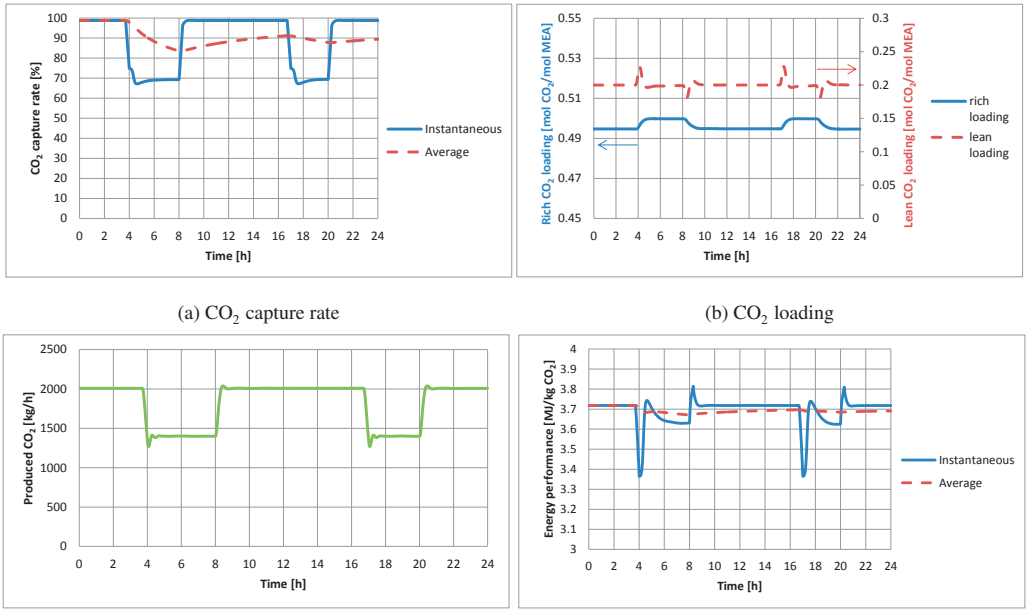

(a) CO_2 capture rate

(b) CO_2 loading

(c) Produced CO_2

(d) Energy performance

Figure 6: Exhaust gas venting

Exhaust gas venting as a mode of flexible operation seems to work satisfactory and is easy to conduct without process modifications. This mode is, however, limited to the maximum CO_2 capture rate at off-peak electricity price periods in order to reach average 90 % capture rate.

4.4. Varying solvent regeneration

In the varying degree of solvent regeneration mode, only the steam rate utilized for solvent regeneration is decreased during peak electricity price periods. This will keep the absorber hydraulics constant. The production plan is

illustrated in Figure 2c where the steam rate to the reboiler is decreased by 24 % in electricity price intensive periods and increased to 111 % when the prices normalizes. The results are presented in the following.

The 24 hour average CO_2 capture rate presented in Figure 7a is 87.2 %, slightly lower than 90 % due to partly off-design and partly suboptimal operation (lower and higher lean loadings). Large variations in lean loading is seen in Figure 7b, which causes slower dynamic responses compared to the exhaust gas venting operating mode. As seen in the figure, the mixing effects of the buffer tank delays the response in lean loading.

The produced CO_2 response shown in Figure 7c is fast and follows the amount of steam provided to the reboiler. Small inverse responses are also seen in this case at the time of load chnage.

The 24 hour average energy consumption is 3.80 MJ/kg CO_2, which is higher than base case due to partly suboptimal operation (higher lean loadings).

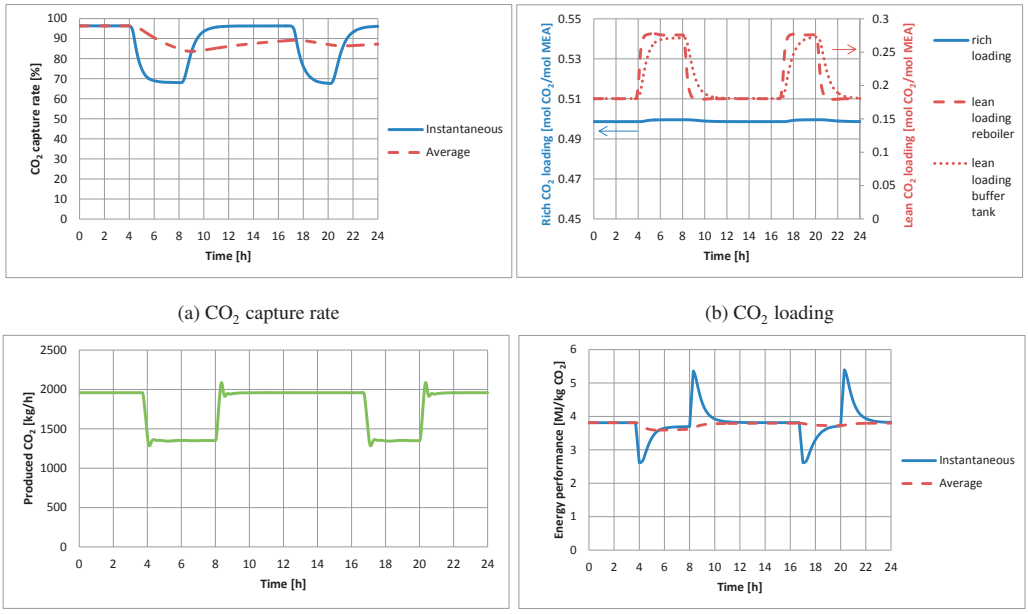

(a) CO_2 capture rate

(b) CO_2 loading

(c) Produced CO_2

(d) Energy performance

Figure 7: Varying solvent regeneration

The total amount of steam saved during peak electricity price periods is 4950 kg which corresponds to 3107 kWh. This means that the additional steam available for generation of electricity during peak electricity price periods is 23.9 %, as for the exhaust gas venting mode.

The mode of varying solvent regeneration seems to work well and is easy to conduct, however, as for flue gas venting this method is also limited to the maximum CO_2 capture rate at off-electricity peak periods in order to reach close to 90 % capture rate in average. The mode of exhaust gas venting performs slightly better due to operation closer

to optimum even at higher capture rates.

4.5. Solvent storage (intermittent stripping)

In the operating mode of solvent storage, fractions of the rich solvent is routed to a solvent storage tank during peak electricity price periods, while it is regenerated at a later stage when the electricity is less expensive. The production plan is illustrated in Figure 2d where 25% solvent is stored during peak electricity price periods. The desorber load (rich solvent flow rate and steam rate to reboiler) is therefore increased to 112% in off-peak electricity price periods in order to regenerate the excess rich solvent.

The 24 hour average in CO_2 capture rate presented in Figure 8a is 90.1 %. Lean and rich CO_2 loadings are kept more or less constant during the whole simulation time as seen in Figure 8b. The produced CO_2 response as shown in Figure 8c is fast and follows the amount of steam provided to the reboiler, and the 24 hour average energy consumption is 3.67 MJ/kg CO_2.

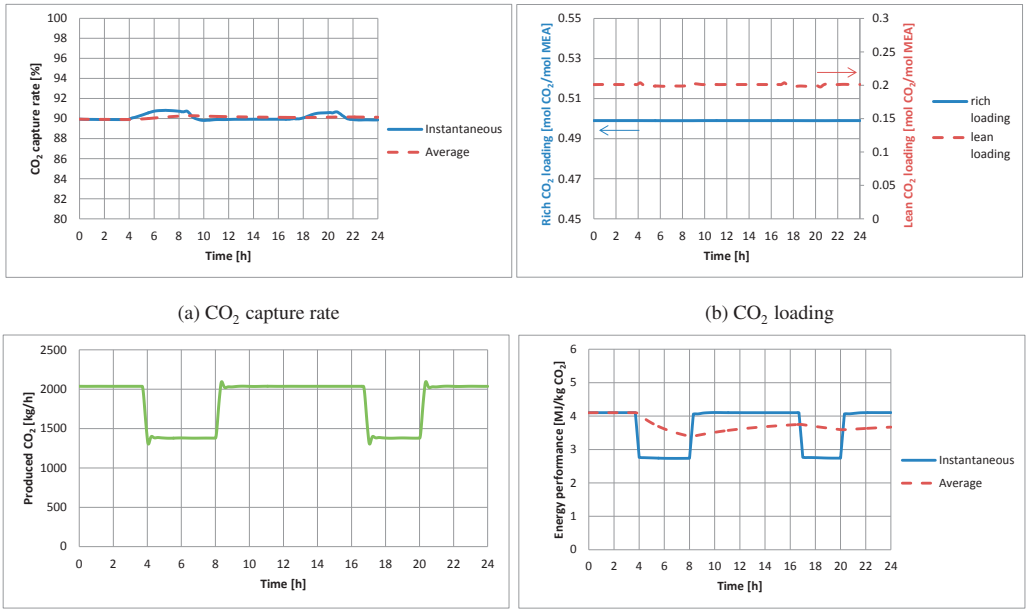

(a) CO_2 capture rate

(b) CO_2 loading

(c) Produced CO_2

(d) Energy performance

Figure 8: Solvent storage

The mode of solvent storage works very well. The capture and energy performances is equal or even slightly improved compared to base case. The total amount of steam saved during peak electricity price periods is 5149 kg which corresponds to 3232 kWh. This means that the additional steam available for generation of electricity during peak electricity price periods is 25 %. However, two large storage tanks are needed in order to conduct this operation

plan, and for 25 % storage a total storage volume of 2x50 m^3 is required. Two tanks of 60 m^3 was utilized in these simulations (to give some extra buffer), and the time varying level of the two tanks is presented in Figure 9.

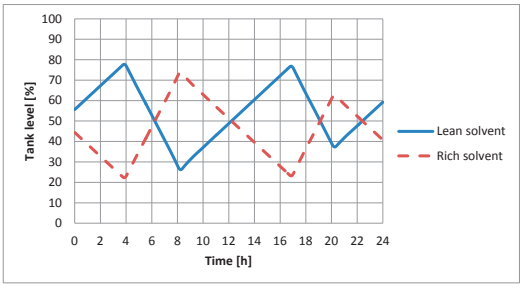

Figure 9: Solvent tank level.

The operating mode is only limited by the solvent storage tanks capacity and regeneration section capacity and ability to operate at part load.

5. Discussion

In this work, various flexible operating modes are assessed through dynamic simulations using K-Spice® general simulation tool. Part load operation, where the power plant is operated at a lower load factor for a given period of time and the capture plant is operated in a load following manner, is one of the modes that are evaluated. Simulations show that the process reacts fast to load changes and is able to stabilize at both part and full load operation. A small increase in the capture rate performance is seen during part load operation which is related to increased heat transfer in the cross heat exchanger and increased solvent residence time in the absorber, allowing lower lean loadings and higher rich loadings, respectively.

Three other scenarios of flexible operation are simulated with the objective of reducing the steam consumption during electricity price intensive periods, while still aiming for 90 % average capture rate. This will allow a larger amount of steam for electricity generation during periods where it is more economical. Only basic control of solvent flow rate and reboiler duty is utilized in the simulations, and no online optimization of the dynamic behavior is performed. However, the potential of the three flexible operating modes is demonstrated and shows to be promising. Only the mode of solvent storage was able to reach the average 90 % capture rate requirement, but the performance of the other two was also close to 90% even with partly off-design absorber operation. Especially the mode of exhaust gas venting has a good potential in reaching 90 % average capture rate by allowing just a small extra amount of steam to the reboiler in off-peak electricity price periods.

As previously mentioned, basic control of solvent and steam flow rates is applied in these simulations. However, as seen for the exhaust gas venting and varying regeneration options, this may lead to suboptimal conditions during off-design operation. An advanced control system like model-predictive-control (MPC) would allow off-design operation

to be performed more optimal and efficiently. In practice a combination of the exhaust gas venting and varying regeneration mode could be more optimal where both the solvent flow rate and steam rate to the reboiler is controlled to set the optimal lean loading for the given conditions and electricity price. Further, a simple predictive electricity price scenario is considered in this study, where the solvent and steam flow rates are set based on an operation plan of relative proportional control. However, for a more realistic and complex scenario of electricity price variations, MPC will have clear benefits in reaching possible operational profit improvements.

For the scenario with exhaust gas venting the lean CO_2 loading keeps more or less constant during the whole simulation time, however, the absorber packing hold-up will be disturbed. For varying degree of solvent regeneration, the absorber L/G will remain constant, but the lean loading will vary in time. The simulations indicate that the latter mode will give a larger disturbance of the overall system, and slower dynamic responses. Further, shifting hydraulic conditions did not seem to cause any significant operational problems, as was the main concern of Lin et al. (2012). This coincides with the operational experience of the Brindisi pilot plant. In fact, operating at lower lean loadings may cause other operational challenges like solvent flashing in the cross heat exchanger (Mangiaracina et al., 2014).

Operating the regeneration section in a cyclic on/off manner as suggested by (Cohen et al., 2010) may lead to significant re-pressurization and stabilization time as described by Mangiaracina et al. (2014). A more realistic approach will be to only store part of the solvent and avoid complete shut-down of the regeneration section. The mode of solvent storage is then only limited by the solvent storage capacity and the regeneration sections maximum capacity and part load operational limits. In the present simulations 25 % solvent storage was evaluated, which requires an available storage volume of 2x50 m^3. A scale-up to full size capture plant connected to a 660 MW coal fired power plant corresponds to 2x11100 m^3 of solvent capacity. The two large storage tanks and the additional amount of solvent required entails extensive additional capital cost. The solvent storage option should therefore be evaluated economically to give a fair basis for comparison to the other suggested modes. This is outside the scope of the present study. However, when comparing to the techno-economic evaluation of Mac Dowell and Shah (2015) for a similar power plant and storage capacity, a 4% improvement in short run marginal cost profitability was probable compared to their base case scenario.

When comparing the other cases investigated by Mac Dowell and Shah (2015) to the present results, the recommended mode differs significantly. Exhaust gas venting, which was considered the least attractive alternative, proves to have great potential in the present work. The reason is that momentary emissions exceeding the 90 % capture rate limit is penalized quite heavily in the work by Mac Dowell and Shah (2015). However, if the time average emissions are considered only, the mode of exhaust gas venting will perform much better and may be suggested as the primary mode with the greatest potential. The formulation of CO_2 emission regulations (momentary or time average) will therefore be of great importance for the economic evaluation of the various modes.

The operating modes of exhaust gas venting and varying solvent regeneration allows the CO_2 emissions to exceed the limits that ensures 90 % capture for short periods. Both these methods are therefore limited to the capture plants maximum capacity during off-peak electricity price periods in order to reach 90 % average capture rate. That means

that the amount of captured CO_2 exceeding the 90 % capture rate defines how much additional CO_2 can be emitted during peak electricity price periods. These methods can have a greater potential if the 90 % average capture rate can be relaxed.

One final remark is that it is still unclear how the downstream processes, that is the CO_2 compression, transportation and storage part of the chain, will perform during varying CO_2 production rate. The power plant LP steam turbine must also be designed for varying loads and enable variable delivery of steam to the reboiler according to the operation plan. These issues should be assessed in order to get a full overview of the potential for overall profit improvements for flexible operation.

6. Conclusion

This work presents an evaluation of various flexible operating modes through dynamic simulations using the K-Spice® general simulation tool. Simulations of load following operation shows that the process reacts fast to load changes and is able to stabilize at both part and full load operation. Solvent storage as flexible operating mode, gives satisfactory results when it comes to average capture rate and energy performance in a varying electricity market. However, considerable investments are required for solvent storage tanks and additional operating solvent. The mode of exhaust gas venting and varying solvent regeneration is able to operate without any process modifications. Exhaust gas venting seems to give favorable average capture rate and energy performance indicators compared to the latter.

Recently, there has been an increasing focus on mapping the potential of flexible capture plant operation. Both technical and economical assessments are available in the literature. However, it is still not clear how the CO_2 compression, transportation and storage part of the chain will perform during varying CO_2 production rate. This should be assessed in order to get a full overview of the potential for overall profit improvements for flexible operation.

Acknowledgments

This work has been performed within the European FP7 OCTAVIUS project (Grant Agreement no 295645).

References

Biliyok, C., Lawal, A., Wang, M. and Seibert, F. (2012). Dynamic modelling, validation and analysis of post-combustion chemical absorption CO_2 capture plant. *Energy Procedia*, 9:428–445.

Bui, M., Gunawan, I., Verheyen, V., Feron, P., Meuleman, E. and Adeloju, S. (2015). Dynamic modelling and optimisation of flexible operation in post-combustion CO_2 capture plants - A review. *Computers and Chemical Engineering*, 61:245–265.

Chalmers, H., Gibbins, J. and Leach, M. (2012). Valuing power plant flexibility with CCS: the case of post-combustion capture retrofits. *Mitigation and Adaptation Strategies for Global Change*, 17:621–649.

Chalmers, H., Lucquiaud, M., Gibbins, J. and Leach, M. (2009). Flexible Operation of Coal Fired Power Plants with Postcombustion Capture of Carbon Dioxide. *Journal of Environmental Engineering*, 135:449–458.

Chikukwa, A., Enaasen, N., Kvamsdal, H. and Hillestad, M. (2012). Dynamic Modeling of Post-combustion CO_2 Capture Using Amines - A Review. *Energy Procedia*, 23:82–91.

Cohen, S. M., Rochelle, G. T. and Webber, M. E. (2010). Turning CO_2 Capture On and Off in Response to Electric Grid Demand: A Baseline Analysis of Emission and Economics. *Journal of Energy Resources Technology*, 132.

Davison, J. (2006). Performance and costs of power plants with capture and storage of CO_2. *Energy*, 32:1163–1176.

Enaasen, N., Zangrilli, L., Mangiaracina, A., Mejdell, T., Kvamsdal, H. M. and Hillestad, M. (2014). Validation of a Dynamic Model of the Brindisi Pilot Plant. *Energy Procedia*, 63:1040–1054.

Garðarsdóttir, S. Ó., Normann, F., Andersson, K., Prölß, K., Emilsdóttir, S. and Johnsson, F. (2015). Post-combustion CO_2 capture applied to a state-of-the-art coal-fired power plant - The influence of dynamic process conditions. *International Journal of Greenhouse Gas Control*, 33:51–62.

Lin, Y.-J., Wong, D. S.-H., and Jang, S.-S. (2012). Control Strategies for Flexible Operation of Power Plant with CO_2 Capture Plant. *AIChE Journal*, 58(9):2697–2704.

Mac Dowell, N. and Shah, N. (2015). The multi-period optimisation of an amine-based CO_2 capture process integrated with a super-critical coal-fired power station for flexible operation. *Computers and Chemical Engineering*, 74:169–183.

Mangiaracina, A., Zangrilli, L., Robinson, L., Kvamsdal, H. M., and Van Os, P. (2014). OCTAVIUS: Evaluation of flexibility and operability of amine based post combustion CO_2 capture at the Brindisi Pilot Plant. *Energy Procedia*, 63:1617–1636.

Wiley, D. E., Ho, M. T. and Donde, L. (2011). Technical and economic opportunities for flexible CO_2 capture at Australian black coal fired power plants. *Energy Procedia*, 4:1893–1900.